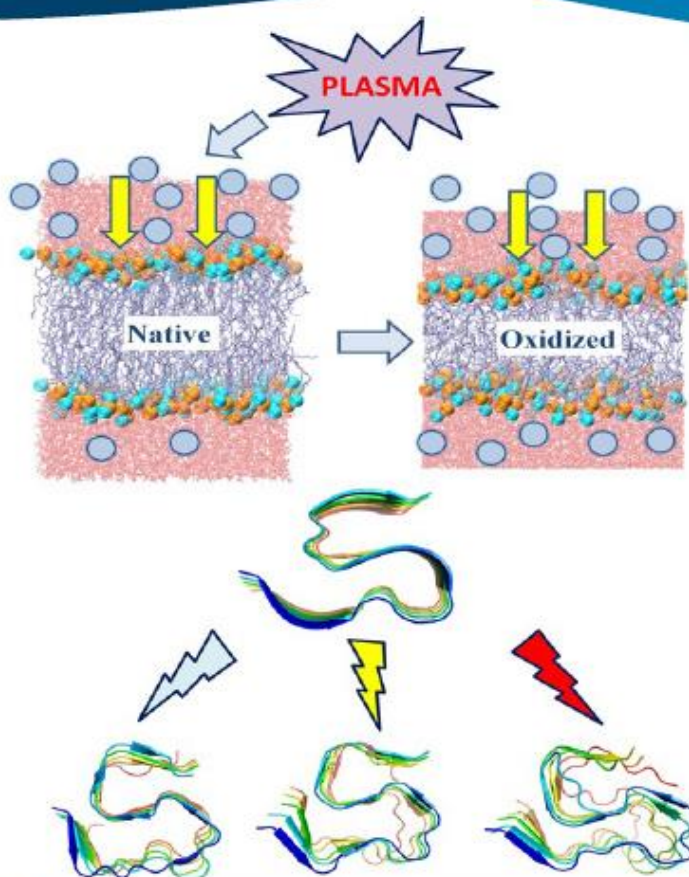


# Molecular level simulations for plasma medicine applications

Proefschrift voorgelegd tot het behalen van de graad van doctor  
in de chemie aan de Universiteit Antwerpen te verdedigen door

Jamoliddin Razzokov



PROMOTOR  
prof. dr. Annemie Bogaerts

Faculteit Wetenschappen  
Departement Chemie  
Antwerpen 2019

 Universiteit  
Antwerpen



Faculteit Wetenschappen

Departement Chemie

Molecular level simulations for plasma medicine applications

Simulaties op moleculair niveau voor toepassingen in  
plasmageneeskunde

Proefschrift voorgelegd tot het behalen van de graad van doctor in de Chemie  
aan de Universiteit Antwerpen te verdedigen door

**Jamoliddin Razzokov**

Promotor: Prof. Dr. Annemie Bogaerts,

Antwerpen 2019

# Table of Contents

Acknowledgements .....	6
CHAPTER 1.....	8
General Background.....	8
1.1. What is plasma?.....	10
1.2. Cold atmospheric plasma (CAP) devices: APPJ and DBD.....	11
1.3. Plasma medicine.....	14
<b>1.3.1 Antibacterial activity of plasma</b> .....	15
<b>1.3.2 Plasma for chronic wound healing</b> .....	16
<b>1.3.3 Plasma for drug delivery</b> .....	18
<b>1.3.4 Plasma destabilizes amyloid aggregates</b> .....	21
<b>1.4. Plasma in cancer treatment</b> .....	23
1.5 Aim of this PhD research .....	33
1.6 References .....	34
Chapter 2. ....	49
Computational methods.....	49
2.1. Introduction .....	51
2.2. Molecular dynamics .....	52
2.3 Umbrella sampling method .....	60
2.4 Docking simulations.....	62
2.6 Conclusion.....	64
2.7 References .....	65
Chapter 3. ....	70
Effect of oxidation on the cell membrane .....	70
3.1 Permeation of plasma species across native and oxidized membranes .....	72
<b>3.1.1 Introduction</b> .....	72
<b>3.1.2 Computational details</b> .....	72
<b>3.1.3 Results and discussion</b> .....	75
<b>3.1.4 Conclusion</b> .....	77
<b>3.1.5 Appendix</b> .....	78
<b>3.1.6 References</b> .....	81
3.2 Possible mechanism of glucose uptake enhanced by CAP.....	85
<b>3.2.1 Introduction</b> .....	85

<b>3.2.2 Computational details</b> .....	85
<b>3.2.3 Results and discussion</b> .....	88
<b>3.2.4 Conclusion</b> .....	89
<b>3.2.5 References</b> .....	91
3.3 Phosphatidylserine flip-flop induced by (plasma) oxidation of the cell membrane .....	93
<b>3.3.1 Introduction</b> .....	93
<b>3.3.2 Computational details</b> .....	94
<b>3.3.3 Results and discussion</b> .....	96
<b>3.3.4 Conclusion</b> .....	98
<b>3.3.5 References</b> .....	100
Chapter 4. ....	103
Effect of oxidation on the structure of proteins .....	103
4.1 Oxidation destabilizes toxic amyloid beta peptide aggregation .....	105
<b>4.4.1 Introduction</b> .....	105
<b>4.1.2 Computational details</b> .....	105
<b>4.1.3 Results and discussion</b> .....	107
<b>4.1.4 Conclusion</b> .....	111
<b>4.1.5 Appendix</b> .....	112
<b>4.1.6 References</b> .....	115
4.2 The effect of RONS on the structure of cytoglobin: A potential tumor suppressor .....	118
<b>4.2.1 Introduction</b> .....	118
<b>4.2.2 Computational details</b> .....	119
<b>4.2.3 Results and discussion</b> .....	120
<b>4.2.4 Conclusion</b> .....	122
<b>4.2.5 References</b> .....	123
4.3 Impact of plasma oxidation on structural features of human epidermal growth factor .....	126
<b>4.3.1 Introduction</b> .....	126
<b>4.3.2 Computational details</b> .....	126
<b>4.3.3 Results and discussion</b> .....	128
<b>4.3.4 Conclusion</b> .....	135
<b>4.3.5 Appendix</b> .....	136
<b>4.3.6 References</b> .....	143
4.4 Impact of plasma oxidation on the interaction between CD47 and SIRP $\alpha$ protein .....	148
<b>4.4.1 Introduction</b> .....	148

<b>4.4.2 Computational details</b> .....	149
<b>4.4.3 Results and discussion</b> .....	151
<b>4.4.4 Conclusion</b> .....	153
<b>4.4.5 References</b> .....	154
Summary and Samenvatting .....	159
Summary, Conclusion and Future Outlook .....	160
Samenvatting, Conclusie en Toekomstplannen .....	163
Academic curriculum vitae .....	167
List of publications included in this thesis .....	169
List of publications not included in this thesis .....	171
Conference contributions .....	173



## Acknowledgements.

The accomplishment of this work would not be possible without the help and support of many people, to whom I wish to express my thankfulness.

I would like to express my greatest appreciation and deep respect to my supervisor and advisor, head of the research group PLASMANT, Prof. Dr. Annemie Bogaerts. Thank you very much for giving me the opportunity of doing my PhD in your group. I am grateful for your permanent encouragement and support, as well as for your useful scientific advices in accomplishing this task. You always find time to teach everything in detail, even when you are very busy. Moreover, you always answer/reply to the questions sent by e-mail (by your students) without any delay, at any time of the day and at any day of a week and this is one of your peculiarities that deserve respect. I feel proud that I am a student of you – a supervisor, who is always willing to help her students with always an affable smile in her face. I learned many nice things from you that are momentous and helpful both in my research career and also in my life. Thank you very much for your support and understanding! *Hartelijk bedankt voor uw ontelbare momenten van hulp en vriendelijke ondersteuning!*

During my PhD, I spent an interesting time with the PLASMANT group members. *O'zbek hamkasblarim (akalim) Umedjon va Maksudbeklarga o'z minnatdorchiligimni bildiraman. Beminnat yordamlaringiz va ilmiy maslahatlaringiz uchun katta raxmat!*

It is also my pleasure to thank Luc Van't dack for the administrative and technical support. Thank you very much for setting up desktop/laptop and making computational research easier and faster.

The Turing HPC infrastructure at the CalcUA core facility of the Universiteit Antwerpen, a division of the Flemish Supercomputer Center VSC, funded by the Hercules Foundation, the Flemish Government (department EWI), and the Universiteit Antwerpen is also acknowledged for calculation support.

I am in debt to my former supervisors, Dr. Aliev Sul-tonmurod, Dr. Shavkat Mamatkulov and Prof. Dr. Paul van der Schoot. Thanks for your sincere advices and support, which helped me in period of my PhD in the PLASMANT group.

I am also forever in debt to my parents, Inotullo Razzokov and Dilbar Razzokova, for their love and blessings, support and understanding, as well as their encouragements in every step of my life. I especially thank my family, my wife Khafiza and son Ib-rokhim for their endless love and understanding.



# **CHAPTER 1.**

## **General Background**



## 1.1. What is plasma?

Plasma is an ionized gas, containing various species, such as electrons, neutral particles, radicals, ions, photons (i.e., infrared radiation (IR), visible and vacuum ultraviolet (VUV) /ultraviolet (UV)) and electromagnetic field. It is also referred as the fourth state of matter. Basically, matter transforms from solid to liquid to gas, and finally to plasma, by increasing the energy of the system (see [Figure 1.1](#)).

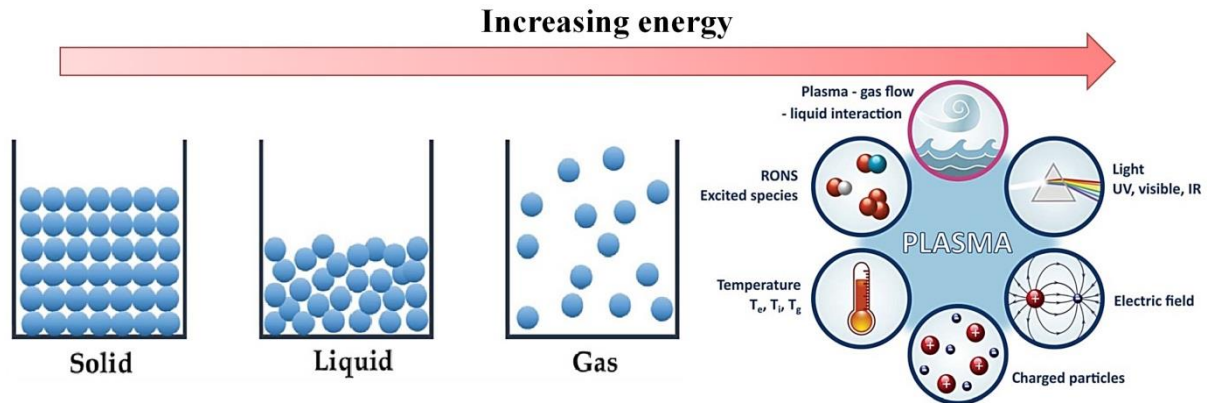


*Figure 1.1. The generation of plasma upon increasing the energy of matter. Figure is adopted from <sup>1</sup> and <sup>2</sup>.*

Plasma can be subdivided into thermal and non-thermal plasma. In thermal plasma, the temperature of all species is virtually the same, and this temperature typically reaches several thousand degrees, but it can also reach several million degrees, like in natural plasmas.<sup>3</sup> The Sun, the solar corona, stars and lightning are common examples of natural thermal plasmas (see [Figure 1.2](#)).

Besides heating, an electric or magnetic field or microwaves also can be utilized to supply sufficient energy to a gas, in order to generate a plasma. This allows to generate non-thermal plasmas. When non-thermal plasmas are operated at atmospheric pressure, they are sometimes referred to as “cold atmospheric plasma” (CAP). They can be obtained in laboratory conditions, and operate at room temperature, by applying an electric field. In these kind of plasmas the temperature of the electrons is much higher than of the heavy particles ( $T_e \gg T_h$ ) and reaches in the order of  $10^4$  K. Thus, CAP devices produce energetic electrons instead of heating the entire gas stream, while the rest of the plasma components remains relatively cold, between 25 and 45 °C.<sup>4,5</sup>

A wide variety of CAP devices have been designed and developed for specific applications in the past two decades.<sup>6-11</sup> Mainly two types of CAP devices, i.e., the atmospheric pressure plasma jet (APPJ) and the dielectric barrier discharge (DBD), are being used for biomedical applications without causing thermal damage. This feature of CAP devices is highly beneficial to treat heat-sensitive materials, such as polymers and living tissue. A further overview about the technical characteristics of both plasma sources is given below.

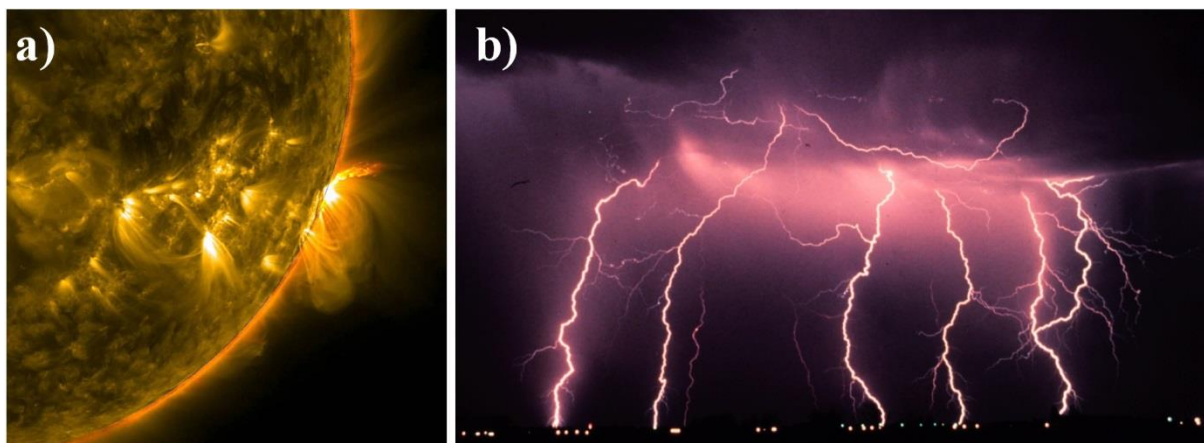


Figure 1.2. *Natural plasmas. a) Solar corona and b) lightning; pictures are taken from nasa.gov.*

## 1.2. Cold atmospheric plasma (CAP) devices: APPJ and DBD

The electrical breakdown of a neutral gas under an external electric field is the most commonly employed way to generate a non-thermal plasma, and it is also used to construct APPJs. This type of devices indirectly delivers plasma species through a continuous gas flow from the discharge device. A schematic illustration of commonly used set-ups of APPJs is given in [figure 1.3](#). Basically, an APPJ is made of two electrodes between which a feed gas (mostly argon, helium, oxygen or a combination) flows at a certain rate. As is clear from [figure 1.3](#), the main differences of the APPJs are the discharge geometry, the position of the electrodes, the electric field configuration, the excitation frequency (e.g., direct current (dc), alternating current (ac), radio frequency (rf) and microwave (MW) driven) and the excitation form (e.g., pulsed or continuous wave).<sup>12</sup> For example, in order to ignite the discharge gas in the device based on geometry 7, it is sufficient to apply 13.56 MHz RF power to the electrode 1 at a voltage between 100-250 V (see [Figure 1.3](#)).<sup>13,14</sup> Marinov *et al.* studied an efficient RF coupling scheme for an APPJ, demonstrating the possibility of sustaining the plasma even at 0.5 W power.<sup>15</sup> These types of plasma jets are called micro-scale atmospheric pressure plasma jet ( $\mu$ APPJ) and have been investigated extensively, both experimentally and by computer simulations within the last decade.<sup>15-18</sup> In these devices the energetic electrons driven by RF power give rise to collisions with the feed gas, which leads to the generation of a cocktail of positive and negative ions, metastable atoms and molecules, reactive oxygen and nitrogen species (RONS), as well as highly energetic photons (e.g., UV). APPJs produce a rather constant, homogenous and non-equilibrium plasma at atmospheric pressure. This plasma is directed through the nozzle to the substrate to treat the samples. An extensive review of various APPJ plasma sources and their applications can be found elsewhere<sup>12,19</sup>. Note that, in literature, plasma jets are termed as ‘APPJ’, but also as ‘plasma bullet’, ‘plasma gun’, ‘plasma pencil’, ‘plasma needle’ and ‘plasma plume’.<sup>20-25</sup>

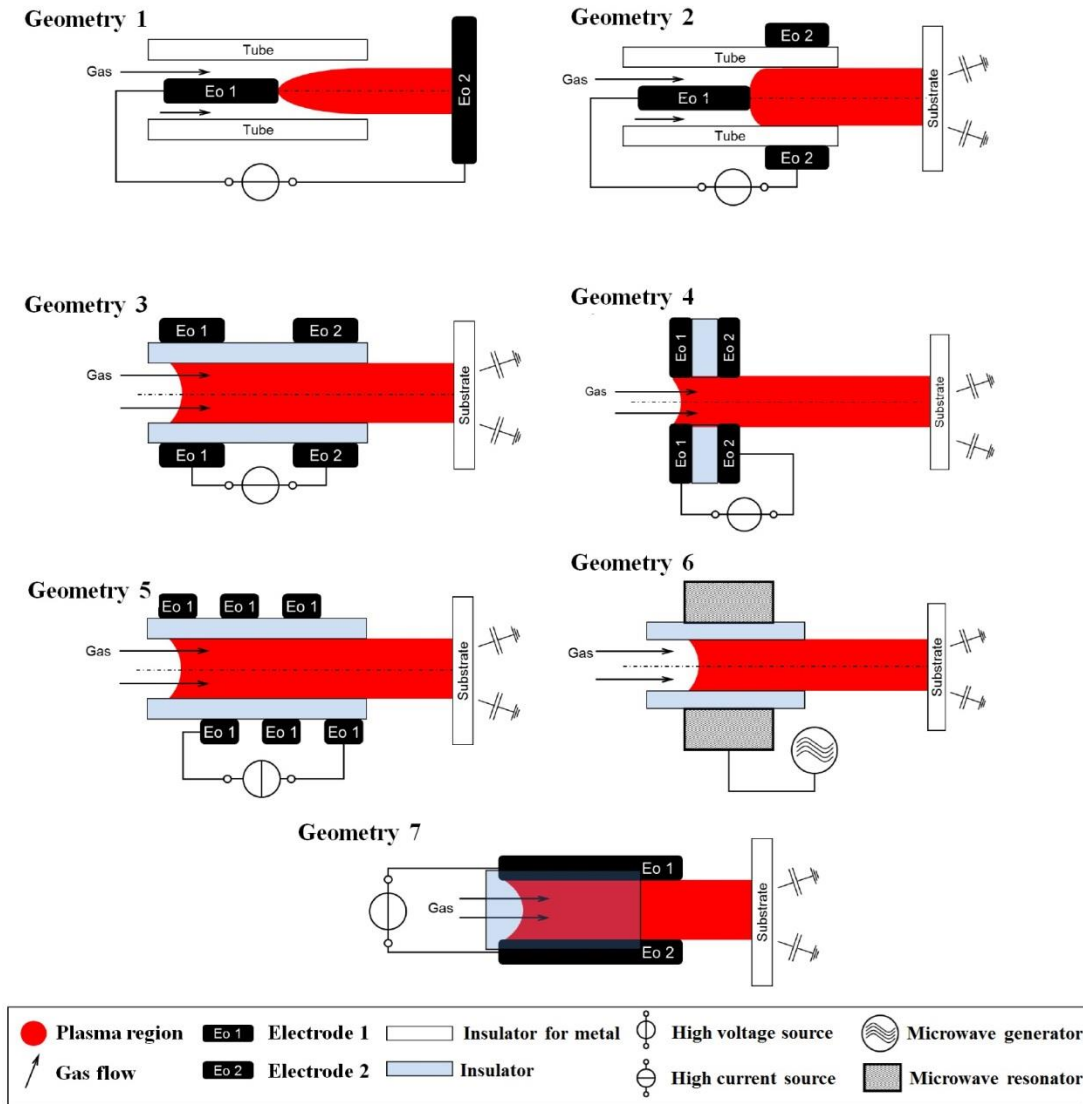


Figure 1.3. Cross sectional representation of the primary geometries of coaxially (geometry 1–6) and rectangular (geometry 7) arranged plasma jets. Figure is adopted from <sup>12</sup>.

Many different user-friendly APPJ sources have been developed, which are compatible for biomedical use.<sup>26-32</sup> Some of them are the kINPen 09 and kINPen MED (INP Greifswald)<sup>33</sup> (design corresponds to geometry 2 in [Figure 1.3](#)), SteriPlas (AdTec Ltd., Japan)<sup>34</sup>, PlasmaDerm (Cinogy GmbH, Germany)<sup>35</sup>, and PlasmaOne (Medical Systems GmbH, Germany), which are commercially available devices that have been used for wound healing, as well as bacterial decontamination.

The other source of non-equilibrium plasma at atmospheric pressure, which is often used for biomedical applications, is the DBD. This type of device also consists of two electrodes and at least one of these electrodes is covered by a dielectric layer.<sup>6</sup> This enables to generate a non-equilibrium atmospheric pressure discharge. [Figure 1.4](#) illustrates various forms of DBD, depending on geometry.

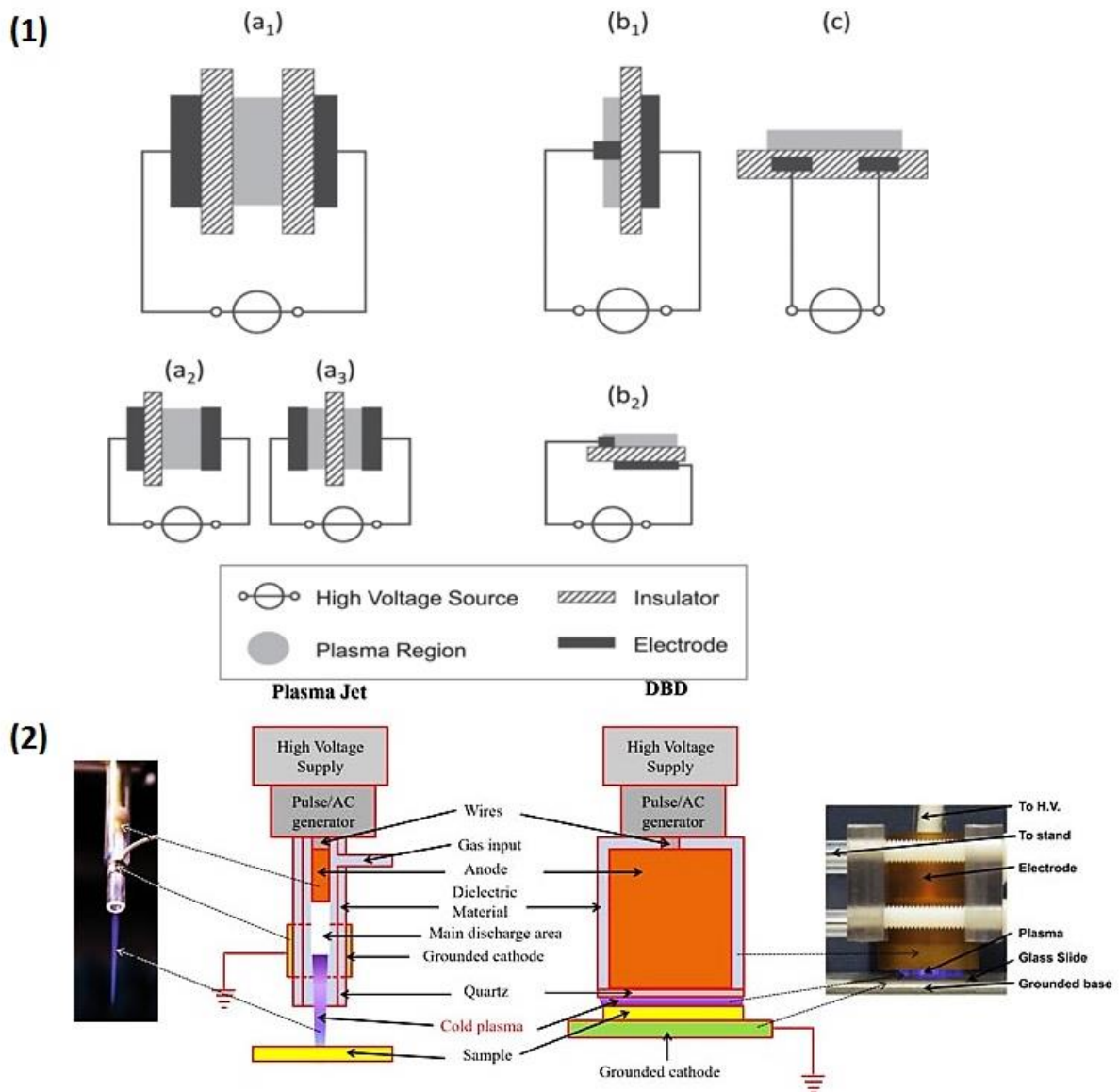


Figure 1.4. (1) Basic planar configurations of DBDs: (a) volume DBD (1-symmetric, 2-asymmetric, 3-floated dielectric); (b) surface DBD (1-symmetric, 2-asymmetric 'actuator' design); (c) coplanar discharge. Figure is adopted from <sup>36</sup>. (2) The plasma jet and DBD device are two main devices employed in biomedical applications. Figure is adopted from <sup>37</sup>.

Figure 1.4 shows the similarities and differences between plasma jet and DBD. The electron density generated by DBD is 2-3 orders of magnitude higher than for APPJs.<sup>6,38</sup> The discharge gap varies between 0.1–10 mm, for a DBD with pulsed high voltage in the range of 1-100 kV/m. Special configurations of DBDs, such as sliding discharge,<sup>39</sup> capillary plasma electrode discharge,<sup>40</sup> microcavity plasma array<sup>41,42</sup> and piezoelectric transformer<sup>43</sup> based devices also have been developed. DBD devices specifically used for medical applications typically contain only one electrode, while the human body itself may serve as the second electrode.<sup>35</sup> In other words, one electrode is also sufficient for functioning of these devices.<sup>44</sup>

From a practical point of view, the APPJ and DBD both have pros and cons. A DBD is capable to cover a larger treatment area than an APPJ, while APPJs are more suitable for targeted spot-like treatments. In most cases, DBDs make use of atmospheric air as the feed

gas. This is one of the advantages, because no additional feed gas is required for functioning of a DBD. On the other hand, APPJs use a feed gas to generate the plasma, and to carry it outside the device, and its composition can be controlled during treatment. Depending on the specific task, different types of gases can be employed for triggering a certain biological outcome.<sup>45</sup> The plasma produced by DBD is more sensitive to the surrounding conditions, e.g., humidity and distance between the device and skin surface, which serves as counter electrode.<sup>46</sup>

In order to increase the efficiency of both APPJs and DBDs in particular tasks, controlling the plasma parameters and understanding their fundamental effects still is one of the challenges, which require further insight. Many investigations aim to reveal the complex interaction of CAP e.g., with aqueous solutions, biological macromolecules, cells and animal models, both experimentally and by computer simulations. These extensive worldwide studies by various research groups have led to the emerging highly interdisciplinary field, called “Plasma medicine”, opening new horizons in the field of medicine. The latter is the main subject of this thesis. The next section highlights the “Plasma medicine” research field in more detail, targeting applications of CAP in medicine.

### **1.3. Plasma medicine**

Plasma medicine is gaining increasing interest, due to its promising biomedical applications. The history of plasma medicine is illustrated in [figure 1.5](#). Plasma medicine started with experiments on the inactivation of bacteria in its early stages.<sup>47</sup> Nowadays, the main tools of plasma medicine (CAP devices), such as APPJ and DBD, have been improved and are widely used, particularly in wound healing, blood coagulation, drug delivery and cancer treatment.<sup>48-51</sup> It is shown that plasma species change the microenvironment of the exposed area, inducing damage to the microorganisms, stimulating cell proliferation (in low dose) and facilitating regeneration of tissue in wound healing, and causing apoptosis (programmed cell death) or even necrosis (premature cell death due to injury e.g., toxins, infections or an overdose of RONS) in cancer treatment.<sup>52</sup> Thus, controlling the treatment time allows to regulate the dosage of CAP-generated species, which are able to penetrate deeper inside the cell. Recently, *in vitro* and *in vivo* experiments have revealed that CAP is also capable to induce immunogenic cell death (ICD).<sup>53-56</sup> In other words, plasma facilitates the detection of cancer cells by the immune system, affecting intracellular signaling pathways that govern ICD.

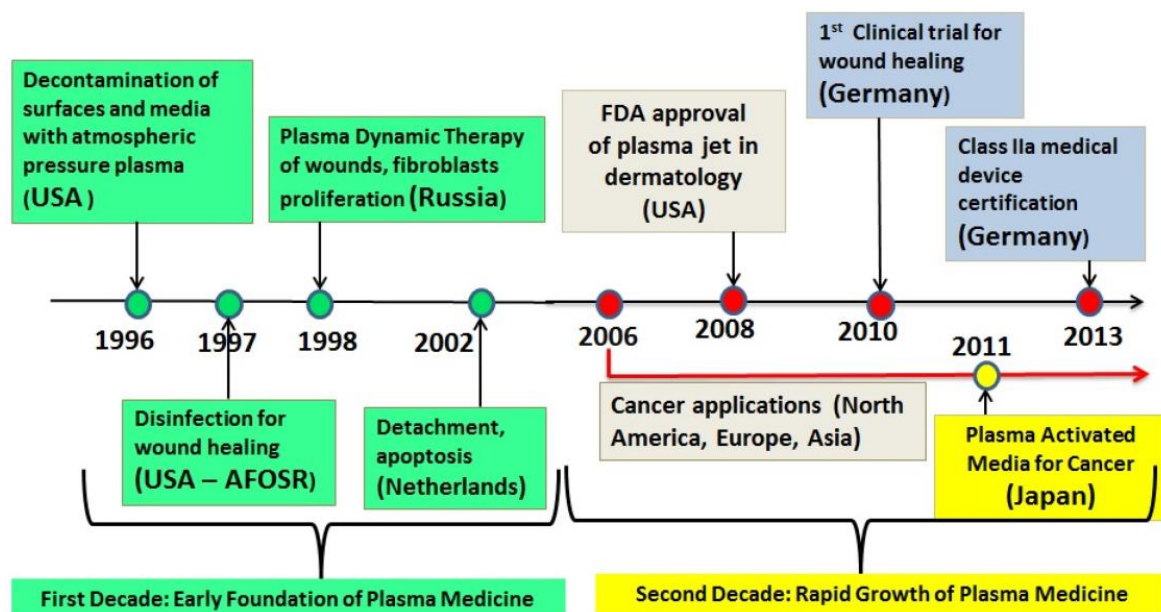


Figure 1.5. The development stages of plasma medicine: major milestones. Figure is adopted from <sup>54</sup>.

In the following sections, the application of CAP for disinfection (1.3.1), wound healing (1.3.2), drug delivery (1.3.3), elimination of amyloid aggregates (1.3.4) and cancer treatment (1.4) will be discussed in detail.

### 1.3.1 Antibacterial activity of plasma

Recent investigations showed that CAP treatment effectively removes many types of bacteria, despite their adaptability for external changes.<sup>58-60</sup> In addition, CAP also demonstrated its potential against viruses and fungi.<sup>61</sup> CAP sources are quite rapid in disinfection of biofilms compared to other traditional methods (e.g., long time exposure of surgical tools in specific liquids).<sup>45,62</sup>

The resistant nature of bacteria is associated with their architecture of the extracellular matrix. This matrix consists of two protective covers, i.e., the outer cell wall and the inner cell membrane. Some types of bacteria have more than two protective layers, forming a rigid protective capsule (e.g., gram positive and gram negative bacteria). Therefore, often antimicrobial agents are less effective to remove deposited bacteria forming biofilms, because they cannot penetrate deep inside, in order to inactivate the biofilms. In contrast, plasma-generated species are able to penetrate deep inside the biofilm, which is not accessible for antimicrobial agents. Katya *et al.* treated biofilms formed by *C. albicans* on the surface of polystyrene wafers by means of a plasma jet, varying the treatment time and composition of the feed gas.<sup>45</sup> The biofilms were exposed to an Ar/O<sub>2</sub> plasma for over 300 s, but 180 s treatment time was found to be sufficient to etch approximately 95% of the biofilm in the treated sample (see Figure 1.6). Besides, argon in combination with oxygen was critical to achieve a high efficacy in biofilm removal with an etching rate of 33 to 67 nm/s. These results indicate that plasma significantly improves the biofilm removal efficiency. Many other

investigations also demonstrated that CAP is capable to efficiently eliminate pathogens, including highly resistant bacteria.<sup>9,63-68</sup>

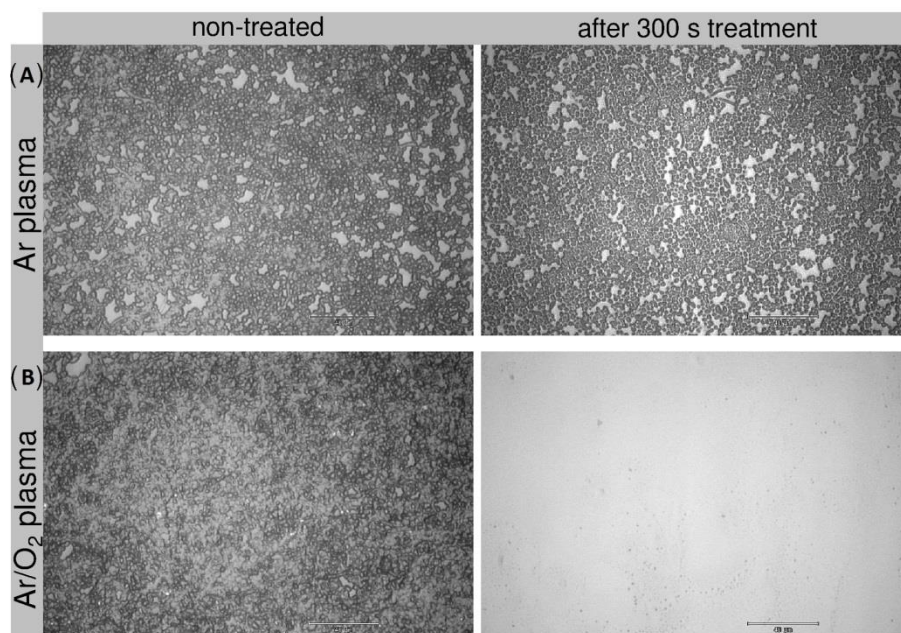


Figure 1.6. *C. albicans* grown in polystyrene wafer. Samples are exposed to: (A) Ar gas discharge plasma and (B) Ar and O<sub>2</sub> mixture gas discharge plasma for 300 s. Figure is adopted from<sup>45</sup>.

The underlying mechanisms of bacterial inactivation was explained by Yusupov *et al.*, performing molecular dynamics (MD) simulations with peptidoglycan (PG), applying reactive force field parameters.<sup>69,70</sup> PG is one of the main building blocks of the gram-positive bacterium *Staphylococcus aureus* murein cell walls. The role of O and O<sub>3</sub> in bond-cleavage (i.e., C–O, C–C and C–N bonds) in the PG structure was determined. The reactions occurred mainly in disaccharides, breaking C–N or C–C bonds. This might lead to destruction of the bacterial cell wall, inactivating bacteria by plasma-generated species.

In order to achieve efficient inactivation of microorganisms by CAP, the optimal parameters (of the device, feed gas, optimal treatment time and operating distance between source and object, contribution of certain reactive species) need to be determined.

### 1.3.2 Plasma for chronic wound healing

Wound healing is a quite complicated series of reactions, in which skin and tissues activate a number of specific biochemical events to repair the injury.<sup>71</sup> These events include four overlapping and precisely programmed phases: hemostasis (aggregated platelets and cross linked fibrin formation i.e., thrombus), inflammation (e.g., blood clotting, removal of bacteria), proliferation (angiogenesis, collagen deposition, epithelialization and wound contraction), and maturation (tissue remodeling).<sup>72</sup> If these natural healing process steps are compromised (e.g., by invasion of microorganisms), it might lead to the formation of non-healing chronic wounds. Therefore, it is important to protect the injury from infections, to speed up the healing period.

Mainly two local factors influence the healing process: oxygenation and infections. The importance of oxygen in preventing infection, induction of angiogenesis, enhancement of keratinocyte differentiation and migration, increasing fibroblast proliferation and collagen synthesis, is discussed in detail in the review of Bishop<sup>73</sup> and Rodrigues *et al.*<sup>74</sup>. Besides, according to a number of studies, the role of RONS, particularly H<sub>2</sub>O<sub>2</sub>, superoxide (O<sup>2-</sup>) and nitric oxide (NO), is found to be essential in wound healing, which is beyond just oxidative elimination of pathogens.<sup>75-77</sup> For instance, NO also participates in an intercellular communication network during the healing process, regulating the behavior of macrophage, keratinocyte and fibroblast.<sup>78</sup> In other words, tissue repair and regeneration steps are highly influenced by the intracellular RONS. Moreover, when the wound is not sufficiently decontaminated, the inflammation step might be prolonged. Once healing fails, the wound enters to the chronic state. This also leads to rapid degradation of growth factors, which slows down the healing process.<sup>79</sup> Another reason for failing of healing chronic ulcers is the presence of *P.aeruginosa* and *Staphylococcus* bacteria. These bacteria form biofilms, developing a microenvironment which becomes more resistant for conventional therapies (e.g., antibiotics). Therefore, the pathogen elimination is a precondition for wound stabilization in order to restore the necessary steps in healing progression. In this regard, chronic wound healing remains one of the challenges in health care. CAP shows great potential for both decontamination of pathogens (see section [1.3.1](#)) and as source of RONS (see section [1.1](#)) to deliver directly to the wound area.

Many investigations have been performed in order to achieve a desired therapeutic effect in wound healing by applying plasma.<sup>33,48,80-82</sup> Maisch *et al.* studied the efficacy of CAP in decolonization of MRSA, *S. aureus* and *E. coli*. using *ex vivo* porcine skin model *in vitro*.<sup>60</sup> They demonstrated that CAP treatment reduced bacteria without harming the porcine skin cells. *In vitro* (cell culture with human fibroblasts) and *in vivo* (mouse skin model) animal data obtained by Arndt *et al.* showed that CAP (with the MicroPlaSter) treatment activated relevant molecules (IL-6, IL-8, MCP-1, TGF- $\beta$ 1, TGF- $\beta$ 2) in dermal fibroblast, enhancing wound healing.<sup>83</sup> These systematic studies with animal models also suggested that CAP treatment supports chronic wound healing in animals.<sup>84-87</sup> This opened a new route for further clinical tests in patients, after verification of the safety of CAP sources in animal models. The clinical tests performed on more than 100 patients by Isbary and collaborators, demonstrated the beneficial effects of CAP (with the MicroPlaSter) treatment for the healing of chronic wounds (see [Figure 1.7](#)).<sup>88,89</sup> Experiments using the kINPen MED in 16 patients also evidenced wound surface reduction in leg ulcers, accelerating the healing process.<sup>90</sup> We also studied the impact of oxidation to the human epidermal growth factor (hEGF) in the context of plasma wound healing, as well as for plasma cancer treatment, by means of both experiments and computer simulations. hEGF is one of the important proteins that stimulate cell growth and differentiation by interacting with its receptor (hEGFR). Thus, regulation of the interaction between these proteins allows to control over the cell proliferation. In this respect, our molecular level simulations helped to understand the fundamentals of the role of CAP in wound healing, of which more details are given in [Chapter 4](#).



Figure 1.7. *Inflamed leg ulcer (a), after 12 (b) and 20 treatments (c). The wound was exposed 5 times per week to an Ar CAP. Significant enhancement was observed in the wound area. Figure is adopted from <sup>89</sup>.*

As we know, CAP sources strongly differ from each other, which makes it difficult to compare the obtained data or summarize the results from a biochemical point of view. In this respect, future wound healing would benefit from categorized, systemic and molecular level approaches, which can provide fundamental insights of each healing phase influenced by CAP.

### 1.3.3 Plasma for drug delivery

Drug delivery is used to transfer pharmaceutical compounds to the cell interior through the cell membrane, in order to reach the desired therapeutic effects.<sup>91</sup> This might be achieved by special chemical formulation, via medical device or in combination with drug-device products.<sup>92-95</sup> A number of investigations demonstrated that the application of CAP also induces transport of drugs to the cytosol (cell interior).<sup>96-102</sup> This approach is relatively new in the field of drug delivery. CAP-based drug delivery and its molecular level mechanism is discussed below.

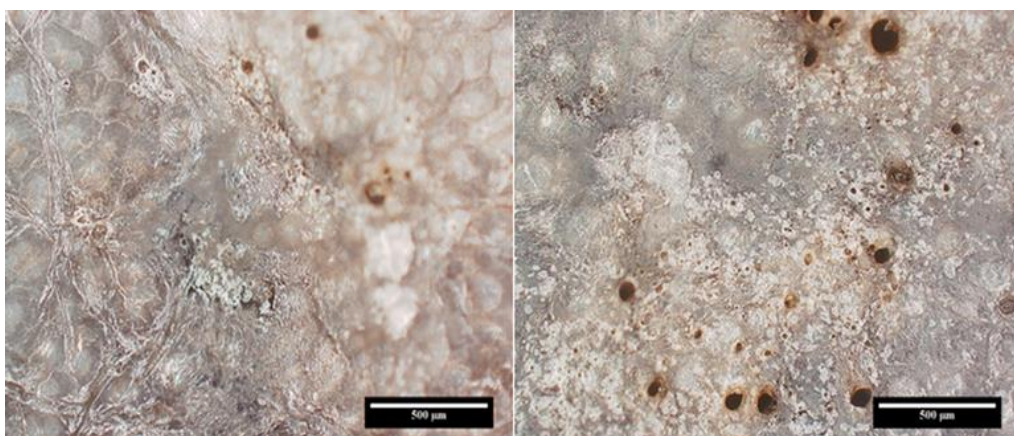


Figure 1.8. *10 s (left) and 30 s (right) skin treatment by a plasma jet. The black spots indicate pores formed during the treatment.*

The primary barrier of the cell is the phospholipid bilayer (PLB). Drugs need to overcome this barrier, in order to ingress to the cell interior. Specifically, the penetration of hydrophilic or lipophilic drugs and drugs with high molecular weight across the PLB is less favorable or

even impossible. Therefore, virus capsids, functionalized nanocarriers or special devices have been used to execute internalization of drugs. One of the widely used methods is electroporation, which helps to enhance the uptake of exogenous medicaments.<sup>103</sup> This method operates by applying an external electric field, creating short high-voltage pulses across any cell membrane to form a temporary pore, which reversibly closes.<sup>104</sup> The applied potential has to be appropriately chosen, otherwise it might induce significant damage and local inflammation. It was also reported that electroporation causes pain, by exciting the underlying nerves.<sup>105</sup> CAP sources can also be used as a complementary tool for drug delivery.<sup>96-102</sup> For instance, Shimuzu and Kristof observed pore formation on the skin after CAP treatment in their drug delivery studies, with creation of a pore, to facilitate drug uptake (see [Figure 1.8](#)).<sup>106</sup> Leduc *et al.* specified the maximum radius of macromolecules that are capable to ingress into HeLa cells, applying a specifically designed CAP device. Vijayarangan *et al.* determined the optimal plasma treatment time (100 s) at frequencies in the range of 10-100 Hz (with an according number of applied pulses between  $10^3$  and  $10^4$ ) for efficient drug uptake in HeLa cells.<sup>99</sup> Ogawa *et al.* and Sakai *et al.* studied gene transfer into various cell lines (HeLa, CHL, HUVEC, HeLa-S3, HT-1080 and MCF-7) by making use of CAP. Their results suggested that the gene uptake was significantly enhanced in CAP-exposed cells in comparison with electroporation. Moreover, CAP treatment facilitated the permeation of a lipophilic drug (Cyclosporine A, with molecular weight of 1203 Da) through the skin model.<sup>96</sup> These experimental observations evidenced that drug delivery with CAP is feasible. However, it is also equally important to obtain molecular level insight in the complex nature of the interactions of plasma-generated species with the cell membrane, for improving our understanding on the drug delivery capabilities of CAP.

Reactive species generated by CAP can induce oxidation of the cell membrane, modifying its composition, such as the phospholipids, cholesterol, etc. The underlying mechanism of ROS interaction with the cell membrane was investigated by reactive and non-reactive MD simulations, validated by experiments.<sup>107</sup> According to reactive MD simulations, two lipid oxidation products were formed (head group and lipid tail oxidation). Mass spectrometry data showed that lipid tail oxidation (aldehyde - ALD) was more prominent than head group oxidation. The calculated area per lipid, as well as the membrane fluidity increased, while the PLB thickness decreased in long term non-reactive MD simulations on PLB with ALD oxidation product. Moreover, MD simulation results indicated that pore formation occurred in highly oxidized PLB.<sup>108</sup> This is also one of the explanations why drug uptake is increased for plasma-treated cells, probably passing through the pores. In order to study the synergistic effect of the electric field together with plasma-induced lipid oxidation, Yusupov *et al.* performed MD simulations, varying the oxidized content of the PLB and applying different values of electric field.<sup>109</sup> This study mimics experimental conditions where CAP impacts to the cell both by oxidation and by inducing an electric field. [Figure 1.9](#) shows that the threshold time of pore formation strongly depends on the oxidation degree of the PLB and the applied electric field. As is clear, pore formation is more prominent in the aldehyde oxidation case, while it is insignificant for peroxidation of the PLB (see [Figure 1.9](#)). The authors explained the behavior of pore formation with the barrier functions of the PLB, in which oxidation led to a decrease of the permeation free energy barriers of the ROS. Pore formation

was detected by the creation of water defects during the simulation. Overall, these MD simulation results revealed the molecular level mechanism of CAP-induced electric field and lipid oxidation on living cells.

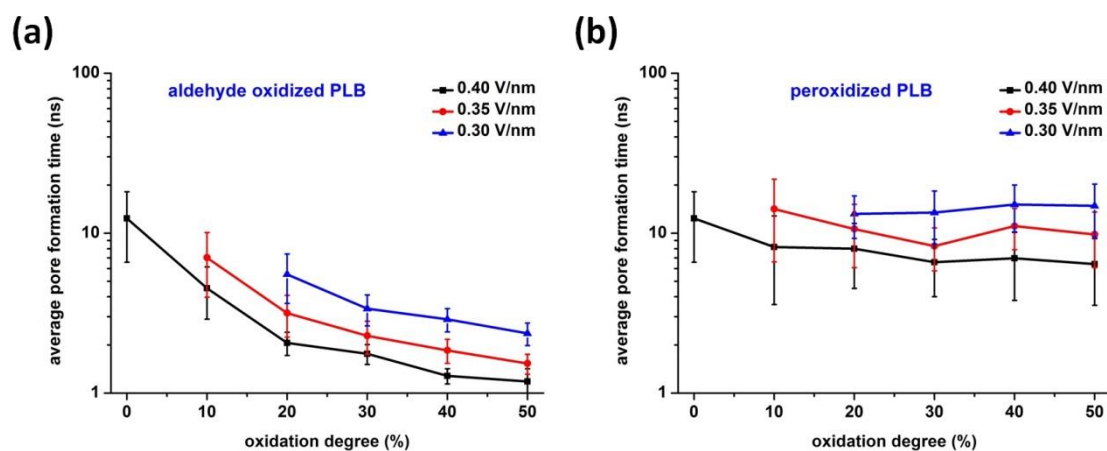


Figure 1.9. Average pore formation time in aldehyde oxidation (a) and peroxidation (b) systems under the influence of three different electric fields.

Recent experiments have evidenced that CAP can also enhance the intracellular uptake of glucose molecules, which is important in diabetes therapy.<sup>110</sup> Diabetes is a chronic disease related to an abnormal increase of the glucose level in the blood. Approximately 75% of glucose in the body is consumed by skeletal muscle cells that are stimulated by insulin.<sup>111,112</sup> Failure of glucose uptake leads to a high level of sugar present in the blood. This is due to one of two mechanisms or a combination of both, i.e., a) disproportional production of insulin or b) inadequate sensitivity of cells to insulin.<sup>113-115</sup> Most of the currently available pharmaceuticals are inefficient in the treatment of diabetes, which requires to find alternative insulin-independent healing methods, in order to increase the glucose uptake by muscle cells. As mentioned above, CAP can be used to regulate glucose homeostasis in muscle cells.<sup>110</sup> The experimental results showed that the glucose uptake is significantly enhanced in skeletal muscle cells, including intracellular  $\text{Ca}^{2+}$  and ROS after plasma treatment, exhibiting the beneficial effects of CAP (see [Figure 1.10](#)). It is clear that the plasma-stimulated glucose uptake efficacy was even higher in comparison with the traditional method (i.e., insulin treatment). Hence, an increase of the cell membrane permeability might play an important role in the delivery of glucose into the cell. The underlying mechanisms, however, still remain unclear, and need more thorough investigations. In this regard, we studied the glucose translocation across native and oxidized membranes employing MD simulations, in order to provide a possible explanation to the mechanism of glucose uptake observed in experiments (see [Chapter 3](#)).

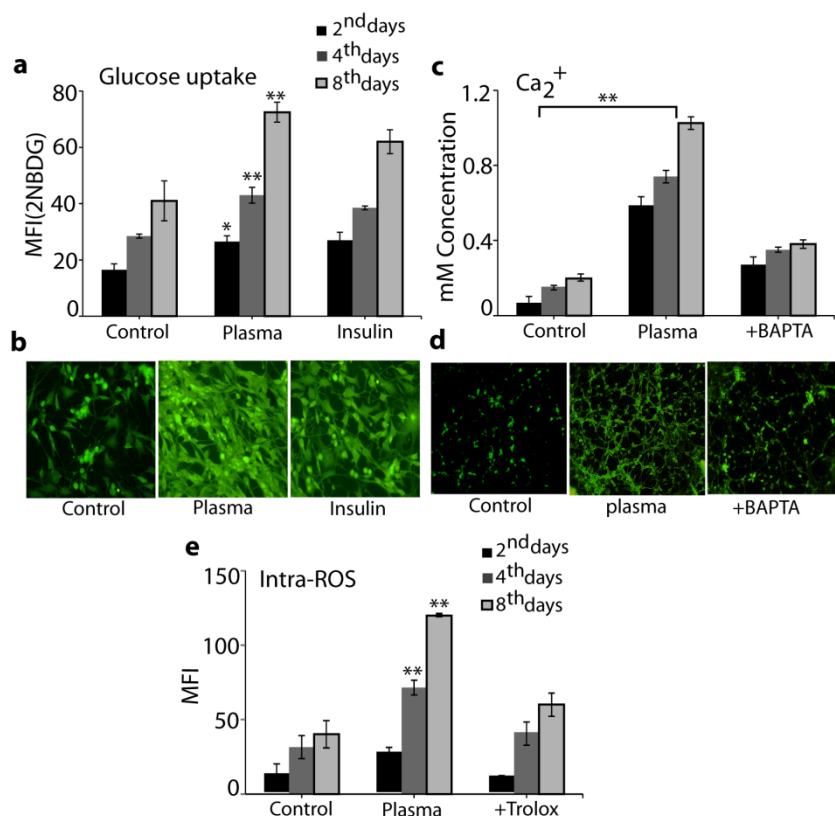


Figure 1.10. Glucose uptake (a) and (b), cytosolic Ca<sup>2+</sup> (c) and (d) and intracellular ROS (e) analysis after treatment with a  $\mu$ s-DBD for 90 s, as well as with insulin ((a) and (b)), chelator BAPTA ((c) and (d)) and trolox (e), measured on day 2, 4 and 8. Fluorescence images of 2NBDG uptake (b) and Ca<sup>2+</sup> (d) were taken on day 8. Obtained from <sup>110</sup>.

We also studied the permeation of RONS and phospholipid flip-flop (in the context of cancer treatment) across native and oxidized PLBs using MD simulations. These computer simulations may serve to gain fundamental insights in the impact of oxidation to the barrier function of the PLB. Besides, revealing the transport processes of molecules occurring in native and oxidized PLBs is challenging or even impractical to obtain by experiments. Detailed MD simulation results will be given in [Chapter 3](#).

### 1.3.4 Plasma destabilizes amyloid aggregates

Self-assembled forms of amyloid beta peptides, i.e., amyloid aggregates, cause many severe diseases, such as Parkinson, diabetes 2, prion and the spongiform encephalopathies.<sup>116,117</sup> Although irrelevant for sporadic Alzheimer's disease (AD), these aggregates of amyloid beta (A $\beta$ ) peptides in neural tissue is one of the many causes of AD.<sup>118</sup> These amyloid aggregates interact with the cell membrane, increasing the permeability, such as the calcium influx, which leads to the activation of apoptotic signaling pathways in neuronal cells.<sup>119,120</sup> Therefore, self-assembled forms of A $\beta$  peptides are correlated with neuronal cell death. This results in abnormal cognitive functioning in patients with AD.<sup>121</sup> In order to inhibit the aggregation of A $\beta$  peptides, various classes of small molecules and

peptides are used, but these drugs either cannot influence the AD progression, or they are still in clinical trials.<sup>122,123</sup>

A number of experimental and computational studies were already performed, aiming at destabilizing the A $\beta$  peptide aggregates. For instance, molecular dynamics (MD) simulations were conducted to study the contribution of the hydrophobic residues Met, Ile, Phe and Val in the stability of A $\beta$  pentamer.<sup>124</sup> The results indicated that these hydrophobic residues play a potential role in the stability of A $\beta$  pentamer. Moreover, in order to investigate the thermodynamics of peptide dissociation in A $\beta$  pentamer, Lemkul *et al.* mutated specific residues of this system.<sup>125</sup> The authors reported that the hydration level around the Asp23-Lys28 salt bridge promotes the A $\beta$  pentamer stability. The impact of oxidation of Met35 residue on the stability of a A $\beta$ <sub>40</sub> monomer structure (i.e., A $\beta$  monomer consisting of 40 AAs) was studied by Brown *et al.*, varying the pH and the salt concentration of the solution, and employing replica exchange MD simulations.<sup>126</sup> Their results showed the reduction of the  $\beta$ -strand content in the structure, invoked by oxidation of the Met35 residue.

A drop in the aggregation rate was also experimentally observed due to Met35 oxidation of A $\beta$  peptides.<sup>127,128</sup> Specifically, in <sup>127</sup>, the post-translational modification of Met35 into methionine sulfoxide significantly attenuated the aggregation of A $\beta$ <sub>1-42</sub> and A $\beta$ <sub>1-40</sub> peptides, thereby reducing their neurotoxicity. The authors proposed that the oxidation of Met35 can be an example oxidative process, which acts advantageously to slow down the progression of AD.<sup>127</sup> The characteristics of A $\beta$ <sub>1-40</sub> peptide aggregation before and after oxidation of Met35 were studied in <sup>128</sup> by Fourier transform ion cyclotron resonance mass spectrometry. The results showed that the formation rate of an A $\beta$ <sub>1-40</sub> trimer and tetramer considerably reduced after oxidation of Met35, in comparison to the native A $\beta$ <sub>1-40</sub> peptide. Furthermore, applying CAP as an oxidation source, Bayliss and coworkers<sup>129</sup> treated amyloid aggregates for 2, 4, 6 and 8 s in aqueous solution (see [Figure 1.11](#)).

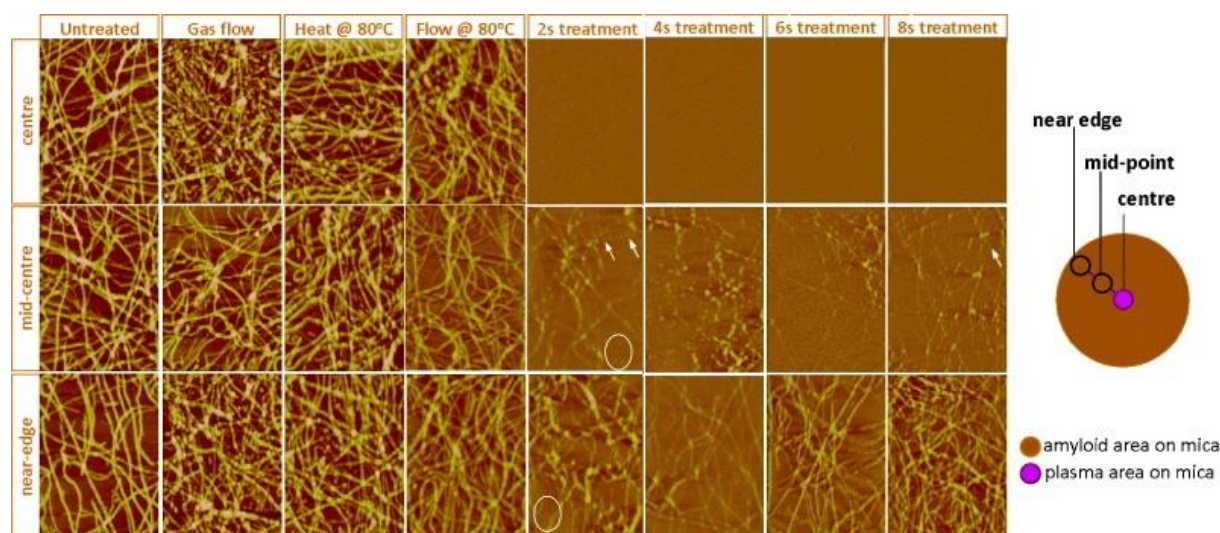


Figure 1.11. Atomic force microscopy (AFM) images of amyloid aggregates. Columns 1-4 illustrate untreated samples, samples treated with only helium flow, heated at 80 °C, and flow in combination with heating at 80 °C, respectively. Columns 5-8 show the results of 2, 4, 6 and 8 s CAP treatment.

As is clear from this figure, the morphology of amyloid aggregates was not changed during the physical treatments. However, the results showed that 2 s of treatment with CAP already led to a significant reduction of the amyloid aggregates. The authors attributed this effect to chemical modifications in the structure, caused by CAP. Moreover, *in vitro* experiments by Karakas and collaborators also demonstrated that plasma treatment led to destruction of  $\alpha$ -synuclein-based amyloid fibrils.<sup>130</sup> Indeed, CAP produces a cocktail of RONS, and the degradation of amyloid aggregates probably occurs upon oxidation by these RONS. However, the molecular level mechanism is far from fully understood. This explains the need for studying the influence of oxidation, in various degrees, on the stability of the A $\beta$  structure. Up to now, there is no computational evidence on the effect of oxidation on the structure and stability of amyloid aggregates. Therefore, we studied the mechanisms of A $\beta$  fibril destabilization at the molecular level, upon increasing oxidative stress, which is presented in detail in [Chapter 4](#).

## 1.4. Plasma in cancer treatment

Biology of cancer cells. The nature of cancer cells is quite complex. Genes of cancerous cells are either changed or damaged.<sup>131</sup> Due to these changes (i.e., mutation), genes stop functioning properly.<sup>132</sup> Many external and internal factors can cause gene mutations: smoking, diet (overuse of alcohol and unhealthy foods), the Sun or other types of radiation, viruses and other infections. It was also revealed that in some cases, mutated genes might be inherited from parents.<sup>133</sup> Researchers have found that a multiple number of mutations (60 or more) cause cancer and they defined the link between mutated genes that are responsible for a certain kind of cancer. However, there are many types of cancers with unknown gene mutations, which need to be determined.

The mutations play a central role in the evolution of cancer.<sup>132</sup> For instance, tumor suppressor genes, oncogenes, and DNA repair genes are the main genes that regulate cell growth and cause the development of cancer. The tumor suppressor genes are categorized as normal genes that govern apoptosis.<sup>134</sup> Besides, they recover mistakes in DNA and they slow down the cell growth, in other words they defend the cell from being cancerous. Once they are deactivated due to certain alteration, the cell starts dividing too fast, causing cancer. Oncogenes are a class of mutated genes that dictate cell growth.<sup>135</sup> Oncogenes are products of proto-oncogenes. Both genes act like an “on/off” switch. The cell division and growth takes place when proto-oncogenes are in “on” state, but they are usually switched off. Contrary, oncogenes are always in activated state (switched on), and this promotes uncontrollable cell growth, resulting in cancer. Mistakes in both oncogenes and tumor suppressor genes can be fixed by DNA repair genes.<sup>136</sup> Sometimes, even these genes cannot repair mistakes, due to accumulation of mutations. As a consequence, abnormal functioning of the cell occurs, disrupting the balance between proliferation and suppression, which causes the development of cancer. The transformation steps of a normal cell into a cancer cell are given in [figure 1.12](#).



Figure 1.12. Transformation of a normal cell into cancerous cells due to gene mutation.

Apparently, many mutations and improper functioning of cancer cells affect the cell morphology, which becomes different from the normal cells. These major differences of cancer and normal cells are given in [Table 1.1](#). Cancer cells do not maintain a specific shape and the nucleus produces an abnormal and disproportionate amount of proteins that function differently.

Table 1.1 Major differences and similarities of cancer and normal cells. The table is taken from [www.drjockers.com](http://www.drjockers.com)

Characteristics/cell type	Cancer cells	Normal cells
Shape	Irregular	Regular
Nucleus	Larger, darker	Proportionate size
Growth	Out of control	In control, systematic
Maturation	Immature	Mortal (apoptosis)
Communication	Don't communicate	Communicate
Visibility	Invisible to immune cells	Visible to immune cells
Blood supply	Tumor angiogenesis	Angiogenesis during repair
Oxygen	Don't like or require oxygen	Require oxygen
Glucose	Love, crave glucose	Require some glucose
Energy efficiency	Very low (5%)	Very high (95%)
Cell environment	Acidic	Alkaline
Nutrient preference	Glucose	Fat, Ketone, Glucose

Normal cells grow by communicating with surrounding cells, and the growth stops when sufficient cells are present. This can be observed during wound healing. Normal cells localize where they belong i.e., liver cells remain in the liver. In contrast, cancer cells continuously proliferate, and they even do not stop when the cells reach the boundaries of a specific area, representing uncontrollable growth. Indeed, cancer cells overproduce growth factor proteins and chemicals that stimulate growth and differentiation, forming a colony of cells, which even become invisible to immune cells. These colonies of cancer cells are able to migrate from one place to another via the blood stream and lymphatic system in the body. In other words, cancer cells can reach other parts of the body and form new tumors. This process is called metastasis. Metastasis is an advanced level of cancer that makes it very difficult to treat patients and it often ends with death. More detailed information about cancer cell biology can be found in literature<sup>137,138</sup>.

Cancer still remains one of the diseases of high mortality rate.<sup>139</sup> There is no general treatment option due to the complex nature of cancer<sup>140</sup> and even therapeutic approaches vary

from one patient to another in the same type of cancer.<sup>141</sup> Currently used conventional methods, such as radiation therapy<sup>142</sup>, photodynamic therapy<sup>143</sup>, chemotherapy<sup>144</sup>, hormonal therapy<sup>145</sup>, or a combination of these therapies, cause some problems in cytotoxicity, side effects and selectivity among cancer and normal cells. For example, the DNA of cancer cells is destroyed by orienting external beams directly to the tumor in *radiation therapy*. The damage to the DNA can be induced directly or indirectly (see [Figure 1.13](#)).<sup>146</sup>

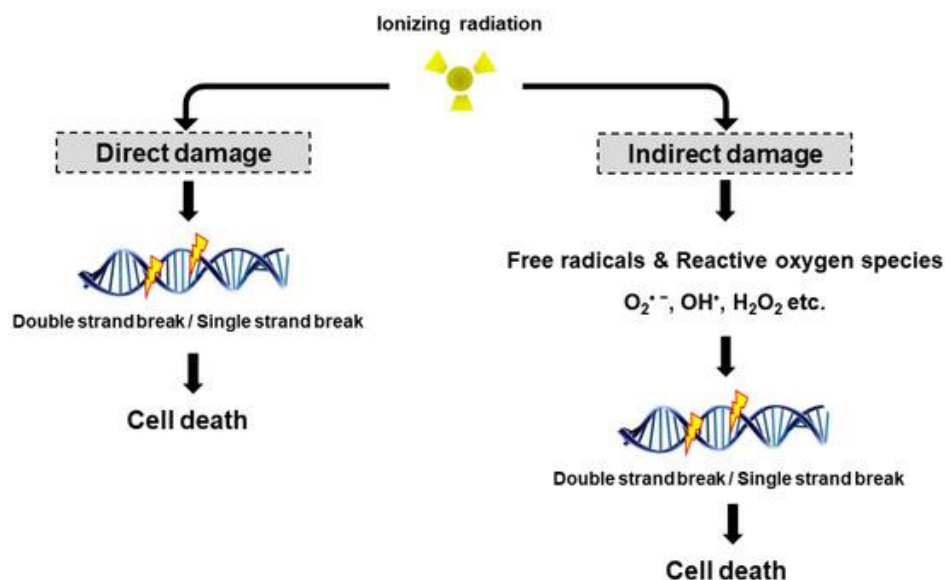


Figure 1.13. *Cell death mechanisms through direct and indirect DNA damage by radiation therapy. Figure is adopted from*<sup>146</sup>.

The direct photon ionization might break the DNA strands during treatment. The DNA helices also can be damaged by indirectly generated ROS, which are created by interaction of radiation with water molecules. As a consequence, cell cycle arrest (i.e., apoptosis) might take place through the activation of intracellular signaling pathways for control of local cancers. The normal cells surrounding the tumor, however, also might be killed during the treatment. Besides, many various side effects of radiation therapy have been observed in cancer treatment.<sup>147-149</sup> Specifically, this therapeutic approach showed detrimental effects, including long term hearing loss, blindness and neurocognitive side effects for children with brain cancer.<sup>150</sup>

Similar to radiation therapy, *photodynamic therapy* (PDT) also has been used for cancer treatment.<sup>151</sup> It uses a photosensitizing chemical substance to kill cancer cells. A photosensitizer in ground state can be activated upon absorption of light inside the cell. Once the latter is in excited state, it starts to generate ROS in the cell. These ROS (singlet oxygen ( $^1O_2$ ), hydroxyl radicals ( $\cdot OH$ ) and superoxide ( $O_2^{\cdot -}$ )) are highly toxic and attack the cell constituents, damaging DNA, proteins and lipids. If oxidative damage is sufficient, it leads to the targeted cell death via apoptosis or necrosis. This method is less efficient towards solid tumors and it strongly depends on the permeability of the photosensitizer into the tumor cells.<sup>147</sup>

*Chemotherapy* is the most common treatment approach to cure cancer.<sup>153</sup> In this method drugs are used to eliminate cancer cells. The previous methods basically target a certain area in the body to kill cancer cells, while chemotherapy can act throughout the entire body. This means chemotherapeutic drugs circulate via the bloodstream and are able to destroy cancer cells in metastatic stages as well. The main purpose is to cure, control or palliate the cancer.

Chemotherapeutics target fast proliferating cells, which is the core nature of cancer cells. However, these drugs cannot see the difference between normal and cancer cells. Thus, normal cells also become a victim of drugs along with cancer cells. This often causes significant side effects. Therefore, each step (i.e., dose, response of cancer cells, side effects) strictly has to be controlled by doctors to find the beneficial balance for patients. Chemo drugs are classified depending on their chemical structure, e.g., alkylating agents, antimetabolites, anti-cancer antibiotics, topoisomerase inhibitors, mitotic inhibitors, etc.<sup>154</sup> For example, alkylating agents prevent cell proliferation by damaging DNA, and this type of drugs is used to treat many cancer types, including leukemia, lymphoma, myeloma, lung, breast and ovary cancer. The dose of these compounds is critical because it also affects bone marrow cells, which produce new blood cells. Besides, a high dose of alkylating drugs, such as cyclophosphamide and ifosfamide, might lead to heart failure and arrhythmias.<sup>155</sup> Antimetabolites destroy cells in the copy stage of chromosomes replacing the RNA and DNA constituents. These compounds also cause myocardial ischemia.<sup>155</sup> Anticancer antibiotics interrupt enzymes that synthesize DNA during the cell cycle. As with other types of drugs, the usage of antibiotics results in various side effects, such as cardio toxicity, nausea, vomiting, mucositis and more.<sup>156</sup> Topoisomerase inhibitors disrupt the topoisomerases proteins, which are involved in dissociation of DNA strands. Mitotic inhibitors are natural compounds extracted from plants. They arrest the cell cycle and are either capable to suppress proteins, making enzymes that are required to form new cells. Topoisomerase and mitotic inhibitors also manifested adverse effects, such as neuropathy, lymphopenia, gastrointestinal and cardiac toxicity, like other chemotherapeutics.<sup>157,158</sup> Therefore, reduced toxicity and highly selectivity chemical compounds still remain a challenge in cancer treatment.

*Hormonal therapy* treats cancer via controlling the endocrine system of the human body. This approach provides or blocks specific hormones to eliminate cancer cells.<sup>159</sup> Several types of cancers, such as prostate, breast and ovarian cancer, are sensitive to hormones. These types of cancer can be treated by manipulating estrogen, testosterone and progestogens hormones that stimulate their growth.<sup>160</sup> Hot flash, fever and vasomotor symptoms are observed side effects of hormonal therapy.<sup>161</sup>

Thus, the above methods all suffer from some disadvantages and cannot fully prevent cancer, due to its complex nature. Therefore, there is a need for further improvement, as well as for new therapies. In recent years, one of the new therapeutic techniques that are being developed for cancer treatment is so-called “*plasma oncology*”.

*Plasma oncology* is one of the branches of plasma medicine.<sup>48,51</sup> Early *in vitro* tests with eukaryotic cells demonstrated various effects, including apoptosis, necrosis, and changes in cell migration, depending on the exposure time.<sup>9</sup> Experiments with cancer cell lines also

showed analogous effects, such as apoptosis and decreased cell migrations.<sup>162,163</sup> Further investigations suggested that CAP selectively kills many cancer cell types, leaving the healthy counterparts less damaged.<sup>164-167</sup> For instance, these beneficial effects of CAP are reported for the following cancers: head and neck cancer,<sup>168,169</sup> brain cancer,<sup>170,171</sup> leukemia,<sup>172,173</sup> lung cancer,<sup>162</sup> breast cancer,<sup>167,174</sup> skin cancer,<sup>175,176</sup> colorectal cancer<sup>177</sup>, gastric cancer,<sup>178</sup> pancreatic cancer,<sup>179</sup> *etc.* This stated selective nature of CAP led to an increase in the number of publications in the field (see [Figure 1.14](#)), although it must be mentioned that not all tests reveal selectivity of cancer cells vs normal cells.

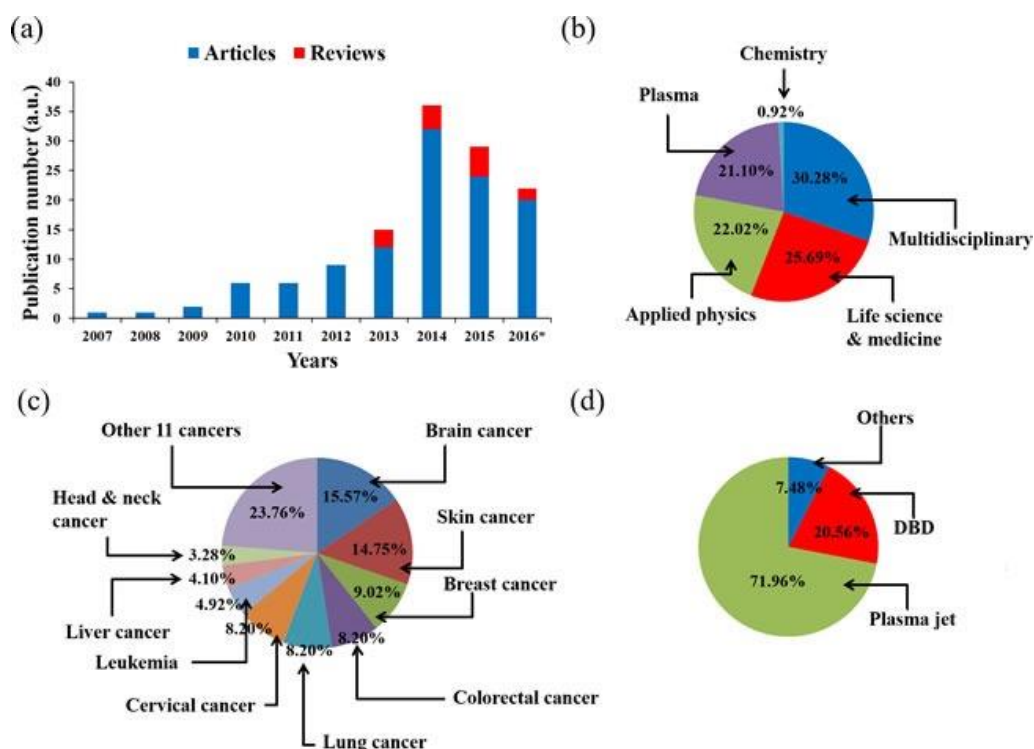


Figure 1.14. The statistics of publications on cancer treatment by application of CAP by 2016. (a) Number of publications. (b) Percentage of articles published in various journal types. (c) Percentage of cancer types studied in these publications. (d) Distribution of plasma devices in these publications. Figure is adopted from<sup>37</sup>.

*In vivo* studies by Walk *et al.* also demonstrated that the growth of neuroblastoma cells injected in mice decreased after 5 min of CAP treatment.<sup>180</sup> The average survival rate was increased almost two times from 15 to 28 days. Another *in vivo* study by Kim *et al.* evidenced no effect of one time treatment on melanoma cells injected in mice.<sup>181</sup> However, four times of exposure was sufficient to prevent the tumor growth. Similar results were obtained with pancreatic,<sup>179</sup> glioma,<sup>182</sup> and bladder cancer cells<sup>164</sup>. These features of CAP might possess advantages over traditional anti-cancer therapies, such as treatment selectivity towards cancer cells, causing no pain in patients, no thermal and electrical damage, as well as low cost.<sup>183-185</sup>

In order to use CAP sources in the clinic, more detailed studies are required. In this regard, the selective nature of CAP towards cancer and normal cells is still not fully understood. Certain aspects of the sensitivity of cancer cells are determined through experimental investigations. For instance, Volotskova *et al.* analyzed each phase of the cell cycle (G1 phase

– the cell physically grows; S phase – synthesis of DNA; G2 phase – preparation for mitosis making proteins and organelles; M phase – cell division) in CAP-treated skin cancer cells.<sup>186</sup> They found that DNA was damaged in the S phase of the cell cycle via the cH2A.X marker and it prevented further processes in the G2 and M phase, resulting in delayed development of cancer cells. The application of CAP on both metastatic liver cancer SK-HEP-1 and normal THLE-2 cells represented a different response against the treatment.<sup>187</sup> The weakened adhesion of cancerous cells in comparison with normal cells was acquired by mechanical and biochemical analyses. The loss of strong adhesion in cancer cells reduces its growth and migration ability.<sup>188</sup> Other studies also showed the vulnerability of melanoma, lung and colon cancer cells in comparison to normal cells.<sup>189-191</sup> It has to be mentioned that CAP treatment also enhances drug sensitivity on multiple myeloma cells.<sup>52</sup> All of these investigations evidence that CAP sources are capable to induce cancer cell death. However, the precise underlying mechanism of CAP on cells still remains poorly understood. Therefore, the topic requires more fundamental investigations, in order to establish the optimal dose of plasma-generated species by various sources, to successfully engage the position of CAP in the clinic.

Cell membrane under oxidative stress. It is generally believed that reactive oxygen and nitrogen species (RONS) generated by plasma play an important role in killing cancer cells.<sup>192,193</sup> The selectivity of CAP towards cancer cells is linked to the elevated level of intracellular ROS and RNS (or RONS) found in cancer cells compared to normal cells.<sup>165,194,195</sup> This might subsequently lead to nitro-oxidative stress of biomolecules inside the cells, which might explain the selectivity of plasma towards cancer cells.<sup>164,165,192,196,197</sup> Indeed, some studies report the selective action of plasma towards cancer cells vs normal cells, although this selectivity is obviously not always observed. In addition, it should be noted that ROS/RNS generation might play a dual role by promoting cancer cell death depending on their relative effects. For instance, the combined action of NO with H<sub>2</sub>O<sub>2</sub> to cause DNA damage, ultimately leading to programmed cell destruction, was evidenced in<sup>198</sup>. In addition, the role of peroxynitrite, which is generated by reaction of NO with superoxide in the cell, was studied in<sup>199-203</sup>. Indeed, cellular damage also needs to be actively translated into a given cell death program by the cellular signaling machinery.<sup>204</sup>

However, before the plasma-induced RONS can cause oxidative damage inside the cells, the plasma species first interact with the cell membrane, chemically modifying or oxidizing its lipids. It is therefore important to study the behaviour of the oxidized cell membrane and its effect on the penetration of various plasma-induced RONS through this cell membrane. More information on the permeation of RONS across native and oxidized PLB will be presented in [Chapter 3](#). Specifically, it is important to understand whether passive transport of RONS is possible or whether pores or transmembrane protein channels, such as aquaporins (AQPs), must be present.

AQPs are transmembrane proteins, which are stated to be important for H<sub>2</sub>O transport across the cell membrane. Besides H<sub>2</sub>O, they can also transport other small molecules, like H<sub>2</sub>O<sub>2</sub>, NO, and NO<sub>3</sub><sup>-</sup>.<sup>205,206</sup> Keidar *et al.* reported that knocking out AQP8 in glioblastoma cells could significantly weaken the toxicity of plasma-treated liquid medium on these cells, which was the first evidence for their role in plasma for cancer treatment.<sup>207</sup> As most cancer

tissues express more AQPs in their cytoplasmic membrane than homologous normal tissues,<sup>205</sup> this could explain why cancer cells are more sensitive to plasma treatment than normal cells. In addition, calculated free energy profiles (FEPs) also showed that the free energy barrier for permeation of H<sub>2</sub>O<sub>2</sub> through AQP1 is approximately three times lower than through the PLB (see [Figure 1.15](#)).<sup>208</sup> Thus, AQP channels are a more favourable pathway for transport of H<sub>2</sub>O<sub>2</sub>, and this might provide one of the molecular level mechanisms of the selectivity of plasma against cancer cells.

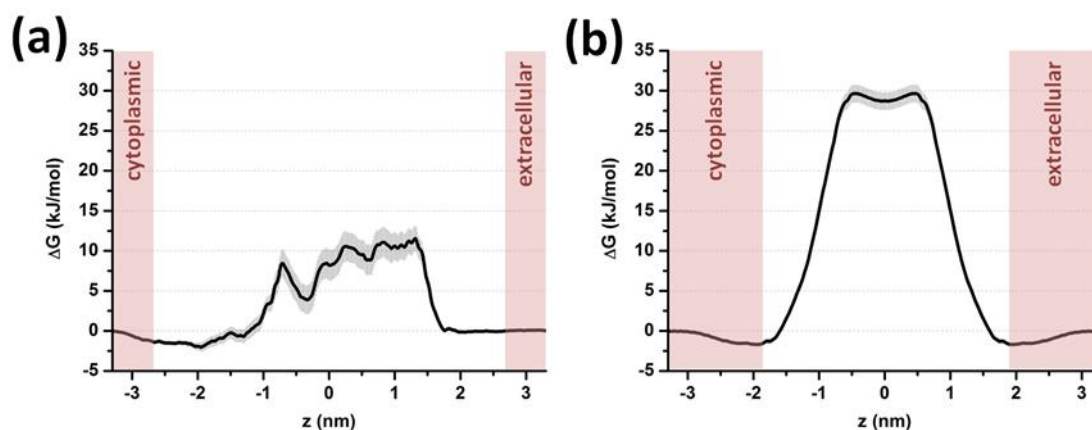


Figure 1.15. FEPs of H<sub>2</sub>O<sub>2</sub> transport through the AQP1 channel (a) and across the PLB (b). The cytoplasmic and extracellular water layers are shown in pink colour. Figure is adopted from<sup>208</sup>.

Furthermore, it is shown by molecular dynamics (MD) simulations that lipid oxidation yields an overall increase in the membrane permeability,<sup>209</sup> a change in the lipid mobility in the phospholipid bilayer (PLB),<sup>210</sup> pore creation and bilayer disintegration<sup>211</sup>. Furthermore, both simulations<sup>108,212</sup> and experiments<sup>213</sup> have revealed that cholesterol can protect oxidized membranes against pore formation. Indeed, liposomes containing 50 mol% cholesterol are resistant against disruption by plasma, whereas cholesterol fractions below 50 mol% lead to increased disruption of liposomes.<sup>213</sup> This result is also of great interest for plasma-based cancer therapy, as cancer cells typically contain less cholesterol in their plasma membrane, so the above observation might also be one of the explanations for the selectivity of plasma treatment towards cancer cells, as they allow the reactive plasma species to reach the cell interior more easily through pore formation. Following this hypothesis, van der Paal *et al.* studied the effect of the cholesterol content on the permeation of ROS (OH, HO<sub>2</sub>, H<sub>2</sub>O<sub>2</sub>, O<sub>2</sub>) across the PLB by means of MD simulations.<sup>212</sup> The calculated FEPs indicated that the presence of (higher concentrations of) cholesterol result in a rise in both the free energy barrier height and width, and it also causes the formation of a local free energy minimum in the center of the PLB (see [Figure 1.16](#)). The latter will hamper the penetration of H<sub>2</sub>O<sub>2</sub> towards the intracellular environment, even when it would succeed to penetrate into the PLB center. The same behaviour also was observed for OH and HO<sub>2</sub>. Despite the difference in FEPs of O<sub>2</sub>, some extra free energy barriers are created upon increasing cholesterol concentration in the PLB. This might serve as an explanation why it is more difficult for RONS to reach the cell interior of normal cells. Cancer cells are more vulnerable to plasma

oxidation due to their lower cholesterol fraction in the cell membrane and thus, plasma treatment might be more selective towards cancer cells.

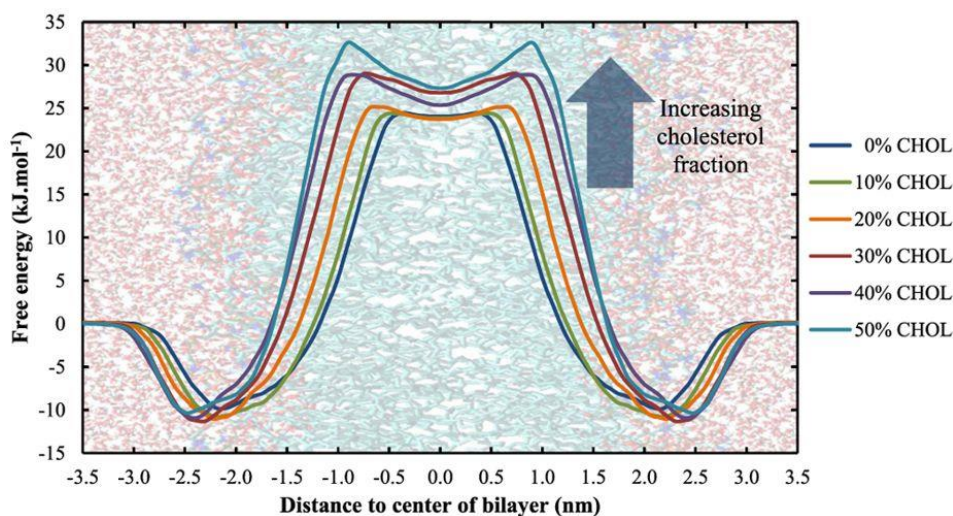


Figure 1.16. FEPs of  $H_2O_2$  across the PLB, for various percentages of cholesterol in the cell membrane. Adopted from <sup>208</sup>.

Van der Paal *et al.* also analysed typical properties of the PLB, as a function of increasing lipid oxidation degree and increasing cholesterol fraction, such as the surface area per lipid, the thickness of the PLB, the water density inside the PLB (used as a measure for the polarity inside the membrane), and the so-called deuterium order parameter, which is a measure for the order of the lipid tails in the PLB (see details in <sup>108</sup>). The PLB thickness was found to drop upon oxidation, followed by a rise when the oxidation approached 100 %, and this was attributed to pore formation. The pore diameter was reported to be 15 Å, which might allow RONS to penetrate and reach the cell interior. The water density in the center of the PLB in case of 100 % oxidation was calculated as a function of the fraction of cholesterol in the bilayer. For a cholesterol concentration up to 11 %, the water density is significant, due to pore formation, while a higher cholesterol concentration resulted in a significant drop in the water density, indicating inhibition of pore formation. As some cancer cells contain less cholesterol in their cell membrane than normal cells, RONS might more easily ingress through their cell membrane, enhancing the oxidative stress inside the cell. Hence, this might again explain why plasma can selectively treat cancer cells, while leaving the normal cells undamaged.

Furthermore, in addition to RONS generation, some plasma sources produce strong electric fields, ranging from a few up to 100 kV/cm,<sup>214-216</sup> which may play an important and synergistic role in plasma-cell interactions,<sup>214</sup> as they are high enough to create pores in the membrane, either temporarily or permanently, i.e., so-called electroporation<sup>217</sup>. Several MD studies have been devoted to electroporation (e.g., <sup>218,219</sup>), but little is known about the synergy between plasma-induced lipid oxidation and the electric field, and more specifically on how this affects the cell membrane permeability. As mentioned above, lipid oxidation

results in a higher permeability of hydrophilic ROS across the PLB, but the permeation free energy barriers are still too high for spontaneous permeation. As discussed in section 1.3.3 on the combined effect of lipid oxidation and electric fields, we observed that lipid oxidation into aldehydes causes a drop of the electric field threshold needed for pore formation in the PLB, as well as a shorter average pore formation time (see Figure 1.9 above).<sup>109</sup> Although the average pore formation times obtained in MD simulations cannot be directly related to the experimental pore formation kinetics, as also explained in <sup>109</sup>, the trends of pore formation times for different values of electric fields and oxidation degrees presented in Figure 1.9 clearly indicate that oxidation of the lipid tails in the PLB facilitates pore formation, by lowering the threshold electric field, as well as the pore formation time, thus clearly illustrating the synergistic effect of the electric field together with lipid oxidation on the permeability of cell membranes.

Effect of RONS on antioxidant proteins. Almost all types of cancer cells represent an elevated level of ROS compared to their counterpart.<sup>194</sup> In order to keep the ROS in this high level for functioning and progression, cancer cells also increase the expression of antioxidant proteins (see Figure 1.17). This results in an increased metabolic activity of cancer cells.

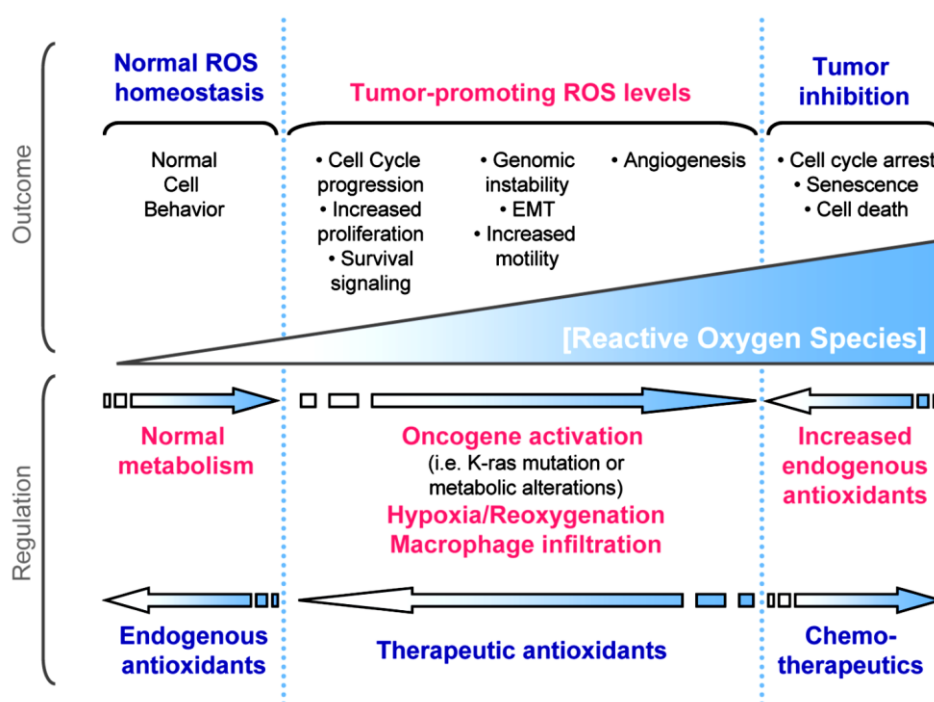


Figure 1.17. The level of ROS in normal vs cancer cells. The tumour inhibition can be achieved by regulating the ROS level in the cell, but therapeutic antioxidants can also return the cell metabolism to the normal state. Figure is adopted from <sup>194</sup>.

The tumor inhibition can be induced via increasing intracellular ROS levels, or by introducing therapeutic antioxidants, thereby helping cancer cells to return back to a normal metabolism. In plasma cancer treatment, the level of endogenous ROS in cancer cells can be enhanced by exposure to CAP-generated exogenous ROS.<sup>170</sup> Once the amount of endogenous ROS achieves a threshold, the cell initiates self-destruction signals, such as apoptosis.

Therefore, antioxidant proteins play a critical role in the cell metabolism. Indeed, the higher concentration of intracellular ROS and RNS found in CAP-treated cancer cells compared to normal cells<sup>165,194,195</sup> cause nitro-oxidative stress in the cell and may even lead to cell death.<sup>164,165,192,196,197</sup> This may result in ROS-induced regulation of intracellular signaling pathways, which can lead to cell cycle arrest and cell death<sup>171,220,221</sup>. In recent reviews, Bauer showed the effect of extracellular ROS in apoptosis-inducing signaling, and in particular the role of ROS in the inactivation of antioxidant proteins (e.g., catalase), which subsequently leads to tumor cell death.<sup>222,223</sup> Interestingly, in his recent investigation, Bauer demonstrated that an increase of endogenous NO concentration causes catalase inactivation and reactivation of intercellular apoptosis signaling, specifically in tumor cells.<sup>197,224</sup> The role of NO in blocking the electron transport chain in mitochondria was also reviewed in literature<sup>225</sup>. It was indicated that NO acts through neutralizing cytochrome C oxidase, thereby resulting in an increase of the intracellular ROS level, followed by triggering mitochondrial apoptosis.<sup>225</sup> Inactivation of glutathione peroxidase by NO and its role in inducing apoptotic cell death was also reported.<sup>226</sup> Moreover, H<sub>2</sub>O<sub>2</sub> in combination with NO caused DNA damage, eventually leading to programmed cell death.<sup>198</sup> In addition, the reaction of NO with superoxide leads to the formation of peroxynitrite in the cell, and the role of peroxynitrite was studied in<sup>199-203</sup>. It was demonstrated that peroxynitrite inactivates catalase,<sup>199</sup> manganese-superoxide dismutase,<sup>200</sup> peroxiredoxin,<sup>201</sup> glutathione peroxidase<sup>202</sup> and glutathione reductase<sup>203</sup>, which overall deteriorates the antioxidant system of the cell. Thus, the cell becomes more vulnerable to the plasma-generated exogenous RONS, due to the impairment of its antioxidant defense system. This in turn leads to a further increase of the intracellular reactive species, causing nitro-oxidative stress in cells.<sup>227,228</sup>

We investigated the impact of RONS on cytoglobin (Cygb), i.e., a redox-active globin, which responds against oxidative stress in the cell.<sup>229-231</sup> The aim was to help understand the cytoprotective role of Cygb on a molecular basis, revealed via experiments and computer simulations. Further detailed information regarding the molecular level studies of Cygb is given in [Chapter 4](#).

Effect of plasma on signaling proteins. As discussed above, mainly globular proteins exhibit antioxidant activity in the cell. There are also many other types of proteins that are involved in regulation of signaling pathways that control cellular homeostasis. One of these proteins is epidermal growth factor (EGF) and its receptor (EGFR). The binding of EGF to its receptor promotes the cell growth and differentiation. Moreover, a pathological role of EGFR was found in breast, glioblastoma and lung cancer.<sup>232</sup> Therefore, we investigated the impact of CAP-induced oxidation on the structure of EGF by computer simulations and experiments (the latter performed by Dr. Lackmann and Dr. Stapelmann at University of Bochum), which is particularly interesting for plasma-induced wound healing and cancer treatment. Further detailed information is given in [Chapter 4](#).

Effect of RONS on cancer cell proteins which downregulate the immune system. It was reported that cancer cells produce specific proteins (i.e., immune checkpoints) on their surface and use them as a mask to escape from the immune system.<sup>233-235</sup> These proteins interact with immune proteins and express a “don’t eat me” signal, suppressing the immune system against

the cancer cells. In order to unmask the cancer cells, the interaction between cancer and immune cell proteins has to be blocked. Recent *in vitro* experiments demonstrated that CAP is also capable to induce immunogenic cell death.<sup>53-56</sup> This can most likely be achieved by oxidation of immune checkpoint proteins, which alters chemical and physical properties, causing structural changes, leading to regulation of the signaling pathways. Therefore, we investigated the effect of (plasma-induced) oxidation on the interaction between cancer and immune cell proteins by MD simulations. More detailed information is given in [Chapter 4](#).

## 1.5 Aim of this PhD research

Biomedical applications of CAP are gaining increasing interest. In particular, CAP seems very promising for various applications, such as bacterial decontamination, wound healing, drug delivery and even cancer treatment. However, the underlying mechanisms at the atomic scale are not yet fully understood. One of the reasons is that the exact mechanisms are difficult to explore experimentally.

CAP generates a rich mixture of reactive oxygen and nitrogen species (RONS), which interact with living cells, inducing molecular level modifications to their components (e.g., lipids, proteins and DNA) upon oxidation. This will influence the intra- and/or intercellular signaling pathways, leading to various alterations in the cellular metabolism, which are stated to cause apoptosis, necrosis or immunogenic cell death. To better understand the effect of plasma on the cellular processes, a fundamental insight in the RONS-cell interactions and in the effect of plasma-induced oxidation, is crucial.

Complementary to experiments, computer simulations allow us to study the underlying processes with nanoscale precision. Thus, in my PhD project, I elucidated the mechanisms of RONS and glucose permeation and PS flip-flop across the native and oxidized cell membrane (see [Chapter 3](#)) by means of MD simulations. Furthermore, I studied the impact of plasma oxidation to globular, fiber-like and signaling proteins in the context of wound healing, Alzheimer's disease and cancer treatment, applying docking and MD simulations (see [Chapter 4](#)).

These findings help to reveal the complex interaction of CAP with the cell constituents in a qualitative way, and serve as an investment in order to develop CAP systems for clinical translation.

## 1.6 References

- 1 Hojnik, N., Cvelbar, U., Tavčar-Kalcher, G., Walsh, J. L. & Križaj, I. Mycotoxin decontamination of food: cold atmospheric pressure plasma versus “classic” decontamination. *Toxins* **9**, 151 (2017).
- 2 Carbone, E and Douat, C. Carbon Monoxide in Plasma and Agriculture: Just a Foe or a Potential Friend? *Plasma Medicine* **8** (2018).
- 3 Boulos, M. I., Fauchais, P. and Pfender, E. *Thermal plasmas: fundamentals and applications*. (Springer Science & Business Media, 2013).
- 4 Cheng, C., Liye, Z. & Zhan, R.-J. Surface modification of polymer fibre by the new atmospheric pressure cold plasma jet. *Surface and Coatings Technology* **200**, 6659-6665 (2006).
- 5 Lee, H. W., Kim, G. J., Kim, J. M., Park, J. K., Lee, J. K. and Kim, G. C. Tooth bleaching with nonthermal atmospheric pressure plasma. *Journal of endodontics* **35**, 587-591 (2009).
- 6 Nehra, V., Kumar, A and Dwivedi, H. Atmospheric non-thermal plasma sources. *International Journal of Engineering* **2**, 53-68 (2008).
- 7 Bárdos, L and Baránková, H. Cold atmospheric plasma: sources, processes, and applications. *Thin Solid Films* **518**, 6705-6713 (2010).
- 8 Mohamed, A., Price, O., Swanson, J., Bowman, A., Chiavarini, L., Stacey, M. and Schoenbach, H. Cold atmospheric pressure air plasma jet for medical applications. *Applied Physics Letters* **92**, 241501 (2008).
- 9 Hoffmann, C., Berganza, C. and Zhang, J. Cold Atmospheric Plasma: methods of production and application in dentistry and oncology. *Medical gas research* **3**, 21 (2013).
- 10 Laroussi, M. and Lu, X. Room-temperature atmospheric pressure plasma plume for biomedical applications. *Applied Physics Letters* **87**, 113902 (2005).
- 11 Isbary, G. *et al.* A first prospective randomized controlled trial to decrease bacterial load using cold atmospheric argon plasma on chronic wounds in patients. *British Journal of Dermatology* **163**, 78-82 (2010).
- 12 Winter, J., Brandenburg, R and Weltmann, K. Atmospheric pressure plasma jets: an overview of devices and new directions. *Plasma Sources Science and Technology* **24**, 064001 (2015).
- 13 Jeong, J.Y., Babayan, S.E., Tu, V.J., Park, J., Henins, I., Hicks, R.F. and Selwyn, G.S. Etching materials with an atmospheric-pressure plasma jet. *Plasma Sources Science and Technology* **7**, 282 (1998).
- 14 Babayan, S., Jeong, Y., Tu, J., Park, J., Selwyn, S. and Hicks, F. Deposition of silicon dioxide films with an atmospheric-pressure plasma jet. *Plasma Sources Science and Technology* **7**, 286 (1998).
- 15 Marinov, D and Braithwaite, N. Power coupling and electrical characterization of a radio-frequency micro atmospheric pressure plasma jet. *Plasma Sources Science and Technology* **23**, 062005 (2014).
- 16 Pipa, A., Ionikh, Y. Z., Chekischev, V., Dünnbier, M and Reuter, S. Resonance broadening of argon lines in a micro-scaled atmospheric pressure plasma jet (argon  $\mu$ APPJ). *Applied Physics Letters* **106**, 244104 (2015).
- 17 Murakami, T., Niemi, K., Gans, T., O'Connell, D. & Graham, W. G. Afterglow chemistry of atmospheric-pressure helium–oxygen plasmas with humid air impurity. *Plasma Sources Science and Technology* **23**, 025005 (2014).
- 18 Niemi, K., Waskoenig, J., Sadeghi, N., Gans, T and O'Connell, D. The role of helium metastable states in radio-frequency driven helium–oxygen atmospheric pressure

- plasma jets: measurement and numerical simulation. *Plasma Sources Science and Technology* **20**, 055005 (2011).
- 19 Laroussi, M and Akan, T. Arc-free atmospheric pressure cold plasma jets: a review. *Plasma Processes and Polymers* **4**, 777-788 (2007).
  - 20 Lu, X., Laroussi, M and Puech, V. On atmospheric-pressure non-equilibrium plasma jets and plasma bullets. *Plasma Sources Science and Technology* **21**, 034005 (2012).
  - 21 Robert, E., Sarron, V., Ries, D., Dozias, S., Vandamme, M and Pouvesle, J.M Characterization of pulsed atmospheric-pressure plasma streams (PAPS) generated by a plasma gun. *Plasma Sources Science and Technology* **21**, 034017 (2012).
  - 22 Sarani, A., Nicula, C., Gonzales, X. F and Thiagarajan, M. Characterization of Kilohertz-Ignited Nonthermal He and He/O<sub>2</sub> Plasma Pencil for Biomedical Applications. *IEEE Transactions on Plasma Science* **42**, 3148-3160 (2014).
  - 23 Laroussi, M., Hynes, W., Akan, T., Lu, X and Tendero, C. The plasma pencil: a source of hypersonic cold plasma bullets for biomedical applications. *IEEE Transactions on plasma science* **36**, 1298-1299 (2008).
  - 24 Choi, J., Mohamed, H., Kang, K., Woo, C., Kim, T. and Lee, K. 900-MHz Nonthermal Atmospheric Pressure Plasma Jet for Biomedical Applications. *Plasma Processes and Polymers* **7**, 258-263 (2010).
  - 25 Sladek, E., Baede, T and Stoffels, E. Plasma-needle treatment of substrates with respect to wettability and growth of Escherichia coli and Streptococcus mutans. *IEEE transactions on plasma science* **34**, 1325-1330 (2006).
  - 26 Weltmann, K. D., Kindel, E., Brandenburg, R., Meyer, C., Bussiahn, R., Wilke, C. and Von Woedtke, T. Atmospheric pressure plasma jet for medical therapy: plasma parameters and risk estimation. *Contributions to plasma physics* **49**, 631-640 (2009).
  - 27 Rupf, S., Lehmann, A., Hannig, M., Schäfer, B., Schubert, A., Feldmann, U. and Schindler, A. Killing of adherent oral microbes by a non-thermal atmospheric plasma jet. *Journal of medical microbiology* **59**, 206-212 (2010).
  - 28 Hofmann, S., Van Gessel, A., Verreycken, T and Bruggeman, P. Power dissipation, gas temperatures and electron densities of cold atmospheric pressure helium and argon RF plasma jets. *Plasma Sources Science and Technology* **20**, 065010 (2011).
  - 29 Brandenburg, R., Ehlbeck, J., Stieber, M., v. Woedtke, T., Zeymer, J., Schlüter, O and Weltmann, K.D. Antimicrobial treatment of heat sensitive materials by means of atmospheric pressure Rf-driven plasma jet. *Contributions to Plasma Physics* **47**, 72-79 (2007).
  - 30 Lu, X., Jiang, Z., Xiong, Q., Tang, Z., Hu, X and Pan, Y. An 11 cm long atmospheric pressure cold plasma plume for applications of plasma medicine. *Applied Physics Letters* **92**, 081502 (2008).
  - 31 Ellerweg, D., Von Keudell, A and Benedikt, J. Unexpected O and O<sub>3</sub> production in the effluent of He/O<sub>2</sub> microplasma jets emanating into ambient air. *Plasma Sources Science and Technology* **21**, 034019 (2012).
  - 32 Lee, K. Kim, S., Byun, H., Kim, T., Kim, C and Park, Y. Biomedical applications of low temperature atmospheric pressure plasmas to cancerous cell treatment and tooth bleaching. *Japanese Journal of Applied Physics* **50**, 08JF01 (2011).
  - 33 Bekeschus, S., Schmidt, A., Weltmann, K.D and von Woedtke, T. The plasma jet kINPen—a powerful tool for wound healing. *Clinical Plasma Medicine* **4**, 19-28 (2016).
  - 34 Arndt, S., Schmidt, A., Karrer, S and von Woedtke, T. Comparing two different plasma devices kINPen and Adtec SteriPlas regarding their molecular and cellular effects on wound healing. *Clinical Plasma Medicine* **9**, 24-33 (2018).
  - 35 Brehmer, F., Haenssle, H.A., Daeschlein, G., Ahmed, R., Pfeiffer, S., Görlitz, A., Simon, D., Schön, M.P., Wandke, D. and Emmert, S. Alleviation of chronic venous leg

- ulcers with a hand-held dielectric barrier discharge plasma generator (PlasmaDerm® VU-2010): results of a monocentric, two-armed, open, prospective, randomized and controlled trial (NCT 01415622). *Journal of the European Academy of Dermatology and Venereology* **29**, 148-155 (2015).
- 36 Brandenburg, R. Dielectric barrier discharges: progress on plasma sources and on the understanding of regimes and single filaments. *Plasma Sources Science and Technology* **26**, 053001 (2017).
- 37 Yan, D., Sherman, J. H and Keidar, M. Cold atmospheric plasma, a novel promising anti-cancer treatment modality. *Oncotarget* **8**, 15977 (2017).
- 38 Isbary, G., Shimizu, T., Li, F., Stolz, W., Thomas, M., Morfill, E and Zimmermann, J. Cold atmospheric plasma devices for medical issues. *Expert review of medical devices* **10**, 367-377 (2013).
- 39 Moreau, E., Sosa, R and Artana, G. Electric wind produced by surface plasma actuators: a new dielectric barrier discharge based on a three-electrode geometry. *Journal of Physics D: Applied Physics* **41**, 115204 (2008).
- 40 Kunhardt, E. E. Generation of large-volume, atmospheric-pressure, nonequilibrium plasmas. *IEEE transactions on plasma science* **28**, 189-200 (2000).
- 41 Becker, K., Koutsospyros, A., Yin, M., Christodoulatos, C., Abramzon, N., Joaquin, C. and Brelles-Marino, G. Environmental and biological applications of microplasmas. *Plasma physics and controlled fusion* **47**, B513 (2005).
- 42 Eden, J and Park, S. Microcavity plasma devices and arrays: A new realm of plasma physics and photonic applications. *Plasma physics and controlled fusion* **47**, B83 (2005).
- 43 Itoh, H., Teranishi, K and Suzuki, S. Discharge plasmas generated by piezoelectric transformers and their applications. *Plasma Sources Science and Technology* **15**, S51 (2006).
- 44 Emmert, S., Brehmer, F., Hänßle, H., Helmke, A., Mertens, N., Ahmed, R., Simon, D., Wandke, D., Maus-Friedrichs, W., Däschlein, G. and Schön, P. Atmospheric pressure plasma in dermatology: Ulcus treatment and much more. *Clinical Plasma Medicine* **1**, 24-29 (2013).
- 45 Fricke, K., Koban, I., Tresp, H., Jablonowski, L., Schröder, K., Kramer, A., Weltmann, K.D., von Woedtke, T and Kocher, T. Atmospheric pressure plasma: a high-performance tool for the efficient removal of biofilms. *PloS one* **7**, e42539 (2012).
- 46 Weltmann, K and Von Woedtke, T. Plasma medicine—current state of research and medical application. *Plasma Physics and Controlled Fusion* **59**, 014031 (2016).
- 47 Laroussi, M., Alexeff, I and Kang, W. L. Biological decontamination by nonthermal plasmas. *IEEE Transactions on Plasma Science* **28**, 184-188 (2000).
- 48 Fridman, G., Friedman, G., Gutsol, A., Shekhter, A.B., Vasilets, V.N and Fridman, A. Applied plasma medicine. *Plasma Processes and Polymers* **5**, 503-533 (2008).
- 49 Kong, G., Kroesen, G., Morfill, G., Nosenko, T., Shimizu, T., Van Dijk, J and Zimmermann, L. Plasma medicine: an introductory review. *New Journal of Physics* **11**, 115012 (2009).
- 50 Morfill, G., Kong, M. G and Zimmermann, J. Focus on plasma medicine. *New Journal of Physics* **11**, 115011 (2009).
- 51 Laroussi, M., Kong, M., Morfill, G and Stolz, W. *Plasma medicine: applications of low-temperature gas plasmas in medicine and biology*. (Cambridge University Press, 2012).
- 52 Xu, D., Luo, X., Xu, Y., Cui, Q., Yang, Y., Liu, D., Chen, H and Kong, M. The effects of cold atmospheric plasma on cell adhesion, differentiation, migration, apoptosis and

- drug sensitivity of multiple myeloma. *Biochemical and biophysical research communications* **473**, 1125-1132 (2016).
- 53 Lin, A., Truong, B., Patel, S., Kaushik, N., Choi, E., Fridman, G., Fridman, A. and Miller, V. Nanosecond-pulsed DBD plasma-generated reactive oxygen species trigger immunogenic cell death in A549 lung carcinoma cells through intracellular oxidative stress. *International journal of molecular sciences* **18**, 966 (2017).
- 54 Lin, A., Xiang, B., Merlino, J., Baybutt, R., Sahu, J., Fridman, A., Snook, E and Miller, V. Non-thermal plasma induces immunogenic cell death in vivo in murine CT26 colorectal tumors. *OncoImmunology*, **9**, e1484978 (2018).
- 55 Bekeschus, S., Clemen, R and Metelmann, H.R. Potentiating Anti-Tumor Immunity with Physical Plasma. *Clinical Plasma Medicine* (2018).
- 56 Bekeschus, S., Mueller, A., Miller, V., Gaipl, U and Weltmann, K.D. Physical plasma elicits immunogenic cancer cell death and mitochondrial singlet oxygen. *IEEE Transactions on Radiation and Plasma Medical Sciences* **2**, 138-146 (2018).
- 57 Laroussi, M. Plasma medicine: a brief introduction. *Plasma* **1**, 47-60 (2018).
- 58 Cotter, J. Maguire, P., Soberon, F., Daniels, S., O’Gara, P and Casey, E. Disinfection of meticillin-resistant *Staphylococcus aureus* and *Staphylococcus epidermidis* biofilms using a remote non-thermal gas plasma. *Journal of Hospital Infection* **78**, 204-207 (2011).
- 59 Pan, J., Sun, K., Liang, Y., Sun, P., Yang, X., Wang, J., Zhang, J., Zhu, W., Fang, J and Becker, K. Cold plasma therapy of a tooth root canal infected with *Enterococcus faecalis* biofilms in vitro. *Journal of endodontics* **39**, 105-110 (2013).
- 60 Maisch, T., Shimizu, T., Li, Y.F., Heinlin, J., Karrer, S., Morfill, G and Zimmermann, J. Decolonisation of MRSA, *S. aureus* and *E. coli* by cold-atmospheric plasma using a porcine skin model in vitro. *PloS one* **7**, e34610 (2012).
- 61 Scholtz, V., Pazlarova, J., Souskova, H., Khun, J and Julak, J. Nonthermal plasma—a tool for decontamination and disinfection. *Biotechnology advances* **33**, 1108-1119 (2015).
- 62 Zaaba, S., Akitsu, T., Ohkawa, H., Katayama-Hirayama, K., Tsuji, M., Shimizu, N and Imanishi, Y. Plasma disinfection and the deterioration of surgical tools at atmospheric pressure plasma. *IEEJ Transactions on Fundamentals and Materials* **130**, 355-361 (2010).
- 63 Kvam, E., Davis, B., Mondello, F and Garner, A. L. Non-thermal atmospheric plasma rapidly disinfects multidrug-resistant microbes by inducing cell surface damage. *Antimicrobial agents and chemotherapy* **4**, 2028-2036 (2012).
- 64 Fernández, A and Thompson, A. The inactivation of *Salmonella* by cold atmospheric plasma treatment. *Food Research International* **45**, 678-684 (2012).
- 65 Park, H., Kumar, N., Park, H., Yusupov, M., Neyts, E., Verlackt, C., Bogaerts, A., Kang, H., Uhm, S., Choi, H. and Attri, P. A comparative study for the inactivation of multidrug resistance bacteria using dielectric barrier discharge and nano-second pulsed plasma. *Scientific reports* **5**, 13849 (2015).
- 66 Joshi, G., Paff, M., Friedman, G., Fridman, G., Fridman, A and Brooks, A. Control of methicillin-resistant *Staphylococcus aureus* in planktonic form and biofilms: a biocidal efficacy study of nonthermal dielectric-barrier discharge plasma. *American journal of infection control* **38**, 293-301 (2010).
- 67 Maisch, T., Shimizu, T., Isbary, G., Heinlin, J., Karrer, S., Klämpfl, G., Li, F., Morfill, G. and Zimmermann, J. Contact-free inactivation of *Candida albicans* biofilm by cold-atmospheric air plasma. *Applied and environmental microbiology* **12**, 4242-4247 (2012).

- 68 Ikawa, S., Kitano, K and Hamaguchi, S. Effects of pH on bacterial inactivation in aqueous solutions due to low-temperature atmospheric pressure plasma application. *Plasma Processes and Polymers* **7**, 33-42 (2010).
- 69 Yusupov, M., Bogaerts, A., Huygh, S., Snoeckx, R., Van Duin, C and Neyts, E. Plasma-induced destruction of bacterial cell wall components: a reactive molecular dynamics simulation. *Journal of Physical Chemistry C* **117**, 5993-5998 (2013).
- 70 Yusupov, M., Neyts, E., Khalilov, U., Snoeckx, R., Van Duin, C and Bogaerts, A. Atomic-scale simulations of reactive oxygen plasma species interacting with bacterial cell walls. *New Journal of Physics* **14**, 093043 (2012).
- 71 Janis, J and Attinger, C. The basic science of wound healing. *Plastic and reconstructive surgery* **117**, 12S-34S (2006).
- 72 Guo, S and DiPietro, L. A. Factors affecting wound healing. *Journal of dental research* **89**, 219-229 (2010).
- 73 Bishop, A. Role of oxygen in wound healing. *Journal of wound care* **17**, 399-402 (2008).
- 74 Rodriguez, G., Felix, N., Woodley, T and Shim, E. K. The role of oxygen in wound healing: a review of the literature. *Dermatologic surgery* **34**, 1159-1169 (2008).
- 75 Semenza, L. HIF-1 and human disease: one highly involved factor. *Genes & development* **14**, 1983-1991 (2000).
- 76 Sen, K. The general case for redox control of wound repair. *Wound Repair and Regeneration* **11**, 431-438 (2003).
- 77 Roy, S., Khanna, S., Nallu, K., Hunt, K and Sen, K. Dermal wound healing is subject to redox control. *Molecular Therapy* **13**, 211-220 (2006).
- 78 Frank, S., Kämpfer, H., Wetzler, C and Pfeilschifter, J. Nitric oxide drives skin repair: novel functions of an established mediator. *Kidney international* **61**, 882-888 (2002).
- 79 Menke, N. B., Ward, K. R., Witten, T. M., Bonchev, G and Diegelmann, F. Impaired wound healing. *Clinics in dermatology* **25**, 19-25 (2007).
- 80 Daeschlein, G., Napp, M., Lutze, S., Arnold, A., von Podewils, S., Guembel, D and Jünger, M. Skin and wound decontamination of multidrug-resistant bacteria by cold atmospheric plasma coagulation. *JDDG: Journal der Deutschen Dermatologischen Gesellschaft* **13**, 143-149 (2015).
- 81 Haertel, B., von Woedtke, T., Weltmann, K.D and Lindequist, U. Non-thermal atmospheric-pressure plasma possible application in wound healing. *Biomolecules & therapeutics* **22**, 477 (2014).
- 82 Nastuta, V., Topala, I., Grigoras, C., Pohoata, V and Popa, G. Stimulation of wound healing by helium atmospheric pressure plasma treatment. *Journal of Physics D: Applied Physics* **44**, 105204 (2011).
- 83 Arndt, S., Unger, P., Wacker, E., Shimizu, T., Heinlin, J., Li, F., Thomas, M., Morfill, E., Zimmermann, L., Bosserhoff, K and Karrer, S. Cold atmospheric plasma (CAP) changes gene expression of key molecules of the wound healing machinery and improves wound healing in vitro and in vivo. *PloS one* **8**, e79325 (2013).
- 84 Kramer, A., Lademann, J., Bender, C., Sckell, A., Hartmann, B., Münch, S., Hinz, P., Ekkernkamp, A., Matthes, R., Koban, I and Partecke, I. Suitability of tissue tolerable plasmas (TTP) for the management of chronic wounds. *Clinical Plasma Medicine* **1**, 11-18 (2013).
- 85 Dobrynin, D., Wu, A., Kalghatgi, S., Park, S., Chernets, N., Wasko, K., Dumani, E., Ownbey, R., Joshi, G., Sensenig, R and Brooks, A.D. Live pig skin tissue and wound toxicity of cold plasma treatment. *Plasma Medicine* **1** (2011).
- 86 Dobrynin, D., Wasko, K., Friedman, G., Fridman, A and Fridman, G. Cold plasma sterilization of open wounds: live rat model. *Plasma Medicine* **1** (2011).

- 87 Rajasekaran, P., Opländer, C., Hoffmeister, D., Bibinov, N., Suschek, C.V., Wandke, D and Awakowicz, P. Characterization of dielectric barrier discharge (DBD) on mouse and histological evaluation of the plasma-treated tissue. *Plasma Processes and Polymers* **8**, 246-255 (2011).
- 88 Isbary, G., Stolz, W., Shimizu, T., Monetti, R., Bunk, W., Schmidt, U., Morfill, E., Klämpfl, G., Steffes, B., Thomas, M and Heinlin, J. Cold atmospheric argon plasma treatment may accelerate wound healing in chronic wounds: Results of an open retrospective randomized controlled study in vivo. *Clinical Plasma Medicine* **1**, 25-30 (2013).
- 89 Heinlin, J., Isbary, G., Stolz, W., Morfill, G., Landthaler, M., Shimizu, T., Steffes, B., Nosenko, T., Zimmermann, L and Karrer, S. Plasma applications in medicine with a special focus on dermatology. *Journal of the European Academy of Dermatology and Venereology* **25**, 1-11 (2011).
- 90 Ulrich, C., Kluschke, F., Patzelt, A., Vandersee, S., Czaika, V.A., Richter, H., Bob, A., Hutten, V., Painsi, C., Hüge, R and Kramer, A. Clinical use of cold atmospheric pressure argon plasma in chronic leg ulcers: A pilot study. *Journal of wound care* **24**, 196-203 (2015).
- 91 Prausnitz, R and Langer, R. Transdermal drug delivery. *Nature biotechnology* **26**, 1261 (2008).
- 92 Veronese, M and Pasut, G. PEGylation, successful approach to drug delivery. *Drug discovery today* **10**, 1451-1458 (2005).
- 93 Ma, Y., Nolte, J and Cornelissen, J. Virus-based nanocarriers for drug delivery. *Advanced drug delivery reviews* **64**, 811-825 (2012).
- 94 Santini, J., John T, Richards, C., Scheidt, R., Cima, J and Langer, R. Microchips as controlled drug-delivery devices. *Angewandte Chemie International Edition* **39**, 2396-2407 (2000).
- 95 Denet, R., Vanbever, R and Pr eat, V. Skin electroporation for transdermal and topical delivery. *Advanced drug delivery reviews* **56**, 659-674 (2004).
- 96 Shimizu, K and Kriřtof, J. Microplasma Drug Delivery. *Plasma Medicine-Concepts and Clinical Applications*. IntechOpen, (2018).
- 97 Ogawa, Y., Morikawa, N., Ohkubo-Suzuki, A., Miyoshi, S., Arakawa, H., Kita, Y and Nishimura, S. An epoch-making application of discharge plasma phenomenon to gene-transfer. *Biotechnology and bioengineering* **92**, 865-870 (2005).
- 98 Sakai, Y., Khajooe, V., Ogawa, Y., Kusuhara, K., Katayama, Y and Hara, T. A novel transfection method for mammalian cells using gas plasma. *Journal of biotechnology* **121**, 299-308 (2006).
- 99 Vijayarangan, V., Delalande, A., Dozias, S., Pouvesle, M., Pichon, C and Robert, E. Cold atmospheric plasma parameters investigation for efficient drug delivery in HeLa cells. *IEEE Transactions on Radiation and Plasma Medical Sciences* **2**, 109-115 (2018).
- 100 Leduc, M., Guay, D., Leask, R and Coulombe, S. Cell permeabilization using a non-thermal plasma. *New Journal of Physics* **11**, 115021 (2009).
- 101 Babaeva, Y and Kushner, J. Intracellular electric fields produced by dielectric barrier discharge treatment of skin. *Journal of Physics D: Applied Physics* **43**, 185206 (2010).
- 102 Shimizu, K., Hayashida, K and Blajan, M. Novel method to improve transdermal drug delivery by atmospheric microplasma irradiation. *Biointerphases* **10**, 029517 (2015).
- 103 Gehl, J. Electroporation: theory and methods, perspectives for drug delivery, gene therapy and research. *Acta Physiologica Scandinavica* **177**, 437-447 (2003).
- 104 A Charoo, N., Rahman, Z., A Repka, M and Murthy, S. Electroporation: an avenue for transdermal drug delivery. *Current drug delivery* **7**, 125-136 (2010).

- 105 Prausnitz, R. The effects of electric current applied to skin: a review for transdermal drug delivery. *Advanced Drug Delivery Reviews* **18**, 395-425 (1996).
- 106 Shimizu, K and Krištof, J. Enhancement of percutaneous absorption on skin by plasma drug delivery method. *Advanced Technology for Delivering Therapeutics*. IntechOpen (2017).
- 107 Yusupov, M., Wende, K., Kupsch, S., Neyts, E., Reuter, S and Bogaerts, A. Effect of head group and lipid tail oxidation in the cell membrane revealed through integrated simulations and experiments. *Scientific Reports* **7**, 5761 (2017).
- 108 Van der Paal, J., Neyts, E., Verlackt, C and Bogaerts, A. Effect of lipid peroxidation on membrane permeability of cancer and normal cells subjected to oxidative stress. *Chemical science* **7**, 489-498 (2016).
- 109 Yusupov, M., Van der Paal, J., Neyts, E. & Bogaerts, A. Synergistic effect of electric field and lipid oxidation on the permeability of cell membranes. *Biochimica et Biophysica Acta (BBA)-General Subjects* **1861**, 839-847 (2017).
- 110 Kumar, N., Shaw, P., Razzokov, J., Yusupov, M., Attri, P., Uhm, S., Choi, H. and Bogaerts, A. Enhancement of cellular glucose uptake by reactive species: a promising approach for diabetes therapy. *RSC advances* **8**, 9887-9894 (2018).
- 111 Khan, A and Pessin, J. Insulin regulation of glucose uptake: a complex interplay of intracellular signalling pathways. *Diabetologia* **45**, 1475-1483 (2002).
- 112 Saltiel, R and Kahn, R. Insulin signalling and the regulation of glucose and lipid metabolism. *Nature* **414**, 799 (2001).
- 113 Kahn, S. The relative contributions of insulin resistance and beta-cell dysfunction to the pathophysiology of type 2 diabetes. *Diabetologia* **46**, 3-19 (2003).
- 114 Cavaghan, K., Ehrmann, A and Polonsky, S. Interactions between insulin resistance and insulin secretion in the development of glucose intolerance. *Journal of clinical investigation* **106**, 329-333 (2000).
- 115 Stumvoll, M., Goldstein, J and van Haefen, W. Type 2 diabetes: principles of pathogenesis and therapy. *The Lancet* **365**, 1333-1346 (2005).
- 116 Ross, A and Poirier, A. Protein aggregation and neurodegenerative disease. *Nature medicine* **10**, S10 (2004).
- 117 Chiti, F and Dobson, M. Protein misfolding, functional amyloid, and human disease. *Annu. Rev. Biochem.* **75**, 333-366 (2006).
- 118 Hamley, W. The amyloid beta peptide: a chemist's perspective. Role in Alzheimer's and fibrillization. *Chemical reviews* **112**, 5147-5192 (2012).
- 119 Yankner, A., Duffy, K and Kirschner, A. Neurotrophic and neurotoxic effects of amyloid b protein: reversal by tachykinin neuropeptides. *Science* **250**, 279-282 (1990).
- 120 Demuro, A., Parker, I and Stutzmann, E. Calcium signaling and amyloid toxicity in Alzheimer disease. *Journal of Biological Chemistry* **285**, 12463-12468 (2010).
- 121 Hardy, A and Higgins, A. Alzheimer's disease: the amyloid cascade hypothesis. *Science* **256**, 184 (1992).
- 122 Raschetti, R., Albanese, E., Vanacore, N and Maggini, M. Cholinesterase inhibitors in mild cognitive impairment: a systematic review of randomised trials. *PLoS medicine* **4**, e338 (2007).
- 123 Salomone, S., Caraci, F., Leggio, G. M., Fedotova, J and Drago, F. New pharmacological strategies for treatment of Alzheimer's disease: focus on disease modifying drugs. *British journal of clinical pharmacology* **73**, 504-517 (2012).
- 124 Liu, F., Liu, Z., Bai, S., Dong, Y and Sun, Y. Exploring the inter-molecular interactions in amyloid- $\beta$  protofibril with molecular dynamics simulations and molecular mechanics Poisson-Boltzmann surface area free energy calculations. *The Journal of Chemical Physics* **136**, 04B610 (2012).

- 125 Lemkul, J and Bevan, R. Assessing the stability of Alzheimer's amyloid protofibrils using molecular dynamics. *Journal of Physical Chemistry B* **114**, 1652-1660 (2010).
- 126 Brown, M., Lemkul, J., Schaum, N and Bevan, R. Simulations of monomeric amyloid  $\beta$ -peptide (1–40) with varying solution conditions and oxidation state of Met35: implications for aggregation. *Archives of biochemistry and biophysics* **545**, 44-52 (2014).
- 127 Johansson, S., Bergquist, J., Volbracht, C., Päiviö, A., Leist, M., Lannfelt, L and Westlind-Danielsson, A. Attenuated amyloid- $\beta$  aggregation and neurotoxicity owing to methionine oxidation. *Neuroreport* **18**, 559-563 (2007).
- 128 Palmblad, M., Westlind-Danielsson, A and Bergquist, J. Oxidation of methionine 35 attenuates formation of amyloid  $\beta$ -peptide 1–40 oligomers. *Journal of Biological Chemistry* **277**, 19506-19510 (2002).
- 129 Bayliss, D., Walsh, L., Shama, G., Iza, F and Kong, G. Reduction and degradation of amyloid aggregates by a pulsed radio-frequency cold atmospheric plasma jet. *New Journal of Physics* **11**, 115024 (2009).
- 130 Karakas, E., Munyanyi, A., Greene, L and Laroussi, M. Destruction of  $\alpha$ -synuclein based amyloid fibrils by a low temperature plasma jet. *Applied Physics Letters* **97**, 143702 (2010).
- 131 Hoeijmakers, H. DNA damage, aging, and cancer. *New England Journal of Medicine* **361**, 1475-1485 (2009).
- 132 Loeb, R and Loeb, A. Significance of multiple mutations in cancer. *Carcinogenesis* **21**, 379-385 (2000).
- 133 Chompret, A., Brugières, L., Ronsin, M., Gardes, M., Dessarps-Freichey, F., Abel, A., Hua, D., Ligoit, L., Dondon, G., Bressac-De Paillerets, B and Frébourg, T. P53 germline mutations in childhood cancers and cancer risk for carrier individuals. *British journal of cancer* **82**, 1932 (2000).
- 134 Greenblatt, M., Bennett, W. P., Hollstein, M and Harris, C. Mutations in the p53 tumor suppressor gene: clues to cancer etiology and molecular pathogenesis. *Cancer research* **54**, 4855-4878 (1994).
- 135 Campbell, M and Der, J. Oncogenic Ras and its role in tumor cell invasion and metastasis. in *Seminars in cancer biology* **14**, 105-114 (2004).
- 136 Curtin, J. DNA repair dysregulation from cancer driver to therapeutic target. *Nature Reviews Cancer* **12**, 801 (2012).
- 137 DeBerardinis, J., Lum, J., Hatzivassiliou, G and Thompson, B. The biology of cancer: metabolic reprogramming fuels cell growth and proliferation. *Cell metabolism* **7**, 11-20 (2008).
- 138 Reya, T., Morrison, J., Clarke, F and Weissman, L. Stem cells, cancer, and cancer stem cells. *Nature* **414**, 105 (2001).
- 139 Siegel, R., Ma, J., Zou, Z and Jemal, A. Cancer statistics, 2014. *CA: a cancer journal for clinicians* **64**, 9-29 (2014).
- 140 Gottesman, M., Lavi, O., Hall, D and Gillet, P. Toward a better understanding of the complexity of cancer drug resistance. *Annual review of pharmacology and toxicology* **56**, 85-102 (2016).
- 141 Cooperberg, R., Broering, M and Carroll, R. Time trends and local variation in primary treatment of localized prostate cancer. *Journal of Clinical Oncology* **28**, 1117 (2010).
- 142 Schulz-Ertner, D and Tsujii, H. Particle radiation therapy using proton and heavier ion beams. *Journal of clinical oncology* **25**, 953-964 (2007).
- 143 Dolmans, E., Fukumura, D and Jain, K. Photodynamic therapy for cancer. *Nature reviews cancer* **3**, 380 (2003).

- 144 Boulikas, T and Vougiouka, M. Recent clinical trials using cisplatin, carboplatin and their combination chemotherapy drugs. *Oncology reports* **11**, 559-595 (2004).
- 145 Collaborators, S. Breast cancer and hormone-replacement therapy in the Million Women Study. *The Lancet* **362**, 419-427 (2003).
- 146 Hur, W and Yoon, S. Molecular pathogenesis of radiation-induced cell toxicity in stem cells. *International journal of molecular sciences* **18**, 2749 (2017).
- 147 Bruheim, K., Guren, M.G., Skovlund, E., Hjermsstad, J., Dahl, O., Frykholm, G., Carlsen, E and Tveit, M. Late side effects and quality of life after radiotherapy for rectal cancer. *International Journal of Radiation Oncology\* Biology\* Physics* **76**, 1005-1011 (2010).
- 148 Peeters, K., van de Velde, J., Leer, W., Martijn, H., Junggeburst, M., Kranenbarg, K., Steup, H., Wiggers, T., Rutten, J and Marijnen, A. Late side effects of short-course preoperative radiotherapy combined with total mesorectal excision for rectal cancer: increased bowel dysfunction in irradiated patients—a Dutch colorectal cancer group study. *Journal of clinical oncology* **23**, 6199-6206 (2005).
- 149 Sjövall, K., Strömbeck, G., Löfgren, A., Bendahl, P. and Gunnars, B. Adjuvant radiotherapy of women with breast cancer—information, support and side-effects. *European Journal of Oncology Nursing* **14**, 147-153 (2010).
- 150 Costa, J. Neurocognitive effects of childhood cancer treatment." *Chemo Fog*. Springer, New York, NY, 26-32 (2010).
- 151 Juarranz, Á., Jaén, P., Sanz-Rodríguez, F., Cuevas, J and González, S. Photodynamic therapy of cancer. Basic principles and applications. *Clinical and Translational Oncology* **10**, 148-154 (2008).
- 152 Agostinis, P. *et al.* Photodynamic therapy of cancer: an update. *CA: a cancer journal for clinicians* **61**, 250-281 (2011).
- 153 DeVita, V. T. & Chu, E. A history of cancer chemotherapy. *Cancer research* **68**, 8643-8653 (2008).
- 154 Bhosle, J. & Hall, G. Principles of cancer treatment by chemotherapy. *Surgery (Oxford)* **27**, 173-177 (2009).
- 155 Monsuez, J., Charniot, J.-C., Vignat, N and Artigou, J. Cardiac side-effects of cancer chemotherapy. *International journal of cardiology* **144**, 3-15 (2010).
- 156 Bhattacharya, B and Mukherjee, S. Cancer therapy using antibiotics. *Journal of Cancer Therapy* **6**, 849 (2015).
- 157 Larsen, A., Escargueil, E and Skladanowski, A. Catalytic topoisomerase II inhibitors in cancer therapy. *Pharmacology & therapeutics* **99**, 167-181 (2003).
- 158 Yue, Q.-X., Liu, X and Guo, D. Microtubule-binding natural products for cancer therapy. *Planta medica* **76**, 1037-1043 (2010).
- 159 Hellerstedt, A and Pienta, K. The current state of hormonal therapy for prostate cancer. *CA: a cancer journal for clinicians* **52**, 154-179 (2002).
- 160 McGuire, W., Horwitz, K., Pearson, O and Segaloff, A. Current status of estrogen and progesterone receptors in breast cancer. *Cancer* **39**, 2934-2947 (1977).
- 161 Winer, E., Hudis, C., Burstein, H., Wolff, A., Pritchard, K., Ingle, J., Chlebowski, R., Gelber, R., Edge, S., Gralow, J and Cobleigh, M. American Society of Clinical Oncology technology assessment on the use of aromatase inhibitors as adjuvant therapy for postmenopausal women with hormone receptor–positive breast cancer: status report 2004. *Journal of clinical oncology* **23**, 619-629 (2005).
- 162 Kim, J., Ballato, J., Foy, P., Hawkins, T., Wei, Y., Li, J and Kim, S. Apoptosis of lung carcinoma cells induced by a flexible optical fiber-based cold microplasma. *Biosensors and Bioelectronics* **28**, 333-338 (2011).

- 163 Recek, N., Cheng, X., Keidar, M., Cvelbar, U., Vesel, A., Mozetic, M. and Sherman, J. Effect of cold plasma on glial cell morphology studied by atomic force microscopy. *PloS one* **10**, e0119111 (2015).
- 164 Keidar, M., Walk, R., Shashurin, A., Srinivasan, P., Sandler, A., Dasgupta, S., Ravi, R., Guerrero-Preston, R. and Trink, B. Cold plasma selectivity and the possibility of a paradigm shift in cancer therapy. *British journal of cancer* **105**, 1295 (2011).
- 165 Kim, S. and Chung, T. Cold atmospheric plasma jet-generated RONS and their selective effects on normal and carcinoma cells. *Scientific reports* **6**, 20332 (2016).
- 166 Utsumi, F., Kajiyama, H., Nakamura, K., Tanaka, H., Hori, M. and Kikkawa, F. Selective cytotoxicity of indirect nonequilibrium atmospheric pressure plasma against ovarian clear-cell carcinoma. *SpringerPlus* **3**, 398 (2014).
- 167 Wang, M., Holmes, B., Cheng, X., Zhu, W., Keidar, M. and Zhang, L. Cold atmospheric plasma for selectively ablating metastatic breast cancer cells. *PloS one* **8**, e73741 (2013).
- 168 Metelmann, H.R., Nedrelow, D., Seebauer, C., Schuster, M., von Woedtke, T., Weltmann, K., Kindler, S., Metelmann, P., Finkelstein, S., Von Hoff, D. and Podmelle, F. Head and neck cancer treatment and physical plasma. *Clinical Plasma Medicine* **3**, 17-23 (2015).
- 169 Kang, S., Cho, J., Chang, J., Shin, Y., Kim, K., Park, J., Yang, S., Lee, J., Moon, E., Lee, K. and Kim, C. Nonthermal plasma induces head and neck cancer cell death: the potential involvement of mitogen-activated protein kinase-dependent mitochondrial reactive oxygen species. *Cell death & disease* **5**, e1056 (2014).
- 170 Vandamme, M., Robert, E., Lerondel, S., Sarron, V., Ries, D., Dozias, S., Sobilo, J., Gosset, D., Kieda, C., Legrain, B. and Pouvesle, J. ROS implication in a new antitumor strategy based on non-thermal plasma. *International journal of cancer* **130**, 2185-2194 (2012).
- 171 Tanaka, H., Mizuno, M., Ishikawa, K., Nakamura, K., Kajiyama, H., Kano, H., Kikkawa, F. and Hori, M. Plasma-activated medium selectively kills glioblastoma brain tumor cells by down-regulating a survival signaling molecule, AKT kinase. *Plasma Medicine* **1** (2011).
- 172 Thiyagarajan, M., Anderson, H. and Gonzales, X. Induction of apoptosis in human myeloid leukemia cells by remote exposure of resistive barrier cold plasma. *Biotechnology and bioengineering* **111**, 565-574 (2014).
- 173 Barekzi, N. and Laroussi, M. Dose-dependent killing of leukemia cells by low-temperature plasma. *Journal of Physics D: Applied Physics* **45**, 422002 (2012).
- 174 Kim, S. J., Chung, T., Bae, S. and Leem, S. Induction of apoptosis in human breast cancer cells by a pulsed atmospheric pressure plasma jet. *Applied Physics Letters* **97**, 023702 (2010).
- 175 Fridman, G., Shereshevsky, A., Jost, M.M., Brooks, A., Fridman, A., Gutsol, A., Vasilets, V. and Friedman, G. Floating electrode dielectric barrier discharge plasma in air promoting apoptotic behavior in melanoma skin cancer cell lines. *Plasma Chemistry and Plasma Processing* **27**, 163-176 (2007).
- 176 Gay-Mimbrera, J., García, M., Isla-Tejera, B., Rodero-Serrano, A., García-Nieto, A.V. and Ruano, J. Clinical and biological principles of cold atmospheric plasma application in skin cancer. *Advances in therapy* **33**, 894-909 (2016).
- 177 Ishaq, M., Evans, M. and Ostrikov, K. Atmospheric pressure gas plasma-induced colorectal cancer cell death is mediated by Nox2-ASK1 apoptosis pathways and oxidative stress is mitigated by Srx-Nrf2 anti-oxidant system. *Biochimica et Biophysica Acta (BBA)-Molecular Cell Research* **1843**, 2827-2837 (2014).

- 178 Hattori, N., Yamada, S., Torii, K., Takeda, S., Nakamura, K., Tanaka, H., Kajiyama, H., Kanda, M., Fujii, T., Nakayama, G. and Sugimoto, H. Effectiveness of plasma treatment on pancreatic cancer cells. *International journal of oncology* **47**, 1655-1662 (2015).
- 179 Partecke, L. Evert, K., Haugk, J., Doering, F., Normann, L., Diedrich, S., Weiss, U., Evert, M., Huebner, N., Guenther, C and Heidecke, C. Tissue tolerable plasma (TTP) induces apoptosis in pancreatic cancer cells in vitro and in vivo. *BMC cancer* **12**, 473 (2012).
- 180 Walk, R., Snyder, J., Srinivasan, P., Kirsch, J., Diaz, S., Blanco, F., Shashurin, A., Keidar, M and Sandler, A. Cold atmospheric plasma for the ablative treatment of neuroblastoma. *Journal of pediatric surgery* **48**, 67-73 (2013).
- 181 Kim, J., Wei, Y., Li, J., Foy, P., Hawkins, T., Ballato, J and Kim, S. Single-cell-level microplasma cancer therapy. *Small* **7**, 2291-2295 (2011).
- 182 Vandamme, M., Robert, E., Pesnel, S., Barbosa, E., Dozias, S., Sobilo, J., Lerondel, S., Le Pape, A and Pouvesle, J. Antitumor effect of plasma treatment on U87 glioma xenografts: preliminary results. *Plasma processes and polymers* **7**, 264-273 (2010).
- 183 Sensenig, R., Kalghatgi, S., Cerchar, E., Fridman, G., Shereshevsky, A., Torabi, B., Arjunan, K., Podolsky, E., Fridman, A., Friedman, G and Azizkhan-Clifford, J. Retracted article: Non-thermal plasma induces apoptosis in melanoma cells via production of intracellular reactive oxygen species. *Annals of biomedical engineering* **39**, 674-687 (2011).
- 184 Thiyagarajan, M., Gonzales, X and Anderson, H. Regulated cellular exposure to non-thermal plasma allows preferentially directed apoptosis in acute monocytic leukemia cells. *Studies in health technology and informatics* **184**, 436-442 (2013).
- 185 Ratovitski, E., Cheng, X., Yan, D., Sherman, J., Canady, J., Trink, B and Keidar, M. Anti-cancer therapies of 21st century: novel approach to treat human cancers using cold atmospheric plasma. *Plasma Processes and Polymers* **11**, 1128-1137 (2014).
- 186 Volotskova, O., Hawley, T., Stepp, M and Keidar, M. Targeting the cancer cell cycle by cold atmospheric plasma. *Scientific reports* **2**, 636 (2012).
- 187 Gweon, B., Kim, M., Bee Kim, D., Kim, D., Kim, H., Jung, H., H. Shin, J and Choe, W. Differential responses of human liver cancer and normal cells to atmospheric pressure plasma. *Applied Physics Letters* **99**, 063701 (2011).
- 188 Moh, M. and Shen, S. The roles of cell adhesion molecules in tumor suppression and cell migration: a new paradox. *Cell adhesion & migration* **3**, 334-336 (2009).
- 189 Panngom, K., Baik, K., Nam, M., Han, J., Rhim, H and Choi, E. Preferential killing of human lung cancer cell lines with mitochondrial dysfunction by nonthermal dielectric barrier discharge plasma. *Cell death & disease* **4**, e642 (2013).
- 190 Georgescu, N and Lupu, A. Tumoral and normal cells treatment with high-voltage pulsed cold atmospheric plasma jets. *IEEE Transactions on Plasma Science* **38**, 1949-1955 (2010).
- 191 Arndt, S., Wacker, E., Li, Y., Shimizu, T., Thomas, H., Morfill, G., Karrer, S., Zimmermann, J and Bosserhoff, A. Cold atmospheric plasma, a new strategy to induce senescence in melanoma cells. *Experimental dermatology* **22**, 284-289 (2013).
- 192 Graves, D. Reactive species from cold atmospheric plasma: implications for cancer therapy. *Plasma Processes and Polymers* **11**, 1120-1127 (2014).
- 193 Lu, X., Naidis, G., Laroussi, M., Reuter, S., Graves, D and Ostrikov, K. Reactive species in non-equilibrium atmospheric-pressure plasmas: Generation, transport, and biological effects. *Physics Reports* **630**, 1-84 (2016).
- 194 Liou, G and Storz, P. Reactive oxygen species in cancer. *Free radical research* **44**, 479-496 (2010).

- 195 Wiseman, H and Halliwell, B. Damage to DNA by reactive oxygen and nitrogen species: role in inflammatory disease and progression to cancer. *Biochemical Journal* **313**, 17 (1996).
- 196 Redza-Dutordoir, M and Averill-Bates, D. Activation of apoptosis signalling pathways by reactive oxygen species. *Biochimica et Biophysica Acta (BBA)-Molecular Cell Research* **1863**, 2977-2992 (2016).
- 197 Bauer, G. Increasing the endogenous NO level causes catalase inactivation and reactivation of intercellular apoptosis signaling specifically in tumor cells. *Redox biology* **6**, 353-371 (2015).
- 198 Filep, J., Lapierre, C., Lachance, S and Chan, J. Nitric oxide co-operates with hydrogen peroxide in inducing DNA fragmentation and cell lysis in murine lymphoma cells. *Biochemical Journal* **321**, 897 (1997).
- 199 Keng, T., Privalle, C., Gilkeson, G and Weinberg, J. Peroxynitrite formation and decreased catalase activity in autoimmune MRL-lpr/lpr mice. *Molecular Medicine* **6**, 779 (2000).
- 200 Surmeli, N., Litterman, N., Miller, A and Groves, J. Peroxynitrite mediates active site tyrosine nitration in manganese superoxide dismutase. Evidence of a role for the carbonate radical anion. *Journal of the American Chemical Society* **132**, 17174-17185 (2010).
- 201 Peshenko, I and Shichi, H. Oxidation of active center cysteine of bovine 1-Cys peroxiredoxin to the cysteine sulfenic acid form by peroxide and peroxynitrite. *Free Radical Biology and Medicine* **31**, 292-303 (2001).
- 202 Padmaja, S., Squadrito, G and Pryor, W. Inactivation of glutathione peroxidase by peroxynitrite. *Archives of biochemistry and biophysics* **349**, 1-6 (1998).
- 203 Savvides, S., cheiwein, M., Böhme, C., Arteel, G., Karplus, P., Becker, K and Schirmer, R. Crystal structure of the antioxidant enzyme glutathione reductase inactivated by peroxynitrite. *Journal of Biological Chemistry* **277**, 2779-2784 (2002).
- 204 Hole, P., Zabkiewicz, J., Munje, C., Newton, Z., Pearn, L., White, P., Marquez, N., Hills, R., Burnett, A., Tonks, A and Darley, R. Overproduction of NOX-derived ROS in AML promotes proliferation and is associated with defective oxidative stress signaling. *Blood*, **19**, 3322-3330 (2013).
- 205 Papadopoulos, M and Saadoun, S. Key roles of aquaporins in tumor biology. *Biochimica et Biophysica Acta (BBA)-Biomembranes* **1848**, 2576-2583 (2015).
- 206 Cordeiro, R. Molecular dynamics simulations of the transport of reactive oxygen species by mammalian and plant aquaporins. *Biochimica et Biophysica Acta (BBA)-General Subjects* **1850**, 1786-1794 (2015).
- 207 Yan, D., Talbot, A., Nourmohammadi, N., Sherman, J., Cheng, X and Keidar, M. Toward understanding the selective anticancer capacity of cold atmospheric plasma—A model based on aquaporins. *Biointerphases* **10**, 040801 (2015).
- 208 Yusupov, M., Yan, D., Cordeiro, R and Bogaerts, A. Atomic scale simulation of H<sub>2</sub>O<sub>2</sub> permeation through aquaporin: toward the understanding of plasma cancer treatment. *Journal of Physics D: Applied Physics* **51**, 125401 (2018).
- 209 Wong-Ekkabut, J., Xu, Z., Triampo, W., Tang, I., Tieleman, D and Monticelli, L. Effect of lipid peroxidation on the properties of lipid bilayers: a molecular dynamics study. *Biophysical journal* **93**, 4225-4236 (2007).
- 210 Beranova, L., Cwiklik, L., Jurkiewicz, P., Hof, M and Jungwirth, P. Oxidation changes physical properties of phospholipid bilayers: fluorescence spectroscopy and molecular simulations. *Langmuir* **26**, 6140-6144 (2010).
- 211 Cwiklik, L and Jungwirth, P. Massive oxidation of phospholipid membranes leads to pore creation and bilayer disintegration. *Chemical Physics Letters* **486**, 99-103 (2010).

- 212 Van der Paal, J., Verheyen, C., Neyts, E and Bogaerts, A. Hampering effect of cholesterol on the permeation of reactive oxygen species through phospholipids bilayer: possible explanation for plasma cancer selectivity. *Scientific reports* **7**, 39526 (2017).
- 213 Svarnas, P., Matrali, S. H., Gazeli, K and Antimisiaris, S. Assessment of Atmospheric-Pressure Guided Streamer (Plasma Bullet) Influence on Liposomes with Different Composition and Physicochemical Properties. *Plasma Processes and Polymers* **12**, 655-665 (2015).
- 214 Hirst, A., Frame, F., Arya, M., Maitland, N and O'Connell, D. Low temperature plasmas as emerging cancer therapeutics: the state of play and thoughts for the future. *Tumor Biology* **37**, 7021-7031 (2016).
- 215 Robert, E., Darny, T., Dozias, S., Iseni, S and Pouvesle, J. New insights on the propagation of pulsed atmospheric plasma streams: From single jet to multi jet arrays. *Physics of Plasmas* **22**, 122007 (2015).
- 216 Begum, A., Laroussi, M and Pervez, M. Atmospheric pressure He-air plasma jet: Breakdown process and propagation phenomenon. *AIP Advances* **3**, 062117 (2013).
- 217 Weaver, J., Smith, K., Esser, A., Son, R and Gowrishankar, T. A brief overview of electroporation pulse strength–duration space: a region where additional intracellular effects are expected. *Bioelectrochemistry* **87**, 236-243 (2012).
- 218 Casciola, M and Tarek, M. A molecular insight into the electro-transfer of small molecules through electropores driven by electric fields. *Biochimica et Biophysica Acta (BBA)-Biomembranes* **1858**, 2278-2289 (2016).
- 219 Marrink, S., De Vries, A and Tieleman, D. Lipids on the move: simulations of membrane pores, domains, stalks and curves. *Biochimica et Biophysica Acta (BBA)-Biomembranes* **1788**, 149-168 (2009).
- 220 Ishaq, M., Evans, M and Ostrikov, K. Effect of atmospheric gas plasmas on cancer cell signaling. *International journal of cancer* **134**, 1517-1528 (2014).
- 221 Yusupov, M., Lackmann, J., Razzokov, J., Kumar, S., Stapelmann, K and Bogaerts, A. Impact of plasma oxidation on structural features of human epidermal growth factor. *Plasma Processes and Polymers* **15**, e1800022 (2018).
- 222 Bauer, G. Tumor cell-protective catalase as a novel target for rational therapeutic approaches based on specific intercellular ROS signaling. *Anticancer research* **32**, 2599-2624 (2012).
- 223 Bauer, G. Targeting extracellular ROS signaling of tumor cells. *Anticancer research* **34**, 1467-1482 (2014).
- 224 Bauer, G. Nitric Oxide Contributes To Selective Apoptosis Induction In Malignant Cells Through Multiple Reaction Steps. *Critical Review in Oncogenesis* **21**, 5-6 (2017).
- 225 Moncada, S and Erusalimsky, J. Does nitric oxide modulate mitochondrial energy generation and apoptosis? *Nature Reviews Molecular Cell Biology* **3**, 214 (2002).
- 226 Asahi, M., Fujii, J., Suzuki, K., Seo, H., Kuzuya, T., Hori, M., Tada, M., Fujii, S and Taniguchi, N. Inactivation of glutathione peroxidase by nitric oxide Implication for cytotoxicity. *Journal of Biological Chemistry* **270**, 21035-21039 (1995).
- 227 Ja Kim, S., Min Joh, H and Chung, T. Production of intracellular reactive oxygen species and change of cell viability induced by atmospheric pressure plasma in normal and cancer cells. *Applied Physics Letters* **103**, 153705 (2013).
- 228 Yan, D., Talbot, A., Nourmohammadi, N., Cheng, X., Canady, J., Sherman, J and Keidar, M. Principles of using cold atmospheric plasma stimulated media for cancer treatment. *Scientific reports* **5**, 18339 (2015).
- 229 Gardner, A., Cook, M and Gardner, P. Nitric oxide dioxygenase function of human cytoglobin with cellular reductants and in rat hepatocytes. *Journal of Biological Chemistry* **31**, 23850-23857 (2010).

- 230 Fordel, E., Thijs, L., Moens, L and Dewilde, S. Neuroglobin and cytoglobin expression in mice: evidence for a correlation with reactive oxygen species scavenging. *FEBS journal* **274**, 1312-1317 (2007).
- 231 Shivapurkar, N., Stastny, V., Okumura, N., Girard, L., Xie, Y., Prinsen, C., Thunnissen, F., Wistuba, I., Czerniak, B., Frenkel, E. and Roth, J. Cytoglobin, the newest member of the globin family, functions as a tumor suppressor gene. *Cancer Research* **68**, 7448-7456 (2008).
- 232 Sigismund, S., Avanzato, D and Lanzetti, L. Emerging functions of the EGFR in cancer. *Molecular oncology* **12**, 3-20 (2018).
- 233 Zhang, C and Fu, Y. Another way to not get eaten. *Nature immunology* **19**, 6 (2018).
- 234 Casey, S., Tong, L., Li, Y., Do, R., Walz, S., Fitzgerald, K., Gouw, A., Baylot, V., Gütgemann, I., Eilers, M and Felsher, D. MYC regulates the antitumor immune response through CD47 and PD-L1. *Science* **352**, 227-231 (2016).
- 235 Chao, M., Jaiswal, S., Weissman-Tsukamoto, R., Alizadeh, A.A., Gentles, A.J., Volkmer, J., Weiskopf, K., Willingham, S., Raveh, T., Park, C and Majeti, R. Calreticulin is the dominant pro-phagocytic signal on multiple human cancers and is counterbalanced by CD47. *Science translational medicine* **2**, 63ra94-63ra94 (2010).



# **Chapter 2.**

## **Computational methods**



## 2.1. Introduction

Computer simulations have become an important tool to obtain insight into various systems in the field of biology, physics, chemistry, engineering, climatology, astrophysics, etc. Computer simulations are based on mathematical models containing algorithms and equations, which are developed as computer programs. The initial conditions and the set of parameters have to be introduced to a computer program, which generates output that allows to predict the behavior of the system. A reliable model, validated by experiments, can be further used for other initial conditions and parameters, to predict the nature of the system under specific conditions. If a computer model lacks to characterize the behavior of the real system, the model has to be further improved (see [Figure 2.1](#)). In other words, computer models serve as a bridge between theory and experiments, and help to understand the system behavior in detail. Moreover, simulations can overcome limitations of experiments, by obtaining insight at nanoscale precision, which even modern technology cannot always reach.

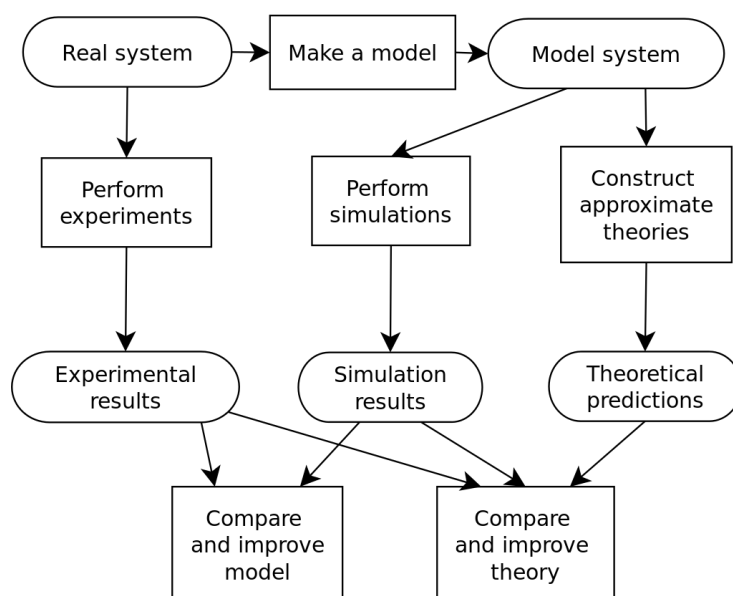


Figure 2.1. *The procedure of developing computer models. Figure is adopted from Wikipedia.org.*

In fact, computer simulations became indispensable in most aspects of modern science. For example, molecular dynamics (MD) simulations originated in the early 1960s, and were applied by Alder and Wainwright<sup>1,2</sup> to investigate the dynamics of liquids. Since the 1970s, the method has been continuously improved and allowed to study the dynamics of biomolecules, including proteins,<sup>3</sup> lipids,<sup>4</sup> and nucleic acids<sup>5</sup>, in 1977, 1980 and 1984, respectively. Nowadays, MD has become a valuable tool to explore systems with biological, biophysical and biochemical relevance, containing millions of atoms, and it is also the method applied in this PhD thesis. Specifically, we investigated the impact of oxidation on the behavior of membrane systems (see [Chapter 3](#)) as well as on the structures of different types of proteins (see [Chapter 4](#)) by means of MD simulations. Therefore, we will provide further detailed information about MD, and the other (related) simulation methods used in this thesis, in the next section.

## 2.2. Molecular dynamics

MD is one of the most widely employed computer simulation methods to describe the physical movement of atoms and molecules. The simulation system contains a fixed number of particles  $N$  (i.e., atoms and molecules), which interact with each other, leading to a dynamic evolution of the system for a certain period of time. In MD simulations, the trajectory of particles is defined by Newton's equation of motion:

$$\mathbf{m}_i \frac{\partial^2 \mathbf{r}_i}{\partial t^2} = \mathbf{F}_i, \quad i = 1, 2, \dots, N \quad (2.1)$$

where  $\mathbf{m}_i$  is the mass of the atom,  $\mathbf{r}_i$  is the position of atom  $i$  and  $\mathbf{F}_i$  is the force acting on atom  $i$  at the corresponding time  $t$ .

The forces acting on the particles in the system can be derived from the potential energy (interatomic interaction potential, also known as the "force field")  $U(\mathbf{r}_1, \mathbf{r}_2, \dots, \mathbf{r}_N)$ , with respect to the atomic positions:

$$\mathbf{F}_i = -\frac{\partial U}{\partial \mathbf{r}_i} \quad (2.2)$$

In classical non-reactive MD simulations, the total potential energy is defined from the sum of bonded ( $U_{bonded}$ ) and non-bonded ( $U_{non-bonded}$ ) energy terms. The  $U_{non-bonded}$  can be defined experimentally or by means of computer simulations.<sup>6-8</sup> It is the sum of Lennard-Jones ( $U_{LJ}$ ) and Coulomb ( $U_C$ ) energy terms:

$$U_{LJ}(r_{ij}) = 4\varepsilon_{ij} \left( \left( \frac{\sigma_{ij}}{r_{ij}} \right)^{12} - \left( \frac{\sigma_{ij}}{r_{ij}} \right)^6 \right) \quad (2.3)$$

where  $\sigma_{ij}$  is the finite distance at which the interaction potential between the particles is zero, and  $\varepsilon$  is the depth of the potential well.

$$U_C(r_{ij}) = \frac{q_i q_j}{4\pi\epsilon_0 r_{ij}} \quad (2.4)$$

where  $q_i$  and  $q_j$  are the charges of the interacting particles and  $r_{ij}$  is the distance between them.

The bonded interaction potential ( $U_{bonded}$ ) depends on a certain number of covalently bonded atoms, i.e., bond stretching (between 2 atoms), bond angle (between 3 atoms) and (improper) dihedral angle (between 4 atoms) interactions (see [Figure 2.2](#) and equations (2.5) – (2.8)):

$$\text{- harmonic bond potential} \quad U_b = \frac{1}{2} \sum_{bonds} k_{ij}^r (r_{ij} - r_{eq})^2 \quad (2.5)$$

$$\text{- harmonic angle potential} \quad U_a = \frac{1}{2} \sum_{angles} k_{ij}^\theta (\theta_{ij} - \theta_{eq})^2 \quad (2.6)$$

$$\text{- dihedral potential} \quad U_d = \sum_{dihedral} \sum_m k_{ijkl}^{\phi,m} (1 + \cos(m\phi_{ijkl} - \gamma_m)) \quad (2.7)$$

$$\text{- improper dihedral potential} \quad U_{id} = \frac{1}{2} \sum_{improper\ dihedral} k_{ijkl}^\Omega (\Omega_{ijkl} - \Omega_{eq})^2 \quad (2.8)$$

where,  $k$  is the force constant associated with the bond, angle, dihedral and improper dihedral potential. The improper dihedral potential makes sure that planar groups (e.g., aromatic rings) remain planar during the simulation.

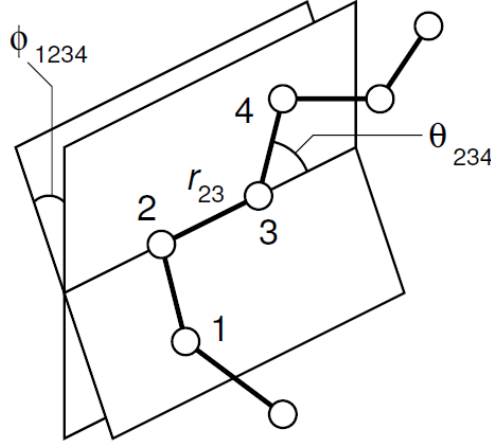


Figure 2.2. Illustration of a chain molecule with indication of the interatomic distance  $r_{23}$ , the bending angle  $\theta_{234}$ , and dihedral angle  $\phi_{1234}$ . Figure is adopted from <sup>9</sup>.

Hence,  $U_{bonded}$  is the sum of bond, angle, dihedral and improper dihedral potential energy terms. Thus, the total potential energy is defined as follows:

$$U = U_{non-bonded} + U_{bonded} = U_{LJ} + U_C + U_b + U_a + U_d + U_{id} \quad (2.9)$$

The equation of motion (2.1) is numerically integrated in MD simulation packages. During the MD simulations the code generates the trajectory of the atoms in the considered system. In order to determine the position of the particles after each time step in the system, various integrator algorithms can be used. One of the commonly employed integrators in MD simulations is the *Verlet integrator*.<sup>10</sup> The integrator has to fulfil two functions: (a) the dynamical properties of the system need to be calculated accurately over time, and (b) the energy of the system must be kept constant for longer time simulations.

Integration algorithm: The *Verlet integrator* is one of the simplest integrators and also computationally effective in MD simulations, due to its stability, accuracy and simplistic character. The current algorithm is derived from two Taylor expansions:

$$\mathbf{r}(t + \delta t) = \mathbf{r}(t) + \frac{d\mathbf{r}(t)}{dt} \delta t + \frac{d^2\mathbf{r}(t)}{2!dt^2} \delta t^2 + \frac{d^3\mathbf{r}(t)}{3!dt^3} \delta t^3 + \mathcal{O}(\delta t^4) \quad (2.10a)$$

$$\mathbf{r}(t - \delta t) = \mathbf{r}(t) - \frac{d\mathbf{r}(t)}{dt} \delta t + \frac{d^2\mathbf{r}(t)}{2!dt^2} \delta t^2 - \frac{d^3\mathbf{r}(t)}{3!dt^3} \delta t^3 + \mathcal{O}(\delta t^4) \quad (2.10b)$$

We obtain the main formula of the integrator after adding both expressions:

$$\mathbf{r}(\mathbf{t} + \delta\mathbf{t}) = 2\mathbf{r}(\mathbf{t}) - \mathbf{r}(\mathbf{t} - \delta\mathbf{t}) + \frac{d^2\mathbf{r}(\mathbf{t})}{2!d\mathbf{t}^2} \delta\mathbf{t}^2 + \mathbf{O}(\delta\mathbf{t}^4) \quad (2.11)$$

where  $\delta\mathbf{t}$  is the time step and  $\mathbf{O}(\delta\mathbf{t}^4)$  is the truncated error. This error can be reduced by applying a small time step  $\delta\mathbf{t}$ . In expression (2.11) the velocity is not explicitly solved. However, the velocity also needs to be determined in order to calculate the kinetic energy in the system. The velocity is typically calculated from the first order difference:

$$\mathbf{v}(\mathbf{t}) = \frac{\mathbf{r}(\mathbf{t} + \delta\mathbf{t}) - \mathbf{r}(\mathbf{t} - \delta\mathbf{t})}{2\delta\mathbf{t}} \quad (2.12)$$

After inserting equation (2.10a) and (2.10b) into equation (2.12) we obtain:

$$\mathbf{v}(\mathbf{t} + \delta\mathbf{t}) = \mathbf{v}(\mathbf{t}) + \frac{\delta\mathbf{t}}{m} \mathbf{F}(\mathbf{t}) + \mathbf{O}(\delta\mathbf{t}^3) \quad (2.13)$$

By means of equation (2.13) we can calculate the total kinetic energy of the N-particle system.

$$E_{kin} = \frac{1}{2} \sum_i^N \mathbf{m}_i \mathbf{v}_i \otimes \mathbf{v}_i \quad (2.14)$$

In order to increase the accuracy, the *velocity Verlet algorithm* is developed. In this algorithm positions, velocities and accelerations at time  $\mathbf{t} + \delta\mathbf{t}$  are obtained from the same quantities at time  $\mathbf{t}$  in the following way:

$$\mathbf{r}(\mathbf{t} + \delta\mathbf{t}) = \mathbf{r}(\mathbf{t}) + \mathbf{v}(\mathbf{t})\delta\mathbf{t} + \frac{d^2\mathbf{r}(\mathbf{t})}{2d\mathbf{t}^2} \delta\mathbf{t}^2 \quad (2.15)$$

$$\mathbf{v}\left(\mathbf{t} + \frac{\delta\mathbf{t}}{2}\right) = \mathbf{v}(\mathbf{t}) + \frac{\delta\mathbf{t}}{2m} \mathbf{F}(\mathbf{t}) \quad (2.16)$$

$$\mathbf{a}(\mathbf{t} + \delta\mathbf{t}) = -\left(\frac{1}{m}\right) \nabla U(\mathbf{r}(\mathbf{t} + \delta\mathbf{t})) \quad (2.17)$$

$$\mathbf{v}(\mathbf{t} + \delta\mathbf{t}) = \mathbf{v}\left(\mathbf{t} + \frac{\delta\mathbf{t}}{2}\right) + \frac{1}{2} \mathbf{a}(\mathbf{t} + \delta\mathbf{t})\delta\mathbf{t} \quad (2.18)$$

The current algorithm represents long time energy conservation with higher precision. Furthermore, both the half step averaged kinetic and potential energy can be computed simultaneously. This algorithm was used in this thesis.

*Periodic boundary conditions (PBCs):* The advantage of PBCs is that they enable to calculate the macroscopic parameters of the system, while the system itself contains fewer particles. PBCs are applied in MD simulations in order to avoid artifacts that are caused by the size of the system during the simulations. Therefore, the system is treated like infinite, despite the original size is finite. The edge effect in a finite system is minimized by using PBCs. In other words, the simulation box is surrounded by replicas of itself (see [Figure 2.3](#)). The atoms interact with each other (i.e., with the nearest one) or with the image in the periodic box. When the particles leave the main box, they reappear in the box from the opposite side, keeping the same velocity. This does not influence the course of the simulation. The trajectory of the particles in the main box is recorded in the MD simulations and used for analysis.

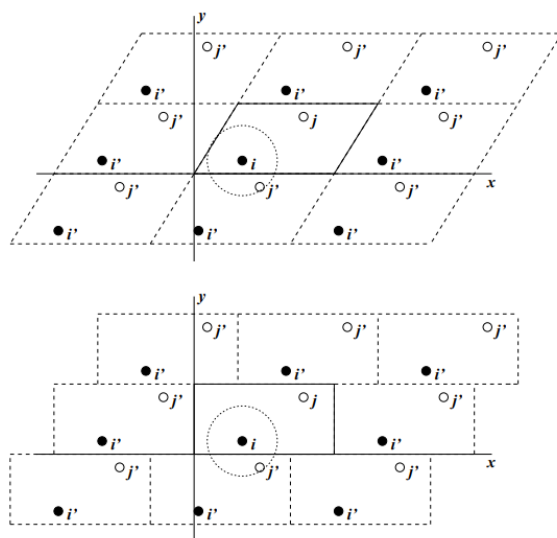


Figure 2.3. Illustration of periodic boundary conditions in two dimensions. The original particles  $i$  and  $j$  and their replicas are described. The figure is adopted from <sup>11</sup>.

Particles are free to diffuse, so they will move from the position where they initially started. When the simulation system contains a large protein, some parts of the protein appear from the opposite side of the box, so the size of the box has to be large enough in order to avoid interaction with its image, as the latter might lead to incorrect results. In the GROMACS package (MD package that we apply), various kinds of box types are implemented to effectively manage the simulation of large molecules and at the same time to save the computational cost, by placing less solvent molecules around the solute. The simulation box is determined by means of three box vectors,  $a$ ,  $b$  and  $c$  (see [Table 2.1](#)).<sup>11</sup>

Table 2.1. The parameters of cubic, rhombic dodecahedron, and truncated octahedron boxes.

box type	image distance	box volume	box vectors			box vector angles		
			$\mathbf{a}$	$\mathbf{b}$	$\mathbf{c}$	$\angle \mathbf{bc}$	$\angle \mathbf{ac}$	$\angle \mathbf{ab}$
cubic	$d$	$d^3$	$d$ 0 0	0 $d$ 0	0 0 $d$	$90^\circ$	$90^\circ$	$90^\circ$
rhombic dodecahedron (xy-square)	$d$	$\frac{1}{2}\sqrt{2}d^3$ $0.707d^3$	$d$ 0 0	0 $d$ 0	$\frac{1}{2}d$ $\frac{1}{2}d$ $\frac{1}{2}\sqrt{2}d$	$60^\circ$	$60^\circ$	$90^\circ$
rhombic dodecahedron (xy-hexagon)	$d$	$\frac{1}{2}\sqrt{2}d^3$ $0.707d^3$	$d$ 0 0	$\frac{1}{2}d$ $\frac{1}{2}\sqrt{3}d$ 0	$\frac{1}{2}d$ $\frac{1}{6}\sqrt{3}d$ $\frac{1}{3}\sqrt{6}d$	$60^\circ$	$60^\circ$	$60^\circ$
truncated octahedron	$d$	$\frac{4}{9}\sqrt{3}d^3$ $0.770d^3$	$d$ 0 0	$\frac{1}{3}d$ $\frac{2}{3}\sqrt{2}d$ 0	$-\frac{1}{3}d$ $\frac{1}{3}\sqrt{2}d$ $\frac{1}{3}\sqrt{6}d$	$71.53^\circ$	$109.47^\circ$	$71.53^\circ$

We used rhombic dodecahedron box types in our simulations, because the volume is approximately 71% of the volume of a cubic box, while it has the same image distance. Moreover, rhombic dodecahedron box types save about 29% of computing time when the

system contains spherical or flexible molecules. Therefore, choosing the appropriate box shape in simulations helps to obtain an optimal spacing, which increases the efficiency of MD simulations.

Cut-off restrictions: As mentioned above, the size of the simulation box has to be specified carefully. According to the *minimum image criterion*, the non-bonded interactions do not have to exceed the half of the shortest box vector. In this respect, the cut-off radius is used to truncate interactions:

$$R_c < \frac{1}{2} \min(\|a\|, \|b\|, \|c\|) \quad (2.19)$$

Otherwise, more than a single image might occur within the cut-off distance. Note that for macromolecular simulations the cut-off restriction is not enough and the solvent molecule should not occur at both sides of the macromolecule. In order to avoid this, each box vector must be larger than the length of the macromolecule plus two times the  $R_c$  distance. This is very important because once particles start interacting with its own image or multiple images, it might cause severe artifacts.

Thermodynamics ensembles in MD: In order to mimic the experimental conditions, the MD simulations should be performed applying specific conditions. For instance, temperature, pressure, volume or energy have to be kept constant during the simulation. It means that a certain simulation ensemble in MD is one of the criteria of a particular task. In general, four thermodynamics ensembles are commonly employed in MD simulations: the canonical ensemble (NVT),<sup>12</sup> isothermal-isobaric ensemble (NPT),<sup>13</sup> microcanonical ensemble (NVE)<sup>14</sup> and grand canonical ensemble ( $\mu$ VT)<sup>15,16</sup>. The collection of microstates of the system corresponds to one of the above mentioned ensembles according to statistical mechanics.

A canonical ensemble corresponds to the system which is in thermal equilibrium with the fixed temperature ( $T$ ) and volume ( $V$ ), with a constant number of particles ( $N$ ).<sup>17</sup> This ensemble is also called NVT ensemble. In an isothermal-isobaric ensemble, the size of the box fluctuates to keep the pressure ( $P$ ) constant during the simulation.<sup>18</sup> In this ensemble, the temperature and number of particles is also kept constant. The NPT ensemble is one of the important ensembles in biochemical/chemical reactions, which are performed at constant pressure. The isothermal-isobaric ensemble is more realistic, because the computation results can be directly compared with experimental data. The microcanonical ensemble is used for isolated systems, which do not exchange energy ( $E$ ) and particles ( $N$ ) with the surrounding environment. Moreover, the volume ( $V$ ) and shape of the considered system also stay constant. Therefore, the ensemble is called NVE and the energy remains the same in all possible states of the system.<sup>16</sup> Thus, the probability of existence of a microstate equal to zero, if the energy of the latter differs from the fixed one. The NVE systems do not evolve in time, despite the motion of particles, because the ensemble strictly conserves the applied energy in the system. Finally, the system can swap energy and particles with the reservoir in the  $\mu$ VT ensemble. Hence, in the grand canonical ensemble, the chemical potential ( $\mu$ ), volume of the box and applied temperature are kept constant, while the total energy and sum of particles can be varied in different possible states of the system. Further information about other

ensembles, such as multicanonical, replica-exchange multicanonical, isoenthalpic–isobaric, Backrub and PertMin ensembles employed in MD simulations are given in literature<sup>19-21</sup>.

In our investigations, we mainly used NVT and NPT ensembles, applying the *Nose-Hoover thermostat* and *Parrinello-Rahman barostat* to control the temperature and pressure (see below).

*Thermostat and barostat.* In order to keep the temperature constant in MD simulations, various thermostats have been developed, such as the *Andersen* thermostat which is based on stochastic randomization,<sup>13</sup> weak-coupling scheme of *Berendsen*,<sup>22</sup> *Nose-Hoover*<sup>12,23</sup> and velocity rescaling scheme<sup>24</sup>.

*Andersen thermostat.* The desired temperature is achieved via random collision of particles with an imaginary heat bath in the Andersen thermostat. For the case of single particle approach, an arbitrary particle is selected and its velocity is reallocated randomly from a Maxwell-Boltzmann distribution at the desired temperature:

$$q(\mathbf{v}_{x,i}) = \left(\frac{m_i}{2\pi k_B T}\right)^{1/2} \exp\left(-\frac{m_i v_{x,i}^2}{2k_B T}\right) \quad (2.20)$$

This expression is used for each component of the particle velocity. The current scheme does not carry out collisions in each time step of MD, rather it regularly adopts the collision frequency or collision time. Therefore, the collision frequency has to be chosen accordingly corresponding to the time scales of molecular motions. In this respect, long time MD simulations lead to sufficient heat bath collisions, thus, the Andersen thermostat accurately generates the canonical ensemble probabilities. However, the calculation of certain parameters, such as diffusion constants for particles, would produce incorrect values because the thermostat does not maintain true molecular kinetics.

*Berendsen thermostat:* The Berendsen thermostat is used to regulate the temperature in the system by velocity rescaling of particles at each time step to keep the targeted temperature. This thermostat is based on the assumption that the considered system is weakly coupled to the external heat bath. Thus, the updated velocities are specified from the current velocities scaling as  $\mathbf{v}'_i = \lambda \mathbf{v}_i$ , where  $\lambda$  is defined as:

$$\lambda^2 = \mathbf{1} + \frac{\delta t}{\tau} \left(\frac{T_{bath}}{T(t)} - \mathbf{1}\right) \quad (2.21)$$

here,  $\delta t$  is the time step and  $\tau$  is the time scale of heat transfer from the reservoir.  $T_{bath}$  is the temperature of the bath and  $T$  is the temperature of the system at time step  $t$ . In this thermostat the energy fluctuations are not captured properly.

*Nose-Hoover thermostat:* MD simulations are mostly performed at constant temperature applying the Nose-Hoover thermostat, due to the accuracy of this method. The algorithm was developed by Nose and additionally improved by Hoover. The heat bath contains imaginary particles in this thermostat and this property makes it more realistic to keep the temperature constant. The friction coefficient  $\xi$  and extra degree of freedom  $s$  for the heat bath were introduced to the Hamiltonian:

$$H = \frac{1}{2} \sum m |p_i|^2 + U(r_N) + \frac{\xi^2 Q}{2} + 3Nk_B T \ln s \quad (2.22)$$

here,  $Q$  is the imaginary mass,  $r$  is the coordinate and  $p$  is the momentum. By means of the following expressions, the time evolution of the particle positions and momenta is controlled:

$$\frac{dr_i}{dt} = v_i ; \quad \frac{dv_i}{dt} = -\frac{1}{m_i} \frac{\partial U(r_N)}{\partial r_i} - \xi v_i ; \quad \frac{d\xi}{dt} = (\sum m |v_i|^2 - 3Nk_B T)/Q ; \quad \frac{d \ln s}{dt} = \xi \quad (2.23)$$

This thermostat also represents weaknesses for specific systems, despite its broad use by the simulation community. Nevertheless, several other methods, such as Nose-Hoover chains,<sup>25</sup> the kinetic moments method,<sup>26</sup> Bauer–Bulgac–Kusnezov scheme,<sup>27</sup> Patra–Bhattacharya full phase thermostat<sup>28</sup> and Braga–Travis configurational thermostat,<sup>29</sup> have been developed in order to enhance the robustness of this approach.

*Parrinello-Rahman barostat.* In order to keep both the temperature and pressure constant during the MD simulations, the system also needs to be coupled to the pressure bath. A number of different techniques have been developed, such as Parrinello-Rahman,<sup>30</sup> weak coupling Berendsen,<sup>31</sup> Martyna-Tuckerman-Tobias-Klein (MTTK)<sup>32</sup> and surface tension barostats, to be applied for specific systems.<sup>33</sup> The above mentioned temperature coupling thermostats (except Andersen) and the Parrinello-Rahman pressure coupling are combined in MD simulations. For the Parrinello-Rahman barostat, the box vectors are represented by the matrix  $b$ :

$$\frac{db^2}{dt^2} = VW^{-1}b'^{-1}(P - P_{ref}) \quad (2.24)$$

where  $V$  is the volume of the box, and  $W$  is the matrix parameter that defines the strength of the coupling. The matrix  $P$  is the current pressure and  $P_{ref}$  is the reference pressure. Accordingly, the modified Hamiltonian is given below:

$$H = U_{pot} + U_{kin} + \sum_i P_{ii}V + \sum_{i,j} \frac{1}{2} W_{ij} \left( \frac{db_{ij}}{dt} \right)^2 \quad (2.25)$$

The equation of motion derived from the Hamiltonian:

$$\frac{d^2 r_i}{dt^2} = \frac{F_i}{m_i} - M \frac{dr_i}{dt} ; \quad M = b^{-1} \left[ b \frac{db'}{dt} + \frac{db}{dt} b' \right] b'^{-1} \quad (2.26)$$

This extra term characterizes friction. However, it has to be noted that it is fictitious and the motion of particles is represented relative to the box vector, e.g., in the GROMACS package. It should be mentioned that if the applied pressure is far from equilibrium in the system, the Parrinello-Rahman barostat might lead to very large box oscillations, which even result in crashes of the simulations. This can be solved by increasing the time constant, or by applying other weak coupling barostats, in order to reach the target pressure. Once the system is in equilibrium, the simulation can be continued, switching to Parrinello-Rahman coupling.

Overall, a number of steps need to be performed in order to produce the final trajectory files in MD simulations (see [Figure 2.4](#)). Further macroscopic parameters can be obtained by analyzing the MD trajectory.

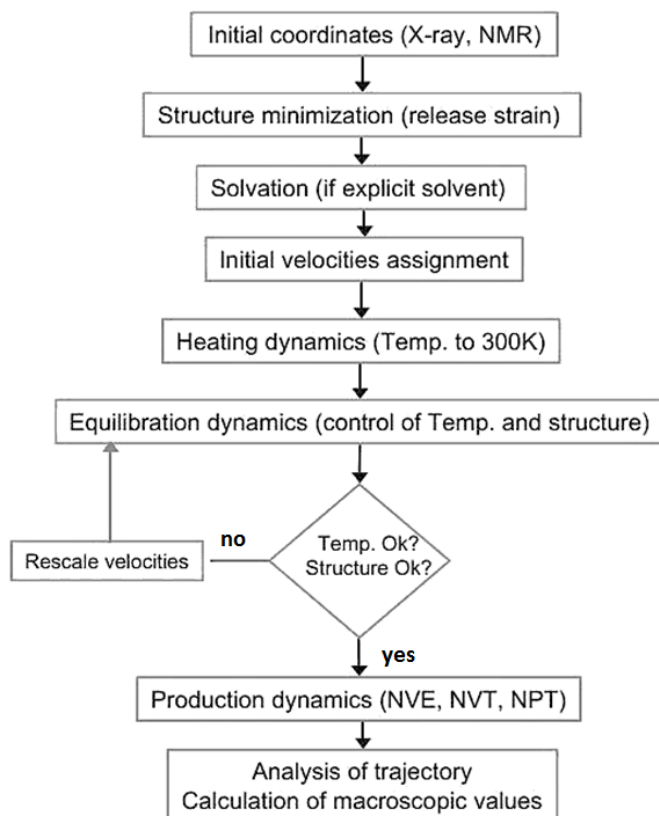


Figure 2.4. Flowchart illustrating the steps followed during MD simulations.

In this PhD thesis, we used MD simulations to study the transport of RONS and glucose as well as flip-flop of phosphatidylserine (PS) across the native and oxidized membrane (see [Chapter 3](#)). We also investigated different types of proteins under oxidative stress (see [Chapter 4](#)). These simulations were performed applying Berendsen and Nose-Hoover thermostat, and Parrinello-Rahman barostat. Both NVT and NPT ensembles were employed in our simulations.

**Force fields in MD simulations.** In order to study biochemical/biophysical processes, various MD force fields have been developed, such as Amber,<sup>34</sup> Charmm,<sup>35</sup> and OPLS<sup>36</sup> (all-atom), GROMOS<sup>37</sup> (united-atom), Martini<sup>38</sup> and Cooke<sup>39</sup> (coarse-grained). In the all-atom force fields, each atom is explicitly included, i.e., all atoms in the system are treated separately (see [Figure 2.5](#)). Besides all-atom force fields, MD simulations can also make use of so-called “united-atom” and “coarse-grained” force fields, which can handle larger systems (typically up to one order of magnitude larger than the system with all-atom force fields), for the same time scales. In united-atom force fields (e.g., GROMOS), all heavy atoms are treated separately, but the H atoms bound to a C atom are combined and treated as one (methyl or methylene) group. This is for instance the case for the apolar tails of phospholipids. Hence, the number of separate particles in the system is reduced, allowing to simulate larger systems (see [Figure 2.5](#)). Moreover, in a coarse-grained method, the atoms comprising entire functional groups, i.e., typically 3-5 heavy atoms (or more) with their H atoms, are represented by coarse-grained particles, which further reduces the number of particles in the system, and thus speeds up the calculations or allows to study larger systems in size. All-atom

simulations are more accurate compared to united-atom and coarse-grained force fields, however, they are more time consuming.

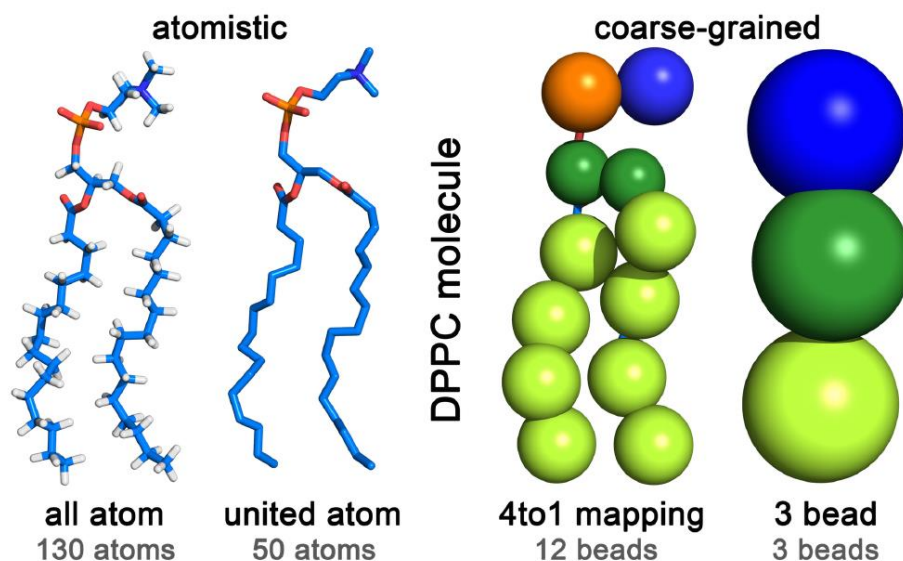


Figure 2.5. Representation of DPPC molecule in all-atom, united-atom, coarse-grained (Martini (4 to 1)) and Cooke three-bead) force fields. Figure is adopted from <sup>39</sup>.

In this thesis, we applied the united-atom force field GROMOS to study the systems that contain membrane, glucose and reactive species (see [Chapter 3](#)). The parameters of the force field for these systems were obtained from <sup>40-43</sup>. We also used the parameter of GROMOS developed by Petrov *et al.*<sup>44</sup> and Margreitter *et al.*<sup>45</sup> in order to study the effect of oxidation on the structures of proteins.

## 2.3 Umbrella sampling method

The calculation of the chemical potential, binding free energy or dissociation free energy is one of the central challenges in the field of biophysics and biochemistry. In this regard, the umbrella sampling (US) method<sup>46</sup> helps to calculate the free energy differences along the reaction coordinate. This is one of the powerful techniques to enhance sampling, by applying the umbrella potential. This method is developed taking into account thermodynamic integration, slow growth, steered MD and Jarzynski-based fast grow techniques. In US, an applied external harmonic bias potential transfers the system from one thermodynamic state to another along the reaction coordinate by a specified direction and a fixed speed (see [Figure 2.6](#)). Thus, from the initial to the final transfer state, the intermediate steps are formed by a series of windows. This series of windows can be separated by a certain distance between the considered molecules (i.e., along the reaction coordinate -  $\xi$ ), extracting a number of individual systems. The dihedral angle, the distance between two atoms or terminal ends of a protein, and more complicated systems that include collective molecules (e.g., membrane and a number of reactive species) can be considered as a reaction coordinate. The separated windows are used further in US MD simulations.

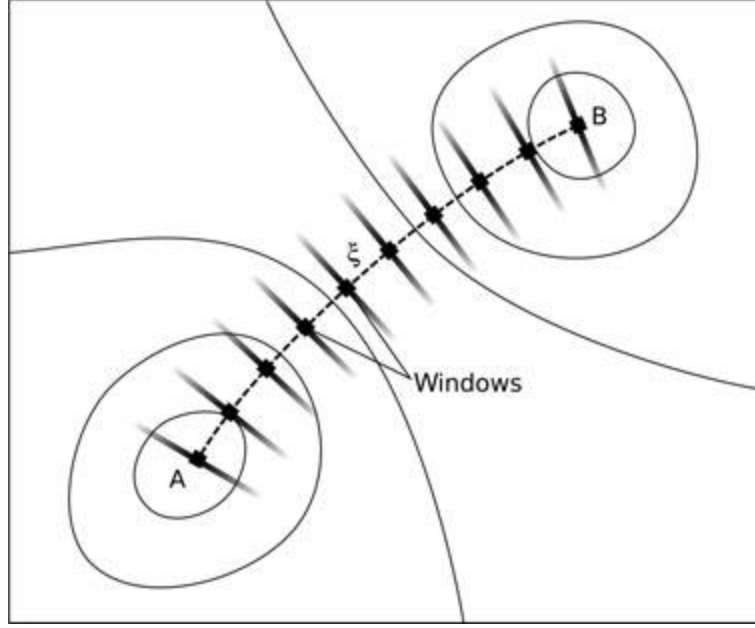


Figure 2.6. Transferring of the system from one thermodynamic state (A) to another (B) along the reaction coordinate ( $\xi$ ) separated by a number of windows/intermediate states. Figure is adopted from <sup>46</sup>.

In MD simulations a reaction coordinate ( $\xi$ ) is continuous between the considered thermodynamic states and the latter can be one or more dimensional. The probability distribution ( $Q(\xi)$ ) along the reaction coordinate  $\xi$  can be determined by integrating through all degrees of freedom, with specified  $\xi$ :

$$Q(\xi) = \frac{\int \delta[\xi(\mathbf{r}) - \xi] \exp[-\beta U] d^N \mathbf{r}}{\int \exp[-\beta U] d^N \mathbf{r}} \quad (2.27)$$

where,  $\beta = 1/k_B T$ ,  $k_B$  being the Boltzmann's constant, N - number of degrees of freedom. Based on equation (2.27) one can calculate the free energy ( $A(\xi)$ ) along the reaction coordinate.

$$A(\xi) = -1/\beta \ln Q(\xi) \quad (2.28)$$

$A(\xi)$  is also called potential of mean force (PMF). In order to apply the method in computer simulations, the system is considered as an ergodic system and the ensemble average  $Q(\xi)$  becomes equal to the time average  $P(\xi)$  for infinite sampling:

$$P(\xi) = \lim_{t \rightarrow \infty} \frac{1}{t} \int_0^t \rho[\xi(t')] dt' \quad (2.29)$$

where,  $\rho$  represents the occurrence of  $\xi$  in a specified interval and  $t$  indicates time. Thus, the PMF can be directly calculated by monitoring of  $P(\xi)$  along the reaction coordinate. The potential changes in US simulations, due to introducing an additional harmonic bias potential  $w_i$  to the system and this is written as:

$$U^b(\mathbf{r}) = U^u(\mathbf{r}) + w_i(\xi) \quad (2.30)$$

where, superscript ‘b’ and ‘u’ denote biased and unbiased quantities, respectively. The relation between  $P_i^b(\xi)$  and  $P_i^u(\xi)$  can be written as (interval operations are given in literature <sup>46</sup>):

$$P_i^u(\xi) = P_i^b(\xi) \exp[\beta w_i(\xi)] / \langle \exp[\beta w_i(\xi)] \rangle \quad (2.31)$$

The PMF can be calculated from equation (2.31):

$$A(\xi) = - \left( \frac{1}{\beta} \right) \ln P_i^b(\xi) - w_i(\xi) - \left( \frac{1}{\beta} \right) \ln \langle \exp[\beta w_i(\xi)] \rangle \quad (2.32)$$

US MD simulations help to calculate the free energy profile (FEP), or potential of mean force (PMF) in a path-dependent manner, using the weighted histogram analysis method (WHAM)<sup>47</sup>. Moreover, this method is also often used to estimate the mechanical properties of macromolecules.<sup>48,49</sup> In addition, US is widely employed to compute the interaction between protein-protein,<sup>50,51</sup> protein-lipid,<sup>52</sup> protein-drug,<sup>53</sup> and drug-membrane<sup>54</sup> under an external perturbation.

In this thesis, we calculated the FEPs of various RONS (namely OH, HO<sub>2</sub>, H<sub>2</sub>O<sub>2</sub>, O<sub>3</sub>, NO, NO<sub>2</sub> and N<sub>2</sub>O<sub>4</sub>) and glucose molecule across native and oxidized phospholipid bilayers (PLBs) applying the US method (see [Chapter 3](#), sections [3.1](#) and [3.2](#) for more details). These simulations enabled us to obtain insight in the effect of plasma oxidation on the permeation of RONS and glucose through the PLBs. Using the same technique we also explored the flip-flop motion of phosphatidylserine (PS) across native and oxidized PLB ([Chapter 3](#), section [3.3](#)). Moreover, we studied the interaction between amyloid fibril monomers ([Chapter 4](#), section [4.1](#)), and we estimated the binding free energy between CD47 and SIRP $\alpha$  proteins ([Chapter 4](#), section [4.4](#)) by means of the US method.

## 2.4 Docking simulations

Docking simulations are mainly used to predict the binding site of proteins/DNA with small molecules. This method is one of the most powerful tools in pharmacy. This technique helps in the rational design of specific drugs that tightly bind to the target biomolecules, affecting their function. It is known that proteins perform a wide variety of tasks in the cell, including enzymatic tasks (single protein) and signaling (two or more proteins). In most cases, particular types of proteins are responsible for a certain kind of disease. Proteins are functionally activated or deactivated due to mutation of amino acids or by interacting with drug molecules. Therefore, it is crucial to investigate hot spots of biomolecules by means of ligands, in order to obtain better insight into biochemical processes that govern cellular homeostasis.

The docking algorithms search and sample configurational space of the examined protein and they generate protein ligand structures for scoring and ranking. The predicted higher ranking poses can be considered as a potential binding position of the ligands for further calculations. For example, the FTMap family of the web server efficiently predicts the binding hot spot of proteins.<sup>55</sup> FTMap samples the positions of 16 small probing organic molecules and identifies the potential ligand binding regions of the protein based on the

lowest binding free energy. These individual probing molecules may bind at various locations of the protein, and thus their clusters specify binding hot spots (so-called binding pockets) of the protein (see [Figure 2.7\(a\)](#)). The probing molecules used in the FTMap server are ethane, ethanol, isopropanol, isobutanol, acetonitrile, methanamine, N,N-dimethylformamide dimethyl ether, benzaldehyde, benzene, cyclohexane, phenol, acetamide, acetone, acetaldehyde and urea (see [Figure 2.7\(b\)](#)). They vary in shape, size and polarity, and can be considered as drug-like molecules.<sup>55</sup>

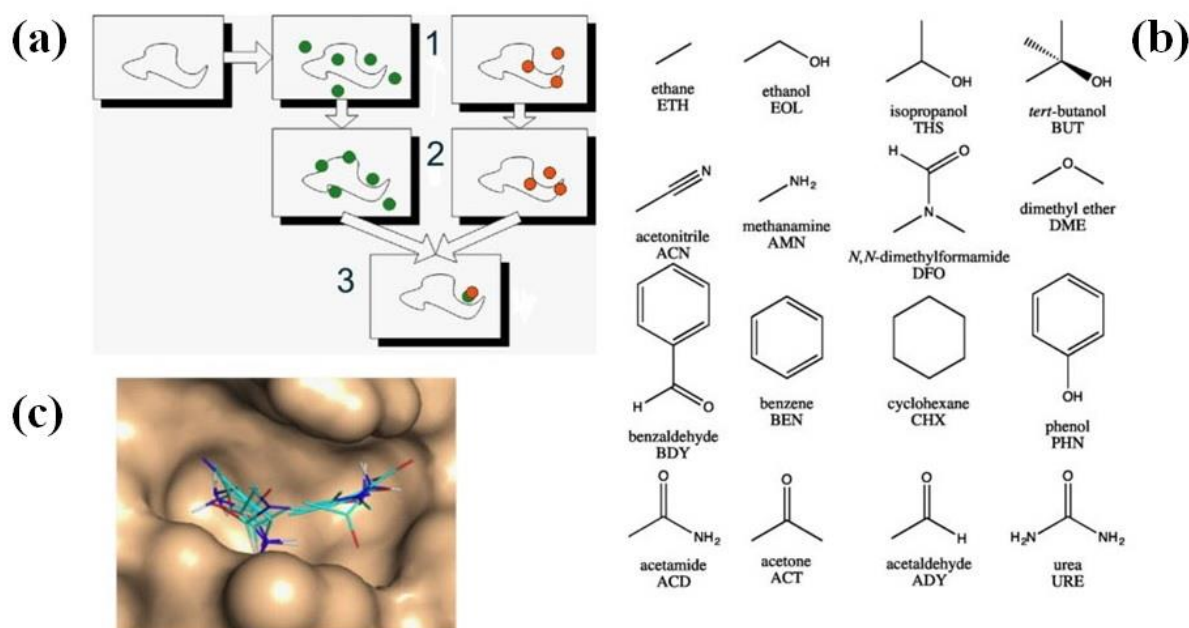


Figure 2.7. (a) Visualization of the processing of the FTMap algorithm. (b) The 16 small drug-like molecules used by the FTMap server. (c) Example of determined consensus cluster.

The hot spot of the protein is identified by means of a mapping algorithm that consists of the following four steps:

1. Each probe molecule samples on a grid around the fixed protein. The energy function considers van der Waals energy with attractive and repulsive contributions and an electrostatic as well as solvation term characterized by the Poisson–Boltzmann continuum model. The algorithm chooses the 2000 best positions of each probing molecule and proceeds to the next stage.

2. These best positions of the probe molecules with the protein complex are energy minimized using the CHARMM potential<sup>56</sup> with an analytical continuum electrostatics model<sup>57</sup>. During the energy minimization run, the protein atoms are fixed, while the probing molecules are free to move.

3. The minimized structures are clustered with 4 Å radius, considering the lowest energy structure. For each probe molecule, six clusters are retained with the lowest energy, that are ranked by their Boltzmann averaged energies.

4. The clusters of the 16 different probe molecules are then clustered into consensus clusters. This clustering stage defines the center of mass for each cluster probe. The highest ranked consensus cluster is selected, using the distance between the center of mass of the cluster centers as a measure for the distance, and 4 Å as the clustering radius (see [Figure 2.7\(c\)](#)).

In this thesis, the FTMap server was used to analyze the functional site of cytoglobin (Cygb) in native and oxidized state (i.e., after formation of a disulfide bridge between cysteine residues). The FTMap effectively predicted the binding hot spots of both native and oxidized Cygb around the heme group, thereby explaining the mechanisms of increased access to the functional site of Cygb observed by experiments (see [Chapter 4](#), section [4.2](#)).

Many different simulation packages have been developed, such as Autodock,<sup>58</sup> Zdock<sup>59</sup> and Haddock,<sup>60</sup> to predict drug-protein and ligand-receptor binding poses. For example, the Zdock program searches for all possible binding modes (poses) in the translational and rotational space between two proteins. Furthermore, it evaluates each pose using an energy-based scoring function (e.g., 3600 predictions per case). The highly ranked poses can be further used to determine the binding free energy between the complex.

## 2.6 Conclusion

The above mentioned calculation methods are capable to describe bonded as well as non-bonded interactions between H/C/O/N/S/P atoms, which are the basic elements of lipids, amino acids, nucleic acids, as well as RONS. Therefore, we have used MD, US, and docking simulations in this thesis for specific model systems, as mentioned at the end of each section.

The specific details of these simulations, as well as the results for the various model systems studied in this PhD thesis, will be described in [Chapters 3](#) and [4](#).

## 2.7 References

- 1 Alder, B and Wainwright, T. Studies in molecular dynamics. I. General method. *Journal of Chemical Physics* 31, 459-466 (1959).
- 2 Alder, B and Wainwright, T. Studies in molecular dynamics. II. Behavior of a small number of elastic spheres. *Journal of Chemical Physics* 33, 1439-1451 (1960).
- 3 McCammon, J. A., Gelin, B. R. & Karplus, M. Dynamics of folded proteins. *Nature* 267, 585 (1977).
- 4 Kox, A., Michels, J and Wiegel, F. Simulation of a lipid monolayer using molecular dynamics. *Nature* 287, 317 (1980).
- 5 Weiner, S. , Kollman, P., Case, D., Singh, U., Ghio, C., Alagona, G., Profeta, S and Weiner, P. A new force field for molecular mechanical simulation of nucleic acids and proteins. *Journal of the American Chemical Society* 106, 765-784 (1984).
- 6 Stone, A. The theory of intermolecular forces. (Clarendon, Oxford, 1996).
- 7 Sprik, M. *Computer simulation in chemical physics*. 211-259 (Springer, 1993).
- 8 Maitland, G. C. *Intermolecular forces: their origin and determination*. (Oxford University Press, 1981).
- 9 Allen, M. Introduction to molecular dynamics simulation. *Computational soft matter: from synthetic polymers to proteins* 23, 1-28 (2004).
- 10 Verlet, L. Computer" experiments" on classical fluids. I. Thermodynamical properties of Lennard-Jones molecules. *Physical review* 159, 98 (1967).
- 11 Abraham, M., Murtola, T., Schulz, R., Páll, S., Smith, J.C., Hess, B and Lindahl, E. GROMACS: High performance molecular simulations through multi-level parallelism from laptops to supercomputers. *SoftwareX* 1, 19-25 (2015).
- 12 Nosé, S. A molecular dynamics method for simulations in the canonical ensemble. *Molecular physics* 52, 255-268 (1984).
- 13 Andersen, H. Molecular dynamics simulations at constant pressure and/or temperature. *Journal of chemical physics* 72, 2384-2393 (1980).
- 14 Kraska, T. Molecular-dynamics simulation of argon nucleation from supersaturated vapor in the NVE ensemble. *Journal of chemical physics* 124, 054507 (2006).
- 15 Lynch, G. and Pettitt, B. Grand canonical ensemble molecular dynamics simulations: Reformulation of extended system dynamics approaches. *Journal of chemical physics* 107, 8594-8610 (1997).
- 16 Hünenberger, P. *Advanced computer simulation*. 105-149 (Springer, 2005).
- 17 Tobias, D. , Martyna, G and Klein, M. Molecular dynamics simulations of a protein in the canonical ensemble. *The Journal of Physical Chemistry* 97, 12959-12966 (1993).

- 18 Tobias, D., Tu, K. and Klein, M. Atomic-scale molecular dynamics simulations of lipid membranes. *Current opinion in colloid & interface science* 2, 15-26 (1997).
- 19 Nakajima, N., Nakamura, H and Kidera, A. Multicanonical ensemble generated by molecular dynamics simulation for enhanced conformational sampling of peptides. *Journal of Physical Chemistry B* 101, 817-824 (1997).
- 20 Haile, J and Graben, H. Molecular dynamics simulations extended to various ensembles. I. Equilibrium properties in the isoenthalpic–isobaric ensemble. *Journal of Chemical Physics* 73, 2412-2419 (1980).
- 21 Davey, J and Chica, R. Improving the accuracy of protein stability predictions with multistate design using a variety of backbone ensembles. *Proteins: Structure, Function, and Bioinformatics* 82, 771-784 (2014).
- 22 Berendsen, H., Postma, J., van Gunsteren, W., DiNola, A and Haak, J. Molecular dynamics with coupling to an external bath. *Journal of chemical physics* 81, 3684-3690 (1984).
- 23 Hoover, W. Canonical dynamics: equilibrium phase-space distributions. *Physical review A* 31, 1695 (1985).
- 24 Bussi, G., Donadio, D and Parrinello, M. Canonical sampling through velocity rescaling. *The Journal of chemical physics* 126, 014101 (2007).
- 25 Martyna, G., Klein, M and Tuckerman, M. Nosé–Hoover chains: The canonical ensemble via continuous dynamics. *Journal of chemical physics* 97, 2635-2643 (1992).
- 26 Hoover, W and Holian, B. Kinetic moments method for the canonical ensemble distribution. *Physics Letters A* 211, 253-257 (1996).
- 27 Kusnezov, D., Bulgac, A and Bauer, W. Canonical ensembles from chaos. *Annals of Physics* 204, 155-185 (1990).
- 28 Patra, P and Bhattacharya, B. A deterministic thermostat for controlling temperature using all degrees of freedom. *Journal of chemical physics* 140, 064106 (2014).
- 29 Braga, C and Travis, K. A configurational temperature Nosé–Hoover thermostat. *Journal of chemical physics* 123, 134101 (2005).
- 30 Parrinello, M and Rahman, A. Polymorphic transitions in single crystals: A new molecular dynamics method. *Journal of Applied physics* 52, 7182-7190 (1981).
- 31 Lin, Y., Pan, D., Li, J., Zhang, L and Shao, X. Application of Berendsen barostat in dissipative particle dynamics for nonequilibrium dynamic simulation. *Journal of chemical physics* 146, 124108 (2017).
- 32 Martyna, G., Tuckerman, M., Tobias, D and Klein, M. Explicit reversible integrators for extended systems dynamics. *Molecular Physics* 87, 1117-1157 (1996).
- 33 Rühle, V. Pressure coupling/barostats. *Journal Club* (2008).
- 34 Wang, J., Wolf, R., Caldwell, J., Kollman, P and Case, D. Development and testing of a general amber force field. *Journal of computational chemistry* 25, 1157-1174 (2004).

- 35 Vanommeslaeghe, K., Hatcher, E., Acharya, C., Kundu, S., Zhong, S., Shim, J., Darian, E., Guvench, O., Lopes, P., Vorobyov, I and MacKerell, A. CHARMM general force field: A force field for drug-like molecules compatible with the CHARMM all-atom additive biological force fields. *Journal of computational chemistry* 31, 671-690 (2010).
- 36 Jorgensen, W., Maxwell, D and Tirado-Rives, J. Development and testing of the OPLS all-atom force field on conformational energetics and properties of organic liquids. *Journal of the American Chemical Society* 118, 11225-11236 (1996).
- 37 Oostenbrink, C., Villa, A., Mark, A and Van Gunsteren, W. A biomolecular force field based on the free enthalpy of hydration and solvation: the GROMOS force-field parameter sets 53A5 and 53A6. *Journal of computational chemistry* 25, 1656-1676 (2004).
- 38 Marrink, S., Risselada, H., Yefimov, S., Tieleman, D and De Vries, A. The MARTINI force field: coarse grained model for biomolecular simulations. *Journal of physical chemistry B* 111, 7812-7824 (2007).
- 39 Cooke, I., Kremer, K and Deserno, M. Tunable generic model for fluid bilayer membranes. *Physical Review E* 72, 011506 (2005).
- 40 Chiu, S., Pandit, S., Scott, H and Jakobsson, E. An improved united atom force field for simulation of mixed lipid bilayers. *Journal of Physical Chemistry B* 113, 2748-2763 (2009).
- 41 Wong-Ekkabut, J., Xu, Z., Triampo, W., Tang, I.M., Tieleman, D and Monticelli, L. Effect of lipid peroxidation on the properties of lipid bilayers: a molecular dynamics study. *Biophysical journal* 93, 4225-4236 (2007).
- 42 Geballe, M., Skillman, A., Nicholls, A., Guthrie, J and Taylor, P. The SAMPL2 blind prediction challenge: introduction and overview. *Journal of computer-aided molecular design* 24, 259-279 (2010).
- 43 Cordeiro, R. Reactive oxygen species at phospholipid bilayers: distribution, mobility and permeation. *Biochimica et Biophysica Acta (BBA)-Biomembranes* 1838, 438-444 (2014).
- 44 Petrov, D., Margreitter, C., Grandits, M., Oostenbrink, C and Zagrovic, B. A systematic framework for molecular dynamics simulations of protein post-translational modifications. *PLoS computational biology* 9, e1003154 (2013).
- 45 Margreitter, C., Reif, M and Oostenbrink, C. Update on phosphate and charged post-translationally modified amino acid parameters in the GROMOS force field. *Journal of computational chemistry* 38, 714-720 (2017).
- 46 Kästner, J. Umbrella sampling. *Wiley Interdisciplinary Reviews: Computational Molecular Science* 1, 932-942 (2011).
- 47 Kumar, S., Rosenberg, J., Bouzida, D., Swendsen, R and Kollman, P. The weighted histogram analysis method for free-energy calculations on biomolecules. I. The method. *Journal of computational chemistry* 13, 1011-1021 (1992).

- 48 Daday, C., Bauer, M., Redondo, P., Gaub, H.E., Lietha, D and Gräter, F. Unfolding Focal Adhesion Kinase: Getting Cellular Insight Through AFM and MD. *Biophysical Journal* 116, 429a (2019).
- 49 Rathore, N., Yan, Q and de Pablo, J. Molecular simulation of the reversible mechanical unfolding of proteins. *Journal of chemical physics* 120, 5781-5788 (2004).
- 50 Lemkul, J. and Bevan, D. Assessing the stability of Alzheimer's amyloid protofibrils using molecular dynamics. *Journal of Physical Chemistry B* 114, 1652-1660 (2010).
- 51 De Meyer, F., Venturoli, M and Smit, B. Molecular simulations of lipid-mediated protein-protein interactions. *Biophysical journal* 95, 1851-1865 (2008).
- 52 Irudayam, S and Berkowitz, M. Binding and reorientation of melittin in a POPC bilayer: computer simulations. *Biochimica et Biophysica Acta (BBA)-Biomembranes* 1818, 2975-2981 (2012).
- 53 Pathak, A. and Bandyopadhyay, T. Unbinding free energy of acetylcholinesterase bound oxime drugs along the gorge pathway from metadynamics-umbrella sampling investigation. *Proteins: Structure, Function, and Bioinformatics* 82, 1799-1818 (2014).
- 54 Meng, F and Xu, W. Drug permeability prediction using PMF method. *Journal of molecular modeling* 19, 991-997 (2013).
- 55 Kozakov, D., Grove, L., Hall, D., Bohnuud, T., Mottarella, S., Luo, L., Xia, B., Beglov, D and Vajda, S. The FTMap family of web servers for determining and characterizing ligand-binding hot spots of proteins. *Nature protocols* 10, 733-755 (2015).
- 56 Brooks, B., Bruccoleri, R., Olafson, B., States, D., Swaminathan, S and Karplus, M. CHARMM: a program for macromolecular energy, minimization, and dynamics calculations. *Journal of computational chemistry* 4, 187-217 (1983).
- 57 Schaefer, M and Karplus, M. A comprehensive analytical treatment of continuum electrostatics. *Journal of Physical Chemistry* 100, 1578-1599 (1996).
- 58 Goodsell, D., Morris, G and Olson, A. Automated docking of flexible ligands: applications of AutoDock. *Journal of Molecular Recognition* 9, 1-5 (1996).
- 59 Pierce, B., Wiehe, K., Hwang, H., Kim, B., Vreven, T and Weng, Z. ZDOCK server: interactive docking prediction of protein-protein complexes and symmetric multimers. *Bioinformatics* 30, 1771-1773 (2014).
- 60 De Vries, S., Van Dijk, M and Bonvin, A. The HADDOCK web server for data-driven biomolecular docking. *Nature protocols* 5, 883 (2010).



# Chapter 3.

## Effect of oxidation on the cell membrane

In this chapter, we discuss how lipid oxidation induces important chemical and biophysical changes in the cell membrane. Specifically, we investigate the transport of RONS (section [3.1](#)) and glucose (section [3.2](#)) as well as flip-flop of PS (section [3.3](#)) across native and oxidized membranes, by means of MD simulations.

The presented data in this chapter is based on the articles published in:

Razzokov, J., Yusupov, M., Cordeiro, R.M. and Bogaerts, A., 2018. Atomic scale understanding of the permeation of plasma species across native and oxidized membranes. *J. Phys. D: Appl. Phys.* 51(36), p.365203

Razzokov, J., Yusupov, M. and Bogaerts, A., 2018. Possible Mechanism of Glucose Uptake Enhanced by Cold Atmospheric Plasma: Atomic Scale Simulations. *Plasma*, 1(1), p.119-125.

Razzokov, J., Yusupov, M., Vanuytsel, S., Neyts, E.C. and Bogaerts, A., 2017. Phosphatidylserine flip-flop induced by oxidation of the plasma membrane: a better insight by atomic scale modeling. *Plasma Process. Polym.* 14(10), p.1700013.



## 3.1 Permeation of plasma species across native and oxidized membranes

### 3.1.1 Introduction

The therapeutic effects of CAPs are related to the reactive oxygen and nitrogen species (ROS and RNS) present in the plasma. The impact of ROS has been extensively studied,<sup>1-15</sup> but the role of RNS in CAP-treatment remains poorly understood at the molecular level. Here, we investigate the permeation of RNS and ROS across native and oxidized phospholipid bilayers (PLBs). The effect of CAP-generated RNS is also important to investigate, as RNS can play an essential role in apoptosis signaling pathways in cancer cells.<sup>8,10,16</sup> Studying the role of RNS (together with the role of ROS) helps to reveal a more complete picture of the selective effect of CAP on cancer cells, since CAP-generated RNS and ROS simultaneously act on the cancer cells, thereby inducing nitrosative and oxidative stress in these cells. The reason for studying oxidized membranes, besides native PLBs, is that CAP can cause lipid oxidation in the cell membrane,<sup>17</sup> and the effect of this oxidation on the transmembrane transport of ROS and RNS should also be studied, and compared with the behavior for non-oxidized (native) PLBs.

Thus, in this section, we present the calculated free energy profiles (FEPs) of RNS (NO, NO<sub>2</sub>, N<sub>2</sub>O<sub>4</sub>) across native and oxidized PLBs, and we compare them with calculated FEPs for ROS (O<sub>2</sub>, O<sub>3</sub>, OH, HO<sub>2</sub>, and H<sub>2</sub>O<sub>2</sub>).

### 3.1.2 Computational details

We performed MD simulations to study the transport of the aforementioned species (i.e., OH, HO<sub>2</sub>, H<sub>2</sub>O<sub>2</sub>, O<sub>3</sub>, NO, NO<sub>2</sub>, N<sub>2</sub>O<sub>4</sub>) through native and oxidized membranes. As a model system we considered the PLB, representing the cell membrane. Each PLB included 128 phospholipids (PLs), equally distributed in both layers of the membrane, together with 8000 water molecules surrounding them (see [Figure 3.1.1\(a\)](#)). We considered a native PLB made of 1,2-dioleoyl-*sn*-glycero-3-phosphocholine (DOPC) and an oxidized PLB made of a 1:1 homogeneous mixture of DOPC and its aldehyde oxidation product (DOPC-ALD) (see [Figure 3.1.1\(b\)](#)). We chose these PLs, because (i) DOPC is one of the main components of the plasma membrane in both the outer and inner leaflet<sup>18</sup>, and (ii) the aldehydes are one of the most commonly observed oxidation products.<sup>19</sup> Indeed, mass spectrometry analysis in our previous study showed that the formation of aldehyde groups (i.e., DOPC-ALD) was prominently observed in CAP-treated vesicles.<sup>17</sup> Note that the cell membrane itself consists of different types of membrane components, including phospholipids, proteins, sterols, etc. Practically, due to the computational cost, we cannot mimic in our simulations the real membrane composition, because even the simplest plasma membrane of a red blood cell consists of over 150 lipid species. Hence, we should focus on the main lipid components and therefore, in our model system we chose DOPC as a primary element of a PLB. This type of lipid molecules is found e.g., in 40, 44% and 24% of the endoplasmic reticulum, mitochondrion membrane and liver cell plasma membrane, respectively.<sup>20</sup>

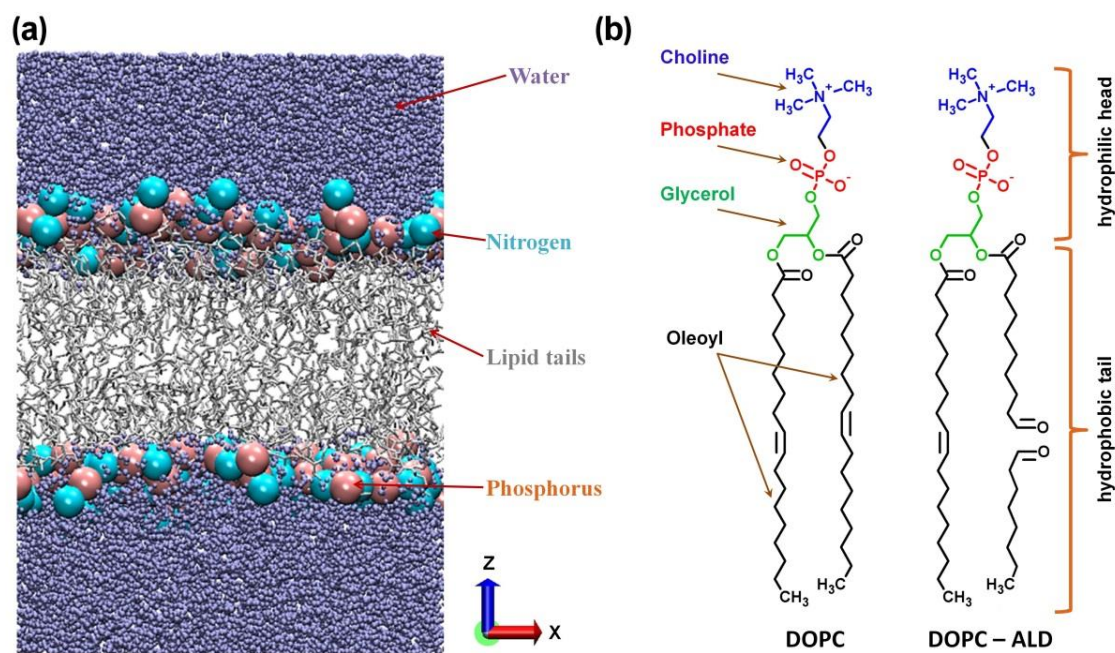


Figure 3.1.1. (a) Native DOPC PLB. The P and N atoms are shown with larger beads for the sake of clarity. (b) Schematic representation of native (DOPC) and oxidized (DOPC-ALD) PLs.

The presence of 50% DOPC-ALD in the oxidized PLB was high enough to observe the effect of oxidation, but low enough so that pore formation did not occur within the simulated time scale.<sup>21</sup> The initial configurations of the native and oxidized PLBs were created by means of the Packmol package.<sup>22</sup> All simulations were performed employing the GROMACS-5.1 package.<sup>23</sup> We used the GROMOS (43A1-S3) united atom force field for native phospholipids, supplemented with additional parameters for the aldehyde derivative.<sup>24</sup> GROMOS-type force field parameters for ROS and RNS were obtained from<sup>25,26</sup>. These parameters were chosen because they have been demonstrated to yield correct water-to-alkane partition coefficients of ROS and RNS, which are essential for the proper description of transmembrane permeation. These parameters were supplemented with the NO force field, which was derived by Cordeiro following the same protocols as in<sup>25</sup> and<sup>26</sup> (see section 3.1.5 Appendix below for further details).

The model membranes were initially energy minimized with the steepest descent algorithm and then equilibrated for 200 ns in the isothermal-isobaric (NPT) ensemble at 1 bar and 310 K. The equilibration runs were performed employing the semi-isotropic Parrinello-Rahman barostat with compressibility and coupling constant of  $4.5 \times 10^{-5} \text{ bar}^{-1}$  and 0.1 ps, respectively, as well as the Nose-Hoover thermostat with a coupling constant of 0.2 ps. The particle mesh Ewald (PME) method was used to treat electrostatic interactions with a real space cut-off of 1.0 nm, in combination with a 0.15 nm spaced-grid for the reciprocal-space interactions. All simulations were carried out using a time step of 2 fs, and periodic boundary conditions were applied in all three directions.

To calculate the FEPs associated to the transmembrane translocation of ROS and RNS, we applied the US method,<sup>27,28</sup> as explained in Chapter 2.

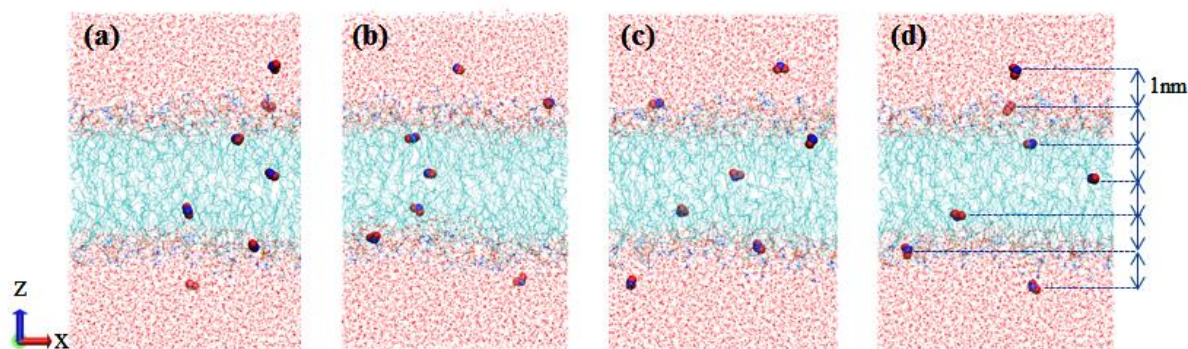


Figure 3.1.2. Four model systems of native DOPC PLB. The model systems are derived from 170 ns (a), 180 ns (b), 190 ns (c) and 200 ns (d) of the equilibration run trajectories. In this example, seven  $\text{NO}_2$  species are inserted in each model system, randomly in the  $xy$  plane, but separated by 1 nm distance in the  $z$ -direction.

In order to save computational resources, US simulations were performed as follows. Four membrane structures were selected from the last 30 ns of equilibration. In each of the US simulations, 7 permeants were distributed along the membrane normal, keeping a distance of 1 nm between each other (Figure 3.1.2). To keep the permeants at their positions with respect to the membrane center, their center-of-mass motion was restricted along the  $z$ -axis by harmonic biases with force constants of  $2000 \text{ kJ}\cdot\text{mol}^{-1}\cdot\text{nm}^{-2}$ . At the  $xy$ -plane, the permeants were still free to move. A US simulation was performed at NPT for each system, comprising 2 ns of equilibration and 4 ns of sampling. The umbrella histograms were collected and an individual FEP was built by the weighted histogram analysis method (WHAM).<sup>29</sup> We performed 10 US simulations (6 ns each) to build one individual FEP; thus, for each FEP  $7 \times 10 = 70$  US windows are defined along the membrane normal, which are separated by 1 Å. For every combination of permeant (i.e., OH,  $\text{HO}_2$ ,  $\text{H}_2\text{O}_2$ ,  $\text{O}_3$ , NO,  $\text{NO}_2$ ,  $\text{N}_2\text{O}_4$ ) and PLB (DOPC, DOPC-ALD), i.e., 14 combinations in total, we calculated between 16 and 24 individual FEPs, which were then averaged. Thus, in total we performed between 0.96 and 1.44  $\mu\text{s}$  of US for each permeant in both DOPC and DOPC-ALD. 1  $\mu\text{s}$  of US simulation takes about 42 days in real computing time. Note that the data collected for the calculation of FEPs strongly depend on the lipid composition surrounding the randomly placed RONS in the PLB. To estimate a true free energy barrier, good statistics is necessary. Moreover, the comparison of the symmetric and full (i.e., asymmetric) FEPs for each RONS is needed to verify the data convergence of the simulations. We obtained very symmetric FEPs, which are a hallmark for convergence of the simulations (see Figure A1 in Appendix).

It should be mentioned that in reality, chemical reactions of RONS might take place in the PLB. However, these processes cannot be revealed by performing conventional non-reactive MD simulations, due to the limitations of the used potential. Nevertheless, the electronic degrees of freedom needed to describe chemical reactions are not explicitly considered in classical MD. Even so, the US simulations help to determine the RONS permeation rate across the PLB before and after oxidation, through calculations of the FEPs. Besides, the most probable accumulation regions for RONS also can be predicted based on the FEPs that give a

possibility to study position-dependent specific interactions in the membrane with possible implications for reactivity.

### 3.1.3 Results and discussion

Figure 3.1.3 shows the FEPs of various ROS and RNS across native and oxidized PLBs. As the hydrophilic ROS (OH, HO<sub>2</sub>, H<sub>2</sub>O<sub>2</sub>) are moved from the aqueous phase to the membrane interior, the FEP first decreases, reaching a minimum at the headgroup region, and then increases as ROS are placed deeper into the native PLB (Figure 3.1.3(a)). In all cases, the free energy barrier is located at the PLB core. Adsorption at the headgroup region is much stronger for H<sub>2</sub>O<sub>2</sub> and HO<sub>2</sub>, and H<sub>2</sub>O<sub>2</sub> has the largest permeation barrier among all hydrophilic ROS. Cordeiro identified specific ROS-membrane interactions that may be responsible for these trends.<sup>25</sup> He proposed that ROS adsorption at the PLB surface is mainly driven by two factors: (i) H-bond interactions between ROS and the PL carbonyl ester groups, and (ii) dispersion interactions with the headgroup region. Although all the hydrophilic ROS investigated are H-bond donors, H<sub>2</sub>O<sub>2</sub> and HO<sub>2</sub> have an extra O atom that leads to stronger dispersion interactions in comparison to the smaller OH radical. That might explain the differences in the adsorption tendencies of the hydrophilic ROS. Besides that, H<sub>2</sub>O<sub>2</sub> is known for its ability to establish twice as many H-bonds in water, as compared to OH and HO<sub>2</sub>.<sup>25</sup> That might explain the largest permeation barrier recorded for H<sub>2</sub>O<sub>2</sub>.

When the PLB is oxidized, the permeation follows similar qualitative trends, but with smaller free energy barriers (Figure 3.1.3(b)). PL oxidation generates functional groups and fragments that increase the hydrophilicity of the membrane core, leading to an increase of the PLB permeability to ROS.<sup>30</sup> Although the permeation barrier still remains relatively high for H<sub>2</sub>O<sub>2</sub>, it becomes significantly lower for OH. Most notably, in the case of HO<sub>2</sub>, PLB oxidation apparently even leads to a change of its partition behavior. The FEPs suggest that HO<sub>2</sub> might develop a preference for the PLB core as oxidation takes place. This effect is especially important because HO<sub>2</sub> is the protonated form of the biologically relevant superoxide radical (O<sub>2</sub><sup>-</sup>). However, we also note that this result is still speculative. The HO<sub>2</sub> model has originally been parametrized to reproduce its experimentally measured hydration free energy.<sup>25</sup> Hydrophobic solvation has not been considered, as there was no reference experimental data available. To draw more conclusive data, one would need to evaluate the performance of the HO<sub>2</sub> model in the description of its solvation free energy in non-polar solvents.

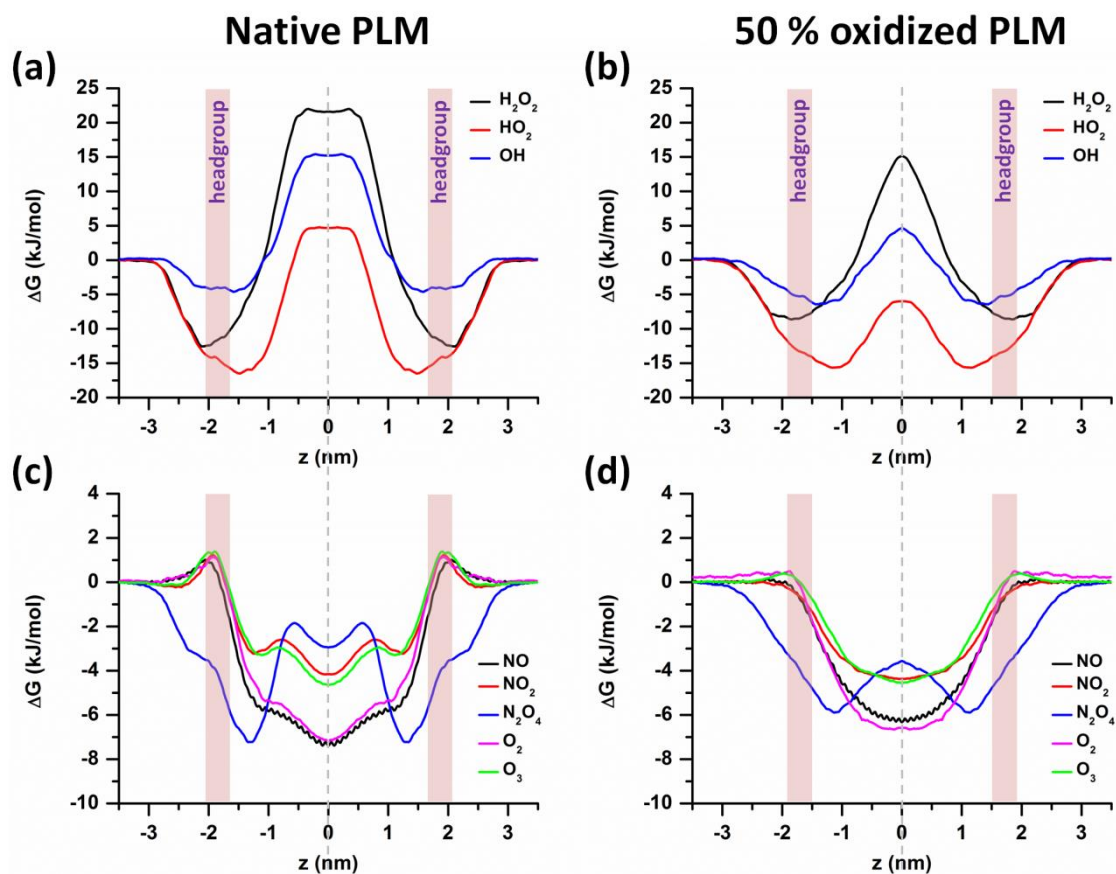


Figure 3.1.3. FEPs of the hydrophilic (a-b) and hydrophobic (c-d) ROS and RNS, across native and 50% oxidized PLBs. The average positions of the headgroup regions (i.e., average position of phosphate atoms, cf. Figure 3.1.1) are indicated by light red color.

The hydrophobic species show a completely different behavior (see Figure 3.1.3(c,d) and note the different scale of the y-axis). In the native PLB, NO, NO<sub>2</sub>, O<sub>2</sub> and O<sub>3</sub> exhibit very low permeation barriers, which are all located at the headgroup region (Figure 3.1.3(c)). The free energy at the PLB core is lower than in the aqueous phase, indicating that these species have a tendency to partition to the PLB interior. The FEPs suggest that O<sub>2</sub> and NO, which are practically non-polar, have the strongest tendency to accumulate in the PLB interior, followed by the triatomic species NO<sub>2</sub> and O<sub>3</sub>, which still conserve a residual dipole moment.<sup>26</sup> N<sub>2</sub>O<sub>4</sub> differentiates from the other species, as it experiences no energy barrier at the headgroup region, but in contrast, a free energy minimum is found close to this region. By moving deeper toward the PLB center, the free energy increases, but reaches values that are closer to the free energy in bulk water. The barrier around the center of the PLB (i.e., at  $\sim |0.7|$  nm) is due to the double bond of the oleoyl tails, which results in bending of the lipid chains. This barrier is also slightly visible for the other hydrophobic species (cf. NO<sub>2</sub> and O<sub>3</sub> in Figure 3.1.3(c)). The results suggest that N<sub>2</sub>O<sub>4</sub> has affinity for the membrane surface, but partitions almost equally between the aqueous phase and the PLB core. The FEP of N<sub>2</sub>O<sub>4</sub> has hybrid characteristics of hydrophilic and hydrophobic species. The geometry of N<sub>2</sub>O<sub>4</sub> is such that it has no dipole moment, but the partial charges that develop at the N and O atoms are relatively large ( $+0.584e$  and  $-0.292e$ , respectively).<sup>26</sup> It might conceivably lead to a strong quadrupole moment, which might explain the tendency of N<sub>2</sub>O<sub>4</sub> to accumulate near the headgroup region,

where it is not as hydrated as in the aqueous phase, but still interacts with the polar PL headgroups. PLB oxidation does not cause significant changes to the permeation of hydrophobic ROS and RNS, except that the FEPs are smoother ([Figure 3.1.3\(d\)](#)). Indeed, the local free energy barriers at  $\sim |0.7|$  nm are gone (cf. [Figure 3.1.3\(c\)](#) and (d)). This is due to the cleavage of the lipid tails and the formation of aldehyde groups (cf. [Figure 3.1.1\(b\)](#) and see [Figure 3.1.3\(d\)](#)). The removal of the local free energy barriers is because of the membrane fluidity: the surface area of the PLB increases and the membrane thickness decreases due to disordering in the lipid tails.<sup>30</sup> Nevertheless, the accumulation position is still in the center of the PLB for hydrophobic species, except for N<sub>2</sub>O<sub>4</sub>.

Taken together, our simulation results agree with previously reported experimental measurements of PLB permeability. Indeed, the permeability of hydrophobic species, like NO and O<sub>2</sub>, was found to be 3-6 orders of magnitude higher than the permeability of hydrophilic ROS, like H<sub>2</sub>O<sub>2</sub>.<sup>31,32</sup> Therefore, membrane-embedded aquaporin channels, or pores created by e.g., strong electric fields,<sup>30</sup> are required to improve the transport of hydrophilic ROS in and out of the cell. Indeed, we recently found that the permeability of H<sub>2</sub>O<sub>2</sub> through AQP is two orders of magnitude higher than through the PLB.<sup>33</sup> In the case of hydrophobic ROS and RNS, transmembrane transport may easily take place even in the absence of channels and pores. This was also demonstrated in literature, where a higher permeability coefficient was reported,<sup>34</sup> e.g., 18-93 cm/s for NO,<sup>32,35,36</sup> 5 cm/s for NO<sub>2</sub><sup>36</sup> and 12-157 cm/s for O<sub>2</sub>,<sup>32,35,37-39</sup> whereas for H<sub>2</sub>O<sub>2</sub> it varies between  $4 \times 10^{-4}$  and  $1.2 \times 10^{-2}$  cm/s.<sup>34</sup> Although all RNS investigated here are hydrophobic, we note that hydrophilic RNS, such as HNO<sub>2</sub>, HNO<sub>3</sub>/NO<sub>3</sub><sup>-</sup> and peroxyntrous acid (ONOOH), can also be generated by plasma processes. However, we could not include these species in the present study, as the force field used in the simulations to describe the behavior of these species is not available yet and therefore we could not yet study their behavior. Future studies will reveal how these hydrophilic RNS interact with native and oxidized PLBs.

As mentioned above, the cell membrane by nature is a complex system and contains different types of membrane components. Consequently, these components might also influence the permeation of RONS into the cytoplasm. It is clear that we cannot study the effect of all these components. Van der Paal *et al.* studied the effect of cholesterol on the FEPs of ROS (i.e., OH, HO<sub>2</sub>, H<sub>2</sub>O<sub>2</sub> and O<sub>2</sub>).<sup>40</sup> He found that the presence of cholesterol increases the lipid order, thereby increasing the free energy barrier for ROS penetration. Hence, we may conclude that the inclusion of cholesterol to our model system might affect the FEPs of the studied RONS, by increasing their free energy barriers. However, we expect that this might eventually lead to the same trends in the FEPs, and thus to the same qualitative conclusions.

### 3.1.4 Conclusion

In general, we can conclude that hydrophobic species, like NO, NO<sub>2</sub>, N<sub>2</sub>O<sub>4</sub>, O<sub>2</sub> and O<sub>3</sub>, can significantly better penetrate across both native and oxidized PLBs, compared to hydrophilic ROS, such as OH, HO<sub>2</sub> and H<sub>2</sub>O<sub>2</sub>, due to the considerably lower free energy barriers.

Oxidation of the PLB caused by e.g., CAP does not strongly affect the free energy barriers of NO, NO<sub>2</sub>, N<sub>2</sub>O<sub>4</sub>, O<sub>2</sub> and O<sub>3</sub>, whereas it reduces the barriers of OH, HO<sub>2</sub> and H<sub>2</sub>O<sub>2</sub>, thereby increasing their translocation probability across the oxidized PLB.

This study is essential for plasma medicine and it is one step towards the understanding of the penetration capabilities of different RONS (generated by CAP) through the native and oxidized cell membrane. Further detailed investigations are needed in order to gain insight into the cooperative role of these species in intracellular signaling processes.

Note that the unique feature of CAP is that it generates a cocktail of various reactive species, ions, UV as well as electric field. Obviously, all these phenomena cannot be captured by our non-reactive MD simulations. Some of them, e.g., the reactions of RONS with the cell membrane components, can be studied using very accurate computational tools, i.e., quantum mechanical (QM) calculations. However, these methods also have limitations, i.e., they operate at standard system sizes in the order of 100 atoms and time scales of picoseconds. This might be overcome by a combination of QM calculations with molecular mechanics (MM, i.e., non-reactive MD simulations), which is called QM/MM method. This method will be investigated in our future studies.

### 3.1.5 Appendix

#### *NO parametrization*

The NO parametrization for calculating the FEP was performed by Cordeiro. Lennard-Jones interaction parameters were taken from atom types OO (oxygen)<sup>25</sup> and NQ (nitrogen)<sup>26</sup>. A bond length of 0.1151 nm was considered.<sup>41</sup> These parameters led to the correct solvation free energy in cyclohexane. Partial charges were initially estimated by electronic structure calculations using the Gaussian 09 software.<sup>42</sup> Calculations were based on density functional theory with the B3LYP functional, the 6-311+G(3df,2pd) basis set and the ChelpG charge fitting scheme. Partial charges were then iteratively scaled to account for solvent-induced polarization effects and yield the correct hydration free energy. Solvation free energies were calculated by the thermodynamic integration method using 21 points for van der Waals and 11 points for Coulomb interactions. Production runs according to the NPT ensemble were performed for 1 ns. Further details about the simulation conditions were the same as in <sup>25</sup> and <sup>26</sup>. In the end, partial charges of +0.02e and -0.02e were found for the O and N atoms, respectively. Table A1 shows the solvation data for our newly derived NO model, as compared to a previous NO force field <sup>43</sup> and to experimental data <sup>44,45</sup>. The results demonstrate that our NO model correctly describes both the aqueous and the hydrophobic solvation of NO, and is therefore suitable for studies of water/membrane partition of this species.

Table A1. Solvation free energies of NO in cyclohexane and water, and the resulting partition coefficients ( $K$ ).

Force field	$\Delta G_{\text{ch}}$ (kJ/mol)	$\Delta G_{\text{w}}$ (kJ/mol)	$\Delta G_{\text{w} \rightarrow \text{ch}}$ (kJ/mol)	$K_{\text{w} \rightarrow \text{ch}}$
Victor <i>et al.</i>	-4.0	7.5	-11.5	103.7
this work	2.5	7.0	-4.5	6.1
experimental	2.1	7.6	-5.5	9.2

*Comparison of full (i.e., non-symmetrized) and symmetrized FEPs*

The obtained FEPs from the US simulations for RONS were perfectly converged. As an example, we show in Fig. A1 the full (i.e., non-symmetrized) and symmetrized FEPs of NO, NO<sub>2</sub>, N<sub>2</sub>O<sub>4</sub> and O<sub>3</sub> for native and 50% oxidized PLBs. As is clear, the full and symmetrized FEPs are almost the same. Overlapping of the full and symmetrized FEPs is a hallmark of convergence of our data.

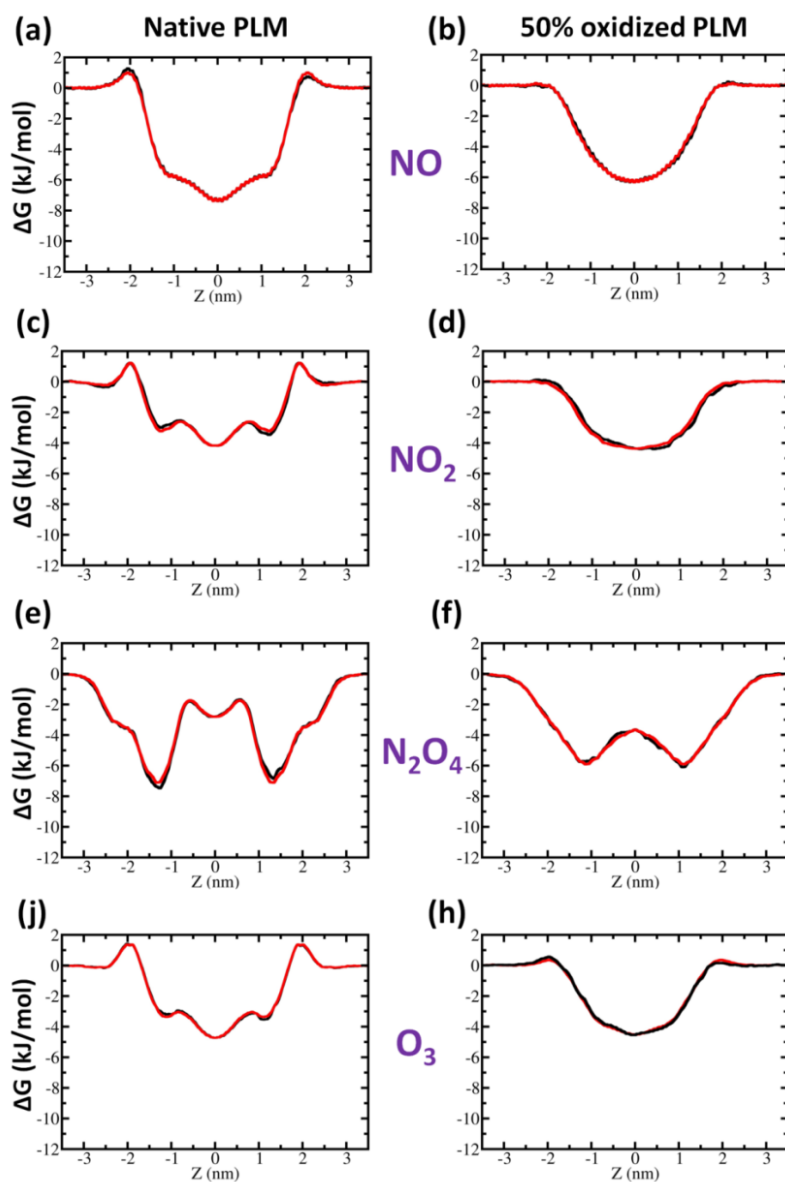


Figure A1. Illustration of the full (— black line) and symmetrized (— red line) free energy profiles of NO (a-b), NO<sub>2</sub> (c-d), N<sub>2</sub>O<sub>4</sub> (e-f) and O<sub>3</sub> (j-h) for native and 50% oxidized PLB.

### 3.1.6 References

- 1 Keidar, M., Walk, R., Shashurin, A., Srinivasan, P., Sandler, A., Dasgupta, S., Ravi, R., Guerrero-Preston, R and Trink, B. Cold plasma selectivity and the possibility of a paradigm shift in cancer therapy. *British journal of cancer* 105, 1295 (2011).
- 2 Barekzi, N and Laroussi, M. Dose-dependent killing of leukemia cells by low-temperature plasma. *Journal of Physics D: Applied Physics* 45, 422002 (2012).
- 3 Vermeulen, S., De Waele, J., Vanuytsel, S., De Backer, J., Van der Paal, J., Ramakers, M., Leysens, K., Marcq, E., Van Audenaerde, J., Smits, E and Dewilde, S. Cold atmospheric plasma treatment of melanoma and glioblastoma cancer cells. *Plasma Processes and Polymers* 13, 1195-1205 (2016).
- 4 Kim, S and Chung, T. Cold atmospheric plasma jet-generated RONS and their selective effects on normal and carcinoma cells. *Scientific reports* 6, 20332 (2016).
- 5 Iseki, S., Nakamura, K., Hayashi, M., Tanaka, H., Kondo, H., Kajiyama, H., Kano, H., Kikkawa, F and Hori, M. Selective killing of ovarian cancer cells through induction of apoptosis by nonequilibrium atmospheric pressure plasma. *Applied Physics Letters* 100, 113702 (2012).
- 6 Liou, G and Storz, P. Reactive oxygen species in cancer. *Free radical research* 44, 479-496 (2010).
- 7 Wiseman, H and Halliwell, B. Damage to DNA by reactive oxygen and nitrogen species: role in inflammatory disease and progression to cancer. *Biochemical Journal* 313, 17 (1996).
- 8 Graves, D. B. Reactive species from cold atmospheric plasma: implications for cancer therapy. *Plasma Processes and Polymers* 11, 1120-1127 (2014).
- 9 Redza-Dutordoir, M and Averill-Bates, D. Activation of apoptosis signalling pathways by reactive oxygen species. *Biochimica et Biophysica Acta (BBA)-Molecular Cell Research* 1863, 2977-2992 (2016).
- 10 Bauer, G. Increasing the endogenous NO level causes catalase inactivation and reactivation of intercellular apoptosis signaling specifically in tumor cells. *Redox biology* 6, 353-371 (2015).
- 11 Yan, D., Sherman, J and Keidar, M. Cold atmospheric plasma, a novel promising anti-cancer treatment modality. *Oncotarget* 8, 15977 (2017).
- 12 Tanaka, H., Mizuno, M., Ishikawa, K., Nakamura, K., Kajiyama, H., Kano, H., Kikkawa, F and Hori, M. Plasma-activated medium selectively kills glioblastoma brain tumor cells by down-regulating a survival signaling molecule, AKT kinase. *Plasma Medicine* 1 (2011).
- 13 Ishaq, M., Evans, M and Ostrikov, K. Effect of atmospheric gas plasmas on cancer cell signaling. *International journal of cancer* 134, 1517-1528 (2014).
- 14 Bauer, G. Tumor cell-protective catalase as a novel target for rational therapeutic approaches based on specific intercellular ROS signaling. *Anticancer research* 32, 2599-2624 (2012).
- 15 Bauer, G. Targeting extracellular ROS signaling of tumor cells. *Anticancer research* 34, 1467-1482 (2014).

- 16 Bauer, G. Nitric Oxide Contributes To Selective Apoptosis Induction In Malignant Cells Through Multiple Reaction Steps. *Critical Reviews in Oncogenesis* **21**, 5-6 (2017).
- 17 Yusupov, M., Wende, K., Kupsch, S., Neyts, E., Reuter, S and Bogaerts, A. Effect of head group and lipid tail oxidation in the cell membrane revealed through integrated simulations and experiments. *Scientific Reports* **7**, 5761 (2017).
- 18 Ingólfsson, H., Melo, M., Van Eerden, F., Arnarez, C., Lopez, C., Wassenaar, T., Periolo, X., De Vries, A., Tieleman, D and Marrink, S. Lipid organization of the plasma membrane. *Journal of the american chemical society* **136**, 14554-14559 (2014).
- 19 Reis, A., Domingues, M., Amado, F. M., Ferrer-Correia, A and Domingues, P. Separation of peroxidation products of diacyl-phosphatidylcholines by reversed-phase liquid chromatography–mass spectrometry. *Biomedical Chromatography* **19**, 129-137 (2005).
- 20 Alberts B, J., Lewis J, Morgan D, Raff M, Roberts K and Walter P Molecular Biology of the Cell. *Garland Science* **6**, (2014).
- 21 Van der Paal, J., Neyts, E., Verlackt, C and Bogaerts, A. Effect of lipid peroxidation on membrane permeability of cancer and normal cells subjected to oxidative stress. *Chemical science* **7**, 489-498 (2016).
- 22 Martínez, L., Andrade, R., Birgin, E and Martínez, J. M. PACKMOL: a package for building initial configurations for molecular dynamics simulations. *Journal of computational chemistry* **30**, 2157-2164 (2009).
- 23 Van Der Spoel, D., Lindahl, E., Hess, B., Groenhof, G., Mark, A and Berendsen, H. GROMACS: fast, flexible, and free. *Journal of computational chemistry* **26**, 1701-1718 (2005).
- 24 Chiu, S., Pandit, S. , Scott, H and Jakobsson, E. An improved united atom force field for simulation of mixed lipid bilayers. *Journal of Physical Chemistry B* **113**, 2748-2763 (2009).
- 25 Cordeiro, R. Reactive oxygen species at phospholipid bilayers: distribution, mobility and permeation. *Biochimica et Biophysica Acta (BBA)-Biomembranes* **1838**, 438-444 (2014).
- 26 Cordeiro, R. Reactive oxygen and nitrogen species at phospholipid bilayers: Peroxynitrous acid and its homolysis products. *Journal of Physical Chemistry B* **34**, 8211-8219 (2018).
- 27 Torrie, G and Valleau, J. Nonphysical sampling distributions in Monte Carlo free-energy estimation: Umbrella sampling. *Journal of Computational Physics* **23**, 187-199 (1977).
- 28 Kästner, J. Umbrella sampling. *Wiley Interdisciplinary Reviews: Computational Molecular Science* **1**, 932-942 (2011).
- 29 Kumar, S., Rosenberg, J., Bouzida, D., Swendsen, R and Kollman, P. The weighted histogram analysis method for free-energy calculations on biomolecules. I. The method. *Journal of computational chemistry* **13**, 1011-1021 (1992).
- 30 Yusupov, M., Van der Paal, J., Neyts, E and Bogaerts, A. Synergistic effect of electric field and lipid oxidation on the permeability of cell membranes. *Biochimica et Biophysica Acta (BBA)-General Subjects* **1861**, 839-847 (2017).

- 31 Möller, M., Li, Q., Lancaster, J and Denicola, A. Acceleration of nitric oxide autoxidation and nitrosation by membranes. *IUBMB life* 59, 243-248 (2007).
- 32 Subczynski, W., Lomnicka, M and Hyde, J. Permeability of nitric oxide through lipid bilayer membranes. *Free radical research* 24, 343-349 (1996).
- 33 Yusupov, M., Yan, D., Cordeiro, R and Bogaerts, A. Atomic scale simulation of H<sub>2</sub>O<sub>2</sub> permeation through aquaporin: toward the understanding of plasma cancer treatment. *Journal of Physics D: Applied Physics* 51, 125401 (2018).
- 34 Möller, M., Lancaster Jr, J and Denicola, A. The interaction of reactive oxygen and nitrogen species with membranes. *Current Topics in Membranes* 61, 23-42 (2008).
- 35 Denicola, A., Souza, J., Radi, R and Lissi, E. Nitric oxide diffusion in membranes determined by fluorescence quenching. *Archives of biochemistry and biophysics* 328, 208-212 (1996).
- 36 Signorelli, S., Möller, M., Coitiño, E and Denicola, A. Nitrogen dioxide solubility and permeation in lipid membranes. *Archives of biochemistry and biophysics* 512, 190-196 (2011).
- 37 Subczynski, W., Hopwood, L and Hyde, J. Is the mammalian cell plasma membrane a barrier to oxygen transport? *Journal of general physiology* 100, 69-87 (1992).
- 38 Subczynski, W., Hyde, J and Kusumi, A. Oxygen permeability of phosphatidylcholine--cholesterol membranes. *Proceedings of the National Academy of Sciences* 86, 4474-4478 (1989).
- 39 Widomska, J., Raguz, M and Subczynski, W. Oxygen permeability of the lipid bilayer membrane made of calf lens lipids. *Biochimica et Biophysica Acta (BBA)-Biomembranes* 1768, 2635-2645 (2007).
- 40 Van der Paal, J., Verheyen, C., Neyts, E and Bogaerts, A. Hampering effect of cholesterol on the permeation of reactive oxygen species through phospholipids bilayer: possible explanation for plasma cancer selectivity. *Scientific reports* 7, 39526 (2017).
- 41 Haynes, W. *CRC handbook of chemistry and physics*. (CRC press, 2014).
- 42 Frisch, M., Trucks, G., Schlegel, H., Scuseria, G., Robb, M., Cheeseman, J., Scalmani, G., Barone, V., Mennucci, B., Petersson, G and Nakatsuji, H. Gaussian 09, *Gaussian Inc., Wallingford CT* (2009).
- 43 Victor, B., Baptista, A and Soares, C. Dioxygen and nitric oxide pathways and affinity to the catalytic site of rubredoxin: oxygen oxidoreductase from *Desulfovibrio gigas*. *Journal of Biological Inorganic Chemistry* 14, 853-862 (2009).
- 44 Young, C. L. *Oxides of nitrogen*. IUPAC Solubility Data Series edn, Vol. 8 (Pergamon Press, 1981).
- 45 Wilhelm, E., Battino, R and Wilcock, R. J. Low-pressure solubility of gases in liquid water. *Chemical reviews* 77, 219-262 (1977).



## 3.2 Possible mechanism of glucose uptake enhanced by CAP

### 3.2.1 Introduction

In this section, we present the glucose translocation across native and oxidized membranes, in order to provide a possible explanation to the mechanism of glucose uptake upon CAP treatment observed in experiments. In particular, we perform MD simulations to calculate the free energy barriers for glucose transport through oxidized and non-oxidized membranes. Comparison of the latter shows the effect of CAP oxidation on the glucose transport across the membrane, which might explain the increased level of glucose uptake after plasma treatment of cells, as observed experimentally.

### 3.2.2 Computational details

#### Simulation setup

We performed MD simulations in order to study the glucose translocation across both intact and oxidized PLBs. The PLB was again considered as a simple model system representing the eukaryotic cell membrane, since it determines the bilayer thickness. A schematic representation of the intact PLB is given in [Figure 3.2.1\(a\)](#). It consists again of 128 phospholipids (PLs), covered by 6000 water molecules, organized in two lamellae (i.e., 64 PLs, with corresponding water layer at the top, and 64 at the bottom). As the PL molecule we used 1,2-dioleoyl-sn-glycero-3-phosphocholine (DOPC) depicted in [Figure 3.2.1\(b\)](#). Glucose molecules were randomly placed in the xy-plane of the upper side of the PLB, i.e., in the water phase, as well as in the lipid tail region, see [Figure 3.2.1\(a\)](#) (and see below for more details).

The simulations were again carried out using the GROMACS package (version 5.1),<sup>1</sup> applying the GROMOS (43A1-S3) force field.<sup>2</sup> To study the effect of oxidized PLs we used again aldehyde oxidation products (see [Figure 3.2.1b](#), DOPC-ALD), which were found to be one of the major oxidation products.<sup>3</sup> Note that CAP yields a cocktail of reactive species and can thus possibly form a range of products upon oxidation of the PLB, but the formation of aldehyde groups (i.e., DOPC-ALD) was prominently observed in CAP-treated vesicles.<sup>4</sup> These oxidation products were also used in other recent simulation studies on various properties of the PLB carried out in our group,<sup>4-6</sup> as well as in [section 3.1](#) above. The force field parameters for the aldehyde groups in the oxidized PLs were obtained from <sup>7</sup> and the parameters of glucose were based on <sup>8</sup>. The Packmol package was again employed to create the initial configurations of the intact and oxidized PLB systems.<sup>9</sup> Two aldehyde oxidation products were created from the non-oxidized (i.e., native) PLBs containing 128 PLs, by replacing 32 and 64 DOPC molecules with DOPC-ALD, corresponding to concentrations of 25% and 50%, respectively. The presence of 25% and 50% DOPC-ALD in the oxidized PLB does not necessarily correspond to experimental oxidation levels, but performing the calculations for lower oxidation degree would require excessive calculation times for the same qualitative conclusions. Hence, this oxidation degree was high enough to observe the effect of oxidation within acceptable calculation time, but low enough so that pore formation did not occur within the simulated time scale.<sup>10</sup>

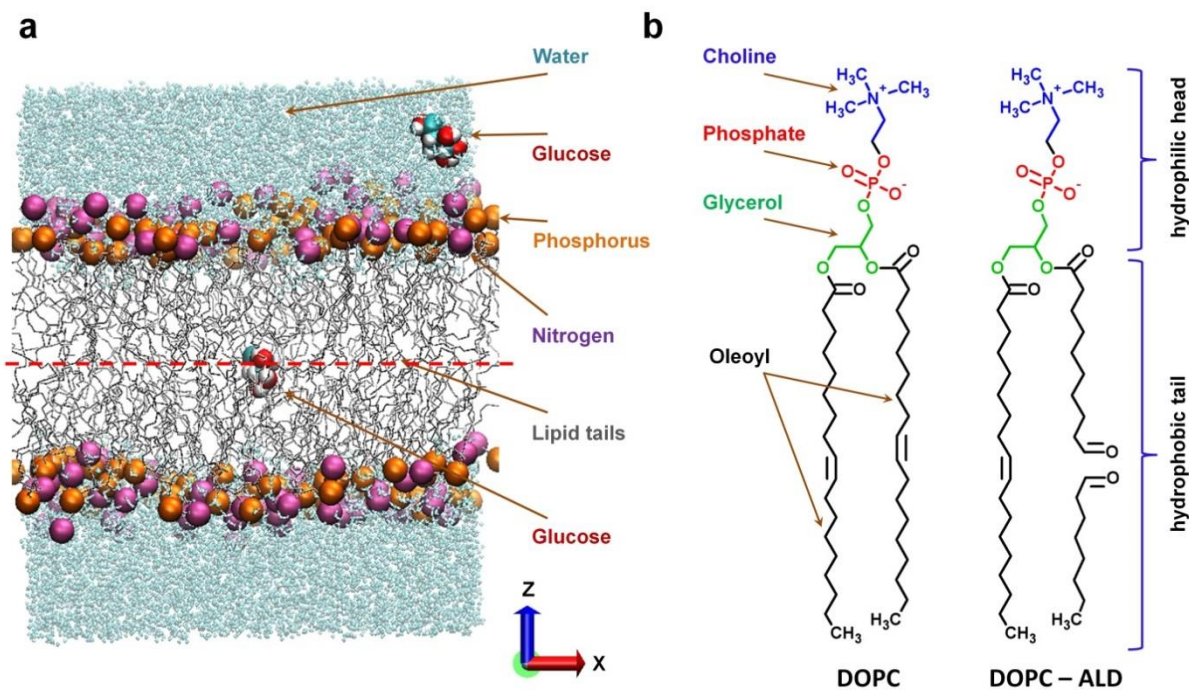


Figure. 3.2.1: (a) Intact or native DOPC PLB, together with two glucose molecules in the water and lipid tail regions. For the sake of clarity, the N and P atoms of DOPC are shown with larger beads. The bilayer center is indicated by the red dashed line. (b) Schematic illustration of native (DOPC) and oxidized (DOPC-ALD) PLs. The headgroup consists of choline, phosphate and glycerol, whereas the lipid tails are two fatty acid chains.

Thus, in total three model systems were studied in our simulations, i.e., native (0%) as well as aldehyde oxidized (25% and 50%) PLBs. For each system, we created four different structures (e.g., four native PLBs) extracted from the last 40 ns trajectory of the 200 ns equilibration run, with 10 ns time interval, in order to obtain an average free energy profile (FEP) of glucose transition across each system (see next section). All structures (i.e., in total 12, including the native PLB) were initially optimized using the steepest descent algorithm and then equilibrated for 200 ns by so-called NPT simulations (i.e., at constant number of particles (N), pressure (P) and temperature (T)), at 310 K and 1 bar, employing the Nose-Hoover thermostat<sup>11</sup> with a coupling constant of 0.2 ps, as well as the semi-isotropic Parrinello-Rahman barostat<sup>12</sup> with a compressibility and coupling constant of  $4.5 \times 10^{-5} \text{ bar}^{-1}$  and 0.1 ps, respectively. For the non-bonded interactions, a 1.1 nm cut-off was applied. The long range electrostatic interactions were described by the particle mesh Ewald (PME) method<sup>13</sup>, using a 1.1 nm cut-off for the real-space interactions in combination with a 0.15 nm spaced-grid for the reciprocal-space interactions. Subsequently, a series of umbrella sampling (US) simulations was run for 20 ns, applying again the NPT ensemble (see next section), of which the last 10 ns was used for further analysis.<sup>14</sup> In all simulations a time step of 2 fs was used. Periodic boundary conditions were applied in all three directions.

### Umbrella sampling simulations

We performed US simulations in order to determine the free energy profiles (FEPs) of glucose translocation across the native and oxidized PLBs. In total we obtain 12 FEPs for all model systems (i.e., four for the native, four for the 25% oxidized, and four for the 50% oxidized PLBs, see previous section) and an averaging was performed over four FEPs for each system. For the calculation of each energy profile, we extracted 32 to 36 windows (36 for the native, 34 for the 25% and 32 for the 50% oxidized PLB, due to a decrease of the bilayer thickness) along the z-axis, which were separated by 0.1 nm. These windows were obtained by pulling glucose molecules against the z-axis direction (see [Figure 3.2.1\(a\)](#)) for 500 ps, using a harmonic bias between these glucose molecules and the center of mass of the PLB, with a force constant of  $2000 \text{ kJ}\cdot\text{mol}^{-1} \text{ nm}^{-2}$  and a pulling rate of  $0.01 \text{ nm}\cdot\text{ps}^{-1}$ . Note that, in principle, slow pulling rates can be used in the pulling simulations. However, dragging the glucose from the water phase into the center of the PLB needs long computation time. Higher pulling rates can solve this issue, but they can lead to significant disturbances in the PLB. Thus, by using an appropriate (standard) pulling rate, we performed short pulling simulations, to save computation time with minimum perturbation on the PLB. One of the glucose molecules (i.e., the glucose in the upper water phase, see [Figure 3.2.1\(a\)](#)) was pulled until it reached the center of mass of the PLB, while the second one moved towards the lower water phase from the center of the bilayer. Thus, each US simulation contained two glucose molecules. In this way we save computational resources, thereby increasing the number of sampling points. Note that these two glucose molecules were separated from each other at least by 3 nm in the z direction, hence, there was no interaction between these two molecules. In principle, we could use three glucose molecules in each US simulation. However, in order to make a minimal disturbance to the PLB system, we chose two glucose molecules instead of three. It should be mentioned that in reality, adsorption or chemical reaction of glucose might take place in the PLB. However, these processes cannot be studied with conventional non-reactive MD simulations, due to the limitations in time and reactivity. Nevertheless, the US simulations can predict how often the glucose transport occurs across the PLB before and after oxidation, through calculation of the FEPs.

As mentioned above, we extracted 32 to 36 US windows from our 500 ps pulling simulation. Hence, 32 to 36 US simulations were performed to construct a single FEP. Each US simulation lasted for 20 ns, and the last 10 ns were used for analysis, i.e., to collect the US histograms and calculate the FEPs. Note that the pulling simulation trajectory is used only to extract windows/frames for the further US simulation to obtain the FEPs. During the pulling simulations the glucose drags water molecules with it into the hydrophobic core of the bilayer, but these molecules escape from the hydrophobic core within the initial 10 ns of US simulation. Thus, the last 10 ns of the US simulation is an adequate time for calculating the FEPs, as there were not any water defects or hydration layers in the hydrophobic part of the membrane. In each US simulation, the glucose molecules could freely travel in the xy-plane but their movement in the z-direction was restricted by applying a harmonic bias with a spring constant of  $2000 \text{ kJ}\cdot\text{mol}^{-1} \text{ nm}^{-2}$ .

FEPs were constructed using a periodic version of the weighted histogram analysis method (WHAM),<sup>14</sup> as implemented in GROMACS. We analyzed our simulation systems for

underestimated possible “hidden barriers” based on literature.<sup>15</sup> We did not define any hidden barriers because in our US simulations the data was sufficiently sampled. Indeed, in the four model systems used, the glucose was randomly positioned in the xy-plane to escape from trapped metastable states and for the estimation of error bars that are associated with choosing the initial model systems. As noted above, the final energy profiles were obtained by averaging over four FEPs for each system, which differ from one another based on their starting structure, to allow for some statistical variations. Thus, in total 410 US simulations were performed for the calculation of the FEPs.

### 3.2.3 Results and discussion

The US MD simulations allow to elucidate the glucose translocation across the native and oxidized PLBs, which gives insight in the possible mechanism of glucose ingress triggered by plasma oxidation of the cell membrane. [Figure 3.2.2\(a\)](#) illustrates the symmetric FEPs of glucose transfer across native as well as oxidized (25% and 50%) PLBs. It is clear that in all three cases the  $\Delta G$  starts to drop when glucose enters from the water phase to the hydrophilic head group region (see [Figure 3.2.1\(b\)](#)). This means that the head group of the PLB is energetically the most favourable region, showing minimum energy for glucose transfer. Moreover, this energy minimum slightly shifts towards the centre of the bilayer in the case of oxidized PLBs. We know from previous studies by Yusupov *et al.* that when lipid tails are oxidized, this eventually leads to a drop of the bilayer thickness.<sup>4,6</sup> In other words, the shortened tail and aldehyde products move towards the water phase, thereby increasing the area and fluidity of the PLB. Consequently, this results in a decrease of the PLB thickness, e.g., the native DOPC bilayer has a thickness of around 3.89 nm, whereas in the case of a 50% DOPC-ALD bilayer, the thickness decreases to 3.33 nm.<sup>6</sup> Therefore, the free energy minima in [Figure 3.2.2](#) are found at around  $|z|=1.9$  nm and  $|z|=1.76$  nm in the case of native and 50% oxidized PLBs, respectively.

Continuing the motion of glucose towards the hydrophobic tail region leads to an increase of the free energy for translocation, representing the role of the membrane as a permeation barrier. In case of the native PLB, the free energy barrier for the permeation of glucose is  $51\pm 3$  kJ/mol, which is within the range of experimental results.<sup>16,17</sup> On the other hand, in the case of 25% and 50% oxidized PLBs, this barrier for the translocation of glucose decreases to values of  $37\pm 4$  kJ/mol and  $28\pm 4$  kJ/mol, respectively (see [Figure 3.2.2](#)). Hence, the obtained results show that the free energy barrier for the transport of glucose molecules across the PLB decreases upon increasing the oxidation degree. This in turn leads to an increase of the probability of glucose permeation to the cell interior. The obtained simulation results can be correlated with the experimental observations,<sup>18,19</sup> as plasma treatment of cells most probably gives rise to oxidation of the cell membrane, thereby increasing the glucose (or other middle-size molecules, as well as  $\text{Ca}^{2+}$ ) translocation rate.

Note that our simulations only provide one possible explanation to an increased level of glucose<sup>18</sup> in cells after plasma treatment, while other mechanisms might play a role as well.<sup>19-21</sup> Therefore, further investigations should be performed to obtain a more complete picture of the plasma effect on the membrane permeability. This might be achieved, for instance, by

silencing the glucose transporter proteins (or GLUTs) and measuring the concentration of intracellular glucose molecules, after CAP treatment. The latter would clearly reveal the role of cell membrane permeability (induced by CAP oxidation of lipids) in transporting glucose molecules.

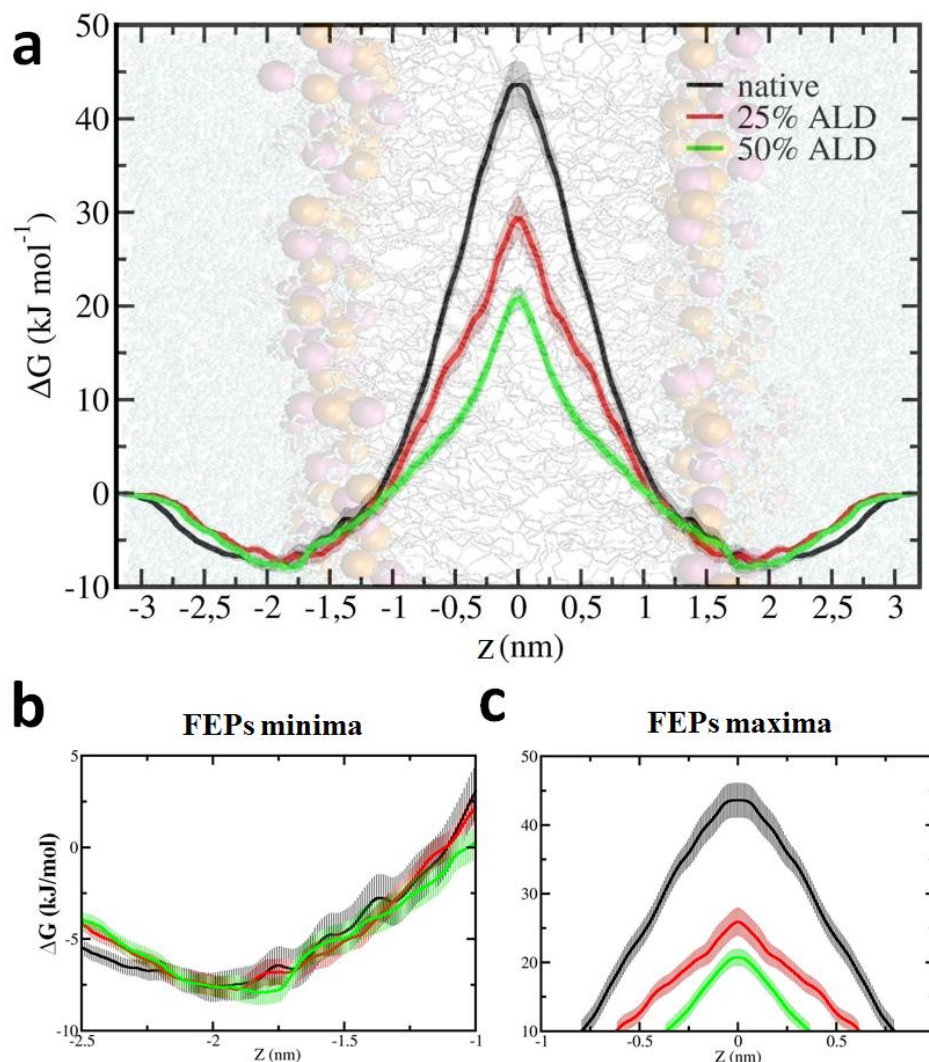


Figure. 3.2.2: (a) Symmetric free energy profiles for the translocation of glucose across native and oxidized PLBs. The PLB is schematically illustrated in the background, to indicate the position of the water layer, the headgroups and the lipid tails. For clarity, the zoomed extrema of the profiles are shown in (b) and (c). Errors associated with the US calculations are depicted in pale color.

### 3.2.4 Conclusion

We performed MD simulations in order to understand the possible mechanisms of cellular glucose uptake induced by CAP treatment. The obtained free energy profiles of glucose across native and oxidized membranes revealed that plasma induced oxidation of the membrane lipids decreases the barrier for translocation of glucose across the membrane. This in turn might possibly explain the increased concentration of glucose observed by

experiments using CAP. Hence, this computational study provides an atomic level insight into the possible process of glucose permeation through the membrane.

### 3.2.5 References

- 1 Van Der Spoel, D., Lindahl, E., Hess, B., Groenhof, G., Mark, A and Berendsen, H. GROMACS: fast, flexible, and free. *Journal of computational chemistry* 26, 1701-1718 (2005).
- 2 Chiu, S., Pandit, S., Scott, H and Jakobsson, E. An improved united atom force field for simulation of mixed lipid bilayers. *Journal of Physical Chemistry B* 113, 2748-2763 (2009).
- 3 Reis, A., Domingues, M., Amado, F., Ferrer-Correia, A and Domingues, P. Separation of peroxidation products of diacyl-phosphatidylcholines by reversed-phase liquid chromatography–mass spectrometry. *Biomedical Chromatography* 19, 129-137 (2005).
- 4 Yusupov, M., Wende, K., Kupsch, S., Neyts, E., Reuter, S and Bogaerts, A. Effect of head group and lipid tail oxidation in the cell membrane revealed through integrated simulations and experiments. *Scientific Reports* 7, 5761 (2017).
- 5 Van der Paal, J., Neyts, E., Verlackt, C and Bogaerts, A. Effect of lipid peroxidation on membrane permeability of cancer and normal cells subjected to oxidative stress. *Chemical science* 7, 489-498 (2016).
- 6 Yusupov, M., Van der Paal, J., Neyts, E and Bogaerts, A. Synergistic effect of electric field and lipid oxidation on the permeability of cell membranes. *Biochimica et Biophysica Acta (BBA)-General Subjects* 1861, 839-847 (2017).
- 7 Wong-Ekkabut, J., Xu, Z., Triampo, W., Tang, I., Tieleman, D and Monticelli, L. Effect of lipid peroxidation on the properties of lipid bilayers: a molecular dynamics study. *Biophysical journal* 93, 4225-4236 (2007).
- 8 Geballe, M. T., Skillman, A. G., Nicholls, A., Guthrie, J and Taylor, P. The SAMPL2 blind prediction challenge: introduction and overview. *Journal of computer-aided molecular design* 24, 259-279 (2010).
- 9 Martínez, L., Andrade, R., Birgin, E and Martínez, J. PACKMOL: a package for building initial configurations for molecular dynamics simulations. *Journal of computational chemistry* 30, 2157-2164 (2009).
- 10 Van der Paal, J., Neyts, E., Verlackt, C and Bogaerts, A. Effect of lipid peroxidation on membrane permeability of cancer and normal cells subjected to oxidative stress. *Chemical Science* 7, 489-498 (2016).
- 11 Hoover, W. G. Canonical dynamics: equilibrium phase-space distributions. *Physical review A* 31, 1695 (1985).
- 12 Parrinello, M and Rahman, A. Polymorphic transitions in single crystals: A new molecular dynamics method. *Journal of Applied physics* 52, 7182-7190 (1981).
- 13 Essmann, U., Perera, L., Berkowitz, M., Darden, T., Lee, H and Pedersen, L. A smooth particle mesh Ewald method. *Journal of chemical physics* 103, 8577-8593 (1995).
- 14 Kästner, J. Umbrella sampling. *Wiley Interdisciplinary Reviews: Computational Molecular Science* 1, 932-942 (2011).
- 15 Neale, C and Pomès, R. Sampling errors in free energy simulations of small molecules in lipid bilayers. *Biochimica et Biophysica Acta (BBA)-Biomembranes* 1858, 2539-2548 (2016).

- 16 Bresseleers, G., Goderis, H and Tობback, P. Measurement of the glucose permeation rate across phospholipid bilayers using small unilamellar vesicles Effect of membrane composition and temperature. *Biochimica et Biophysica Acta (BBA)-Biomembranes* 772, 374-382 (1984).
- 17 Sweet, C and Zull, J. Activation of glucose diffusion from egg lecithin liquid crystals by serum albumin. *Biochimica et Biophysica Acta (BBA)-Biomembranes* 173, 94-103 (1969).
- 18 Kumar, N., Shaw, P., Razzokov, J., Yusupov, M., Attri, P., Uhm, H., Choi, E. and Bogaerts, A. Enhancement of cellular glucose uptake by reactive species: a promising approach for diabetes therapy. *RSC advances* 8, 9887-9894 (2018).
- 19 Sasaki, S., Hokari, Y., Kumada, A., Kanzaki, M and Kaneko, T. Direct plasma stimuli including electrostimulation and OH radical induce transient increase in intracellular Ca<sup>2+</sup> and uptake of a middle-size membrane-impermeable molecule. *Plasma Processes and Polymers* 15, 1700077 (2018).
- 20 Vijayarangan, V., Delalande, A., Dozias, S., Pouvesle, J., Pichon, C and Robert, E. Cold atmospheric plasma parameters investigation for efficient drug delivery in HeLa cells. *IEEE Transactions on Radiation and Plasma Medical Sciences* 2, 109-115 (2018).
- 21 Leduc, M., Guay, D., Leask, R and Coulombe, S. Cell permeabilization using a non-thermal plasma. *New Journal of Physics* 11, 115021 (2009).

## 3.3 Phosphatidylserine flip-flop induced by (plasma) oxidation of the cell membrane

### 3.3.1 Introduction

The cellular antioxidant mechanism maintains a redox homeostasis by preventing a build-up of ROS, which endanger cellular health due to their oxidizing properties.<sup>1</sup> Whenever the redox homeostasis is compromised, either by antioxidant depletion or the increased presence of ROS, the cell enters a state of oxidative stress.<sup>2,3</sup> If excessive amounts of oxidative stress are presented to the cell, it will undergo programmed cell death, i.e. apoptosis. This is exploited for example when treating cancer cells with radiotherapy<sup>4</sup> or with CAP.<sup>5,6</sup>

Apoptosis can be the result of many different harmful attacks to cellular health, of which oxidative stress is one example, and it results in the phagocytic uptake of dead cells, which are fragmented into apoptotic bodies with intact plasma membranes.<sup>7</sup> To facilitate the uptake, apoptotic cells will present various markers on their external plasma membrane, which function as “come get me” and “eat me” signals.<sup>8</sup> One of these markers is phosphatidylserine (PS), a lipid normally situated in the inner leaflet of the plasma membrane.<sup>9</sup> If the apoptotic pathway is activated, PS will flip from the inner leaflet into the outer leaflet through a flip-flop mechanism and act as an “eat me” signal for lymphocytic cells.<sup>10</sup> While the effect of PS flip-flop is known, and it is suggested to occur due to the action of scramblases,<sup>11</sup> the mechanism remains to be unraveled,<sup>12</sup> although there are some studies trying to explain this mechanism by means of so-called push-in, sliding or rotational flip-flop models<sup>13,14</sup> (see below).

Apart from activating apoptosis, excessive oxidative stress can also oxidize the membrane lipids,<sup>15</sup> which increases the rate of PS flip-flop, as shown by Volinsky *et al.*<sup>16</sup> Through molecular dynamics (MD) simulations, they observed a reduction of  $20 \pm 5$  kJ/mol in the flip-flop energy barrier in the presence of 20% oxidized phosphatidylcholine in the lipid bilayer.<sup>16</sup> The same effects were also qualitatively observed by means of fluorescence spectroscopy of oxidized liposome bilayers.<sup>16</sup> However, although this study presents valuable knowledge on the influence of oxidized membranes on the PS flip-flop, the authors only compared non-oxidized membranes to a membrane with a fixed amount of oxidation.<sup>16</sup> Hence, the impact of increasing levels of membrane oxidation on the PS flip-flop energy barrier has not been characterized by atomic level simulations up to now.

Therefore, in this section we study the flip-flop motion of PS across the plasma membrane as a function of increasing oxidation degree of the membrane. For this purpose, we calculated the free energy profiles of PS flip-flop across the membrane. The aim of this study is to reveal the atomistic details of the PS flip-flop mechanism, and to link it to the oxidative damage of the plasma membrane, which eventually may facilitate the flip-flop motion of PS.

## 3.3.2 Computational details

### Simulation setup

To study the flip-flop motion of PS across the (oxidized) membrane, we performed MD simulations based on the GROMOS (43A1-S3) force field.<sup>17</sup> The parameters for peroxide groups in the oxidized phospholipids (PLs, see [Figure 3.3.1\(b\)](#)) were obtained from<sup>18</sup>. As a model system we used the phospholipid bilayer (PLB) shown in [Figure 3.3.1\(a\)](#), representing the cell membrane. It again consists of 128 PLs arranged in two leaflets and covered with 5120 water molecules on top and bottom layers. The PL investigated is palmitoyl-oleoyl-phosphatidylcholine (POPC) presented in [Figure 3.3.1\(b\)](#).

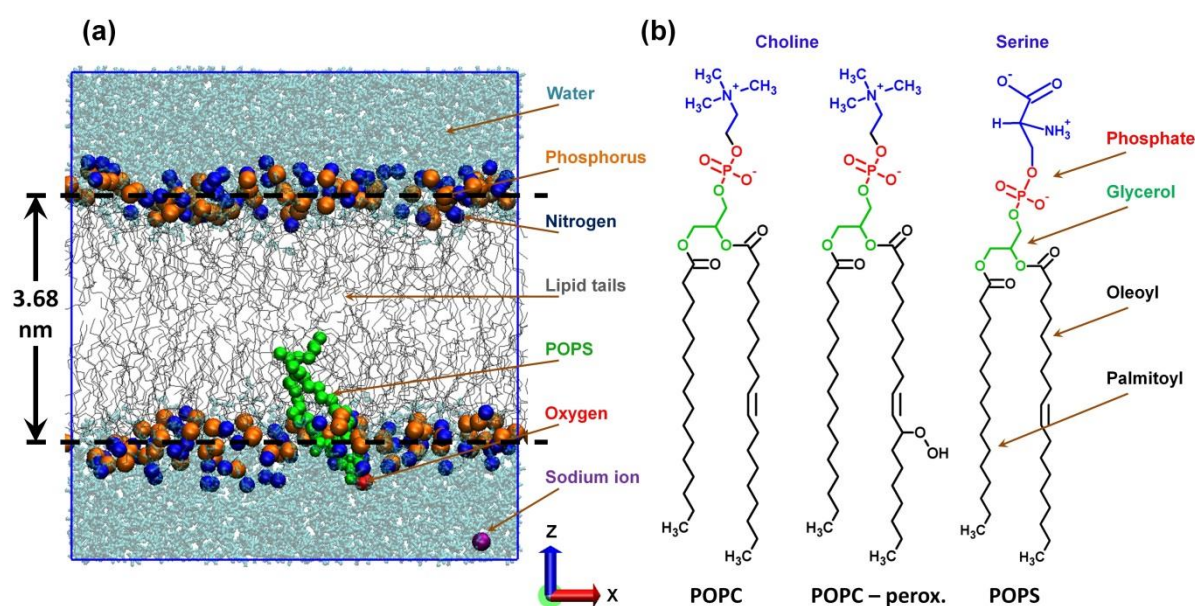


Figure 3.3.1. (a) Native POPC PLB, together with a single POPS at the bottom layer. The P and N atoms of POPC are depicted with bigger beads, for the sake of clarity. The simulation box is presented by the blue rectangle. (b) Schematic illustrations of the native (POPC) and peroxidized (POPC-perox.) PLs as well as POPS. The color legend also applies to the other similar figures below.

The bottom leaflet contains a single palmitoyl-oleoyl-phosphatidylserine (POPS) molecule replacing one of the PLs, so it contains 63 POPC molecules and one POPS molecule (see [Figure 3.3.1\(a\)](#)). Note that we simply write PS instead of POPS in the discussion below, for the sake of simplicity.

To study the effect of the oxidized PLs, the oxidation product of POPC, i.e., a peroxide, is included in the simulated systems (see [Figure 3.3.1\(b\)](#)). This peroxide was chosen because it was one of the two major oxidation products of POPC and it is the end product of the main lipid peroxidation reaction.<sup>19</sup> To create membranes oxidized to various degrees, 12.5, 25, 37.5, or 50% of the POPC molecules in the native PLB structure are replaced by the peroxidized PLs.

The initial configuration of each simulation system was again created using the Packmol package.<sup>20</sup> For each peroxidation degree (i.e., 12.5, 25, 37.5 and 50 %), six different structures were created, placing PS at a random position in the x and y direction, while keeping its z position unchanged (cf. [Figure 3.3.1\(a\)](#)). In order to neutralize the negatively charged PS, a sodium cation shown in [Figure 3.3.1\(a\)](#) is placed in the water phase of the system and is fixed in all three directions to avoid its interaction with PS. Periodic boundary conditions are applied in all three directions.

The simulations were again performed in the NPT ensemble by applying the semi-isotropic Parinello-Rahman barostat<sup>21</sup> and the Nose-Hoover thermostat<sup>22</sup>. The temperature of the systems was kept fixed at 300 K using a relaxation time of 0.2 ps.<sup>23</sup> The applied reference pressure was 1 atmosphere combined with a compressibility of  $4.5 \times 10^{-5} \text{ bar}^{-1}$  and a coupling constant of 1 ps. For the non-bonded interactions, a 1.1 nm cut-off was applied for the van der Waals interactions. The long range electrostatic interactions, on the other hand, were described by the particle mesh Ewald (PME) method,<sup>24</sup> using a 1.1 nm cut-off for the real-space interactions in combination with a 0.15 nm spaced-grid for the reciprocal-space interactions and a fourth-order B-spline interpolation.

All simulation systems (i.e., in total 30, including the native PLB) were optimized using the steepest descent algorithm and then equilibrated for 150 ns in the NPT ensemble. Subsequently, umbrella sampling (US) simulations (see below) were run for 90 ns applying again the NPT ensemble, of which the last 20 ns was used for further analysis.<sup>25</sup> In all simulations a time step of 2 fs was used. All simulations and analyses mentioned in this study were performed using the GROMACS 5.1 package.<sup>26</sup>

### **Umbrella sampling simulation**

As mentioned above, US simulations were performed in order to determine the free energy profiles of PS translocation across the native and peroxidized PLBs. For each energy profile, we extracted 42 windows along the z-axis, which are separated by 0.12 nm. These windows were obtained by pulling one of the oxygen atoms on the head group of PS (see red color in [Figure 3.3.1\(a\)](#) and cf. [Figure 3.3.1\(b\)](#)) along the z-axis for 500 ps, using a harmonic bias between this atom and the center of mass of the PLB, with a force constant of  $1000 \text{ kJ} \cdot \text{mol}^{-1} \cdot \text{nm}^{-2}$  and a pulling rate of  $0.01 \text{ nm} \cdot \text{ps}^{-1}$ . Each window was then equilibrated for 90 ns, and the last 20 ns were used for analysis, i.e., to collect the US histograms. Free energy profiles are constructed using a periodic version of the weighted histogram analysis method (WHAM),<sup>27</sup> as implemented in GROMACS<sup>28</sup>. The final energy profiles were obtained by averaging over six US runs for each system, which differ from one another based on their starting structure, to allow for some statistical variations. Subsequently, the energy barriers with associated standard deviations (see below) were obtained by calculating the difference between energy minimum and maximum in each energy profile and averaging them again over six US simulations. Thus, in total 1260 US simulations were performed for the calculation of the free energy profiles.

### 3.3.3 Results and discussion

[Figure 3.3.2](#) shows an example of the pulling simulation, i.e., the PS transition from the inner leaflet to the outer leaflet under the applied force. It is clear that the transition of PS from one leaflet to the other is accompanied with the formation of a narrow water channel (see [Figure 3.3.2\(b,c\)](#)). This is in agreement with other MD studies,<sup>29-31</sup> where the authors showed the lipid flip-flop motion to occur by means of water channels, i.e., along hydrophilic pores created in the membrane. Analysis of the mechanism of the PS flip-flop motion shows that the translocation of PS begins with changing of the orientation of its hydrophilic head, followed by the rotation of PS, entering into the hydrophobic core of the bilayer, which is beyond its equilibrium position (see [Figure 3.3.2\(b\)](#)). This is accompanied with the formation of spontaneous water defects around the headgroup of PS. Finally, this bidirectional motion of PS ends up with joining the opposite leaflet (see [Figure 3.3.2\(c\)](#)).

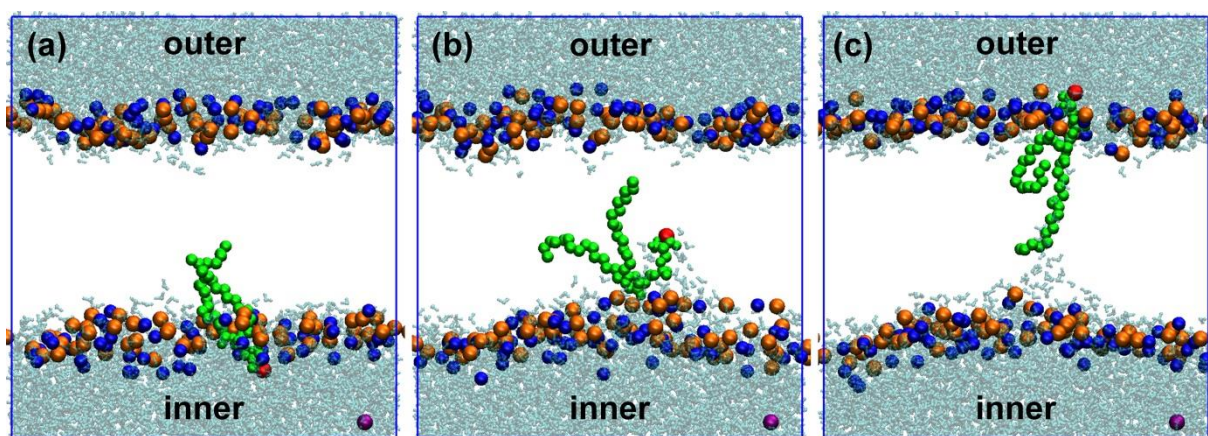


*Figure 3.3.2. Snapshots from MD simulations, illustrating the PS flip-flop motion from the inner leaflet to the outer leaflet of the native PLB in time frames of (a) 0 ps (cf. [Figure 3.3.1\(a\)](#)), (b) 268 ps and (c) 500 ps. The lipid tails of the POPC molecules are removed, to illustrate more clearly the presence of water molecules around PS during its flip-flop motion in (b,c). The color code is the same as in [Figure 3.3.1\(a\)](#). Note that (a), (b) and (c) correspond to the beginning, intermediate and final snapshots of a single pulling simulation.*

The observed trajectory of the PS translocation corresponds to one of the three mechanisms suggested in<sup>13,14</sup>, i.e., to the “rotational flip-flop” mechanism. In summary, the flip-flop motion of PS takes place in the presence of water pores in the PLB. This indicates that the occurrence of spontaneous lipid flip-flop is energetically unfavorable, as also evidenced below. In general, the flip-flop motion of lipids directly depends on the acyl chain length and the structure of the headgroup of the PLB.<sup>32,33</sup> Moreover, the oxidation of lipids in the PLB also plays an essential role in the occurrence of lipid flip-flop motion.<sup>16</sup> This is what we will now study in more detail.

The effect of lipid oxidation on the PS flip-flop motion is depicted in [Figure 3.3.3](#). It illustrates the free energy profiles of PS translocation across a PLB with different peroxidation levels. Note that these profiles are calculated for the PS flip-flop motion from inner to outer leaflet (cf. [Figure 3.3.2](#)). However, our test simulations showed similar profiles

for the flip-flop of PS from outer to inner leaflet, i.e., within the standard deviations (the results are not given). This is probably attributed to the equal concentration of oxidized lipids assumed in both sides of the bilayer in our model. It is clear that, the  $\Delta G$  starts to rise when the PS moves towards the hydrophobic core and reaches its maximum at the center of the membrane. Moreover, the free energy barriers decrease by increasing the oxidation degree (see [Figure 3.3.3](#)). This is also obvious from [Figure 3.3.4\(a\)](#), where the calculated free energy barriers are plotted as a function of the oxidation degree. For the native PLB the calculated free energy barrier is  $93 \pm 4 \text{ kJ}\cdot\text{mol}^{-1}$ , which is within the range of free energy barriers given in literature (i.e.,  $75\text{-}120 \text{ kJ}\cdot\text{mol}^{-1}$ )<sup>16,29,31,34</sup>.

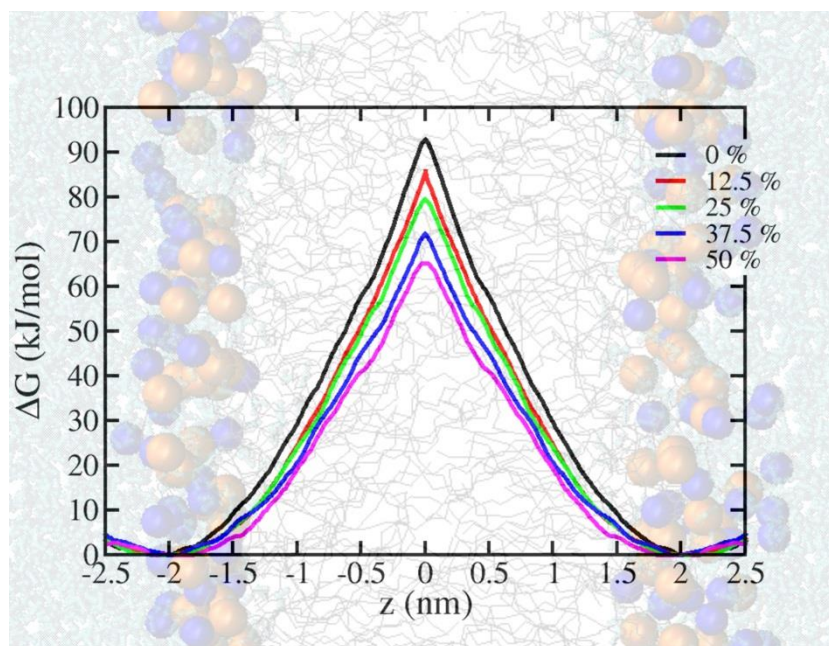


Figure 3.3.3. Symmetrized free energy profiles for the translocation of PS across the PLB with different peroxidation levels.

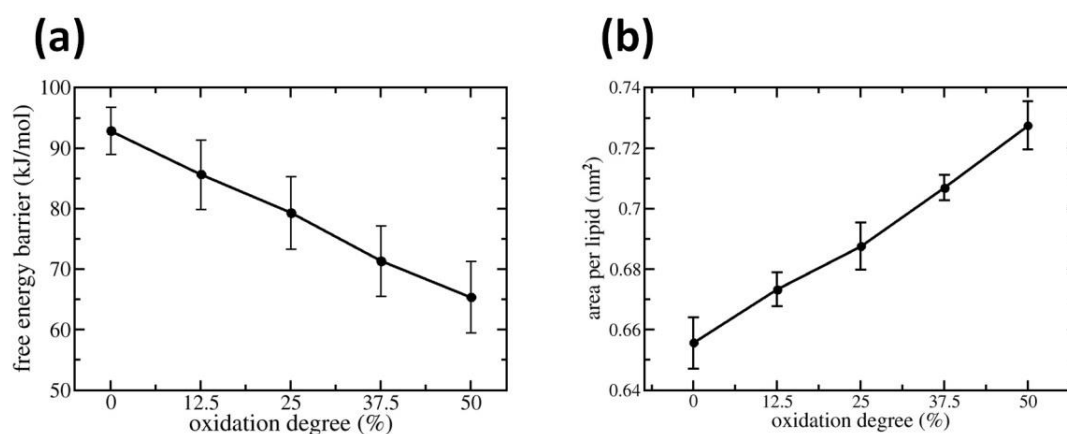


Figure 3.3.4. (a) Free energy barrier for the translocation of PS across a PLB, and (b) average area per lipid, both calculated as a function of the peroxidation degree of the PLB.

It is evident that, the free energy barriers linearly decrease upon increasing the oxidation degree. The energy barrier in the case of a 50% peroxidized PLB is  $65\pm 6 \text{ kJ}\cdot\text{mol}^{-1}$  (see [Figure 3.3.4\(a\)](#)), which means that it drops by  $\sim 30\%$  compared to the native PLB. Moreover, even in low concentration (i.e., 12.5%, which is close to experimental values<sup>35</sup>) a drop of the energy barrier by  $\pm 7 \text{ kJ}\cdot\text{mol}^{-1}$  is observed, which indicates an increase of the flip-flop rate. Thus, we can conclude that the oxidation of the lipids in the PLB facilitates the flip-flop motion of PS by decreasing its free energy barrier. This is also observed in<sup>16</sup>, where the authors showed a drop in free energy barrier when the lipids are oxidized by 20%, although for a different oxidation product. Moreover, fluorescence measurements indicated that the flip-flop time of PS significantly decreases in oxidized POPC liposomes, i.e., from  $>2$  weeks (native) to  $\sim 9$  hours (oxidized).<sup>16</sup> The authors suggested that the creation of transient pore-like defects is induced by lipid oxidation, which in turn facilitates the PS flip-flop motion.<sup>16</sup> Thus, the bidirectional motion of lipids must be a pore mediated process, i.e., it should occur through the water pores in protein free membranes.<sup>16</sup> As is obvious from [Figure 3.3.3](#), the calculated free energy barriers in our US simulations are still too high for PS translocation to occur across the bilayer, which indicates that hydrophilic pores are indeed necessary to enable the flip-flop motion of PS. Similar considerations were made in<sup>31</sup>. It was reported that the calculated free energy barrier required for lipid flip-flop motion (i.e.,  $80 \text{ kJ}\cdot\text{mol}^{-1}$ ) is in good agreement with the energy of pore formation in experiments (i.e.,  $75\text{-}100 \text{ kJ}\cdot\text{mol}^{-1}$ ).<sup>31</sup> In summary, despite the fact that the oxidation of the PLs leads to a reduction of the energy barrier for the translocation of PS, there is still a need for water pores in order to traverse PS from the inner leaflet to the outer leaflet.

The drop in free energy barrier upon oxidation of the PLs can be explained by analyzing the calculated area per lipid in the PLB (see [Figure 3.3.4\(b\)](#)). It can be seen from the figure that the area per lipid increases linearly upon increasing the oxidation level. This is in good agreement with experimental as well as theoretical data.<sup>18,36</sup> Indeed, Itri *et al.* clearly demonstrated by means of giant unilamellar vesicles that fully oxidized lipids lead to an increase of the total surface area of the bilayer by  $\sim 14.5\%$ .<sup>36</sup> This was also shown in<sup>18</sup> applying MD simulations, where a  $\sim 15\%$  increase in area per lipid was observed for a 100% peroxidized POPC membrane.<sup>18</sup> Our test simulations for a 100% peroxidized PLB also showed a 15% increase in area per lipid, which is in line with the above mentioned results.

The main reason for enlargement of the bilayer surface (and thus the area per lipid) is the bending of the polar oxidized groups from the hydrophobic core towards the water interface, as also described in literature<sup>18,37,38</sup>. This increases the chance for deeper penetration of water molecules, i.e., towards the hydrophobic part of the membrane,<sup>39</sup> thereby increasing the permeability of the bilayer. The latter leads to an increase of the probability of pore formation, as well as a decrease of the barrier for PS flip-flop, thereby enhancing the PS translocation rate.<sup>16</sup>

### 3.3.4 Conclusion

We performed US MD simulations, in order to study the PS flip-flop motion in the presence of different concentrations of lipid peroxides in a POPC membrane. We showed an

expansion of the membrane area upon increasing the oxidation level of the lipids, which causes a noticeable change in the membrane permeability, in line with previous modeling results from our group<sup>39</sup> and experimental results from literature<sup>16,40</sup>. As a result, the energy barrier for PS flip-flop across the membrane drops upon increasing peroxidation level, which plays a vital role in apoptosis signaling. Note that PS translocation occurs quite naturally and spontaneously in a timescale of days, but this is far too long to be observed during our MD simulations. However, based on our MD results we can conclude that the drop of free energy barrier upon oxidation of the PLB makes PS flip-flop a “more frequent” event across the PLB.

This study is particularly interesting for plasma medicine, as plasma generates reactive oxygen species and electric fields, both of which can lead to (a) oxidation of the lipids, as well as (b) pore formation (i.e., electroporation) in the cell membrane, thereby increasing the PS flip-flop rate, which eventually results in apoptosis of cancer cells. In general, this study is of interest for applications where reactive oxygen species and strong electric fields both come into play.

### 3.3.5 References

- 1 Graves, D. Reactive species from cold atmospheric plasma: implications for cancer therapy. *Plasma Processes and Polymers* 11, 1120-1127 (2014).
- 2 Bauer, G. Increasing the endogenous NO level causes catalase inactivation and reactivation of intercellular apoptosis signaling specifically in tumor cells. *Redox biology* 6, 353-371 (2015).
- 3 Bauer, G. Nitric Oxide Contributes To Selective Apoptosis Induction In Malignant Cells Through Multiple Reaction Steps. *Critical Reviews in Oncogenesis* 21, 5-6 (2017).
- 4 Yusupov, M., Wende, K., Kupsch, S., Neyts, E., Reuter, S and Bogaerts, A. Effect of head group and lipid tail oxidation in the cell membrane revealed through integrated simulations and experiments. *Scientific Reports* 7, 5761 (2017).
- 5 Ingólfsson, H., Melo, M., Van Eerden, F., Arnarez, C., Lopez, C., Wassenaar, T., Periole, X., De Vries, A., Tieleman, D and Marrink, S. Lipid organization of the plasma membrane. *Journal of the american chemical society* 136, 14554-14559 (2014).
- 6 Reis, A., Domingues, M., Amado, F., Ferrer-Correia, A and Domingues, P. Separation of peroxidation products of diacyl-phosphatidylcholines by reversed-phase liquid chromatography–mass spectrometry. *Biomedical Chromatography* 19, 129-137 (2005).
- 7 Alberts, A., Lewis J., Morgan, D., Raff, M., Roberts, K and Walter, P. Molecular Biology of the Cell. *Garland Science* 6, (2014).
- 8 Van der Paal, J., Neyts, E., Verlackt, C and Bogaerts, A. Effect of lipid peroxidation on membrane permeability of cancer and normal cells subjected to oxidative stress. *Chemical science* 7, 489-498 (2016).
- 9 Martínez, L., Andrade, R., Birgin, E and Martínez, J. M. PACKMOL: a package for building initial configurations for molecular dynamics simulations. *Journal of computational chemistry* 30, 2157-2164 (2009).
- 10 Van Der Spoel, D., Lindahl, E., Hess, B., Groenhof, G., Mark, A and Berendsen, H. GROMACS: fast, flexible, and free. *Journal of computational chemistry* 26, 1701-1718 (2005).
- 11 Chiu, S., Pandit, S., Scott, H and Jakobsson, E. An improved united atom force field for simulation of mixed lipid bilayers. *Journal of Physical Chemistry B* 113, 2748-2763 (2009).
- 12 Cordeiro, R. Reactive oxygen species at phospholipid bilayers: distribution, mobility and permeation. *Biochimica et Biophysica Acta (BBA)-Biomembranes* 1838, 438-444 (2014).
- 13 Cordeiro, R. Reactive oxygen and nitrogen species at phospholipid bilayers: Peroxynitrous acid and its homolysis products. *Journal of Physical Chemistry B* 34, 8211-8219 (2018).
- 14 Torrie, G and Valleau, J. Nonphysical sampling distributions in Monte Carlo free-energy estimation: Umbrella sampling. *Journal of Computational Physics* 23, 187-199 (1977).
- 15 Kästner, J. Umbrella sampling. *Wiley Interdisciplinary Reviews: Computational Molecular Science* 1, 932-942 (2011).

- 16 Kumar, S., Rosenberg, J. M., Bouzida, D., Swendsen, R and Kollman, P. The weighted histogram analysis method for free-energy calculations on biomolecules. I. The method. *Journal of computational chemistry* 13, 1011-1021 (1992).
- 17 Yusupov, M., Van der Paal, J., Neyts, E and Bogaerts, A. Synergistic effect of electric field and lipid oxidation on the permeability of cell membranes. *Biochimica et Biophysica Acta (BBA)-General Subjects* 1861, 839-847 (2017).
- 18 Möller, M., Li, Q., Lancaster, J and Denicola, A. Acceleration of nitric oxide autoxidation and nitrosation by membranes. *IUBMB life* 59, 243-248 (2007).
- 19 Subczynski, W., Lomnicka, M and Hyde, J. Permeability of nitric oxide through lipid bilayer membranes. *Free radical research* 24, 343-349 (1996).
- 20 Yusupov, M., Yan, D., Cordeiro, R and Bogaerts, A. Atomic scale simulation of H<sub>2</sub>O<sub>2</sub> permeation through aquaporin: toward the understanding of plasma cancer treatment. *Journal of Physics D: Applied Physics* 51, 125401 (2018).
- 21 Möller, M., Lancaster Jr, J and Denicola, A. The interaction of reactive oxygen and nitrogen species with membranes. *Current Topics in Membranes* 61, 23-42 (2008).
- 22 Denicola, A., Souza, J., Radi, R and Lissi, E. Nitric oxide diffusion in membranes determined by fluorescence quenching. *Archives of biochemistry and biophysics* 328, 208-212 (1996).
- 23 Signorelli, S., Möller, M., Coitiño, E and Denicola, A. Nitrogen dioxide solubility and permeation in lipid membranes. *Archives of biochemistry and biophysics* 512, 190-196 (2011).
- 24 Subczynski, W., Hopwood, L and Hyde, J. Is the mammalian cell plasma membrane a barrier to oxygen transport? *Journal of general physiology* 100, 69-87 (1992).
- 25 Subczynski, W., Hyde, J and Kusumi, A. Oxygen permeability of phosphatidylcholine--cholesterol membranes. *Proceedings of the National Academy of Sciences* 86, 4474-4478 (1989).
- 26 Widomska, J., Raguz, M and Subczynski, W. Oxygen permeability of the lipid bilayer membrane made of calf lens lipids. *Biochimica et Biophysica Acta (BBA)-Biomembranes* 1768, 2635-2645 (2007).
- 27 Van der Paal, J., Verheyen, C., Neyts, E and Bogaerts, A. Hampering effect of cholesterol on the permeation of reactive oxygen species through phospholipids bilayer: possible explanation for plasma cancer selectivity. *Scientific reports* 7, 39526 (2017).
- 28 Haynes, W. M. *CRC handbook of chemistry and physics*. (CRC press, 2014).
- 29 Frisch, M., Trucks, G., Schlegel, H., Scuseria, G., Robb, M., Cheeseman, J., Scalmani, G., Barone, V., Mennucci, B., Petersson, G and Nakatsuji, H. Gaussian 09, *Gaussian Inc., Wallingford CT* (2009).
- 30 Victor, B., Baptista, A and Soares, C. Dioxygen and nitric oxide pathways and affinity to the catalytic site of rubredoxin: oxygen oxidoreductase from *Desulfovibrio gigas*. *Journal of Biological Inorganic Chemistry* 14, 853-862 (2009).
- 31 Young, C. L. *Oxides of nitrogen*. IUPAC Solubility Data Series edn, Vol. 8 (Pergamon Press, 1981).
- 32 Wilhelm, E., Battino, R and Wilcock, R. Low-pressure solubility of gases in liquid water. *Chemical reviews* 77, 219-262 (1977).



# Chapter 4.

## Effect of oxidation on the structure of proteins

In this chapter, we present the results of the effect of plasma oxidation on fiber-like (section [4.1](#)), globular (section [4.2](#)) and signaling proteins (sections [4.3](#) and [4.4](#)), obtained by docking and MD simulations.

The presented data in this chapter is based on the articles published in:

Razzokov, J., Yusupov, M. and Bogaerts, A. 2019. Oxidation destabilizes toxic amyloid beta peptide aggregation. *Sci Rep.* (in press)

De Backer J, Razzokov J, Hammerschmid D, Mensch C, Hafideddine Z, Kumar N, van Raemdonck G, Yusupov M, Van Doorslaer S, Johannessen C, Sobott F, Bogaerts A, Dewilde S. 2018. The effect of reactive oxygen and nitrogen species on the structure of cytoglobin: A potential tumor suppressor. *Redox Biol.* 19, 1-10.

Yusupov, M, Lackmann, J.W, Razzokov, J, Kumar, S, Stapelmann, K. and Bogaerts, A. 2018. Impact of plasma oxidation on structural features of human epidermal growth factor. *Plasma Process. Polym.* 15(8), p.1800022.



## 4.1 Oxidation destabilizes toxic amyloid beta peptide aggregation

### 4.4.1 Introduction

The aggregation of insoluble amyloid beta (A $\beta$ ) peptides in the brain is known to trigger the onset of neurodegenerative diseases, such as Alzheimer's disease. In spite of the massive number of investigations, the underlying mechanisms to destabilize the A $\beta$  aggregates are still poorly understood. Some studies indicate the importance of oxidation to destabilize the A $\beta$  aggregates. In particular, oxidation induced by CAP has demonstrated promising results in eliminating these toxic aggregates.

In this section, we present the results of MD simulations performed to study the effect of oxidized residues on the stability of A $\beta$  aggregates, taking A $\beta$  pentamer as a model system. We applied again the US method<sup>1,2</sup> to estimate the interaction between the monomers of the A $\beta$  aggregate.<sup>3-5</sup> As in our previous studies,<sup>6,7</sup> we consider different oxidation states (i.e., 3% , 9% and 15 %), by modifying various amino acids (AAs) according to their reported reactivity.<sup>8</sup> We also calculate the potential mean forces to determine the dissociation free energy of one of the monomers of the A $\beta$  structure upon increasing oxidation degree. The aim of this study is to reveal the mechanism of A $\beta$  fibril destabilization at the molecular level, upon increasing oxidative stress.

### 4.1.2 Computational details

#### Simulation setup

We performed MD simulations in order to elucidate the stability of native and oxidized A $\beta$  pentamer at the molecular level. The simulations were again carried out using the GROMACS<sup>9</sup> program package (version 5.1), applying the GROMOS 45a3 force field.<sup>10</sup> We employed the solid-state NMR structure of A $\beta_{11-42}$  pentamer (see [Figure 4.1.1](#)) obtained from the Protein Data Bank (ID: 2MXU).<sup>11</sup> In this structure 10 residues in the N-terminal do not maintain a stable conformation and therefore are not relevant to further aggregation. The N and C terminal ends of each peptide are acetylated and capped with an amide group, respectively.

The native structure of A $\beta$  pentamer (i.e., A $\beta_{11-42}$  pentamer, see [Figure 4.1.1\(a\)](#)) was placed in a triclinic box, spacing the atoms at least 1.1 nm from the boundaries of the simulation box. Subsequently, the box was filled with an SPC water model<sup>12</sup> surrounding the A $\beta$  pentamer structure and 0.1 M of NaCl was added to the system to mimic the physiological environment. Besides the native A $\beta$  pentamer, we created three oxidized structures, called OX1, OX2 and OX3, which contain 3, 9 and 15% of oxidized residues, respectively. These oxidized systems were prepared using a web server Viena-PTM 2.0<sup>13</sup> by replacing the residues of the native A $\beta$  pentamer with oxidized ones. The force field parameters of the oxidized residues were obtained from<sup>14</sup>. These oxidized systems were also placed in a simulation box filled with water, applying the above mentioned steps.

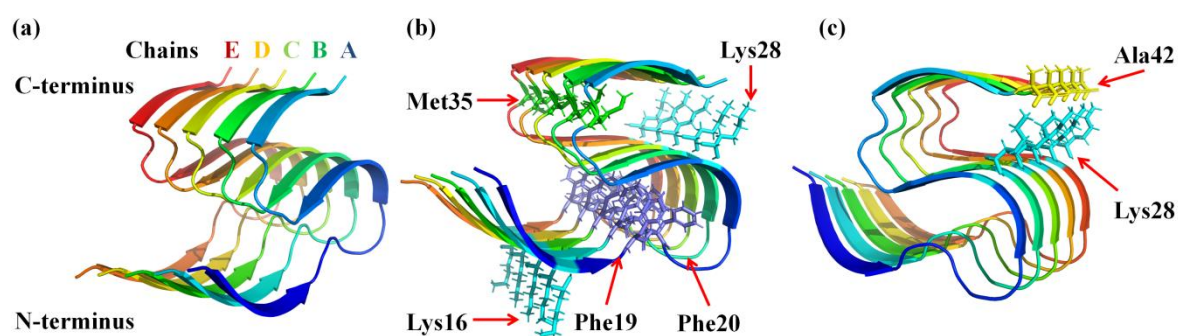


Figure 4.1.1. Cartoon view of the  $A\beta_{11-42}$  pentamer structure. (a) Each chain of the  $A\beta_{11-42}$  pentamer structure with C- and N-terminal ends is depicted with a different color. (b) AA residues of the  $A\beta$  pentamer structure that are modified to create the oxidized structures; oxidation of these AAs occurs in each of the chains (thus five Met35, five Phe19 and Phe20, five Lys16 and Lys28 residues are depicted in licorice view). (c) AAs of the  $A\beta_{11-42}$  pentamer structure (i.e., Lys28 (cyan) and Ala42 (yellow)) that form a salt bridge in each chain.

The four different model systems (i.e., native, OX1, OX2 and OX3) were energy minimized with the steepest descent algorithm. Subsequently, a 50 ps equilibration run was performed employing the NVT ensemble (i.e., a system with constant number of particles N, volume V and temperature T), applying the position restraint to the heavy atoms of  $A\beta$  pentamer. Next, a 250 ns production run was conducted using the NPT ensemble (i.e., a system with constant number of particles N, pressure P and temperature T) in the absence of a restraint. The simulations were carried out at 310 K and 1 bar, employing the Nose-Hoover thermostat<sup>15</sup> with a coupling constant of 0.5 ps and the isotropic Parrinello-Rahman barostat<sup>16</sup> with a compressibility and coupling constant of  $4.5 \times 10^{-5} \text{ bar}^{-1}$  and 2 ps, respectively. A 1.0 nm cut-off distance was applied for the van der Waals interactions. The long range electrostatic interactions were described by the particle mesh Ewald (PME) method.<sup>17</sup> The production run trajectory was used for data collection, i.e., to calculate the root mean square deviation (RMSD),<sup>18</sup> the solvent accessible surface area (SASA)<sup>19</sup> and the side chain hydrogen bonds between the neighboring peptides. For the computation of the secondary structural changes of  $A\beta$  pentamer, we used the secondary structure assignment program STRIDE<sup>20</sup>, by averaging the data of the MD trajectory acquired from the last 50 ns. The pymol visualizing tool was used to prepare images in this study.<sup>21</sup>

### Umbrella sampling

The starting structure of  $A\beta$  pentamer in our US simulations was extracted from the final frame of the production run. The  $A\beta$  pentamer structure was placed in a rectangular box and the size of the box was chosen adequately for pulling the monomer out of the  $A\beta$  pentamer structure along the z-axis. After salination of the system with 0.1 M of NaCl, the system was equilibrated implementing the above mentioned steps (see previous section). Subsequently, applying an external force, the center of mass (COM) of chain A (see [Figure 4.1.1\(a\)](#)) was pulled along the z-axis and chain B was restrained and used as a reference for the pulling simulation. The external force induces displacement of the peptide (chain A in our case) in the simulated system and it allows to calculate the energy in a path dependent manner, i.e., along

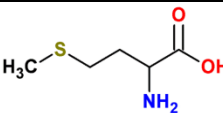
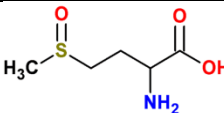
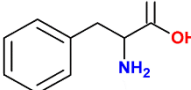
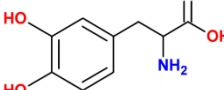
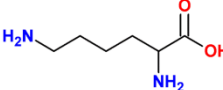
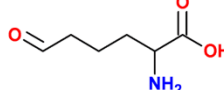
the reaction coordinate. The pulling simulation lasted for 500 ps, applying 1000 kJ/(mol\*nm<sup>2</sup>) spring constant with a pulling rate of 0.01 nm/ps. We extracted 50 windows, calculating the distance between the COM of chain A and B, each separated by 0.1 nm along the z-axis. Each umbrella window was then equilibrated for 100 ps, followed by 20 ns of the US simulations. The output files generated from the US simulations were analyzed employing the weighted histogram analysis method (WHAM)<sup>22</sup> to calculate the potential mean force (PMF). The error associated with the PMF was estimated employing the bootstrapping method.<sup>23</sup>

### Selection of AAs for the creation of the oxidized structures

Takai *et al.* have determined the chemical modification of AAs by treating them individually with CAP and they reported the following order for the reactivity of the AAs (in order of decreasing reactivity): Met → Cys → Trp → Phe → Tyr → the rest of the AAs.<sup>8</sup> Based on these results, and because the native Aβ pentamer structure does not contain Cys, Trp and Tyr, we decided to modify Met35, Phe19, Phe20, Lys16 and Lys28 of each chain in the Aβ pentamer. Lysine residues were chosen because one of these residues, particularly Lys28, is involved in the formation of the Lys28-Ala42 salt bridge (see [Figure 4.1.1\(c\)](#)), and we want to study the influence of the disruption of this bridge on the stability of Aβ pentamer, through oxidation of Lys28.

Specifically, we changed Met35 to methionine sulfoxide, Phe19 and Phe20 to 3,4-dihydroxyphenylalanine and Lys16 and Lys28 to allysine (see [Table 4.1.1](#)). In this way, we created three different oxidation degrees of Aβ pentamer, assumed to happen upon oxidation by CAP, i.e., OX1, OX2 and OX3, as given in [Table 4.1.1](#).

*Table 4.1.1. Modified AAs to create the oxidized Aβ pentamer structures. The choice of the specific AAs for modification is based on the results of<sup>8</sup>.*

Oxidation	Modified AAs in Aβ	Native AA	Oxidized AA	Oxidation percentage (%)
OX1	Met35			3
OX2	OX1 + Phe19, Phe20			9
OX3	OX2 + Lys16, Lys28			15

### 4.1.3 Results and discussion

[Figure 4.1.2](#) illustrates the time evolution of the root mean square deviation (RMSD) of the backbone of the native and oxidized Aβ pentamer structures.

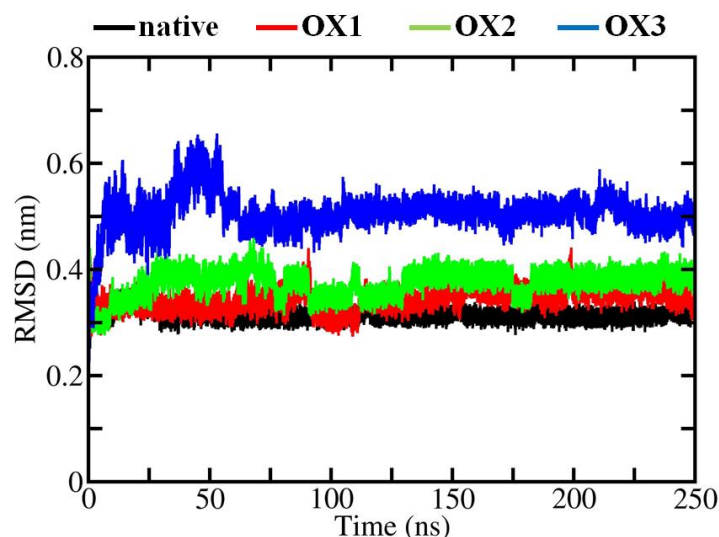


Figure 4.1.2. RMSD of the backbone of the native, OX1, OX2 and OX3 A $\beta$  pentamer structures.

The RMSD of the native A $\beta$  pentamer structure is the most stable with the lowest fluctuations. In the case of OX1, the RMSD fluctuations slightly increase. Oxidation of the Met35 residue leads to small destabilization in the structure (cf. also [Figure 4.1.3](#) below). A further increase of the oxidation level leads to even higher fluctuations in the RMSD (see OX2 and OX3 in [Figure 4.1.2](#)). The calculated average value of the RMSD increases upon increasing oxidation (see section 4.1.5. Appendix; [Table A1](#)). This indicates that the oxidized structures become more flexible, affecting their conformations. However, the salt bridge Lys28-Ala42 (see [Figure 4.1.1\(c\)](#)) in the native, OX1 and OX2 structures maintains its integrity in the A $\beta$  pentamer (see [Figure 4.1.3](#)), whereas in OX3, the mobility of the C-terminal in each chain increases after oxidation of Lys28, leading to a disruption of the salt bridge interaction. This in turn results in a higher solvent accessibility and conformational changes in the system (cf. the results given in section 4.1.5. Appendix; [Tables A1](#) and [A2](#)). Indeed, the SASA analysis confirms that the overall solvent accessibility rises upon increasing oxidation of the A $\beta$  pentamer structure (see [Table A1](#)).

To support our RMSD and SASA results, we performed secondary structure analysis to obtain detailed information on the conformational changes. The main conformation of the native structure consists of  $\beta$ -sheets, i.e., 73.3% ([Table 4.1.2](#)). The content of these  $\beta$ -sheets reduces in the OX3 structure, turning them into other conformations, e.g., to coil structures (see [Table 4.1.2](#)). The fraction of  $\beta$ -sheet conformation in OX3 decreases by 9.3% compared to the native structure, which is most likely due to the absence of the salt bridge. In OX1 and OX2 we observed the increased  $\beta$ -sheet content. Nevertheless, the flexibility and SASA of these structures are still higher than in the native case, whereas the hydrogen bonds between the chains are lower (see [Table A1](#) in section 4.1.5. Appendix). Thus, these results overall indicate that despite the increase of the  $\beta$ -sheet content, oxidation in general leads to complex conformational changes, thereby resulting in a destabilization of the A $\beta$  pentamer.

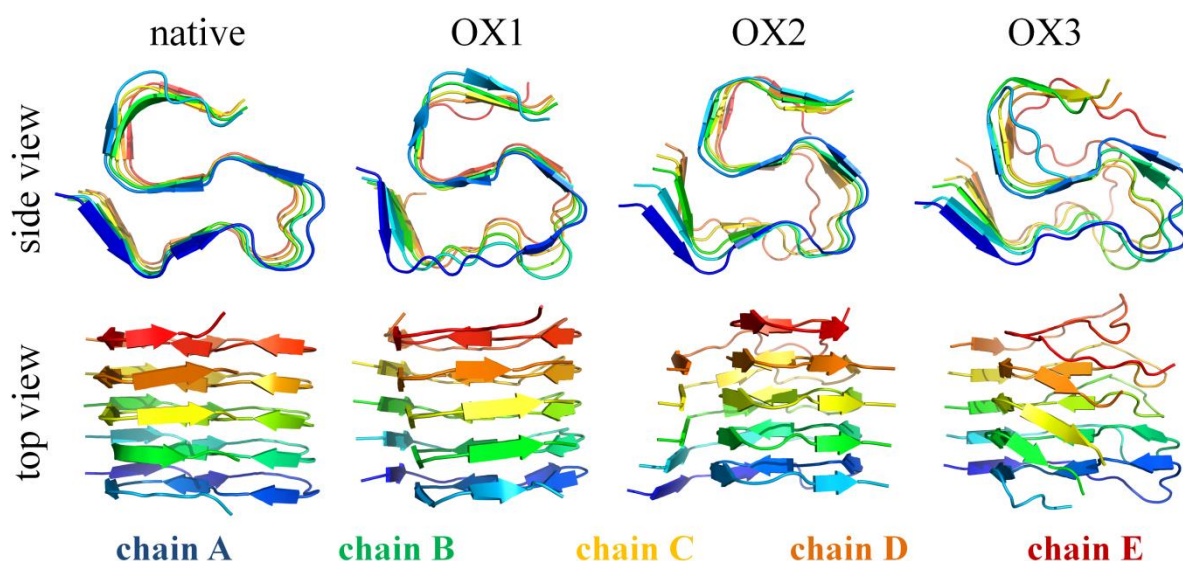


Figure 4.1.3. Last snapshots of the 250 ns MD simulations, showing the structures of native A $\beta$  pentamer, OX1, OX2 and OX3, both in side and top view, to illustrate the conformational changes of the native and oxidized A $\beta$  pentamer structures.

Note that the hydrogen bonds between the chains are one of the factors that strengthen the inter-peptide interactions. Hence, a decrease in the number of hydrogen bonds results in weakening of the binding energy between the chains of A $\beta$  pentamer.

Table 4.1.2. Secondary structure analysis of the native and oxidized A $\beta$  pentamer structures. The values denote the relative occurrence (in %) of the various conformations.

System	$\beta$ -sheet	$\beta$ -bridge	Turn	Coil	$\alpha$ -, 3- and 5-helix
native	73.3	2.1	9.7	14.9	0
OX1 (3%)	80.0	0.8	7.3	11.9	0
OX2 (9%)	74.7	0.8	8.7	15.8	0
OX3 (15%)	64.0	1.2	12.6	22.2	0

In order to quantitatively estimate the interactions between the chains of the native and oxidized structures, we performed US simulations to determine the dissociation free energies of the terminal peptides (i.e., energy between chain A and B). The dissociation free energy profiles help us to draw conclusions about the stability of the A $\beta$  pentamer structures. [Figure 4.1.4](#) illustrates the PMF profile of the terminal chain A pulled against chain B. The difference between the minimum and maximum values of the PMF gives us the dissociation (or binding) free energy.

It is clear from [Figure 4.1.4](#) that the terminal chain A of the native A $\beta$  pentamer totally disintegrates at 3.1 nm distance, whereas in the oxidized structures it can dissociate even at shorter distances, i.e., 2.40, 2.27 and 2.61 nm in the cases of OX1, OX2 and OX3, respectively. This indicates that the interaction between chain A and B weakens upon increasing oxidation, and at the same time, the PMF values also decrease. The calculated dissociation free energies are found to be -248.93, -235.39, -181.05 and -178.17 kJ/mol for

native, OX1, OX2 and OX3, respectively (see [Table 4.1.3](#)). Hence, a higher oxidation level leads to a lower binding free energy, which is most pronounced in the case of OX3. The small difference in binding free energy between the OX2 and OX3 system (i.e., 2.88 kJ/mol) is probably due to the twist of the OX3 structure (see [Figure 4.1.3](#)), which leads to a formation of extra hydrogen bonds between chains A and C, although their relative occurrence is quite low (see [Table A3](#) in section [4.1.5](#). Appendix).

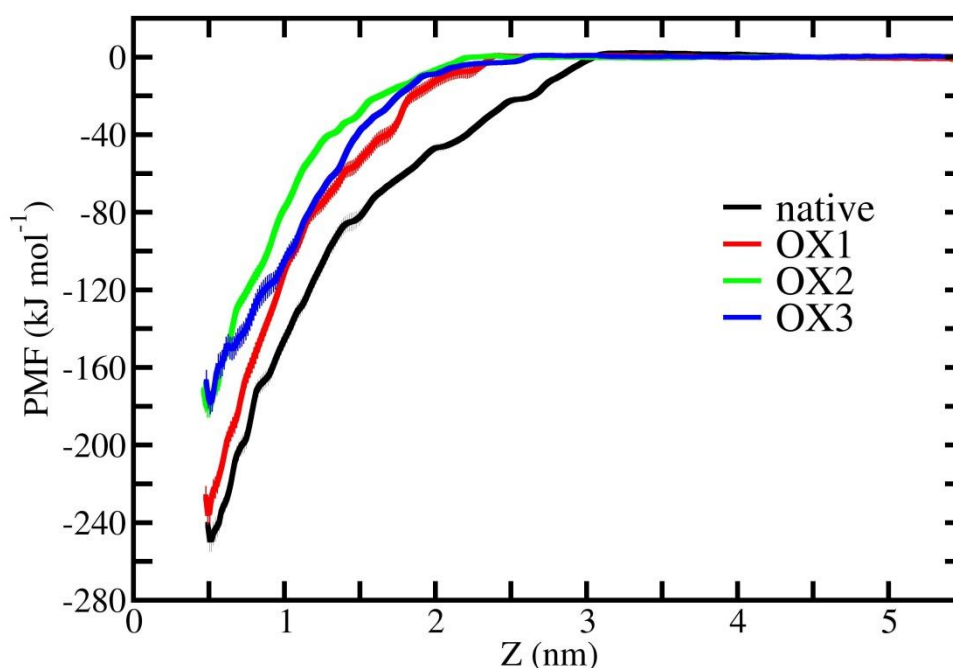


Figure 4.1.4. PMF profiles of the native and oxidized  $A\beta$  pentamer structures. The errors associated with sampling are presented in pale color.

Thus, we can conclude that oxidation of  $A\beta$  pentamer leads to a higher flexibility and more conformational changes in the structure, thereby increasing the solvent accessibility. This is more obvious in the case of OX3 due to the disruption of the salt bridge interaction. Moreover, oxidation results in a decrease of the inter-peptide binding free energy, eventually destabilizing the amyloid beta aggregation process.

Table 4.1.3. Binding free energies  $\Delta G$  for native and oxidized  $A\beta$  pentamer structures.  $\Delta\Delta G$  represents the loss of energy compared to the native case.

System/	$\Delta G$ (kJ/mol)	$\Delta\Delta G$ (kJ/mol)
native	- 248.93	-
OX1 (3%)	- 235.39	+ 13.54
OX2 (9%)	- 181.05	+ 67.88
OX3 (15%)	- 178.17	+ 70.76

Bayliss and co-workers showed that 2 s of treatment with CAP already significantly reduces the amyloid aggregates.<sup>24</sup> They also investigated the effect of heat (80°C) and gas flow (without discharge) and the combination of both, and found that these physical treatments have little impact on the morphology of the amyloid aggregates. Instead, the chemical effects caused by CAP-generated ROS were found to play a vital role in degradation of the amyloid aggregates.<sup>24</sup> Our simulation results are in qualitative agreement with this experimental observation, and they can explain the underlying mechanisms. Indeed, we find that (CAP-induced) oxidation of A $\beta$  pentamer leads to a lower inter-peptide binding free energy, eventually resulting in degradation of the amyloid aggregates. We also checked the effect of heat (80°C) on the flexibility, the solvent accessibility, the conformation and the binding free energy between chains A and B of the A $\beta$  pentamer (see [Tables A1](#) and [A2](#) and [Figure A2](#) in section 4.1.5. Appendix). In general, we can conclude that this high temperature does not strongly influence the binding free energy, despite the elevated fluctuations and conformational changes observed in the system. The calculated binding free energy is found to be -239.4 kJ/mol (see [Figure A2](#)), which is quite close to the value of OX1 (cf. [Table 4.1.3](#)). Thus, we can conclude that the salt bridge plays an essential role in the stability of the A $\beta$  pentamer, and disruption of this interaction (through e.g., oxidation by CAP, or ROS created in another way) leads to destabilization, resulting eventually in degradation of the amyloid aggregates. It has to be mentioned that in reality, chemical reactions between (CAP-generated) ROS and amyloid aggregates take place, resulting in oxidation of the AAs or even breakage of the peptide bonds.<sup>24</sup> This can lead to even higher damages in the amyloid aggregates. Chemical reactions cannot be studied by our non-reactive MD simulations, but our US simulations help to gain valuable information about the consequences of oxidation in the A $\beta$  pentamer stability.

#### 4.1.4 Conclusion

We studied the effect of oxidation on the stability of A $\beta$  pentamer, employing MD and US simulations. The results unambiguously demonstrate that a low and moderate degree of oxidation (OX1 and OX2) have insignificant impact on the conformation and stability, whereas a higher oxidation degree (OX3), i.e., leading to disruption of the salt bridge, yields a considerable disturbance of the structure. This is a hallmark for the possible inhibition of A $\beta$  pentamer aggregation. In this regard, the salt bridge plays a key role in the integrity and stability of the A $\beta$  pentamer structure.

Our results are in qualitative agreement with experiments where a CAP source was used to eliminate amyloid aggregates, and they can explain the underlying mechanisms. Indeed, CAP-generated reactive oxygen species (ROS) cause oxidation in the amyloid aggregates through chemical modifications (i.e., not through physical effects like heat and gas flow), ultimately leading to degradation of the aggregates.

Thus, CAP-induced oxidation could be beneficial to eliminate toxic amyloid beta aggregates that cause several diseases, including AD. Based on these considerations, we suggest to examine the effects of CAP (or plasma-treated liquids<sup>25</sup>) on these diseases by means of *in vivo* experiments. In addition, the computational investigations would also be

useful to study more complex conformations of highly neurotoxic amyloid fibrils given in literature<sup>26-29</sup>.

## 4.1.5 Appendix

### MD simulations

We performed MD simulations for 250 ns after energy minimization and subsequent equilibration simulations. The last 50 ns trajectory was used to analyze the average values of the backbone root mean square deviation (RMSD), the solvent accessible surface area (SASA) and the hydrogen bonds between neighboring chains ([Table A1](#)), as well as the secondary structure ([Table A2](#)) and the relative occurrence of hydrogen bonds between the chains A and C in OX3 system ([Table A3](#)).

*Table A1. Average RMSD of the backbone (nm), SASA (nm<sup>2</sup>) and number of hydrogen bonds between the chains, with associated standard deviations, for the native and three oxidized A $\beta$  pentamer structures, as well as the native structure after heat treatment.*

Systems	RMSD	SASA	h-bonds
native	0.31±0.01	73.55±1.17	31.09±2.42
OX1 (3%)	0.36±0.01	74.63±1.33	27.32±2.28
OX2 (9%)	0.39±0.02	75.79±1.31	26.64±2.42
OX3 (15%)	0.52±0.03	76.89±1.29	23.70±2.35
native 80 °C	0.47±0.16	77.30±1.41	25.12±2.63

*Table A2. Secondary structure analysis for the native and three oxidized A $\beta$  pentamer structures, as well as the native structure after heat treatment.*

Systems	$\beta$ -sheet	$\beta$ -bridge	Turn	coil	$\alpha$ -, 3- and 5-helix
native	73.3	2.1	9.7	14.9	0
OX1 (3%)	80.0	0.8	7.3	11.9	0
OX2 (9%)	74.7	0.8	8.7	15.8	0
OX3 (15%)	64.0	1.2	12.6	22.2	0
native 80 °C	70.0	2.0	10.0	18.0	0

*Table A3. Hydrogen bonds formed between chains A and C in the OX3 system. Data is collected from the analysis of 10,000 frames of the last 50 ns.*

Number of h-bonds	Relative occurrence (%)
0	99.35
1	0.61
2	0.04

To support our RMSD results, we performed a principle component analysis (PCA) for the native and oxidized A $\beta$  pentamer structures, where we studied the collective motion of the alpha carbons by plotting the projection of the first eigenvector (representing the direction of the highest motion) versus the projection of the second eigenvector (representing the second

highest motion). In other words, the PCA results show the total phase space that each A $\beta$  pentamer structure is able to occupy. The PCA results are presented in [Figure A1](#). In general, we can conclude that the oxidation leads to an increase of the total phase space occupied by the structure, thereby resulting in an increased flexibility.

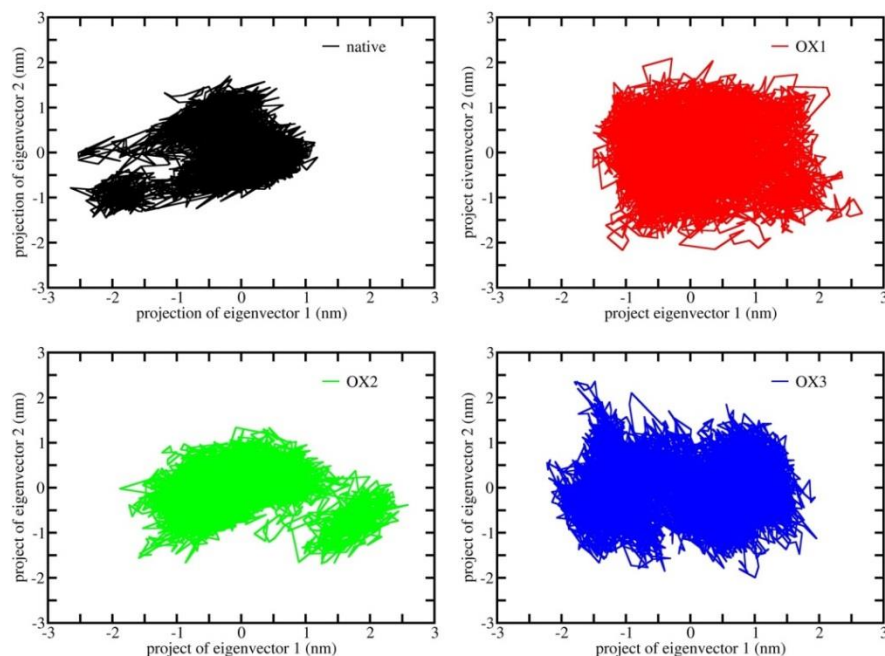


Figure A1. PCA results obtained for the native and oxidized A $\beta$  pentamer structures, collecting the data from the last 50 ns of MD simulations.

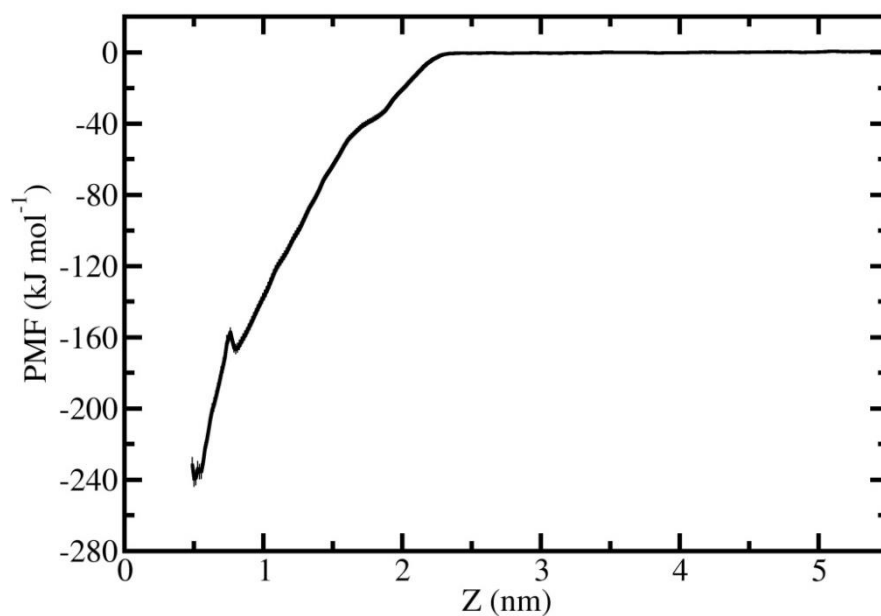


Figure A2. PMF profile of the native A $\beta$  pentamer structure at 80°C.

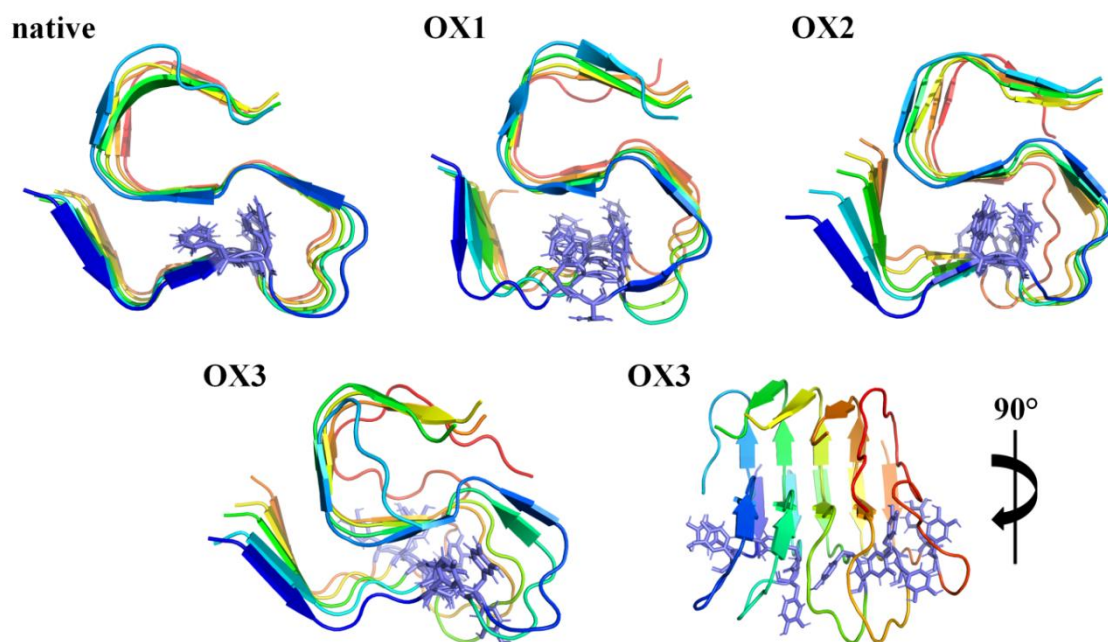


Figure A3. Arrangement of Phe19 and Ph20 in the hydrophobic core of the native, OX1, OX2 and OX3 system.

## 4.1.6 References

- 1 Kästner, J. Umbrella sampling. *Wiley Interdisciplinary Reviews: Computational Molecular Science* 1, 932-942 (2011).
- 2 Souaille, M and Roux, B. Extension to the weighted histogram analysis method: combining umbrella sampling with free energy calculations. *Computer physics communications* 135, 40-57 (2001).
- 3 Lemkul, J and Bevan, D. Assessing the stability of Alzheimer's amyloid protofibrils using molecular dynamics. *Journal of Physical Chemistry B* 114, 1652-1660 (2010).
- 4 Schwierz, N., Frost, C., Geissler, P and Zacharias, M. From A $\beta$  Filament to Fibril: Molecular Mechanism of Surface-Activated Secondary Nucleation from All-Atom MD Simulations. *Journal of Physical Chemistry B* 121, 671-682 (2017).
- 5 Schwierz, N., Frost, C., Geissler, P and Zacharias, M. Dynamics of seeded A $\beta$ 40-fibril growth from atomistic molecular dynamics simulations: Kinetic trapping and reduced water mobility in the locking step. *Journal of the American Chemical Society* 138, 527-539 (2016).
- 6 De Backer, J., Razzokov, J., Hammerschmid, D., Mensch, C., Hafideddine, Z., Kumar, N., van Raemdonck, G., Yusupov, M., Van Doorslaer, S., Johannessen, C., Sobott, F., Bogaerts, A., and Dwilte, S. The effect of reactive oxygen and nitrogen species on the structure of cytoglobin: A potential tumor suppressor. *Redox Biology* 19, 1-10, (2018).
- 7 Yusupov, M., Lackmann, J.W., Razzokov, J., Kumar, S., Stapelmann, K. and Bogaerts, A. Impact of plasma oxidation on structural features of human epidermal growth factor. *Plasma Processes and Polymers* 8, 1800022 (2018):.
- 8 Takai, E., Kitamura, T., Kuwabara, J., Ikawa, S., Yoshizawa, S., Shiraki, K., Kawasaki, H., Arakawa, R and Kitano, K. Chemical modification of amino acids by atmospheric-pressure cold plasma in aqueous solution. *Journal of Physics D: Applied Physics* 47, 285403 (2014).
- 9 Van Der Spoel, D., Lindahl, E., Hess, B., Groenhof, G., Mark, A and Berendsen, H. GROMACS: fast, flexible, and free. *Journal of computational chemistry* 26, 1701-1718 (2005).
- 10 Schuler, L. D., Daura, X and Van Gunsteren, W. An improved GROMOS96 force field for aliphatic hydrocarbons in the condensed phase. *Journal of Computational Chemistry* 22, 1205-1218 (2001).
- 11 Xiao, Y., Ma, B., McElheny, D., Parthasarathy, S., Long, F., Hoshi, M., Nussinov, R. and Ishii, Y. A $\beta$  (1-42) fibril structure illuminates self-recognition and replication of amyloid in Alzheimer's disease. *Nature structural & molecular biology* 22, 499 (2015).
- 12 Berendsen, H., Postma, J., van Gunsteren, W and Hermans, J. *Intermolecular forces* 331-342 (Springer, 1981).
- 13 Margreitter, C., Petrov, D and Zagrovic, B. Vienna-PTM web server: a toolkit for MD simulations of protein post-translational modifications. *Nucleic acids research* 41, W422-W426 (2013).
- 14 Petrov, D., Margreitter, C., Grandits, M., Oostenbrink, C and Zagrovic, B. A systematic framework for molecular dynamics simulations of protein post-translational modifications. *PLoS computational biology* 9, e1003154 (2013).

- 15 Hoover, W. Canonical dynamics: equilibrium phase-space distributions. *Physical review A* 31, 1695 (1985).
- 16 Parrinello, M and Rahman, A. Polymorphic transitions in single crystals: A new molecular dynamics method. *Journal of Applied physics* 52, 7182-7190 (1981).
- 17 Essmann, U., Perera, L., Berkowitz, M., Darden, T., Lee, H and Pedersen, L. A smooth particle mesh Ewald method. *The Journal of chemical physics* 103, 8577-8593 (1995).
- 18 Maiorov, V and Crippen, G. Size-independent comparison of protein three-dimensional structures. *Proteins: Structure, Function, and Bioinformatics* 22, 273-283 (1995).
- 19 Eisenhaber, F., Lijnzaad, P., Argos, P., Sander, C and Scharf, M. The double cubic lattice method: efficient approaches to numerical integration of surface area and volume and to dot surface contouring of molecular assemblies. *Journal of Computational Chemistry* 16, 273-284 (1995).
- 20 Frishman, D and Argos, P. Knowledge-based protein secondary structure assignment. *Proteins: Structure, Function, and Bioinformatics* 23, 566-579 (1995).
- 21 DeLano, W. The PyMOL molecular graphics system. <http://pymol.org> (2002).
- 22 Kumar, S., Rosenberg, J. M., Bouzida, D., Swendsen, R and Kollman, P. The weighted histogram analysis method for free-energy calculations on biomolecules. I. The method. *Journal of computational chemistry* 13, 1011-1021 (1992).
- 23 Hub, J and de Groot, B. Does CO<sub>2</sub> permeate through aquaporin-1? *Biophysical Journal* 91, 842-848 (2006).
- 24 Bayliss, D., Walsh, J. L., Shama, G., Iza, F and Kong, M. Reduction and degradation of amyloid aggregates by a pulsed radio-frequency cold atmospheric plasma jet. *New Journal of Physics* 11, 115024 (2009).
- 25 Van Boxem, W., Van der Paal, J., Gorbaney, Y., Vanuytsel, S., Smits, E., Dewilde, S and Bogaerts, A. Anti-cancer capacity of plasma-treated PBS: effect of chemical composition on cancer cell cytotoxicity. *Scientific reports*, 1, 16478 (2017)
- 26 Wälti, M.A., Ravotti, F., Arai, H., Glabe, C.G., Wall, J., Böckmann, A., Güntert, P., Meier, B and Riek, R. Atomic-resolution structure of a disease-relevant A $\beta$  (1–42) amyloid fibril. *Proceedings of the National Academy of Sciences* 34, E4976-E4984 (2016)
- 27 Gremer, L., Schölzel, D., Schenk, C., Reinartz, E., Labahn, J., Ravelli, R., Tusche, M., Lopez-Iglesias, C., Hoyer, W., Heise, H and Willbold, D. Fibril structure of amyloid- $\beta$  (1–42) by cryo-electron microscopy. *Science* 6359, 116-119 (2017)
- 28 Colvin, M., Silvers, R., Ni, Q., Can, T., Sergeev, I., Rosay, M., Donovan, K., Michael, B., Wall, J., Linse, S and Griffin, R. Atomic resolution structure of monomeric A $\beta$ 42 amyloid fibrils. *Journal of the American Chemical Society* 30, 9663-9674 (2016)
- 29 Schütz, A., Vagt, T., Huber, M., Ovchinnikova, O., Cadalbert, R., Wall, J., Güntert, P., Böckmann, A., Glockshuber, R. and Meier, B. Atomic-resolution three-dimensional structure of amyloid  $\beta$  fibrils bearing the Osaka mutation. *Angewandte Chemie International Edition* 1, 331-335 (2015)



## 4.2 The effect of RONS on the structure of cytoglobin: A potential tumor suppressor

### 4.2.1 Introduction

As the major regulators of the redox balance in the cell, proteins, and specifically redox-sensitive proteins, are interesting to investigate, mainly through oxidative modification of redox-sensitive cysteine residues.<sup>1</sup> Cytoglobin (Cygb) is one of these proteins that exhibit several functions, including oxygen transport, NO-dioxygenase activity, ROS scavenger and tumor suppression.<sup>2-4</sup> Some of these suggested features are still not fully understood, but in general CYGB is able to defend the cell from oxidative stress. This indicates that CYGB is a redox-sensitive protein type. It was suggested that the sensitivity of CYGB might occur via heme-coordination and/or formation of inter/intramolecular disulfide bridges between cysteine residues (Cys38 and Cys83).<sup>5,6</sup> In this respect, CAP treatment helps to investigate the CYGB behaviour by means of CAP-generated RONS, to test and further classification of the proposed models. Most importantly, it might elucidate the role of CYGB in cell protection against oxidative stress. De Backer *et al.* experimentally studied recombinant CYGB, upon treatment for 30 s, 1, 3, 5 and 10 min by CAP.<sup>7</sup> The structural modifications of CYGB were identified by electronic circular dichroism (CD), UV–Vis spectroscopy, and resonance Raman spectroscopy. Mass spectrometry (MS) was also performed, considering the native and denatured states of the protein. It was shown that CAP induced modification of amino acids of CYGB during the treatment (see [Table 4.2.1](#)). There was no treatment-time-dependent increase in the number of oxidized amino acids. This indicates that oxidation may occur rapidly. Besides, it was found that the longer time treatment caused nitration of the heme group. Furthermore, plasma treatment of Cygb resulted in the formation of intermolecular disulfide bridges between cysteine residues (Cys38 and Cys83) and potentially also intramolecular disulfide bridges.

Table 4.2.1 *Oxidative modifications of CYGB. The table is adopted from* <sup>7</sup>.

tris-buffer							
Amino Acid	# AA in sequence	Control	30s	1min	3min	5min	10min
Methionine (M)	6	2	3	4	4	3	4
Tyrosine (Y)	5	2	3	3	2	3	2
Tryptophan (W)	3		1	2	2	2	2
Phenylalanine (F)	8	1	1	1	1	1	1
Aspartic acid (D)	5			1	2	2	1
Asparagine (N)	5		3	3	1	2	
Proline (P)	13			1			3
Histidine (H)	6		1	1	1		1
TOTAL	51	5	12	16	13	13	14

To support these experiments, we applied MD and docking simulations, to investigate the effect of the intermolecular disulfide bond on the structural conformation of Cygb.

## 4.2.2 Computational details

### Simulation setup

We performed molecular dynamics (MD) and docking simulations in order to elucidate the functionality of native and oxidized (modified) Cygb at the molecular level. The simulations were again carried out using the GROMACS<sup>8</sup> program package (version 5.1), applying the GROMOS 45a3 force field<sup>9</sup>. The coordinate file (with the initial configuration) of Cygb was obtained from the Protein Data Bank (PDB ID: 1V5H).<sup>10</sup> The native structure of Cygb<sub>SH-SH</sub> was placed in a dodecahedron box, with size chosen in such a way that there was initially 1.0 nm buffer distance between the protein and the boundary of the simulation box. This was done in order to avoid long distance interactions (i.e. Coulomb and van der Waals interactions) between Cygb<sub>SH-SH</sub> and its periodic images. The box was then filled with water molecules surrounding the Cygb<sub>SH-SH</sub> molecule, employing the SPC water model<sup>11</sup>, and sodium counter ions were added to neutralize the system. Periodic boundary conditions were applied in all directions.

The experimental investigations given above indicate that CAP treatment of Cygb<sub>SH-SH</sub> leads to the formation of a disulfide bond in between the cysteine amino acids (i.e., Cys38 and Cys83), i.e., Cygb<sub>S-S</sub>. In order to study the effect of this bond on the conformation of Cygb, we manually created this disulfide linkage using Avogadro software.<sup>12</sup> Subsequently, we applied energy minimization to optimize the modified structure, using the steepest descent algorithm. The length of the disulfide bond after the energy minimization is 2.05 Å, which exactly corresponds to the disulfide bond length given in literature<sup>13,14</sup>. We repeated the above-mentioned MD procedure (i.e., the creation of the box and addition of water molecules, as well as counter ions) to create the simulation system with modified Cygb<sub>S-S</sub>.

Thus, we used two model systems, i.e., native Cygb<sub>SH-SH</sub> and modified Cygb<sub>S-S</sub> covered with water as a starting structure for the calculations. The systems were minimized in three steps, by applying three optimization algorithms, i.e., steepest descent, conjugate gradient and low-memory Broyden-Fletcher-Goldfarb-Shanno (L-BFGS).<sup>15</sup> Subsequently, a 500 ps equilibration run was performed employing the NVT ensemble (i.e., a system with constant number of particles N, volume V and temperature T). Next, a 150 ns production run was performed using NPT dynamics (i.e., a system with constant number of particles N, pressure P and temperature T). The NPT simulations were carried out at 300 K and 1 bar pressure, employing the velocity-rescaling thermostat with a coupling constant of 0.1 ps and the isotropic Parrinello-Rahman barostat,<sup>16,17</sup> with a compressibility and coupling constant of  $4.5 \times 10^{-5} \text{ bar}^{-1}$  and 2 ps, respectively. A 1.4 nm cut-off distance was applied for the van der Waals interactions. The long range electrostatic interactions were described by the particle mesh Ewald (PME) method,<sup>18</sup> using again 1.4 nm cut-off for the real-space interactions in combination with a 0.15 nm spaced-grid for the reciprocal-space interactions.

## Docking simulations.

In the docking simulations, binding hot spots of equilibrated native Cygb<sub>SH-SH</sub> and modified Cygb<sub>S-S</sub> were predicted using the FTMap family of the web server.<sup>19</sup> The detailed information about FTMap algorithm is given in [Chapter 2](#) (section [2.4](#)). We made use of VMD,<sup>20</sup> and Pymol<sup>21</sup> visualizing tools for preparation of the images.

### 4.2.3 Results and discussion

Figure 4.2.1 illustrates the last snapshots of the equilibrated native Cygb<sub>SH-SH</sub> and modified Cygb<sub>S-S</sub> molecules (depicted in yellow and green, respectively). The E helix of Cygb is located at the distal side of the heme group, while the F helix is positioned at the proximal side. The disulfide linkage in Cygb<sub>S-S</sub> clearly influences its conformation and hence, the positions of the E and F helices are shifted relative to native Cygb<sub>SH-SH</sub> (cf. the yellow and green dashed lines). In order to calculate the distances between the helices, we choose residues Ala82 and Ala88 in the F helix and Ala107 and Ala112 in the E helix. These amino acids are positioned at the end of the black dashed lines, but they are not shown in the figure for the sake of clarity. The calculated distances between these amino acids located in the E and F helices are also given in [Table 4.2.2](#), indicating the minor change in the modified Cygb<sub>S-S</sub>. It is also obvious from [Figure 4.2.1](#) that there is a negligible shift of the heme group in the modified Cygb<sub>S-S</sub> molecule compared to native Cygb<sub>SH-SH</sub>. Hence, the formation of the disulfide bridge between the cysteine residues does not alter the local orientation of the heme group and imidazole planes of the histidines (i.e., His81, His113) bound to the heme: the imidazole planes do not rotate versus each other. This was also reported in literature by experimental investigations.<sup>22</sup> For further analysis of the structural changes in both native and modified Cygb, we extracted the frames from the MD trajectories. The analysis of the consecutive MD frames indicated that the His117 residue located nearby the heme group (see [Figure 4.2.2](#)) substantially changes its position in modified Cygb<sub>S-S</sub>. Indeed, the calculated distance between the heme iron and one of the nitrogen atoms of His117 (located in the imidazole ring) is almost doubled in modified Cygb<sub>S-S</sub> (see [Table. 4.2.2](#)), which is due to the conformational change caused by the disulfide bond. To get more insight into the consequences of this disulfide bond formation, we investigated the binding hot spots of both native Cygb<sub>SH-SH</sub> and modified Cygb<sub>S-S</sub>.

*Table 4.2.2. Distance between amino acids located in the F and E helices as well as between the N atom of His117 and the Fe atom of the heme group of the Cygb (cf. Figure 4.2.1).*

amino acids	Cygb <sub>SH-SH</sub> (Å)	Cygb <sub>S-S</sub> (Å)
Ala88-Ala107	9.07±0.04	9.77±0.04
Ala82-Ala112	10.47±0.04	10.82 ±0.04
His117 <sub>NE2</sub> -Heme <sub>Fe</sub>	6.63±1.30	13.48±0.09

We extracted ten Cygb structures with 1 ns time interval using the last 10 ns trajectory of the equilibrated (so-called production) run. These structures were employed to examine the structural dependencies of the binding hot spots of Cygb. Here we present only one of the results out of ten, as the other nine results were very similar. We obtained three different

binding pockets (with lowest binding energies) in both native Cygb<sub>SH-SH</sub> and modified Cygb<sub>S-S</sub>. One of these binding pockets is depicted in [Figure 4.2.2](#) as meshed region. We do not show the other two meshed regions, as we are focusing on the catalytic site of Cygb (i.e., the heme group).

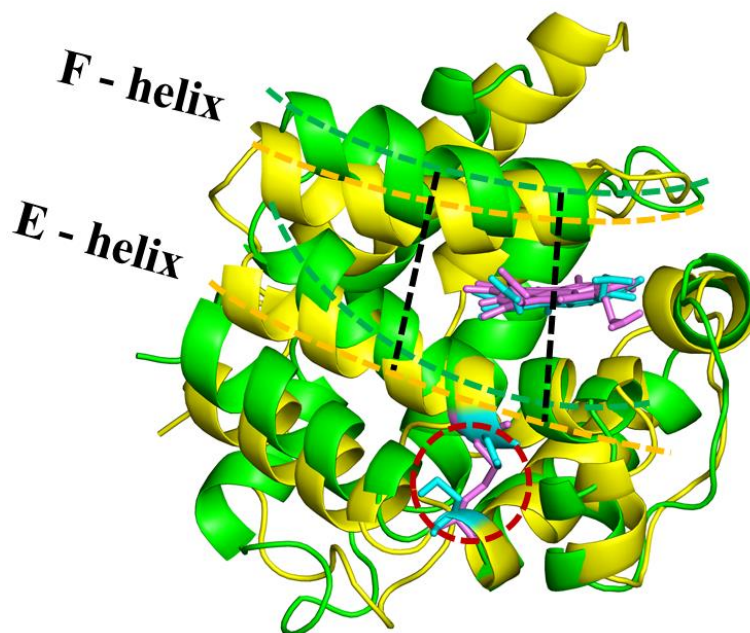


Figure 4.2.1. Aligned structures of CYGB<sub>SH-SH</sub> (yellow) and CYGB<sub>S-S</sub> (green). The distances between Ala<sub>88</sub>-Ala<sub>107</sub> and Ala<sub>82</sub>-Ala<sub>112</sub> are depicted by black dashed lines. The yellow and green dashed lines are plotted to indicate shifted positions of the E- and F-helices. The heme group and cysteine residues of both CYGB<sub>SH-SH</sub> and CYGB<sub>S-S</sub> are presented in licorice view in blue and pink, respectively. The disulfide (S-S) bridge is shown within the red dashed circle.

As mentioned above, the formation of a disulfide bond between the cysteine residues leads to a change of the Cygb conformation, and this results in a doubling of the distance between the highly localized His177 residue and the heme group in modified Cygb<sub>S-S</sub> (see [Table 4.2.2](#) and cf. [Figure 4.2.2](#) (a) and (c) or [Figure 4.2.2](#) (b) and (d)). Accordingly, this results in the heme group to become more accessible to the probing molecules (see overlap between heme group and meshed regions in [Figure 4.2.2](#) (c) and (d)). Our binding hot spot analysis indeed showed that in the case of modified Cygb<sub>S-S</sub> the binding pocket is located around the heme group, whereas in the native case it is found with limited access to the heme group, i.e., around the helices (cf. [Figure 4.2.2](#) (a) and (c), or [Figure 4.2.2](#) (b) and (d)). This again confirms that in native Cygb<sub>SH-SH</sub> the access to the heme group is more limited than in modified Cygb<sub>S-S</sub>. Besides, we found that the His117 residue plays a vital role in either limiting or increasing access to the heme group, performing like a gate function for Cygb<sub>SH-SH</sub> and Cygb<sub>S-S</sub>. Hence, the formation of disulfide bonds in Cygb increases the binding affinity (through involvement of the heme group), which is in line with our experimental observations.<sup>7</sup> Thus, our MD simulation results and the binding hot spot analysis give more insight into the experimental observations by De Backer et al., at the molecular scale.

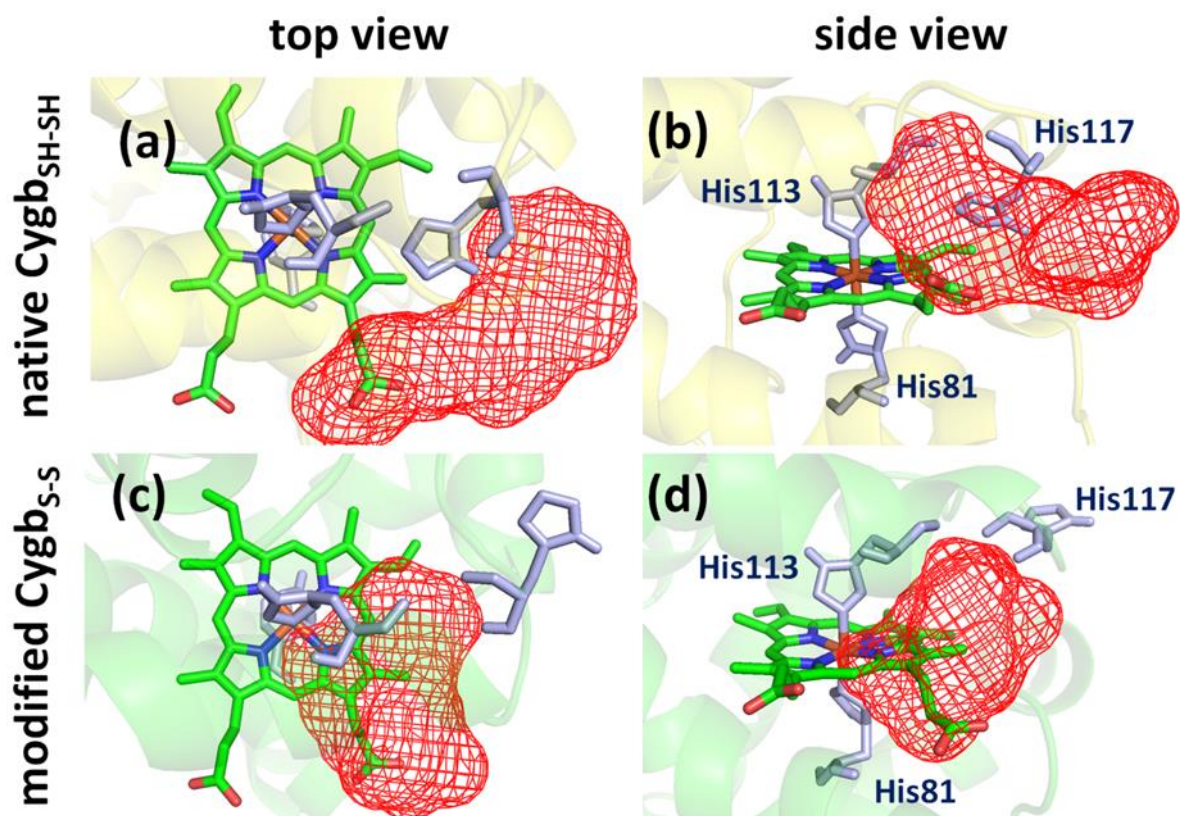


Figure 4.2.2. Binding hot spot of native  $Cygb_{SH-SH}$  (a-b) and modified (c-d)  $Cygb_{S-S}$  presented as red meshed regions. The helices in the structures are represented in pale colors, for the sake of clarity. The heme group and the histidine residues (81, 113, 117) are shown in green and light purple colors and licorice views, respectively. It is clear that in native  $Cygb_{SH-SH}$  the access to the heme group is more limited than in modified  $Cygb_{S-S}$ .

#### 4.2.4 Conclusion

In general, we can conclude that the disulfide bond formation affects the  $Cygb$  structure, thereby opening the access to the heme group through the gate functioning of His117, which in turn leads to a higher binding affinity. In addition, the modification of  $Cygb_{S-S}$  should lead to intense peroxidation as well as a higher scavenger activity of  $Cygb_{S-S}$ .

## 4.2.5 References

- 1 Barford, D. The role of cysteine residues as redox-sensitive regulatory switches. *Current opinion in structural biology* 14, 679-686 (2004).
- 2 Gardner, A., Cook, M and Gardner, P. Nitric oxide dioxygenase function of human cytoglobin with cellular reductants and in rat hepatocytes. *Journal of Biological Chemistry* 110, 132340 (2010).
- 3 Fordel, E., Thijs, L., Moens, L and Dewilde, S. Neuroglobin and cytoglobin expression in mice: evidence for a correlation with reactive oxygen species scavenging. *FEBS journal* 274, 1312-1317 (2007).
- 4 Shivapurkar, N., Stastny, V., Okumura, N., Girard, L., Xie, Y., Prinsen, C., Thunnissen, F.B., Wistuba, I.I., Czerniak, B., Frenkel, E and Roth, J. Cytoglobin, the newest member of the globin family, functions as a tumor suppressor gene. *Cancer Research* 68, 7448-7456 (2008).
- 5 Tsujino, H., Yamashita, T., Nose, A., Kukino, K., Sawai, H., Shiro, Y and Uno, T.. Disulfide bonds regulate binding of exogenous ligand to human cytoglobin. *Journal of inorganic biochemistry* 135, 20-27 (2014).
- 6 Zhou, D., Hemann, C., Boslett, J., Luo, A., Zweier, J and Liu, X. Oxygen binding and nitric oxide dioxygenase activity of cytoglobin are altered to different extents by cysteine modification. *FEBS open bio* 7, 845-853 (2017).
- 7 De Backer, J., J., Razzokov, J., Hammerschmid, D., Mensch, C., Hafideddine, Z., Kumar, N., van Raemdonck, G., Yusupov, M., Van Doorslaer, S., Johannessen, C., Sobott, F., Bogaerts, A., and Dwilide, S. The effect of reactive oxygen and nitrogen species on the structure of cytoglobin: A potential tumor suppressor. *Redox Biology* 19, 1-10, (2018).
- 8 Van Der Spoel, D., Lindahl, E., Hess, B., Groenhof, G., Mark, A and Berendsen, H. GROMACS: fast, flexible, and free. *Journal of computational chemistry* 26, 1701-1718 (2005).
- 9 Schuler, L. D., Daura, X and Van Gunsteren, W. An improved GROMOS96 force field for aliphatic hydrocarbons in the condensed phase. *Journal of Computational Chemistry* 22, 1205-1218 (2001).
- 10 Sugimoto, H., Makino, M., Sawai, H., Kawada, N., Yoshizato, K and Shiro, Y. Structural basis of human cytoglobin for ligand binding. *Journal of molecular biology* 339, 873-885 (2004).
- 11 Berendsen, H. J., Postma, J. P., van Gunsteren, W and Hermans, J. *Intermolecular forces* 331-342 (Springer, 1981).
- 12 Hanwell, M., Curtis, D., Lonie, D., Vandermeersch, T., Zurek, E and Hutchison, G. Avogadro: an advanced semantic chemical editor, visualization, and analysis platform. *Journal of cheminformatics* 4, 17 (2012).
- 13 Katti, S., LeMaster, D and Eklund, H. Crystal structure of thioredoxin from *Escherichia coli* at 1.68 Å resolution. *Journal of molecular biology* 212, 167-184 (1990).
- 14 Wiita, A., Ainavarapu, S., Huang, H and Fernandez, J. Force-dependent chemical kinetics of disulfide bond reduction observed with single-molecule techniques. *Proceedings of the National Academy of Sciences* 103, 7222-7227 (2006).

- 15 Shanno, D. Conditioning of quasi-Newton methods for function minimization. *Mathematics of computation* 24, 647-656 (1970).
- 16 Bussi, G., Donadio, D and Parrinello, M. Canonical sampling through velocity rescaling. *The Journal of chemical physics* 126, 014101 (2007).
- 17 Parrinello, M and Rahman, A. Polymorphic transitions in single crystals: A new molecular dynamics method. *Journal of Applied physics* 52, 7182-7190 (1981).
- 18 Essmann, U., Perera, L., Berkowitz, M., Darden, T., Lee, H and Pedersen, L. A smooth particle mesh Ewald method. *Journal of chemical physics* 103, 8577-8593 (1995).
- 19 Kozakov, D., Grove, L.E., Hall, D., Bohnuud, T., Mottarella, S., Luo, L., Xia, B., Beglov, D and Vajda, S. The FTMap family of web servers for determining and characterizing ligand-binding hot spots of proteins. *Nature protocols* 10, 733-755 (2015).
- 20 Humphrey, W., Dalke, A and Schulten, K. VMD: visual molecular dynamics. *Journal of molecular graphics* 14, 33-38 (1996).
- 21 DeLano, W. The PyMOL molecular graphics system. <http://pymol.org> (2002).
- 22 Vinck, E., Van Doorslaer, S., Dewilde, S and Moens, L. Structural change of the heme pocket due to disulfide bridge formation is significantly larger for neuroglobin than for cytoglobin. *Journal of the American Chemical Society* 126, 4516-4517 (2004).



## 4.3 Impact of plasma oxidation on structural features of human epidermal growth factor

### 4.3.1 Introduction

The epidermal growth factor receptor (EGFR) is known to be involved in several cancer types,<sup>1</sup> because an overproduction or overstimulation of EGFR has a severe impact on the cell cycle by inducing proliferation, survival and differentiation.<sup>2</sup> Furthermore, a variant of EGFR in humans is described as a favorable marker for breast cancer diagnosis.<sup>3</sup> Besides EGFR, its ligand EGF is also investigated concerning its role in various cancer types.<sup>4</sup> EGF is a small 53 amino acid (AA) protein, which binds to EGFR thanks to its specific structure.<sup>2</sup> While EGF does not seem to have cancer-inducing capabilities, it triggers chemotaxis, mitogenesis, motogenesis and cytoprotection, allowing the promotion of cancer growth.<sup>5</sup> However, exactly these triggers are highly beneficial in wound healing, making EGF the typical double-edged sword in cancer treatment.<sup>6</sup>

EGF is probably present both during the application of plasma to wounds as well as during cancer treatment. Investigating the impact of plasma treatment on EGF is therefore of great interest to improve our understanding how plasma interacts with several components of the human body, relevant for both wound healing and cancer treatment. Indeed, it is well known that CAP treatment can have a strong impact on proteins by over-oxidizing disulfide bonds, structure denaturing, as well as introducing modifications at various amino acids (AAs).<sup>7-9</sup>

In the present chapter, we present the results of non-reactive MD simulations carried out to investigate the effect of oxidation on the human EGF (hEGF) protein. As treatment times vary significantly between wound healing and cancer inactivation, we considered a range of different oxidation degrees, mimicking both short and long treatment times, to cover both the application of wound healing and cancer treatment. To support the performed simulations, we used the results of Fourier transform infrared (FTIR) spectroscopy, carried out at University of Bochum by Dr J. Lackmann and Dr K. Stapelmann. Using the theoretical analysis of the solvent accessible surface area (SASA) and data from literature,<sup>9</sup> we created the oxidized hEGF proteins through modification of specific AAs. The effect of these modifications on the protein was then investigated applying MD simulations. As only the modifications affecting the binding efficacy of hEGF to EGFR are important for signal transduction, we focused on the overall structure. To complement the protein structure analysis, circular dichroism (CD) spectroscopy was performed by Dr J. Lackmann at University of Bochum on the treated hEGF, again to support the simulations by analyzing if any structural changes occurred in the hEGF structure. Finally, docking simulations and free energy calculations were performed between hEGF and the EGFR domain to obtain insight in their binding affinity.

### 4.3.2 Computational details

As mentioned above, hEGF is a small protein consisting of 53 AA residues with three disulfide bonds formed between the cysteine residues (see [Figure A1](#) in section [4.3.5](#). Appendix). The crystal structure of this protein is available in the Protein Data Bank (PDB

ID: 2KV4,<sup>10</sup> sequence available from UniProtKB #Q6QBS2\_HUMAN<sup>11</sup>). As a model system in our simulations we used the hEGF protein surrounded with water. After equilibration of this model system at 300 K in the NPT ensemble for 300 ns, we applied oxidation to the system through modification of the AA residues. In this study we employed three model systems for oxidized hEGFs, which are called OX1, OX2 and OX3. Since the creation of these oxidized structures was based on our modeling and, in part, experimental results (see below), we assumed that the oxidation degrees used in our simulations for OX1, OX2 and OX3 can be broadly correlated to treatment times of various length. These model systems were also equilibrated at 300 K using an NPT ensemble for 800 ns. Details about the equilibration of the native and oxidized hEGFs with water layer surrounding them, are given in section [4.3.5](#). Appendix.

All MD simulations were again carried out using the GROMACS 5.1 package,<sup>12-14</sup> applying the GROMOS54A7 force field<sup>15</sup>. In the case of the oxidized hEGFs, i.e., with the modified AAs, we used the parameters of the GROMOS force field obtained from<sup>16,17</sup>. The last 30 ns of the equilibration was used for analysis of the results. Specifically, we calculated the solvent accessible surface area (SASA) of each AA residue in the native hEGF, to find out the highly exposed AAs to the solvent (see section [4.3.5](#). Appendix for more details). These AAs are then used to create the oxidized hEGF structures (see details in section [4.3.4](#)). We also carried out principle component analysis (PCA) to examine the structural modifications. For computation of the secondary structure of the proteins, we used the secondary structure assignment program STRIDE,<sup>18</sup> by averaging the data obtained from 100 snapshots of the MD trajectory taken at every 300 ps from the last 30 ns. To compare how much the oxidized hEGFs were structurally altered from the native one, we performed alignment of these structures using the final snapshots of the MD simulations, applying VMD visualizing tool.<sup>19</sup> Finally, we calculated the root mean square deviations (RMSDs) of the alpha carbons of the native and oxidized hEGFs, to determine the flexibility of these structures.

As mentioned above, to mimic the different CAP treatment times, we modified the native hEGF to create various oxidized states (which we call OX1, OX2 and OX3), using the results of the SASA analysis, in combination with the chemical reactivity and modification of the AAs, given in<sup>9</sup>. In addition, FTIR analysis was used by Dr. J. Lackmann and Dr. K. Stapelmann, to provide a general idea if the chosen modifications are valid. Detailed information about the hEGF modification procedure is given in section [4.3.4](#). [Table 4.3.1](#) summarizes the applied modifications of the AAs in the oxidized structures.

Using the AAs listed in [Table 4.3.1](#), we modified 23, 38 and 53% of the (53) AAs of the native hEGF to create the oxidized hEGF structures. These oxidation degrees were chosen based on data obtained with the plasma source as described in<sup>7</sup>, as explained in detail in section [4.3.4](#).

We also performed docking simulations using the Z-DOCK v2.3 program<sup>20,21</sup> to estimate the binding affinities between native and oxidized hEGF proteins with the hEGF receptor (hEGFR, PDB ID: 1IVO<sup>22</sup>). Additionally, we applied the molecular mechanics generalized Born surface area (MM/GBSA) method<sup>23</sup> to calculate binding free energies of native and

oxidized hEGF proteins with the hEGFR. Details of the docking simulations and free energy calculations are given in Appendix.

Table 4.3.1. AAs involved in the creation of various oxidized states of the hEGF protein. The chemical structures of these (un)modified AAs are given in Table A1 of the Appendix.

AA in native hEGF	modified AA in oxidized hEGF
methionine (MET)	methionine sulfoxide
cysteine (CYS)	cysteic acid
tryptophan (TRP)	6-hydroxytryptophan
tyrosine (TYR)	3,4-dihydroxyphenylalanine
histidine (HYS)	2-oxo-histidine
proline (PRO)	pyroglutamic acid
lysine (LYS)	allysine
glutamine (GLN)	4-hydroxyglutamine
valine (VAL)	3-hydroxyvaline
leucine (LEU)	4-hydroxyleucine

### 4.3.3 Results and discussion

As mentioned in previous section, we used the results of SASA and the chemical reactivity and modification of AAs deduced from <sup>9</sup> for modification of specific AAs (see below) in order to create the oxidized hEGF structures (OX1, OX2 and OX3). To support the performed simulations, hEGF protein was treated for three different treatment times from short (45 s) over long (300 s) to very long (600 s). While no direct correlation between the simulated oxidation states and treatment times is possible, we tried to approximate low, high, and even higher modified states as applied in our simulations. To this aim, we chose a treatment time used for clinical application (45 s), as well as two treatment times known to induce high levels of modifications in proteins, as shown in <sup>7</sup>.

Takai *et al.* studied the chemical modifications of AAs, as well as their reactivity, by individually treating them with CAP for 5 and 10 min.<sup>9</sup> Based on high-resolution mass spectrometry, they observed chemical modifications of 14 AAs (among the 20 naturally occurring AAs) after plasma treatment. Moreover, they found that some AAs, i.e., MET and CYS, have higher chemical reactivity than other AAs. Although the experimental conditions of our study and the study of Takai *et al.* are somewhat different, we assume that we can still deduce the chemical reactivity and oxidation products of AAs obtained in <sup>9</sup>, since both CAP sources generate a cocktail of RONS, which results in both cases in the oxidation of AAs. In our model system we have 18 types of AAs (see [Figure. 4.3.1](#) below). Based on the results of Takai *et al.* <sup>9</sup>, we excluded asparagine (ASN), serine (SER), aspartic acid (ASP), glycine (GLY) and alanine (ALA) from the oxidation, and we used the following order for the reactivity of the other AAs in our modifications (in order of decreasing reactivity): MET → CYS → TRP → TYR → HIS → the rest of the AAs. We also excluded glutamic acid (GLU), isoleucine (ILE) and arginine (ARG) from the modifications, as we either did not have the GROMOS force field parameters <sup>16,17</sup> for these modifications or the available parameters did not correspond to the modifications obtained in <sup>9</sup> for these AAs. Hence, we modified 10 types

of AAs (or in total 28 AAs) of the native hEGF, which contain newly formed C-OH, S=O or C=O bonds (see [Table A1](#) in the Appendix).

The native hEGF contains more than one type of the same AAs (*e.g.*, CYS<sub>6</sub>, CYS<sub>14</sub>, CYS<sub>20</sub>, etc., see [Figure 4.3.1](#)) and the selection of the initial AAs for modification depends on the SASA results. The results of the SASA analysis for each AA residue of the native hEGF are given in [Figure 4.3.1](#).

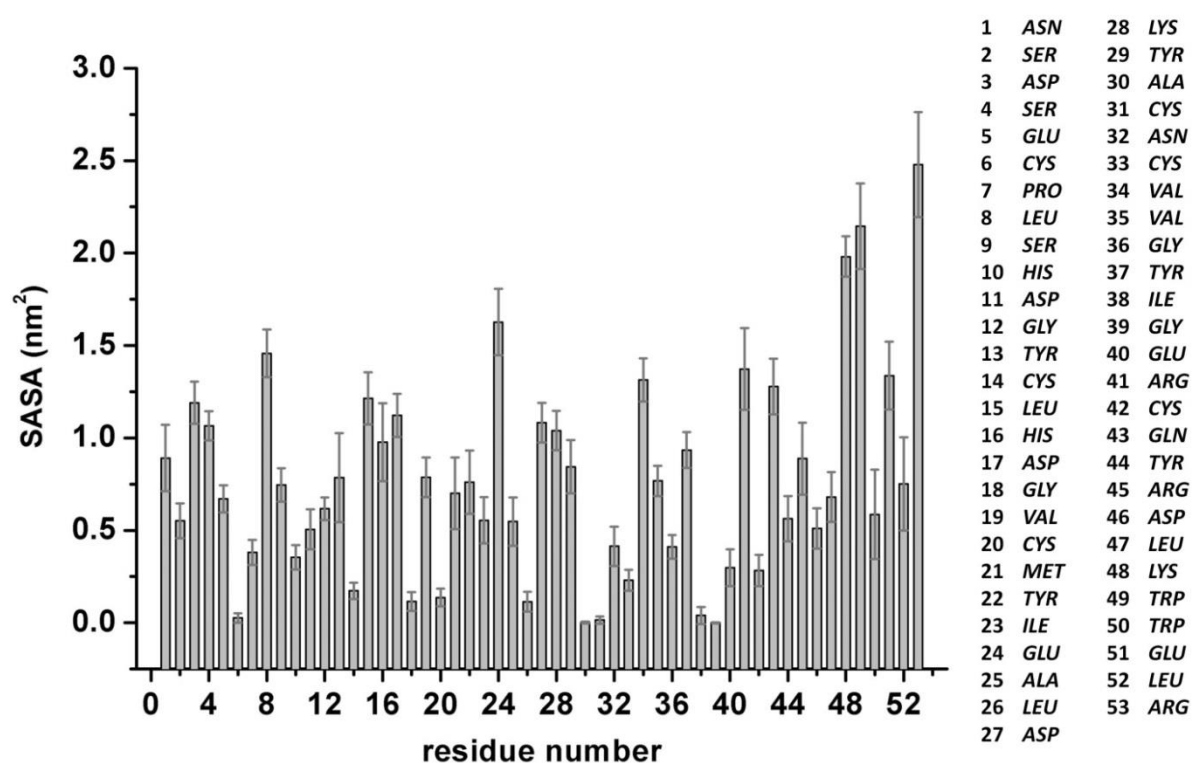


[Figure 4.3.1](#). Theoretical analysis of the solvent accessible surface area (SASA) of each AA in the native hEGF structure. The AA residues are listed at the right.

It is obvious that among the 53 AA residues, some are highly exposed to solvent (*e.g.*, ARG<sub>53</sub>, TRP<sub>49</sub>, LYS<sub>48</sub>, GLU<sub>24</sub>, SER<sub>9</sub>), whereas other AAs (*e.g.*, GLY<sub>18</sub>, LEU<sub>26</sub>, ALA<sub>30</sub>, ILE<sub>38</sub>, GLY<sub>39</sub>) have less access to solvent. Moreover, all CYS<sub>6</sub>, CYS<sub>14</sub>, CYS<sub>20</sub>, CYS<sub>31</sub>, CYS<sub>33</sub>, CYS<sub>42</sub> residues also have less contact with solvent due to their location in the core of the structure (cf. [Figure A1](#)(a) in the Appendix). However, as discussed above, due to the high chemical reactivity of CYS, we need to take these residues into account, even if they are less exposed to solvent. Nevertheless, the choice of the initial CYS residues for modification will depend on their surface area given in [Fig. 4.3.1](#), i.e., CYS<sub>33</sub> and CYS<sub>42</sub> (bound to each other, see [Table 4.3.2](#)) will be modified before CYS<sub>14</sub> and CYS<sub>31</sub>, etc. In addition, FTIR data ([Figure 4.3.2](#)) can be used to gain insight into some chemical changes after plasma treatment. While no structural information can be obtained from FTIR data due to the drying of the samples prior to measurements, some changes in the spectra can be used to gain insight into some chemical modifications occurring after plasma treatment. Therefore, FTIR is a convenient way to investigate if certain decisions during the simulation are valid. The plasma treatment leads to

chemical changes in the hEGF protein, indicated by the FTIR data. Multiple bands show a peak broadening after treatment, whereas new signals occur or are shifted in the spectrum.

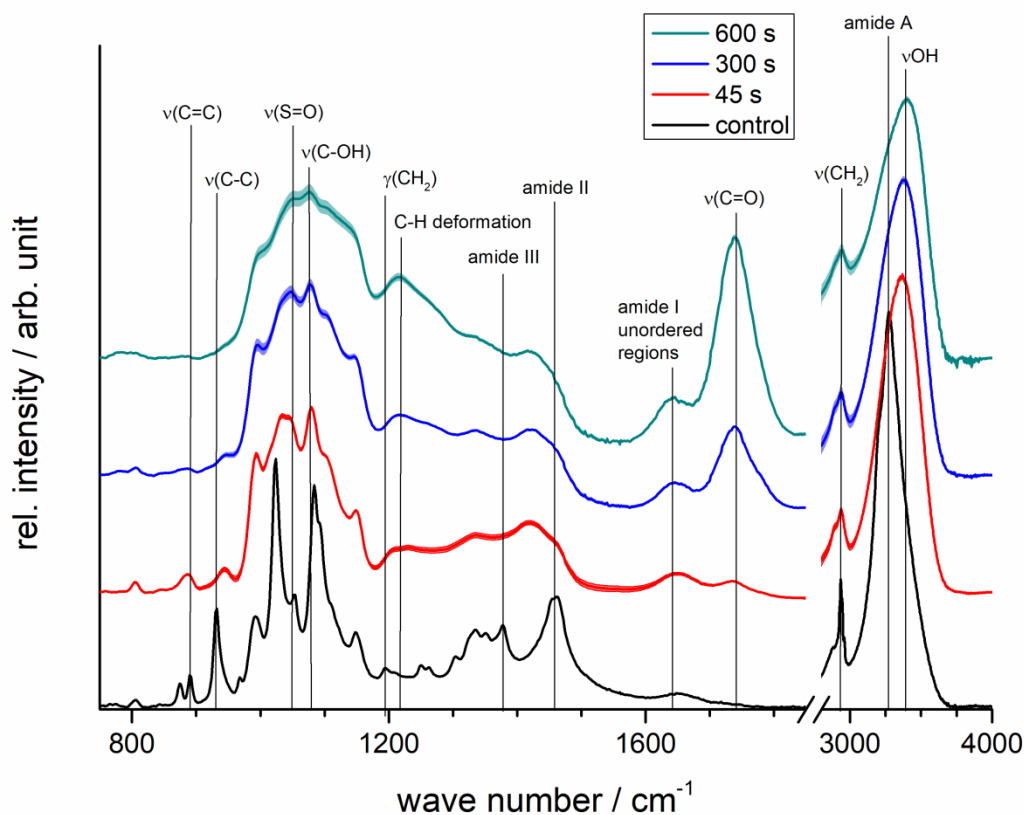


Figure 4.3.2. FTIR spectra of plasma-treated hEGF. The mean and standard error (shaded area) for each treatment time are shown. Spectra were stacked with a fixed factor of 0.03 to increase readability.

One well-known signal at  $1068\text{ cm}^{-1}$  increases with plasma treatment time, which can be annotated as  $\nu(\text{S}=\text{O})$ , indicating the presence of oxidized sulfur residues. Furthermore, a strong signal occurs at  $1750\text{ cm}^{-1}$ , indicating the formation of oxidized carbons, as this signal can be annotated as  $\nu(\text{C}=\text{O})$ . Furthermore, peak broadening is observed for the TRP double signals at  $1300\text{ cm}^{-1}$  and  $1040\text{ cm}^{-1}$ . Such shifts can be induced by an incomplete addition of a hydroxyl groups to the TRP residue. While structural changes cannot be directly identified due to the drying process during sample generation, the broadening of amide bands is typically described as a marker for thermodynamically unstable  $\alpha$ -helices<sup>24,25</sup>, which might be induced by the presence of chemically modified AAs interrupting the normal AA interactions. While no good assessment of amide A is possible due to the overlay with the  $\nu(\text{OH})$  signal, it would be expected that part of the very strong  $\nu(\text{OH})$  signal stems from the underlying broadened amide I band, as indicated by its slight shoulder corresponding to the original amid A signal. In addition, broadening of amide I and II can easily be observed.

Taken together, FTIR measurements indicate that S=O and OH groups are already introduced after 45 s of treatment, which is in good agreement with previous studies<sup>7,26</sup>. This means that we should mostly concentrate on modifications of the thiol-containing AAs, MET

and CYS (see [Table 4.3.2](#) below as well as [Table A1](#) in the Appendix). In the case of 300 s and longer, the intensity of the  $\nu(\text{C-OH})$  signal is lower, whereas the  $\text{C=O}$  formation is increased. These results, taken together with competition assays conducted by Takai *et al.*<sup>9</sup>, indicate that besides thiol oxidation, simulated changes should be introduced to HIS and LYS.

Thus, based on the combined results of FTIR spectroscopy, SASA analysis and the reactivity and modification of AAs deduced from<sup>9</sup>, we defined which residues are modified, to create the oxidized hEGF structures with different percentages, as detailed in [Table 4.3.2](#).

*Table 4.3.2. AAs modified at different levels of oxidation, to create the oxidized hEGFs (OX1, OX2 and OX3). The choice of the specific AAs for modification is based on the results of<sup>9</sup>, in combination with SASA results and in part FTIR data.*

Oxidation	AAs to be modified and their positions in hEGF	Percentage of oxidation (%)
OX1	LEU <sub>8</sub> , TYR <sub>13</sub> , HIS <sub>16</sub> , MET <sub>21</sub> , TYR <sub>22</sub> , TYR <sub>29</sub> , CYS <sub>33</sub> , TYR <sub>37</sub> , CYS <sub>42</sub> , TYR <sub>44</sub> , TRP <sub>49</sub> , TRP <sub>50</sub>	23
OX2	AAs of OX1 + HIS <sub>10</sub> , CYS <sub>14</sub> , LEU <sub>15</sub> , VAL <sub>19</sub> , CYS <sub>31</sub> , VAL <sub>34</sub> , GLN <sub>43</sub> , LYS <sub>48</sub>	38
OX3	AAs of OX2 + CYS <sub>6</sub> , PRO <sub>7</sub> , CYS <sub>20</sub> , LEU <sub>26</sub> , LYS <sub>28</sub> , VAL <sub>35</sub> , LEU <sub>47</sub> , LEU <sub>52</sub>	53

It is clear that in each oxidation case (i.e., OX1, OX2 or OX3) we oxidized a pair of CYS residues (i.e., each to cysteic acid, see [Table A1](#)), which were bound together prior to modification via disulfide bonds (cf. [Figure A1](#)). More specifically, for OX1 we oxidized CYS<sub>33</sub> and CYS<sub>42</sub>; for OX2, we oxidized in addition also CYS<sub>14</sub> and CYS<sub>31</sub>; finally for OX3 we also oxidized CYS<sub>6</sub> and CYS<sub>20</sub> (see [Table 4.3.2](#)). The oxidation of these CYS residues to cysteic acids leads to the dissociation of the disulfide bonds between these residues. These bonds are important, since they help to stabilize the structure of the protein. Hence, breakage of these bonds leads to conformational changes, which we indeed observed below.

### Conformational changes in the oxidized hEGF proteins

[Figure 4.4.3](#) illustrates the time evolution of the RMSD of the alpha carbons for each oxidation state, as well as for native hEGF. The native hEGF reaches its equilibration after ~100 ns and stays stable in the rest of the simulation time, yielding an RMSD fluctuating around 0.6 nm. In contrast, the oxidized hEGF structures obtain their stability at a much longer time, i.e., at around 650 ns. Moreover, an increasing oxidation level leads to higher fluctuations of the RMSD (see OX2 and OX3). This indicates that the oxidized structures become more flexible, which is due to their conformational changes, as well as the breakage of the disulfide bonds (see above). The conformational change in the case of OX1 is lower compared to OX2 and OX3 (as will be illustrated below), which is also obvious from their relative RMSD values, i.e., 0.5 nm (for OX1) versus 1 nm (for OX2 and OX3), see [Figure 4.3.3](#).

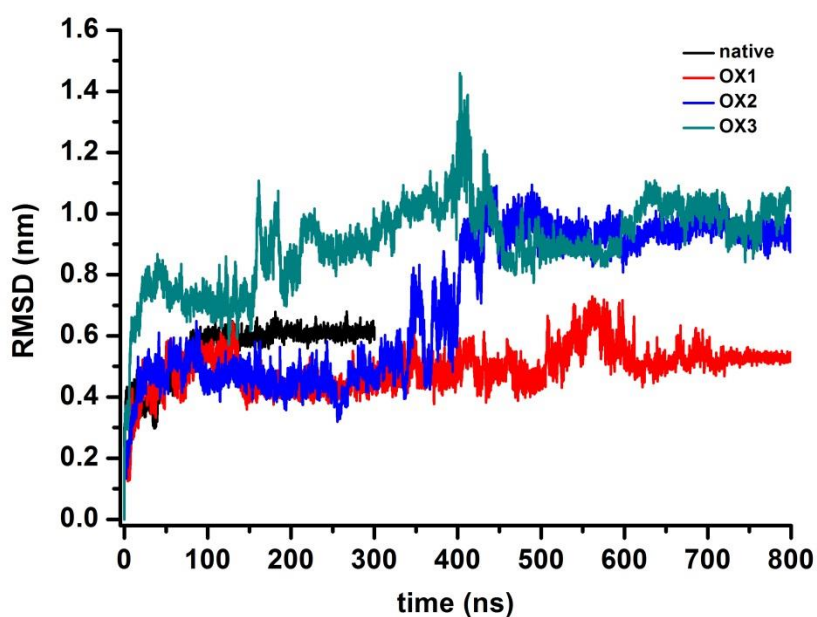


Figure 4.3.3. MD simulations: RMSD of the alpha carbons of the native (black) and oxidized hEGF proteins (red, blue and cyan, respectively).

To further support the RMSD results, we performed a PCA for the native and oxidized hEGF structures, where the collective motion of the alpha carbons is studied by plotting the projection of the first eigenvector (representing the direction of the highest motion) versus the projection of the second eigenvector (representing the second highest motion). In other words, the PCA results show the total phase space that each protein is able to occupy. The results of the PCA are presented in [Figure 4.3.4](#). In the case of OX1 we do not see significant effect of oxidation on the overall structure, i.e., the phase space occupied by OX1 is almost the same as for the native hEGF, despite the fact that one of the disulfide bonds (out of three) is already broken. This indicates that this low oxidation degree does not significantly affect the structural stability and flexibility, and does not lead to drastic conformational changes. On the other hand, in the OX2 and OX3 structures we clearly see higher structural fluctuations, indicating a higher flexibility of these systems. OX3 corresponds to the highest oxidation degree, where all three disulfide bonds are dissociated, thereby having the highest occupation in the phase space. This is also clear from [Figure 4.3.5](#), where the alignments of the oxidized structures with the native hEGF are shown. As is obvious from [Figure 4.3.5](#), the OX1 structure exhibits a better alignment with the native hEGF, whereas OX2 and OX3 show significant deviations. Moreover, in all oxidation cases the structures lose their  $\beta$ -sheet conformations, which are responsible for the structural stability. Furthermore, the helical structures also start to form at random sites, which is more visible in the case of OX3. Thus, we can conclude that a higher level of oxidation may lead to completely new conformations in the hEGF protein (see [Figure 4.3.5](#)). The latter is also clear from [Table 4.3.3](#), presenting the results of the secondary structure analysis for the native and oxidized hEGFs.

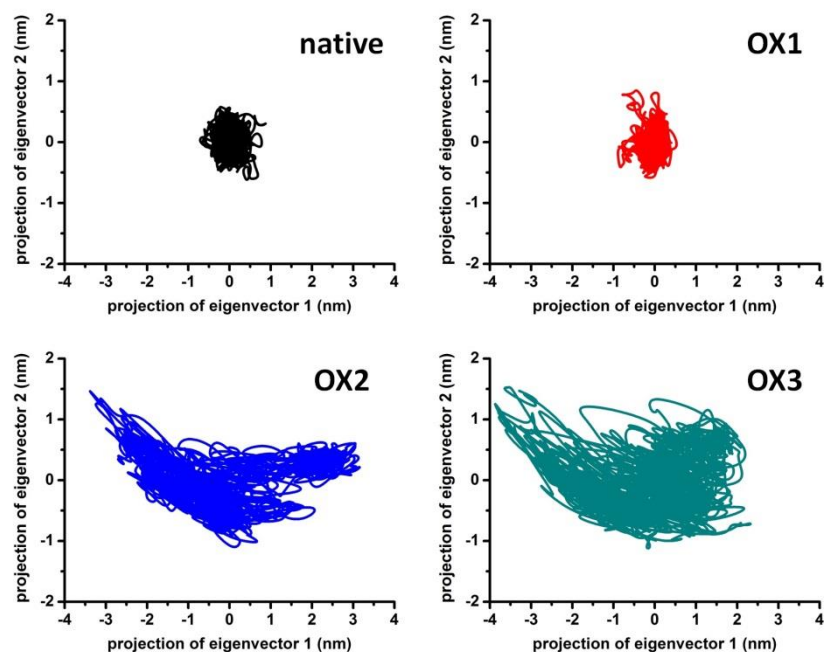


Figure 4.3.4. PCA results obtained for the native and oxidized hEGF structures, collecting the data from the last 30 ns of the simulations.

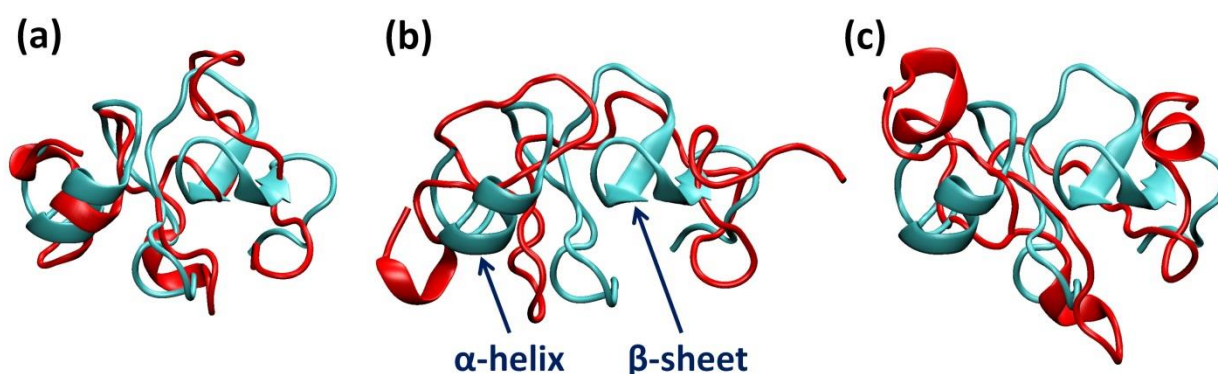


Figure 4.3.5. Alignment of the OX1 (a), OX2 (b) and OX3 (c) structures (red) with the native hEGF (cyan). The last snapshots of the MD simulations are used to illustrate the conformational changes of the oxidized hEGFs compared to the native hEGF.

Table 4.3.3. Secondary structure analysis of the native and oxidized hEGFs. The values given denote the relative occurrence (in %) of the various conformations.

structure	$\alpha$ -helix	$3_{10}$ -helix	$\pi$ -helix	$\beta$ -sheet	$\beta$ -bridge	turn	coil
Native	11.2	0.6	0.0	10.9	2.3	48.7	26.4
OX1	7.6	3.9	0.0	0.0	0.0	65.6	22.8
OX2	0.0	1.4	0.0	0.0	8.0	66.5	24.1
OX3	7.4	3.4	5.8	0.5	4.3	44.9	33.7

These structural modifications, leading to conformational changes, obviously affect the binding free energies of the hEGFs with their hEGFRs. Indeed, as shown in the Appendix (Figures A2 and A3 and Tables A2, A3 and A4), our docking simulations and MM/GBSA calculations revealed that the binding free energies of native and modified hEGFs with their hEGFR are -105.15, -71.21, -63.85 and -49.49 kcal/mol for the native, OX1, OX2 and OX3 structures, respectively, showing that higher oxidation causes a lower interaction. For more details about the docking and MM/GBSA results, see the Appendix.

To support our simulation results on the impact of treatment on the hEGF structure, Dr. Lackmann performed CD spectroscopy (Figure 4.3.6).

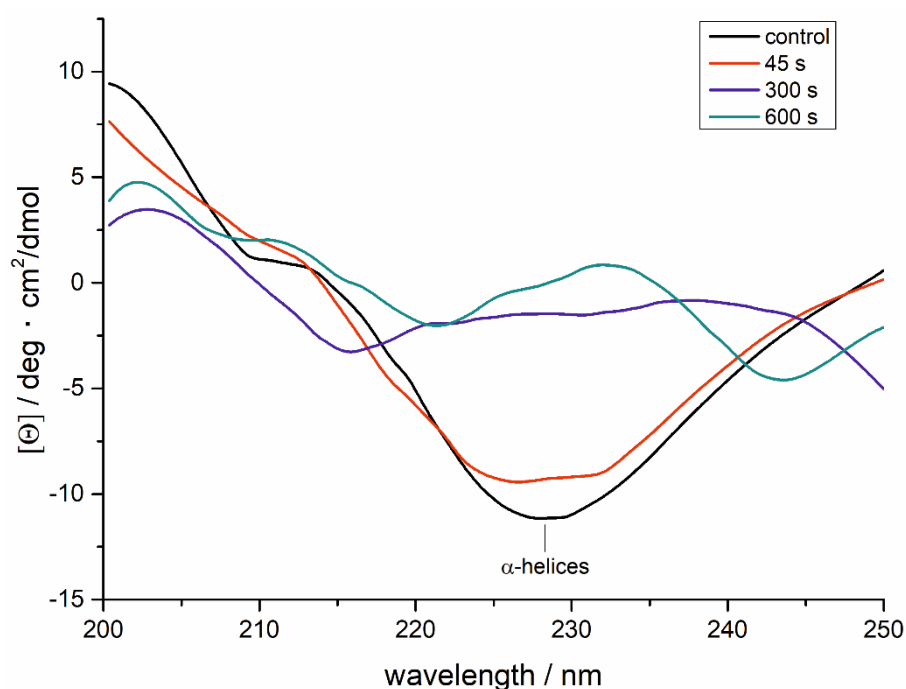


Figure 4.3.6. Secondary structure analysis of plasma-treated hEGF by CD spectroscopy.

The CD data indicate that 45 s of treatment cause only slight alterations in the hEGF secondary structure compared to the control spectrum, whereas longer treatments (300 s and 600 s) result in a stronger disturbance of the secondary structure of the hEGF, especially in the region around 225 nm, which indicates a strong impact on the  $\alpha$ -helices. Although our computational and experimental results cannot directly be compared, due to the complex nature of the plasma which is difficult to describe by modeling, our simulation results on the conformational changes are overall in good qualitative agreement with the results of the CD spectroscopy. Due to the nature of DBD treatment, a significant decrease in pH can be expected, especially during longer treatment times and considering the low buffer concentrations necessary for CD spectroscopy. However, crystallization data on hEGF showed that all relevant structural features are retained by hEGF at low pH compared to physiological pH<sup>27</sup>. Narhi et al. investigated the relevance of the disulfide bonds in hEGF on its secondary structure by CD spectroscopy at pH 3.<sup>28</sup> While the presented spectra do not perfectly agree, most likely due to different buffers as well as pH conditions, it is apparent

that disulfide bonds play a major role in determining the secondary structure of hEGF. Taking into account the strong impact of DBD treatment on disulfide bonds and its capability to oxidize disulfide bonds to *e.g.* cysteine sulfonic acid (R-SO<sub>3</sub>H)<sup>29</sup>, differences in CD spectra might be due to the formation of sulfur-containing residues all with a negative charge, thereby further promoting unfolding of the structure, as shown for longer treatment times. The additional introduction of C=O bounds, as indicated by FTIR spectroscopy, might also assist in the unfolding process.

Thus, we can conclude from our simulation results that the lower oxidation (*i.e.*, OX1) has comparatively less effect on the binding affinity of hEGF with its receptor (see above). This most likely does not strongly influence the signaling pathways in a cell, and thereby the cell proliferation, which might explain why CAP at short treatment times is beneficial for chronic wound healing.<sup>30</sup> On the other hand, higher oxidation of hEGF (*i.e.*, OX2 and OX3) causes clearly less interaction with its hEGFR, which most probably causes a disturbance of the signaling pathways in a cell, ultimately leading to a disruption of the cell proliferation. This might explain the effect of CAP at longer treatment times on inhibiting cancer cell proliferation and even cancer cell death.<sup>31,32</sup>

#### 4.3.4 Conclusion

We show that a low amount of modified amino acids caused by CAP treatment does not cause significant structural changes in hEGF, and thus, has comparatively lower impact on the hEGF interaction with hEGFR. So we might expect only limited disturbance of the signaling pathways and hence of the cell proliferation. This is favorable in *e.g.*, wound healing, where treatment with CAP at short treatment times or mild conditions indeed does not (or little) affect the cell proliferation, while being effective in decontamination of pathogens.<sup>33</sup> On the other hand, analysis of the results for a higher oxidation degree (used to approximate longer CAP treatment times) of hEGF shows a significant effect on the structural conformation and the binding affinity with EGFR, and this will most probably cause inhibition of the cell growth or proliferation. This might be important in cancer treatment by means of CAP, as higher doses of oxidation arrest the cell growth, leading to apoptosis or even necrosis.<sup>34,35</sup>

It should be noted that CAP treatment of cells is a complex process, and the interaction of signaling proteins with their receptors is only one of the steps of the entire mechanism of cell proliferation. Nevertheless, our study might contribute to a better understanding of one of the possible mechanisms of (inhibition of) cell proliferation, by means of oxidation of signaling proteins. For more conclusive insight, the impact of plasma-treated hEGF should be analyzed *in vitro* to complement the simulations and the current experimental data, *e.g.*, by applying hEGF to cell culture and compare the cellular response. In addition, experimental validation of the MM/GBSA simulations should be performed using *e.g.*, artificial membrane systems populated with hEGFR.

### 4.3.5 Appendix

#### MD simulations

[Figure A1](#) illustrates the human epidermal growth factor (hEGF) protein consisting of 53 AAs with three intermolecular disulfide bonds created between cysteine residues.

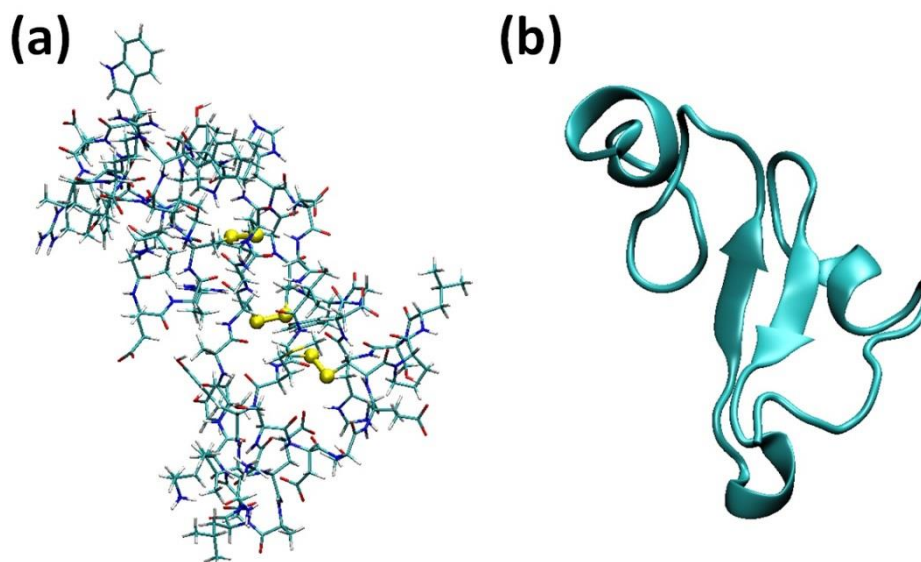


Figure A1. Crystal structure of hEGF (PDB ID: 2KV4) shown in licorice (a) and cartoon (b) views. The sulfur atoms of the cysteine residues and the disulfide bonds between them are illustrated in yellow color in (a), for the sake of clarity.

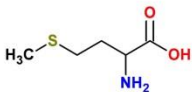
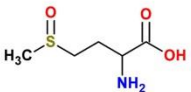
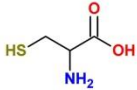
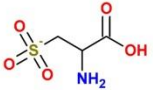
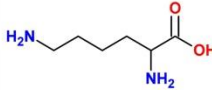
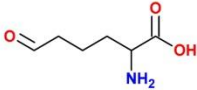
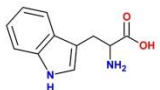
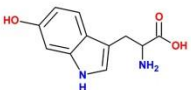
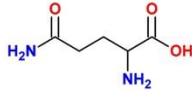
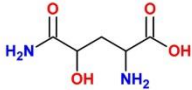
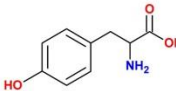
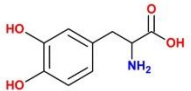
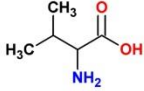
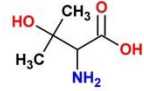
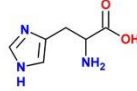
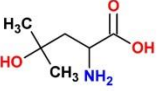
As a model system in our simulations we used hEGF surrounded with SPC water molecules in combination with counter ions.<sup>36</sup> The latter were used to neutralize the total charge of the system. The system was initially energy minimized using the steepest descent algorithm, followed by equilibration in the NPT-ensemble for 300 ns. In the latter case the Bussi thermostat<sup>37</sup> in combination with a coupling constant of 0.1 ps and the isotropic Parrinello-Rahman barostat<sup>38</sup> with a compressibility of  $4.5 \times 10^{-5} \text{ bar}^{-1}$  and a coupling constant of 2 ps, were utilized. The temperature and pressure of the system were kept at 300 K and 1 atm, respectively. Periodic boundary conditions were applied in all Cartesian directions and a time step of 2 fs was used in all simulations. For non-bonded (i.e., van der Waals and Coulomb) interactions, a 1.0 nm cut-off was employed, using the particle mesh Ewald method<sup>39</sup> for the electrostatic interactions, in combination with a 0.12 nm spaced-grid for the reciprocal-space interactions and a fourth-order B-spline interpolation.

After equilibration of the system, the last 30 ns trajectory was used to analyze the solvent accessible surface area (SASA) of each residue in the hEGF protein. The SASA was calculated using the so-called “rolling-ball” algorithm developed by Shrake and Rupley<sup>40</sup>, where a spherical probe with a particular radius (typically 0.14 nm) moves on the surface of the protein to determine the surface area accessible to solvent. Thus, it gives information about the AAs that are mostly exposed to solvent. Subsequently, these specific AAs were

used to create the oxidized hEGFs. The choice of the residues for modification, however, does not solely depend on the SASA results, but also on the chemical reactivity and modification of the AAs, as deduced from Takai *et al.*<sup>9</sup> The results of Fourier-transform infrared (FTIR) spectroscopy, obtained in the experiments by Dr. Lackmann (see above), were then used to give a general idea whether the chosen modifications are valid. Thus, applying the modifications to the specific AA residues (see [Table A1](#)), we created three oxidized hEGF proteins with different degrees of oxidation, which are called OX1, OX2 and OX3. Subsequently, these structures were also equilibrated in the NPT-ensemble for 800 ns, using the same procedure as given above. Again the last 30 ns trajectory was used for further analysis.

[Table A1](#) lists the applied modifications of the AAs in the oxidized structures. All of these modified residues contain either S=O, or C=O, or C-OH as newly formed bonds.

*Table A1. List and chemical structures of the 10 AAs used for the creation of the various oxidized hEGF proteins (OX1, OX2 and OX3).*

<b>AA in native hEGF</b>	<b>modified AA in oxidized hEGF</b>	<b>AA in native hEGF</b>	<b>modified AA in oxidized hEGF</b>
 methionine (MET)	 methionine sulfoxide	 proline (PRO)	 pyroglutamic acid
 cysteine (CYS)	 cysteic acid	 lysine (LYS)	 allysine
 tryptophan (TRP)	 6-hydroxytryptophan	 glutamine (GLN)	 4-hydroxyglutamine
 tyrosine (TYR)	 3,4-dihydroxyphenylalanine	 valine (VAL)	 3-hydroxyvaline
 histidine (HIS)	 2-oxo-histidine	 leucine (LEU)	 4-hydroxyisoleucine

## Docking simulations

In our docking simulations we used five protein structures, i.e., the hEGF receptor (hEGFR) and four different ligands (i.e., native hEGF, OX1, OX2 and OX3).

Receptor structure: The target crystal structure of the hEGFR was retrieved from the Protein Data Bank (PDB ID: 1IVO), which is available in dimeric form. Prior to protein-

protein docking simulations the monomer of the hEGFR was prepared in the following steps: assignment of bond orders, addition of H atoms, removal of all conserved crystallographic water molecules, as well as optimization of side-chain conformation. The prepared structure was then energy minimized using the CHARMM force field.<sup>41,42</sup>

**Ligand structures:** The equilibrated structures of the native and modified proteins (oxidized hEGFs) were obtained from our MD simulations. Therefore, only H atoms were added before performing protein-protein docking. Note that the docking simulations of this study, as well as Molecular Mechanics Poisson-Boltzmann Surface Area (MM-PBSA) calculations, were performed by our collaborator Dr. S. Kumar from Gachon University, Korea.

**Protein-protein docking:** The protein-protein docking simulations were performed using the Z-DOCK v2.3 program.<sup>20,21</sup> In Z-DOCK, the receptor protein and ligands were treated as rigid bodies and all six rotational and translational degrees of freedom were fully explored. We employed the 6° sampling method, which can produce 54000 prediction poses per target.<sup>43</sup> For better pose selection, all the docked poses were further ranked by the ZRank scoring function.<sup>44</sup>

All the docked and ranked poses were clustered with a RMSD cutoff of 10 Å and the top poses from the largest cluster were selected.

### **MM/GBSA calculations for binding free energy estimation**

MM/GBSA (i.e., molecular mechanics generalized Born surface area) is a method for calculating the binding free energies between receptor and ligand.<sup>45</sup> It combines molecular mechanics energy together with implicit solvation energy. The binding free energy is derived from the difference between the energies of the bound complex and the unbound protein receptor and ligand. It consists of various energy terms that originate from different types of physico-chemical interactions.<sup>46</sup> The energies are computed using the OPLS3 force field and the generalized-Born/surface area continuum solvent model.<sup>47,48</sup>

The binding free energy is calculated using the following equation:

$$\Delta G_{\text{bind}} = G_{\text{complex}} - (G_{\text{protein}} + G_{\text{ligand}}), \quad (2)$$

$$\text{where } G = E_{\text{MM}} + G_{\text{sol}} + G_{\text{SA}}$$

The  $E_{\text{MM}}$  is the force field derived energy, whereas  $G_{\text{sol}}$  is the electrostatic solvation energy.  $G_{\text{SA}}$  describes the non-polar contributions to the solvation free energy estimated using the SASA. No corrections for entropic changes were considered.<sup>46,49,50</sup>

In this work, we computed protein-ligand binding affinities on higher ranked poses from Z-dock using the MM/GBSA method, known as VSBG2.0 energy model.<sup>51,52</sup> Each pose was minimized using local minimization feature in prime. The protein in each pose was treated as flexible within 10Å from the bound ligand.

## Protein-protein docking and free energy calculation results

The selected native, and structurally modified OX1, OX2, OX3 ligands were docked into the binding pocket of the hEGFR receptor. A total of 2000 poses were generated and scored by the ZDock score. Moreover, in order to improve the prediction accuracy, all the ZDock prediction poses were reranked using the ZRank scoring function. The top reranked pose was selected for each ligand.

The results of the docking simulations are shown in [Table A2](#). The binding affinity of the native hEGF with the hEGFR is the highest, i.e., -99.19 kcal/mol, whereas it is in between for OX1 and OX2 and the lowest for OX3, i.e., -72.26, -61.76 and -47.89 kcal/mol, respectively.

Likewise, the calculated binding free energies of top poses follow similar trends, where native hEGF with hEGFR has the highest free energy of binding compared to OX1, OX2 and OX3 (see [Table A4](#) below).

*Table A2. Binding affinity of the native and oxidized hEGF proteins (in kcal/mol). ZDock Score is the binding affinity score. ZRank Score is the reranking of ZDock Score based on a scoring function, i.e., the sum of ZRankVdW, ZRank Elec. and ZRank Solv., respectively, where ZRankVdW is the non-bonded interaction energy term, ZRank Elec. is the Coulomb interaction energy term and ZRank Solv. is the desolvation energy term calculated by pairwise atomic contact energy (ACE) function<sup>53</sup>.*

Ligands	ZDock Score	ZRank Score	ZRankVdW	ZRank Elec.	ZRank Solv.
Native	14.16	-99.19	-95.24	-2.95	-1.00
OX1	12.18	-72.26	-73.96	1.88	-0.18
OX2	12.34	-61.76	-66.69	-3.34	8.27
OX3	11.98	-47.89	-43.24	-12.82	8.17

[Figure A2](#) illustrates the best binding poses of native and oxidized hEGFs among all obtained poses for the ligand-receptor complex.

The chemical nature of the hEGFR's binding site residues bound with the native protein was hydrophobic (aliphatic), i.e., LEU<sub>17</sub>, GLY<sub>18</sub>, polar (acidic), i.e., ASP<sub>22</sub>, ASP<sub>323</sub>, ASP<sub>355</sub>, basic (polar, positive charged), i.e., ARG<sub>353</sub>, LYS<sub>465</sub> and nucleophilic (polar, charged), i.e., SER<sub>440</sub> (see [Figure A2](#)). Moreover, a network of the H-bonds with GLY<sub>18</sub> (3.40Å), ASP<sub>323</sub> (2.93Å), SER<sub>440</sub> (3.50Å) and LYS<sub>465</sub> (2.60Å), electrostatic interactions with ASP<sub>355</sub> (5.59Å) and LYS<sub>465</sub> (4.61Å), as well as hydrophobic interactions with the backbone atom of ARG<sub>353</sub> (4.44Å) AA residues, was observed (see [Table A3](#)).

In the docking pose, the chemical nature of the binding site residues bound with OX1 was hydrophobic (aliphatic), i.e., GLY<sub>18</sub>, LEU<sub>348</sub>, polar amide, i.e., GLN<sub>16</sub>, GLN<sub>384</sub>, polar (acidic), i.e., ASP<sub>22</sub>, ASP<sub>355</sub>, basic (polar, positive charged), i.e., LYS<sub>465</sub>, polar uncharged residue, i.e., SER<sub>418</sub>, SER<sub>468</sub>, and hydrophobic (aliphatic), i.e., PHE<sub>347</sub> and PRO<sub>349</sub> (see [Figure A2](#)). Moreover, the OX1 displayed a network of the H-bonds with ASP<sub>355</sub> (2.97Å), GLN<sub>384</sub> (3.05Å), SER<sub>418</sub> (2.54, 2.58 and 2.81Å, i.e., multiple interactions with the ligand AAs), LYS<sub>465</sub> (2.88Å) and SER<sub>468</sub> (2.74Å), electrostatic interactions with ASP<sub>355</sub> (4.01Å) and

LYS<sub>465</sub> (5.27Å), as well as hydrophobic (aliphatic) interactions with LEU<sub>353</sub> (5.20Å) AA residues (see [Table A3](#)).

The docking pose in the binding site revealed that the chemical nature of the binding site residues bound with OX2 was hydrophobic (aliphatic), i.e., LEU<sub>382</sub>, ALA<sub>415</sub>, ILE<sub>438</sub>, ILE<sub>466</sub>, basic (polar, positive charged), i.e., HIS<sub>409</sub>, ARG<sub>29</sub>, LYS<sub>443</sub>, LYS<sub>465</sub>, hydrophobic (aromatic), i.e., PRO<sub>349</sub>, PHE<sub>412</sub> and polar uncharged, i.e. THR<sub>464</sub>, SER<sub>468</sub> (see [Figure A2](#)). Similarly, the OX2 also displayed a network of the H-bonds with ARG<sub>29</sub> (2.02Å), LYS<sub>443</sub> (2.97Å), LYS<sub>465</sub> (3.79Å) and THR<sub>464</sub> (3.19Å), electrostatic interactions with ARG<sub>29</sub> (5.00Å) and hydrophobic interactions with LEU<sub>382</sub> (3.73Å), HIS<sub>409</sub> (3.76Å) ILE<sub>438</sub> (5.02) and ALA<sub>415</sub> AA residues (see [Table A3](#)).

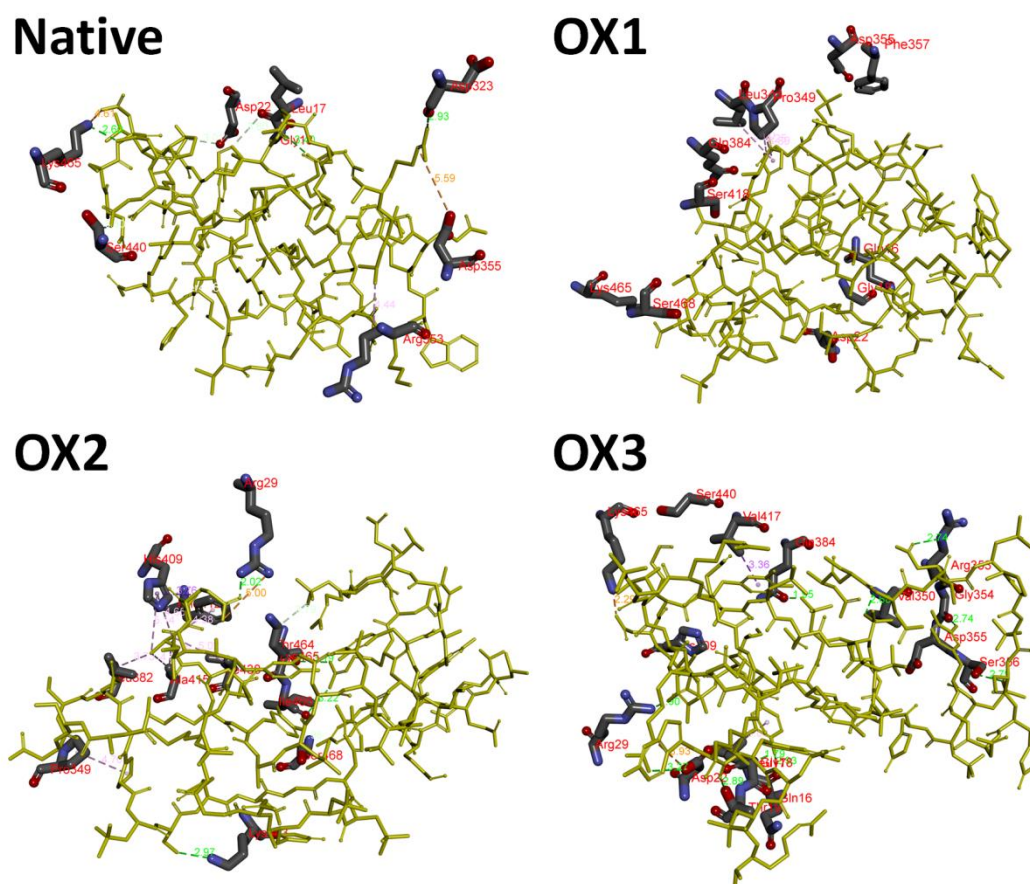


Figure A2. Docked complex of the native hEGF, OX1, OX2 and OX3 ligands with the hEGFR. The ligands are shown in yellow color, for the sake of clarity.

[Figure A2](#) also shows the best binding pose among all the poses obtained for the OX3-hEGFR complex and the chemical nature of the binding site residues bound with OX3 was hydrophobic (aliphatic), i.e., LEU<sub>17</sub>, GLY<sub>18</sub>, VAL<sub>350</sub>, GLY<sub>354</sub>, VAL<sub>417</sub>, basic (polar, positive charged), i.e., ARG<sub>29</sub>, ARG<sub>353</sub>, HIS<sub>409</sub>, LYS<sub>465</sub>, polar uncharged, i.e. THR<sub>19</sub>, SER<sub>356</sub>, SER<sub>440</sub>, polar (acidic), i.e., ASP<sub>22</sub>, ASP<sub>355</sub> and polar amide, i.e., GLN<sub>16</sub>, GLN<sub>384</sub>. Moreover, the OX3 also displayed a network of the H-bonds with ARG<sub>29</sub> (1.90Å), ASP<sub>22</sub> (3.27Å), THR<sub>19</sub> (2.89Å), GLN<sub>384</sub> (1.95Å) and SER<sub>356</sub> (2.79Å), electrostatic interactions with ASP<sub>22</sub> (3.93Å)

and LYS<sub>465</sub> (2.29Å) as well as hydrophobic interactions with LEU<sub>17</sub> (5.08Å) and VAL<sub>417</sub> (3.36Å) AA residues (see [Table A3](#)).

We applied the MM/GBSA method to make quantitative estimates for the binding free energies ( $\Delta G_{\text{bind}}$ ) between the (un)modified hEGFs and hEGFR, using the structures obtained from our docking simulations. The calculations revealed that the native hEGF has a higher free energy of binding with hEGFR compared to OX1, OX2 and OX3, as summarized in [Table A4](#). It is clear that the van der Waals energy term ( $\Delta G_{\text{vdw}}$ ) has a major contribution to the total free energy of binding in all cases. Moreover, the generalized Born solvation term ( $\Delta G_{\text{solv}}$ ) has a higher contribution to the global free energy, especially in the cases of native and OX2, whereas OX3 has the lowest contribution. On the other hand, the electrostatic term ( $\Delta G_{\text{elect}}$ ) is only favorable for OX3, and the lowest contribution of this term is for OX2. Thus, the MM/GBSA results indicate that any of the physico-chemical energy components (i.e.,  $\Delta G_{\text{vdw}}$ ,  $\Delta G_{\text{elect}}$  and  $\Delta G_{\text{solv}}$ ) have a predominant role in the total binding energy, showing the complex nature of the interaction between the hEGF and hEGFR.

*Table A3. AA residues of the hEGFR, binding with the native and oxidized hEGF.*

Proteins	Interacting AAs of the receptor	AAs displaying H-bonds	AAs displaying electrostatic interactions	AAs displaying hydrophobic (aliphatic/aromatic) interactions
Native	LEU <sub>17</sub> , GLY <sub>18</sub> , ASP <sub>22</sub> , ASP <sub>323</sub> , ARG <sub>353</sub> , ASP <sub>355</sub> , SER <sub>440</sub> , LYS <sub>465</sub>	GLY <sub>18</sub> (3.40Å), ASP <sub>323</sub> (2.93Å), SER <sub>440</sub> (3.50Å), LYS <sub>465</sub> (2.60Å)	ASP <sub>355</sub> (5.59Å), LYS <sub>465</sub> (4.61Å)	ARG <sub>353</sub> (4.44Å)
OX1	GLY <sub>18</sub> , GLN <sub>16</sub> , ASP <sub>22</sub> , PHE <sub>347</sub> , LEU <sub>348</sub> , PRO <sub>349</sub> , ASP <sub>355</sub> , GLN <sub>384</sub> , SER <sub>418</sub> , LYS <sub>465</sub> , SER <sub>468</sub>	ASP <sub>355</sub> (2.97Å), GLN <sub>384</sub> (3.05Å), LYS <sub>465</sub> (2.88Å), SER <sub>468</sub> (2.74Å), SER <sub>418</sub> (2.54, 2.58, 2.81Å)	ASP <sub>355</sub> (4.01Å), LYS <sub>465</sub> (5.27Å)	LEU <sub>353</sub> (5.20Å)
OX2	ARG <sub>29</sub> , PRO <sub>349</sub> , LEU <sub>382</sub> , HIS <sub>409</sub> , PHE <sub>412</sub> , ALA <sub>415</sub> , ILE <sub>438</sub> , LYS <sub>443</sub> , THR <sub>464</sub> , LYS <sub>465</sub> , ILE <sub>466</sub> , SER <sub>468</sub>	ARG <sub>29</sub> (2.02Å), LYS <sub>443</sub> (2.97Å), LYS <sub>465</sub> (3.79Å), THR <sub>464</sub> (3.19Å)	ARG <sub>29</sub> (5.00Å)	LEU <sub>382</sub> (3.73Å), HIS <sub>409</sub> (3.76Å), ILE <sub>438</sub> (5.02), ALA <sub>415</sub>
OX3	GLN <sub>16</sub> , LEU <sub>17</sub> , GLY <sub>18</sub> , THR <sub>19</sub> , ASP <sub>22</sub> , ARG <sub>29</sub> , VAL <sub>350</sub> , ARG <sub>353</sub> , GLY <sub>354</sub> , SER <sub>356</sub> , GLN <sub>384</sub> , HIS <sub>409</sub> , VAL <sub>417</sub> , SER <sub>440</sub> , ASP <sub>355</sub> , LYS <sub>465</sub>	ARG <sub>29</sub> (1.90Å), ASP <sub>22</sub> (3.27Å), THR <sub>19</sub> (2.89Å), GLN <sub>384</sub> (1.95Å), SER <sub>356</sub> (2.79Å)	ASP <sub>22</sub> (3.93Å), LYS <sub>465</sub> (2.29Å)	LEU <sub>17</sub> (5.08Å), VAL <sub>417</sub> (3.36Å)

Thus, based on the MM/GBSA results we can conclude that the conformational changes induced by oxidation lead to a lower binding affinity of the oxidized hEGFs with the hEGFR.

Table A4. Binding free energies of the native and oxidized hEGFs with hEGFR protein, calculated by the MM/GBSA method (in kcal/mol), including individual energy terms.

Ligands	$\Delta G_{\text{bind}}$	$\Delta G_{\text{vdw}}$	$\Delta G_{\text{elect}}$	$\Delta G_{\text{solv}}$	$\Delta G_{\text{other}}$
Native	-105.15	-119.42	62.64	-41.25	-7.12
OX1	-71.21	-110.08	37.70	6.12	-4.95
OX2	-63.84	-128.57	148.45	-81.96	-1.76
OX3	-49.49	-111.37	13.04	81.89	-33.05

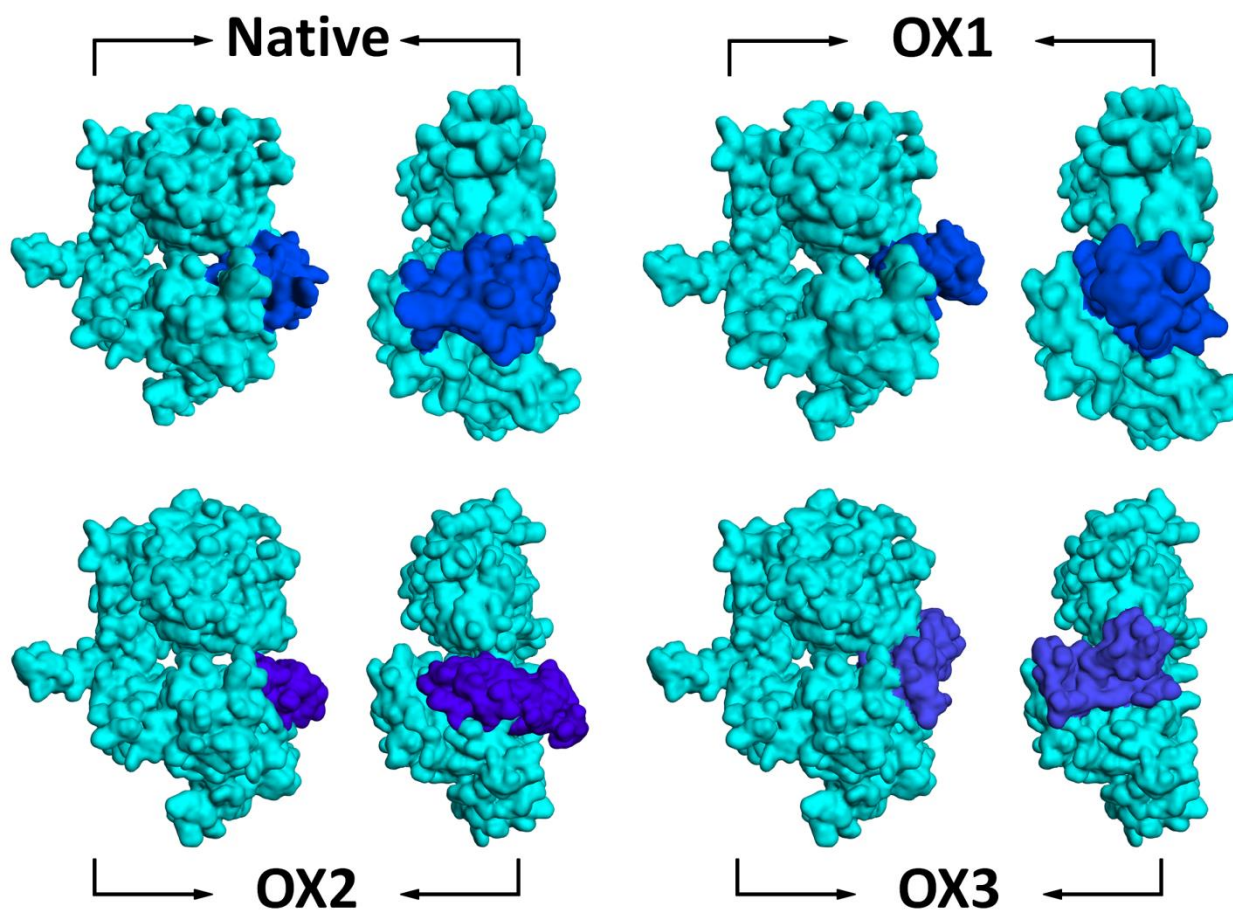


Figure A3. Binding positions of the native and oxidized hEGFs (blue) with the hEGF receptor (cyan). The structures are shown both in side view and front view (left and right, respectively). The corresponding binding free energies are -105.15, -71.21, -63.85 and -49.49 kcal/mol, for the native protein, OX1, OX2 and OX3, respectively.

### 4.3.6 References

- 1 Iqbal, N and Iqbal, N. Human epidermal growth factor receptor 2 (HER2) in cancers: overexpression and therapeutic implications. *Molecular biology international* 2014, 1-9, (2014).
- 2 Berlanga-Acosta, J., Gavilondo-Cowley, J., López-Saura, P., González-López, T., Castro-Santana, M.D., López-Mola, E., Guillén-Nieto, G. and Herrera-Martinez, L. Epidermal growth factor in clinical practice—a review of its biological actions, clinical indications and safety implications. *International wound journal* 6, 331-346 (2009).
- 3 Wang, J., Yin, J., Yang, Q., Ding, F., Chen, X., Li, B and Tian, X.. Human epidermal growth factor receptor 4 (HER4) is a favorable prognostic marker of breast cancer: a systematic review and meta-analysis. *Oncotarget* 7, 76693 (2016).
- 4 Henson, E and Gibson, S. Surviving cell death through epidermal growth factor (EGF) signal transduction pathways: implications for cancer therapy. *Cellular signalling* 18, 2089-2097 (2006).
- 5 Stoscheck, C and King, L. Role of epidermal growth factor in carcinogenesis. *Cancer research* 46, 1030-1037 (1986).
- 6 Herbst, R. Review of epidermal growth factor receptor biology. *International Journal of Radiation Oncology Biology Physics* 59, S21-S26 (2004).
- 7 Lackmann, J., Baldus, S., Steinborn, E., Edengeiser, E., Kogelheide, F., Langklotz, S., Schneider, S., Leichert, L., Benedikt, J., and Awakowicz, P. A dielectric barrier discharge terminally inactivates RNase A by oxidizing sulfur-containing amino acids and breaking structural disulfide bonds. *Journal of Physics D: Applied Physics* 48, 494003 (2015).
- 8 Choi, S., Attri, P., Lee, I., Oh, J., Yun, J.-H., Park, J. H., Choi, E. H., and Lee, W. Structural and functional analysis of lysozyme after treatment with dielectric barrier discharge plasma and atmospheric pressure plasma jet. *Scientific Reports* 7, 1027 (2017).
- 9 Takai, E., Kitamura, T., Kuwabara, J., Ikawa, S., Yoshizawa, S., Shiraki, K., Kawasaki, H., Arakawa, R and Kitano, K. Chemical modification of amino acids by atmospheric-pressure cold plasma in aqueous solution. *Journal of Physics D: Applied Physics* 47, 285403 (2014).
- 10 Huang, H., Mohan, S and Yu, C. The NMR solution structure of human epidermal growth factor (hEGF) at physiological pH and its interactions with suramin. *Biochemical and biophysical research communications* 402, 705-710 (2010).
- 11 Brandenburg, R. Dielectric barrier discharges: progress on plasma sources and on the understanding of regimes and single filaments. *Plasma Sources Science and Technology* 26, 053001 (2017).
- 12 Abraham, M., van der Spoel, D., Lindahl, E and Hess, B. the GROMACS development team, GROMACS User Manual version 5.1. 2, (2016).
- 13 Abraham, M., Murtola, T., Schulz, R., Páll, S., Smith, J. C., Hess, B., and Lindahl, E. GROMACS: High performance molecular simulations through multi-level parallelism from laptops to supercomputers. *SoftwareX* 1, 19-25 (2015).

- 14 Van Der Spoel, D., Lindahl, E., Hess, B., Groenhof, G., Mark, A. E and Berendsen, H. *et al.* GROMACS: fast, flexible, and free. *Journal of computational chemistry* 26, 1701-1718 (2005).
- 15 Schmid, N., Eichenberger, A. P., Choutko, A., Riniker, S., Winger, M., Mark, A. E., and van Gunsteren, W. Definition and testing of the GROMOS force-field versions 54A7 and 54B7. *European biophysics journal* 40, 843 (2011).
- 16 Petrov, D., Margreitter, C., Grandits, M., Oostenbrink, C and Zagrovic, B. A systematic framework for molecular dynamics simulations of protein post-translational modifications. *PLoS computational biology* 9, e1003154 (2013).
- 17 Margreitter, C., Reif, M and Oostenbrink, C. Update on phosphate and charged post-translationally modified amino acid parameters in the GROMOS force field. *Journal of computational chemistry* 38, 714-720 (2017).
- 18 Frishman, D and Argos, P. Knowledge-based protein secondary structure assignment. *Proteins: Structure, Function, and Bioinformatics* 23, 566-579 (1995).
- 19 Humphrey, W., Dalke, A and Schulten, K. VMD: visual molecular dynamics. *Journal of molecular graphics* 14, 33-38 (1996).
- 20 Chen, R., Li, L and Weng, Z. ZDOCK: an initial-stage protein-docking algorithm. *Proteins: Structure, Function, and Bioinformatics* 52, 80-87 (2003).
- 21 Pierce, B., Hourai, Y and Weng, Z. Accelerating protein docking in ZDOCK using an advanced 3D convolution library. *PloS one* 6, e24657 (2011).
- 22 Ogiso, H., Ishitani, R., Nureki, O., Fukai, S., Yamanaka, M., Kim, J.-H., Saito, K., Sakamoto, A., Inoue, M and Shirouzu, M. Crystal structure of the complex of human epidermal growth factor and receptor extracellular domains. *Cell* 110, 775-787 (2002).
- 23 Genheden, S and Ryde, U. The MM/PBSA and MM/GBSA methods to estimate ligand-binding affinities. *Expert Opin Drug Discov* 10, 449-461 (2015).
- 24 Chirgadze, Y and Nevskaya, N. Infrared spectra and resonance interaction of amide-I vibration of the antiparallel-chain pleated sheet. *Biopolymers* 15, 607-625 (1976).
- 25 Barth, A. Infrared spectroscopy of proteins. *Biochimica et Biophysica Acta (BBA)-Bioenergetics* 1767, 1073-1101 (2007).
- 26 Kogelheide, F., Kartaschew, K., Strack, M., Baldus, S., Metzler-Nolte, N., Havenith, M., Awakowicz, P., Stapelmann, K and Lackmann, J. FTIR spectroscopy of cysteine as a ready-to-use method for the investigation of plasma-induced chemical modifications of macromolecules. *Journal of Physics D: Applied Physics* 49, 084004 (2016).
- 27 Lu, H., Chai, J., Li, M., Huang, B., He, C and Bi, R. Crystal structure of human epidermal growth factor and its dimerization. *Journal of Biological Chemistry* 276, 34913-34917 (2001).
- 28 Narhi, L., Arakawa, T., Mcginley, M., Rohde, M and Westcott, R. Circular dichroism of reduced and oxidized recombinant human epidermal growth factor. *Chemical Biology & Drug Design* 39, 182-187 (1992).
- 29 Klinkhammer, C., Verlackt, C., Kogelheide, F., Bogaerts, A., Metzler-Nolte, N., Stapelmann, K., Havenith, M and Lackmann, J. Elucidation of Plasma-induced Chemical Modifications on Glutathione and Glutathione Disulphide. *Scientific reports* 7, 13828 (2017).

- 30 Emmert, S., Brehmer, F., Hänßle, H., Helmke, A., Mertens, N., Ahmed, R., Simon, D., Wandke, D., Maus-Friedrichs, W and Däschlein, G. Atmospheric pressure plasma in dermatology: Ulcus treatment and much more. *Clinical Plasma Medicine* 1, 24-29 (2013).
- 31 Keidar, M. Plasma for cancer treatment. *Plasma Sources Science and Technology* 24, 033001 (2015).
- 32 Hirst, A., Frame, F., Maitland, N and O'Connell, D. Low temperature plasma: a novel focal therapy for localized prostate cancer? *BioMed research international* 1-15, (2014).
- 33 Daeschlein, G., Assadian, O., Kloth, L., Meinel, C., Ney, F and Kramer, A. Antibacterial activity of positive and negative polarity low-voltage pulsed current (LVPC) on six typical Gram-positive and Gram-negative bacterial pathogens of chronic wounds. *Wound repair and regeneration* 15, 399-403 (2007).
- 34 Dezest, M., Chavatte, L., Bourdens, M., Quinton, D., Camus, M., Garrigues, L., Descargues, P., Arbault, S., Burlet-Schiltz, O and Casteilla, L. Mechanistic insights into the impact of Cold Atmospheric Pressure Plasma on human epithelial cell lines. *Scientific reports* 7, 41163 (2017).
- 35 Hirst, A., Simms, M., Mann, V., Maitland, N., O'Connell, D and Frame, F. Low-temperature plasma treatment induces DNA damage leading to necrotic cell death in primary prostate epithelial cells. *British journal of cancer* 112, 1536 (2015).
- 36 Berendsen, H. J., Postma, J. P., van Gunsteren, W and Hermans, J. *Intermolecular forces* 331-342 (Springer, 1981).
- 37 Bussi, G., Donadio, D and Parrinello, M. Canonical sampling through velocity rescaling. *Journal of Chemical Physics* 126, 014101 (2007).
- 38 Parrinello, M and Rahman, A. Polymorphic transitions in single crystals: A new molecular dynamics method. *Journal of Applied physics* 52, 7182-7190 (1981).
- 39 Essmann, U., Perera, L., Berkowitz, M., Darden, T., Lee, H and Pedersen, L. A smooth particle mesh Ewald method. *Journal of chemical physics* 103, 8577-8593 (1995).
- 40 Shrake, A and Rupley, J. Environment and exposure to solvent of protein atoms. Lysozyme and insulin. *Journal of molecular biology* 79, 351-371 (1973).
- 41 Brooks, B., Bruccoleri, R., Olafson, B., States, D., Swaminathan, S and Karplus, M. CHARMM: a program for macromolecular energy, minimization, and dynamics calculations. *Journal of computational chemistry* 4, 187-217 (1983).
- 42 Best, R., Zhu, X., Shim, J., Lopes, P., Mittal, J., Feig, M and MacKerell Jr, A. Optimization of the additive CHARMM all-atom protein force field targeting improved sampling of the backbone  $\phi$ ,  $\psi$  and side-chain  $\chi_1$  and  $\chi_2$  dihedral angles. *Journal of chemical theory and computation* 8, 3257-3273 (2012).
- 43 Vreven, T., Hwang, H and Weng, Z. Exploring angular distance in protein-protein docking algorithms. *PLoS One* 8, e56645 (2013).
- 44 Pierce, B and Weng, Z. ZRANK: reranking protein docking predictions with an optimized energy function. *Proteins: Structure, Function, and Bioinformatics* 67, 1078-1086 (2007).

- 45 Massova, I and Kollman, P. Combined molecular mechanical and continuum solvent approach (MM-PBSA/GBSA) to predict ligand binding. *Perspectives in drug discovery and design* 18, 113-135 (2000).
- 46 Mena-Ulecia, K., Vergara-Jaque, A., Poblete, H., Tiznado, W and Caballero, J. Study of the affinity between the protein kinase PKA and peptide substrates derived from kemptide using molecular dynamics simulations and MM/GBSA. *PloS one* 9, e109639 (2014).
- 47 Kurczab, R. The evaluation of QM/MM-driven molecular docking combined with MM/GBSA calculations as a halogen-bond scoring strategy. *Acta Crystallographica Section B: Structural Science, Crystal Engineering and Materials* 73 (2017).
- 48 Harder, E., Damm, W., Maple, J., Wu, C., Reboul, M., Xiang, J., Wang, L., Lupyan, D., Dahlgren, M., Knight, J and Kaus, J. OPLS3: a force field providing broad coverage of drug-like small molecules and proteins. *Journal of chemical theory and computation* 12, 281-296 (2015).
- 49 Homeyer, N and Gohlke, H. Free energy calculations by the molecular mechanics Poisson– Boltzmann surface area method. *Molecular Informatics* 31, 114-122 (2012).
- 50 Adasme-Carreño, F., Muñoz-Gutierrez, C., Caballero, J and Alzate-Morales, J. Performance of the MM/GBSA scoring using a binding site hydrogen bond network-based frame selection: the protein kinase case. *Physical Chemistry Chemical Physics* 16, 14047-14058 (2014).
- 51 Du, J., Sun, H., Xi, L., Li, J., Yang, Y., Liu, H and Yao, X. Molecular modeling study of checkpoint kinase 1 inhibitors by multiple docking strategies and prime/MM–GBSA calculation. *Journal of computational chemistry* 32, 2800-2809 (2011).
- 52 Li, J., Abel, R., Zhu, K., Cao, Y., Zhao, S and Friesner, R. The VSGB 2.0 model: a next generation energy model for high resolution protein structure modeling. *Proteins: Structure, Function, and Bioinformatics* 79, 2794-2812 (2011).
- 53 Zhang, C., Vasmatzis, G., Cornette, J and DeLisi, C. Determination of atomic desolvation energies from the structures of crystallized proteins1. *Journal of molecular biology* 267, 707-726 (1997).



## 4.4 Impact of plasma oxidation on the interaction between CD47 and SIRP $\alpha$ protein

### 4.4.1 Introduction

The immune system patrols the human body 24/7, fighting against pathogens, infections and cancer cells. The problem is that the immune system doesn't always recognize cancer cells as a foreign. Cancer cells produce specific proteins on the surface and use them as a protective shield to escape from the immune system.<sup>1-3</sup> Cancer immunotherapy aims to overcome this barrier, helping the immune system to identify cancer cells, as well as strengthen their resistance to destroy them.<sup>4</sup> In order to uncover the cancer cells, the patient's own T-cells are used. T-cells are trained in the lab, i.e., genetically engineered by adding chimeric antigen (CAR). Large numbers of these CAR T-cells are given back by infusion to the patient after growing in the lab. Modified T-cells easily detect and launch precise attack to cancer cells. Treatment takes only a few weeks but is too expensive: it costs around 200~350 thousand USD per full treatment.<sup>5,6</sup> Several side effects are also reported in cancer immunotherapy, in application of different strategies, such as adoptive T-cell transfer, peptide-based vaccines, checkpoint blockers, etc.<sup>7-11</sup> Despite these cons of immunotherapy, the survival rate significantly increased among cancer patients.<sup>12,13</sup> Indeed, the contribution of immune checkpoint inhibitors (ICIs) in this success is substantial.<sup>14,15</sup> For highly resistant forms of malignancies, where ICIs are less effective, often combination therapy with ICIs is needed.<sup>16</sup> In order to find the optimal strategy to improve the response of tumors, conventional therapies combined with ICIs are under extensive clinical trial.<sup>17-19</sup> Recently, it has been determined through *in vitro* experiments that CAP is also capable to induce immunogenic cell death (ICD).<sup>20-23</sup>

As mentioned above, CAP can be used as an alternative option to treat cancer cells. In clinical trials, the size of the tumor reduced considerably when CAP is used.<sup>24</sup> It is believed that the effect relies on increased intracellular oxidative damage induced by RONS, which ends up with arresting the cell cycle. Currently, research on plasma cancer treatment is mainly focused on examining the sensitivity of various cancer cell types, applying different CAP exposure times, varying feed gases, as well as different devices (plasma jet or DBD).<sup>25</sup> However, the contribution of the immune system in these treatments is generally overlooked. Lin *et al.* showed that plasma treatment facilitates detection of cancer cells by the immune system via ICD,<sup>20,21,26</sup> through the expression of damage associated molecular patterns (DAMPs) *in vitro*.<sup>20,27</sup> DAMP initiates signals such as "find me" via adenosine triphosphate and "eat me" via surface exposed calreticulin for immune cells. These both markers were observed in the experiments, which led to ICD. One of the positive signs of plasma treatment is that the migratory as well as anti-tumor function of antigen presenting cells (APC) was enhanced. APCs are the most vulnerable cells, which are often destroyed by conventional therapy, such as radiation therapy.<sup>28</sup> Bekeschus *et al.* studied the immunomodulatory features of CAP towards OVCAR-3 and SKOV-3 ovarian cancer cell lines.<sup>29</sup> Analysis of tumor cell supernatants indicated the role of small particles and interleukin 8 and 18, with MCP1 presumably driving activation in monocytes. Monocyte activation affects the macrophage polarization and this is one of the steps to cause immune response against cancer cells.

In fact, the experimental investigations in plasma-induced ICD are in premature stages. Besides, the precise action of plasma-generated RONS is still vague. In this regard, fundamental research is of prime importance, in order to get more complete insight in the molecular level mechanisms of ICD.

Cancer cells are known to produce specific proteins on their surface as a protective shield, to suppress immune responses against them.<sup>1-3</sup> For example, programmed death ligand (PD-L1) is upregulated in cancer cells and binding of the latter with its receptor PD-1 downregulates T-cell cytotoxicity.<sup>30</sup> Moreover, CD47 is also overexpressed in many cancer cell types. CD47 interacts with signal regulatory proteins (SIRP $\alpha$ ) and transfers a “don’t eat me” signal, inhibiting macrophage mediated destruction.<sup>31</sup> Regulation of the interactions between these so-called immune checkpoint proteins and their receptors via specific blockers are currently in clinical trial.<sup>14,15</sup> These monotherapies have significantly improved patient outcome, but when multiple immune checkpoint inhibitors (or blockers) are used in combination, the therapeutic response is further enhanced.<sup>32</sup> We can hypothesize that plasma-generated RONS can oxidize multiple immune checkpoint proteins on the surface of tumors, which act to suppress the immune system. Thus, this application of plasma might lead to a completely new paradigm in cancer immunotherapy, enhancing the immune system. In order to validate this paradigm, fundamental research is crucial to obtain more insight in the molecular level mechanisms of plasma-induced cancer immunotherapy.

Computer simulations have been successfully used as a powerful tool to study protein-protein interactions in many different fields.<sup>33,34</sup> Specifically, molecular level functions of immune checkpoint proteins are being investigated by MD simulations. For instance, Du *et al.* investigated the high affinity of PD-1 mutant using MD simulations, which helps to design engineered PD-1 mutants to modulate the PD-1/PD-L1 interaction.<sup>35</sup> The MHC binding with different peptides and their receptors has also been studied by MD simulations.<sup>36</sup> In general, the effect of mutations in proteins and drugs that block the binding of immune checkpoint proteins to receptors has been studied for PD-1 and PD-L1, CD47 and SIRP $\alpha$ , and CD86 and CTLA-4.<sup>31,37</sup>

We also investigated the interaction between CD47 and SIRP $\alpha$  by means of computer simulations. The cancer cells use CD47 as a protective shield from being engulfed by the immune system. Thus, targeting regulation of interaction between CD47 and SIRP $\alpha$  might be used for immune therapeutic purposes in cancer treatment. This can most likely be achieved by plasma induced oxidation of CD47, which alters its chemical and physical properties, causing structural changes, leading to regulation of the signaling pathways.

To date, the interaction between immune cell and cancer cell proteins under oxidative stress, as induced by plasma, has not been investigated yet by computer simulations, but is crucial for better insight in plasma cancer immunotherapy. In this regard, we studied the impact of plasma oxidation on the interaction between CD47 and SIRP $\alpha$  protein.

## 4.4.2 Computational details

### Simulation setup

We performed MD simulations in order to elucidate the stability of native and oxidized CD47 at the molecular level. The simulations were again carried out using the GROMACS<sup>38</sup> program package (version 5.1), applying the GROMOS 45a3 force field.<sup>39</sup> We employed the CD47-SIRP $\alpha$  complex structure (see [Figure 4.4.1](#)) obtained from the Protein Data Bank (ID: 4CMM).<sup>40</sup> The N and C terminal ends of each peptide are acetylated and capped with an amide group, respectively.

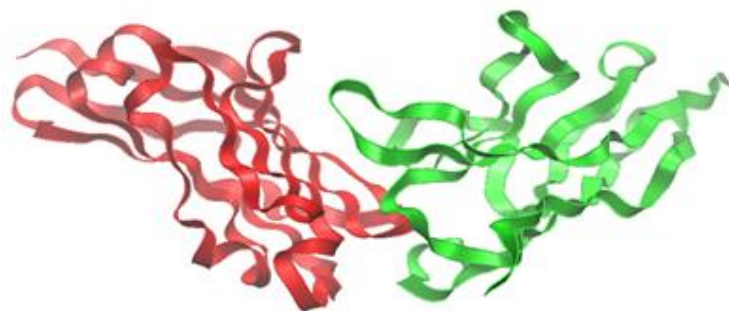


*Figure 4.4.1. Ribbon view of CD47 (red) and SIRP $\alpha$  (green) proteins.*

The native structure of the CD47-SIRP $\alpha$  complex ([Figure 4.4.1](#)) was placed in a dodecahedron box, spacing the atoms at least 1.1 nm from the boundaries of the simulation box. Subsequently, the box was filled with SPC water model<sup>41</sup> surrounding the CD47-SIRP $\alpha$  complex structure and 0.1 M of NaCl was added to neutralize the system. Besides the native CD47, we created an oxidized structure of CD47, by oxidizing 25% of the residues and we named it as OX. The modification of amino acids (AAs) involved in the creation of the oxidized state of the CD47 protein is given in previous section (see Table 4.3.1). The chemical structures of these (un)modified AAs are given in Table A1 of the Appendix of the previous section. These oxidized systems were prepared using a web server Viena-PTM 2.0<sup>42</sup> by replacing the residues of the native CD47 with oxidized ones. The force field parameters of the oxidized residues were obtained from <sup>43</sup>. This oxidized system was also placed in a simulation box filled with water, applying the above mentioned steps.

The two different model systems (i.e., native and OX) were energy minimized with the steepest descent algorithm. Subsequently, a 50 ps equilibration run was performed employing the NVT ensemble, applying the position restraint to the heavy atoms of the proteins. Next, a 150 ns production run was conducted using the NPT ensemble in the absence of a restraint. The simulations were carried out at 310 K and 1 bar, employing the Nose-Hoover thermostat<sup>44</sup> with a coupling constant of 0.5 ps and the isotropic Parrinello-Rahman barostat<sup>45</sup> with a compressibility and coupling constant of  $4.5 \times 10^{-5} \text{ bar}^{-1}$  and 2 ps, respectively. A 1.0 nm cut-off distance was applied for the van der Waals interactions. The long range electrostatic interactions were described by the particle mesh Ewald (PME) method.<sup>46</sup> The production run trajectory was used for data collection, i.e., to calculate the root mean square deviation (RMSD),<sup>47</sup> the solvent accessible surface area (SASA)<sup>48</sup> and the side chain hydrogen bonds between CD47 and SIRP $\alpha$ . The VMD visualizing tool was used to prepare images in this study.<sup>49</sup>

## **Umbrella sampling**

The starting structure of CD47- SIRP $\alpha$  in our US simulations was extracted from the final frame of the production run. The CD47- SIRP $\alpha$  structure was placed in a rectangular box and the size of the box was chosen adequately for pulling the SIRP $\alpha$  out of the CD47 structure along the  $z$ -axis. After adding counterions to the system with 0.1 M (NaCl), the system was equilibrated implementing the above mentioned steps (see previous section). Subsequently, applying an external force, the center of mass (COM) of SIRP $\alpha$  (see Figure 4.4.1) was pulled along the  $z$ -axis and CD47 was restrained and used as a reference for the pulling simulation. The external force induces displacement of SIRP $\alpha$  in the simulated system and it allows to calculate the energy in a path dependent manner, i.e., along the reaction coordinate. The pulling simulation lasted for 300 ps, applying 1000 kJ $\cdot$ mol $^{-1}$ nm $^2$  spring constant with a pulling rate of 0.01 nm/ps. We extracted 30 windows, calculating the distance between the COM of chain A and B, each separated by 0.1 nm along the  $z$ -axis. Each umbrella window was then equilibrated for 100 ps, followed by 20 ns of the US simulations. The output files generated from the US simulations were analyzed employing the weighted histogram analysis method (WHAM)<sup>50</sup> to calculate the potential mean force (PMF). The error associated with the PMF was estimated employing the bootstrapping method.<sup>51</sup>

#### 4.4.3 Results and discussion

[Figure 4.4.2](#) illustrates the time evolution of the RMSD of the backbone of the native and oxidized CD47 structures. The RMSD of the native CD47 structure is stable with low fluctuations. In the case of OX the RMSD fluctuations are increased. Oxidation of the CD47 residue leads to destabilization in the structure.

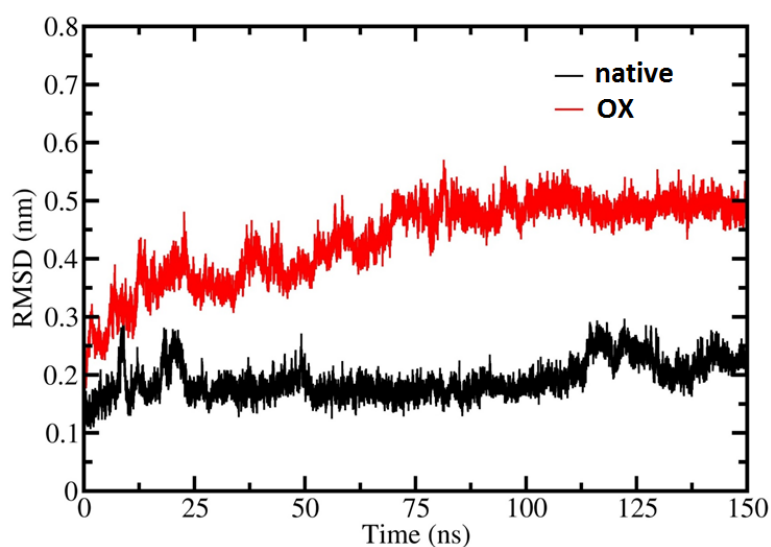


[Figure 4.4.2](#). *RMSD of the backbone of the native and oxidized structures of CD47.*

Further, we calculated the SASA of native and oxidized CD47 (see [Table 4.4.1](#)). The SASA is also increased in the oxidized structure of CD47 in comparison with native CD47. The higher fluctuations and increased SASA in oxidized CD47 lead to a drop in the number of hydrogen bonds between SIRP $\alpha$  protein and CD47 (cf. [Table 4.4.1](#)). Besides, it was

determined that two salt bridges (i.e., Lys6-Glu54 and Lys39-Asp100) between CD47 and SIRP $\alpha$  were disrupted after oxidation of the CD47 structure.

Table 4.4.1. Average SASA and number of hydrogen bonds between the proteins, with associated standard deviations, for the native and oxidized CD47 structures.

Systems	SASA (nm <sup>2</sup> ) CD47	H-bonds (CD47-SIRP $\alpha$ )
native	66.36 $\pm$ 1.36	14.06 $\pm$ 2.60
OX (25%)	69.67 $\pm$ 1.37	9.34 $\pm$ 2.28

In order to quantitatively estimate the interactions between CD47 (native and oxidized) and SIRP $\alpha$ , we performed US simulations to determine the binding free energies between these proteins. The binding free energy profiles help us to draw conclusions about the stability of interaction between the considered structures. [Figure 4.4.3](#) illustrates the PMF profile of SIRP $\alpha$  pulled against CD47. The difference between the minimum and maximum values of the PMF gives us the dissociation (or binding) free energy.

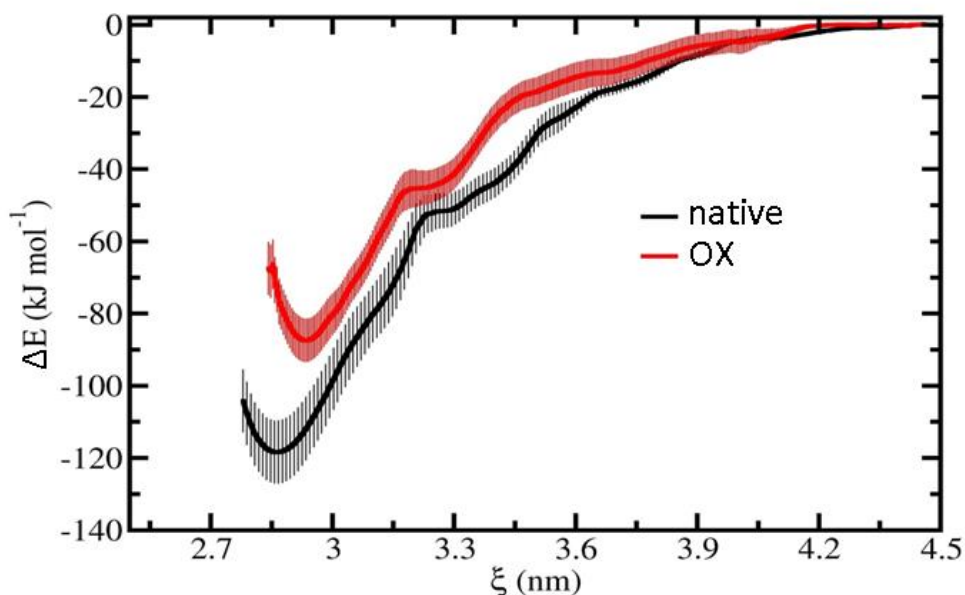


Figure 4.4.3. PMF profiles of the native and oxidized CD47 structures. The errors associated with the sampling are presented in pale color.

[Figure 4.4.3](#) shows that SIRP $\alpha$  totally disintegrates at 1.5 nm distance of the native CD47, whereas in the oxidized structure it can dissociate even at shorter distances, i.e., ~1.3 nm. This indicates that the interaction between CD47 and SIRP $\alpha$  weakens after oxidation of CD47 takes place. The calculated dissociation free energies are found to be -119 and -89 kJ/mol for the native and OX system, respectively. Hence, oxidation leads to a lower binding free energy. Note that, in reality, chemical reactions of RONS might occur on CD47, oxidizing the AAs or breaking the peptide bonds. This probably induces even higher damage to the

structure of CD47. However, reaction processes cannot be revealed by conventional non-reactive MD simulations, through the applied potential. Despite these limitations, the US simulations assist to determine consequences of oxidation to the interaction between CD47 and SIRP $\alpha$ , through calculations of the PMFs.

#### **4.4.4 Conclusion**

Our MD simulation results indicate that oxidation of CD47 leads to a higher flexibility, thereby increasing the solvent accessibility. The obtained US MD simulation results show that oxidation of CD47 reduces the inter-protein binding free energy and this might disrupt the “don’t eat me” signal for immune cells. This can be linked to the experiments performed by Dr. Lin within our group, as plasma treatment oxidizes CD47, thereby disturbing the “don’t eat me” signal, blocking CD47’s function. Blockage of the “don’t eat me” signal might eventually lead to engulfing the cancer cell by the immune cells.

#### 4.4.5 References

- 1 Zhang, C and Fu, Y. Another way to not get eaten. *Nature immunology* 19, 6 (2018).
- 2 Casey, S., Tong, L., Li, Y., Do, R., Walz, S., Fitzgerald, K.N., Gouw, A.M., Baylot, V., Gütgemann, I., Eilers, M. and Felsher, D. MYC regulates the antitumor immune response through CD47 and PD-L1. *Science* 352, 227-231 (2016).
- 3 Chao, M., Jaiswal, S., Weissman-Tsukamoto, R., Alizadeh, A., Gentles, A., Volkmer, J., Weiskopf, K., Willingham, S., Raveh, T., Park, C and Majeti, R. Calreticulin is the dominant pro-phagocytic signal on multiple human cancers and is counterbalanced by CD47. *Science translational medicine* 2, 63ra94-63ra94 (2010).
- 4 Galluzzi, L., Vacchelli, E., Bravo-San Pedro, J., Buqué, A., Senovilla, L., Baracco, E., Bloy, N., Castoldi, F., Abastado, J., Agostinis, P and Apte, R. Classification of current anticancer immunotherapies. *Oncotarget* 5, 12472 (2014).
- 5 June, C., O'Connor, R., Kawalekar, O., Ghassemi, S and Milone, M. CAR T cell immunotherapy for human cancer. *Science* 359, 1361-1365 (2018).
- 6 Hettle, R., Corbett, M., Hinde, S., Hodgson, R., Jones-Diette, J., Woolacott, N. and Palmer, S. The assessment and appraisal of regenerative medicines and cell therapy products: an exploration of methods for review, economic evaluation and appraisal. *Health technology assessment*, 1-204 (2017).
- 7 Weber, J., Yang, J., Atkins, M and Disis, M. Toxicities of immunotherapy for the practitioner. *Journal of Clinical Oncology* 33, 2092 (2015).
- 8 Bonifant, C., Jackson, H., Brentjens, R and Curran, K. Toxicity and management in CAR T-cell therapy. *Molecular Therapy-Oncolytics* 3 (2016).
- 9 Davila, M., Riviere, I., Wang, X., Bartido, S., Park, J., Curran, K., Chung, S.S., Stefanski, J., Borquez-Ojeda, O., Olszewska, M and Qu, J. Efficacy and toxicity management of 19-28z CAR T cell therapy in B cell acute lymphoblastic leukemia. *Science translational medicine* 6, 224ra225-224ra225 (2014).
- 10 Kroschinsky, F., Stölzel, F., von Bonin, S., Beutel, G., Kochanek, M., Kiehl, M and Schellongowski, P. New drugs, new toxicities: severe side effects of modern targeted and immunotherapy of cancer and their management. *Critical Care* 21, 89 (2017).
- 11 Heinzerling, L., Ott, P., Hodi, F., Husain, A., Tajmir-Riahi, A., Tawbi, H., Pauschinger, M., Gajewski, T., Lipson, E and Luke, J. Cardiotoxicity associated with CTLA4 and PD1 blocking immunotherapy. *Journal for immunotherapy of cancer* 4, 50 (2016).
- 12 Sharma, P., Wagner, K., Wolchok, J and Allison, J. Novel cancer immunotherapy agents with survival benefit: recent successes and next steps. *Nature Reviews Cancer* 11, 805 (2011).
- 13 Morrison, C., Pabla, S., Conroy, J., Nesline, M., Glenn, S., Dressman, D., Papanicolaou-Sengos, A., Burgher, B., Andreas, J., Giamo, V and Qin, M. Predicting response to checkpoint inhibitors in melanoma beyond PD-L1 and mutational burden. *Journal for immunotherapy of cancer* 6, 32 (2018).
- 14 Wolchok, J., Kluger, H., Callahan, M., Postow, M., Rizvi, N., Lesokhin, A., Segal, N., Ariyan, C., Gordon, R and Reed, K. Nivolumab plus ipilimumab in advanced melanoma. *New England Journal of Medicine* 369, 122-133 (2013).

- 15 Snyder, A., Makarov, V., Merghoub, T., Yuan, J., Zaretsky, J., Desrichard, A., Walsh, L., Postow, M., Wong, P and Ho, T. Genetic basis for clinical response to CTLA-4 blockade in melanoma. *New England Journal of Medicine* 371, 2189-2199 (2014).
- 16 Patel, S and Minn, A. Combination Cancer therapy with immune checkpoint blockade: mechanisms and strategies. *Immunity* 48, 417-433 (2018).
- 17 Li, X., Shao, C., Shi, Y and Han, W. Lessons learned from the blockade of immune checkpoints in cancer immunotherapy. *Journal of hematology & oncology* 11, 31 (2018).
- 18 Langer, C., Gadgeel, S., Borghaei, H., Papadimitrakopoulou, V., Patnaik, A., Powell, S. F., Gentzler, R., Martins, R., Stevenson, J and Jalal, S. Carboplatin and pemetrexed with or without pembrolizumab for advanced, non-squamous non-small-cell lung cancer. *The Lancet Oncology* 17, 1497-1508 (2016).
- 19 Pfirschke, C., Engblom, C., Rickelt, S., Cortez-Retamozo, V., Garris, C., Pucci, F., Yamazaki, T., Poirier-Colame, V., Newton, A., and Redouane, Y. Immunogenic chemotherapy sensitizes tumors to checkpoint blockade therapy. *Immunity* 44, 343-354 (2016).
- 20 Lin, A., Truong, B., Patel, S., Kaushik, N., Choi, E., Fridman, G., Fridman, A., and Miller, V. Nanosecond-pulsed DBD plasma-generated reactive oxygen species trigger immunogenic cell death in A549 lung carcinoma cells through intracellular oxidative stress. *International journal of molecular sciences* 18, 966 (2017).
- 21 Lin, A., Xiang, B., Merlino, D. , Baybutt, T., Sahu, J., Fridman, A., Snook, A and Miller, V. Non-thermal plasma induces immunogenic cell death in vivo in murine CT26 colorectal tumors. *OncoImmunology* 9, e1484978 (2018).
- 22 Bekeschus, S., Clemen, R and Metelmann, H. Potentiating Anti-Tumor Immunity with Physical Plasma. *Clinical Plasma Medicine* (2018).
- 23 Bekeschus, S., Mueller, A., Miller, V., Gaipf, U and Weltmann, K.. Physical plasma elicits immunogenic cancer cell death and mitochondrial singlet oxygen. *IEEE Transactions on Radiation and Plasma Medical Sciences* 2, 138-146 (2018).
- 24 Metelmann, H., Nedrelow, D., Seebauer, C., Schuster, M., von Woedtke, T., Weltmann, K., Kindler, S., Metelmann, P., Finkelstein, S., and Von Hoff, D. Head and neck cancer treatment and physical plasma. *Clinical Plasma Medicine* 3, 17-23 (2015).
- 25 Dubuc, A., Monsarrat, P., Virard, F., Merbahi, N., Sarrette, J., Laurencin-Dalicioux, S., and Cousty, S. Use of cold-atmospheric plasma in oncology: a concise systematic review. *Therapeutic advances in medical oncology* 10, (2018).
- 26 Lin, A., Gorbanev, Y., De Backer, J., Van Loenhout, J., Van Boxem, W., Lemièrre, F., Cos, P., Dewilde, S., Smits, E and Bogaerts, A. Non-Thermal Plasma as a Unique Delivery System of Short-Lived Reactive Oxygen and Nitrogen Species for Immunogenic Cell Death in Melanoma Cells. *Advanced Science*, 1802062 (2019).
- 27 Lin, A., Truong, B., Pappas, A., Kirifides, L., Oubarri, A., Chen, S., Lin, S., Dobrynin, D., Fridman, G and Fridman, A. Uniform nanosecond pulsed dielectric barrier discharge plasma enhances anti-tumor effects by induction of immunogenic cell death in tumors and stimulation of macrophages. *Plasma processes and polymers* 12, 1392-1399 (2015).

- 28 Manda, K., Glasow, A., Paape, D and Hildebrandt, G. Effects of ionizing radiation on the immune system with special emphasis on the interaction of dendritic and T cells. *Frontiers in oncology* 2, 102 (2012).
- 29 Bekeschus, S., Wulf, C., Freund, E., Koensgen, D., Mustea, A., Weltmann, K and Stope, M. Plasma Treatment of Ovarian Cancer Cells Mitigates Their Immuno-Modulatory Products Active on THP-1 Monocytes. *Plasma* 1, 201-217 (2018).
- 30 Zak, K., Kitel, R., Przetocka, S., Golik, P., Guzik, K., Musielak, B., Dömling, A., Dubin, G and Holak, T. Structure of the complex of human programmed death 1, PD-1, and its ligand PD-L1. *Structure* 23, 2341-2348 (2015).
- 31 Weiskopf, K., Ring, A., Ho, M., Volkmer, J., Levin, A., Volkmer, A., Özkan, E., Fernhoff, N., van de Rijn, M and Weissman, I. Engineered SIRP $\alpha$  variants as immunotherapeutic adjuvants to anticancer antibodies. *Science* 341, 88-91 (2013).
- 32 Larkin, J., Chiarion-Sileni, V., Gonzalez, R., Grob, J. J., Cowey, C. L., Lao, C. D., Schadendorf, D., Dummer, R., Smylie, M., and Rutkowski, P. Combined nivolumab and ipilimumab or monotherapy in untreated melanoma. *New England Journal of Medicine* 373, 23-34 (2015).
- 33 Scott, D., Bayly, A., Abell, C and Skidmore, J. Small molecules, big targets: drug discovery faces the protein-protein interaction challenge. *Nature Reviews Drug Discovery* 15, 533 (2016).
- 34 Kortemme, T., Joachimiak, L., Bullock, A., Schuler, A., Stoddard, B and Baker, D. Computational redesign of protein-protein interaction specificity. *Nature Structural and Molecular Biology* 11, 371 (2004).
- 35 Du, J., Qin, Y., Wu, Y., Zhao, W., Zhai, W., Qi, Y., Wang, C and Gao, Y. The design of high affinity human PD-1 mutants by using molecular dynamics simulations (MD). *Cell Communication and Signaling* 16, 25 (2018).
- 36 Knapp, B., Demharter, S., Esmailbeiki, R and Deane, C. M. Current status and future challenges in T-cell receptor/peptide/MHC molecular dynamics simulations. *Briefings in bioinformatics* 16, 1035-1044 (2015).
- 37 Lee, J., Lee, H., Shin, W., Chae, J., Choi, J., Kim, S., Lim, H., Heo, T., Park, K and Lee, Y. Structural basis of checkpoint blockade by monoclonal antibodies in cancer immunotherapy. *Nature communications* 7, 13354 (2016).
- 38 Van Der Spoel, D., Lindahl, E., Hess, B., Groenhof, G., Mark, A and Berendsen, H. *et al.* GROMACS: fast, flexible, and free. *Journal of computational chemistry* 26, 1701-1718 (2005).
- 39 Schuler, L. D., Daura, X and Van Gunsteren, W. F. An improved GROMOS96 force field for aliphatic hydrocarbons in the condensed phase. *Journal of Computational Chemistry* 22, 1205-1218 (2001).
- 40 Hatherley, D., Lea, S., Johnson, S and Barclay, A. Polymorphisms in the human inhibitory signal-regulatory protein  $\alpha$  do not affect binding to its ligand CD47. *Journal of Biological Chemistry* 289, 10024-10028 (2014).
- 41 Berendsen, H., Postma, J., van Gunsteren, W and Hermans, J. *Intermolecular forces* 331-342 (Springer, 1981).

- 42 Margreitter, C., Petrov, D and Zagrovic, B. Vienna-PTM web server: a toolkit for MD simulations of protein post-translational modifications. *Nucleic acids research* 41, W422-W426 (2013).
- 43 Petrov, D., Margreitter, C., Grandits, M., Oostenbrink, C and Zagrovic, B. A systematic framework for molecular dynamics simulations of protein post-translational modifications. *PLoS computational biology* 9, e1003154 (2013).
- 44 Hoover, W. Canonical dynamics: equilibrium phase-space distributions. *Physical review A* 31, 1695 (1985).
- 45 Parrinello, M and Rahman, A. Polymorphic transitions in single crystals: A new molecular dynamics method. *Journal of Applied physics* 52, 7182-7190 (1981).
- 46 Essmann, U., Perera, L., Berkowitz, M., Darden, T., Lee, H and Pedersen, L. A smooth particle mesh Ewald method. *The Journal of chemical physics* 103, 8577-8593 (1995).
- 47 Maiorov, V and Crippen, G. Size-independent comparison of protein three-dimensional structures. *Proteins: Structure, Function, and Bioinformatics* 22, 273-283 (1995).
- 48 Eisenhaber, F., Lijnzaad, P., Argos, P., Sander, C and Scharf, M. The double cubic lattice method: efficient approaches to numerical integration of surface area and volume and to dot surface contouring of molecular assemblies. *Journal of Computational Chemistry* 16, 273-284 (1995).
- 49 Humphrey, W., Dalke, A and Schulten, K. VMD: visual molecular dynamics. *Journal of molecular graphics* 14, 33-38 (1996).
- 50 Kumar, S., Rosenberg, J., Bouzida, D., Swendsen, R and Kollman, P. A. The weighted histogram analysis method for free-energy calculations on biomolecules. I. The method. *Journal of computational chemistry* 13, 1011-1021 (1992).
- 51 Hub, J and de Groot, B. Does CO<sub>2</sub> permeate through aquaporin-1? *Biophysical Journal* 91, 842-848 (2006).



# **Summary and Samenvatting**

## Summary, Conclusion and Future Outlook

Cancer still remains one of the diseases with highest mortality rate. There is a need for novel cancer therapies, as current therapies have their limitations. One possible new therapy is “plasma oncology”, which is one of the branches of plasma medicine. In clinical trials, the size of the tumor reduced considerably when using cold atmospheric plasma (CAP). Moreover, many *in vitro* and *in vivo* studies also demonstrated the beneficial effects of CAP against many cancer cell lines. Despite these promising findings in plasma oncology, the molecular level mechanisms are still poorly understood. In order to accurately and effectively control CAP application in the clinic, the precise mechanisms of the interaction of plasma agents with cells and biomolecules need to be elucidated.

Thus, next to experimental studies, computer simulations may provide fundamental insight about the occurring processes, both in the plasma and in interaction with biomolecules, which is difficult or even impossible to obtain by experimental tools. Therefore, in this PhD thesis, we investigated the effect of oxidation on the characterization of the PLBs and on various types of proteins, in the context of plasma oncology, and plasma medicine in general.

The plasma-generated reactive oxygen and nitrogen species (RONS) interact with the cell membrane during CAP treatment. These RONS induce oxidation of the phospholipids. Therefore, it is important to investigate translocation of RONS across native and oxidized cell membranes. We calculated free energy profiles of RONS in [Chapter 3](#) (section [3.1](#)), and our results indicate that the free energy barrier decreases for hydrophilic species (such as OH, HO<sub>2</sub> and H<sub>2</sub>O<sub>2</sub>) upon oxidation of the PLB, while hydrophobic species (like NO, NO<sub>2</sub>, N<sub>2</sub>O<sub>4</sub>, O<sub>2</sub> and O<sub>3</sub>) can significantly better penetrate across both native and oxidized PLBs. These findings are an important step towards the understanding of the penetration capabilities of different RONS through the native and oxidized cell membrane.

It was experimentally demonstrated that CAP treatment increases the glucose uptake in skeletal muscle cells. The glucose uptake is important for diabetes treatment, because cells of diabetic patients become resistant, leading to high levels of glucose in the blood. By means of MD simulations, we studied the possible mechanisms of glucose uptake stimulated by CAP treatment in [Chapter 3](#) (section [3.2](#)). The computed free energy profiles of glucose through native and oxidized PLBs revealed that plasma-induced oxidation of the membrane lipids decreases the barrier for translocation of glucose across the membrane. This might possibly explain the increased concentration of glucose observed by experiments using CAP.

Further, in [Chapter 3](#) (section [3.3](#)) we studied the flip-flop motion of phosphatidylserine (PS) across native and oxidized PLBs. PS is one of the lipids that is involved in activation of the “eat me” signal for lymphocytes when found in the upper leaflet of the PLB. Our results showed that the energy barrier for PS flip-flop across the PLB drops upon increasing peroxidation level.

Overall, we can conclude from [Chapter 3](#) that oxidation of the lipids results in expansion of the membrane area, which causes a noticeable change in the membrane permeability.

In [Chapter 4](#), we studied the effect of oxidation on one of the abundant cell constituents, i.e., proteins.

Experiments demonstrated that CAP exposure efficiently degrades amyloid fibrils in aqueous solutions. As amyloid beta ( $A\beta$ ) peptide aggregates trigger neurodegenerative diseases in brain, such as Alzheimer's disease, we studied in [Chapter 4](#) (section [4.1](#)) the effect of oxidation on the stability of the  $A\beta$  pentamer, employing MD and umbrella sampling (US) simulations, mimicking the experimental conditions. The results demonstrated that low and moderate degrees of oxidation have insignificant impact on the conformation and stability, whereas a higher oxidation degree, leading to disruption of the salt bridge, yields a considerable disturbance of the structure. We performed US simulations to calculate the dissociation free energies of the terminal peptides in the pentamer structure. These calculations also showed that the dissociation free energy drops upon increasing the oxidative percentage in the structure. This is a molecular level hallmark for the possible inhibition of  $A\beta$  pentamer aggregation by CAP oxidation.

In [Chapter 4](#) (section [4.2](#)) we performed MD and docking simulations in order to investigate the role of CAP oxidation on the enzymatic function of cytoglobin (Cygb). Our results indicated that the disulfide bond formation in Cygb influences its structure, thereby opening the access to the heme group through the gate functioning of His117, which in turn leads to a higher binding affinity. In other words, the modification of  $Cygb_{S-S}$  should lead to intense peroxidation, as well as a higher scavenger activity of  $Cygb_{S-S}$ . Our results are in line with experimental observations by J. De Backer. Moreover, they provide molecular level insight that Cygb plays a role in the cellular response against oxidative stress.

Further, in [Chapter 4](#) (section [4.3](#)) we investigated the structural conformation and binding affinity of human epidermal growth factor (hEGF) to its receptor, under oxidative stress. hEGF is one of the important signaling proteins playing a role in wound healing, as well as cancer treatment. Our MD and docking simulations show that a low amount of oxidation has minor effect on the binding affinity of hEGF with its receptor. This most likely does not strongly influence the signaling pathways in a cell, and thereby the cell proliferation, which might explain why CAP at short treatment times is beneficial for chronic wound healing. A higher level of oxidation of hEGF causes less interaction with its receptor, which most probably causes a disturbance of the signaling pathways in a cell, ultimately leading to a disruption of the cell proliferation. This might explain the effect of CAP at longer treatment times on inhibiting cancer cell proliferation and even cancer cell death.

Finally, in [Chapter 4](#) (section [4.4](#)) we studied the interaction between immune cell and cancer cell proteins under oxidative stress). More specifically, we studied the impact of plasma oxidation on the interaction between CD47 and SIRP $\alpha$  protein, because CD47 expresses a "don't eat me" signal through binding to SIRP $\alpha$  protein, downregulating the immune cells against cancer cells. Our US MD simulations show that oxidation of CD47 reduces the inter-protein binding free energy that might disrupt the "don't eat me" signal for immune cells. Blockage of the "don't eat me" signal might eventually lead to engulfing the

cancer cell by the immune cells. This protein-protein interaction study might help to get better insight in plasma for cancer immunotherapy.

In conclusion, our MD investigations have tried to provide molecular level insight in the underlying mechanisms of some plasma medicine applications, with major focus on cancer. Experiments have indeed demonstrated that the treatment of cancer cells with CAP leads to cancer cell death. However, in order to translate this basic research towards clinical applications, much more scientific work is needed to expand our knowledge on CAP-cell interactions. Besides clinical trials, needed to further evaluate the clinical applicability of CAP, the plasma medicine community would benefit from acquiring more detailed insight in the underlying mechanisms, by fundamental investigations. Recently, studies have revealed that plasma may help to stimulate the patient's anti-cancer immune response via induction of immunogenic cancer cell death (ICD). This is a new paradigm of plasma treatment for cancer: 'plasma oncoimmunotherapy'. In spite of the promising results, experimental investigations in plasma-induced ICD are still in premature stages, and the precise action of plasma is still unclear. Therefore, the underlying mechanisms require more fundamental investigations. I would therefore like to perform atomic scale computer simulations in order to precisely determine the role of plasma in immune-oncology, by investigating the effect of plasma-induced oxidation on the interaction mechanism of signaling proteins, which normally inhibit the cytotoxicity of the immune cells. These investigations will help to elucidate the molecular level mechanisms of the role of plasma-generated RONS in cancer immunotherapy.

## Samenvatting, Conclusie en Toekomstplannen

Kanker is momenteel nog steeds een van de ziekten met het hoogste sterftecijfer. Er is dus behoefte aan nieuwe kankertherapieën, omdat de huidige therapieën hun beperkingen hebben. Een mogelijke nieuwe therapie is "plasma oncologie", een van de takken van plasmageneeskunde. In klinische studies nam de tumor aanzienlijk af bij het gebruik van koud atmosferisch plasma (CAP). Bovendien toonden vele *in vitro* en *in vivo* studies ook de gunstige effecten van CAP tegen een groot aantal kankercellijnen. Ondanks deze veelbelovende bevindingen in de plasma-oncologie, worden de mechanismen op moleculair niveau nog steeds slecht begrepen. Om CAP in klinische toepassingen accuraat en effectief te kunnen gebruiken, moeten de precieze mechanismen die aan de basis liggen van de interactie van plasma-componenten met cellen en biomoleculen worden opgehelderd.

Naast experimentele studies, kunnen computersimulaties fundamenteel inzicht verschaffen over de onderliggende processen, zowel in het plasma als in interactie met biomoleculen, wat experimenteel soms moeilijk of zelfs onmogelijk te verkrijgen is. Daarom hebben we in dit proefschrift onderzoek gedaan naar het effect van oxidatie op de karakterisatie van osfolipide dubbellen (PLB's) en op verschillende soorten eiwitten, in de context van plasma-oncologie en plasmageneeskunde in het algemeen.

De plasma-gegenereerde reactieve zuurstof- en stikstofdeeltjes (RONS) komen in interactie met het celmembraan tijdens CAP-behandeling. Deze RONS induceren oxidatie van de fosfolipiden. Daarom is het belangrijk om de translocatie van RONS doorheen niet-geoxideerde en geoxideerde celmembranen te onderzoeken. We berekenden vrije energieprofielen van RONS in [Hoofdstuk 3](#) (sectie [3.1](#)) en onze resultaten geven aan dat de vrije energiebarrière afneemt voor hydrofiele deeltjes (zoals OH, HO<sub>2</sub> en H<sub>2</sub>O<sub>2</sub>) na oxidatie van de PLB, terwijl hydrofobe deeltjes (zoals NO, NO<sub>2</sub>, N<sub>2</sub>O<sub>4</sub>, O<sub>2</sub> en O<sub>3</sub>) veel beter kunnen doordringen, in zowel niet-geoxideerde als geoxideerde PLB's. Deze bevindingen zijn een belangrijke stap op weg naar het beter begrijpen van hoe verschillende RONS door niet-geoxideerde en geoxideerde celmembranen kunnen doordringen.

Er werd experimenteel aangetoond dat CAP-behandeling de glucoseopname in skeletspiercellen verhoogt. De glucoseopname is belangrijk voor de behandeling van diabetes, omdat cellen van diabetische patiënten resistent worden, wat leidt tot hoge glucosespiegels in het bloed. Met behulp van moleculaire dynamics (MD) simulaties hebben we in [Hoofdstuk 3](#) (sectie [3.2](#)) de mogelijke mechanismen van glucoseopname onderzocht, gestimuleerd door CAP-behandeling. De berekende vrije energieprofielen van glucose door niet-geoxideerde en geoxideerde PLB's toonden aan dat plasma-geïnduceerde oxidatie van de membraanlipiden de barrière vermindert voor translocatie van glucose over het membraan. Dit zou mogelijk de verhoogde glucoseconcentratie kunnen verklaren, die wordt waargenomen in experimenten met CAP.

Verder hebben we in [Hoofdstuk 3](#) (sectie [3.3](#)) de flip-flop beweging van fosfatidylserine (PS) bestudeerd over niet-geoxideerde en geoxideerde PLB's. PS is een van de lipiden die betrokken is bij activering van het "eat me" -signaal voor lymfocyten in de bovenste laag van

de PLB. Onze resultaten toonden aan dat de energiebarrière voor PS-flip-flop over de PLB afneemt bij het verhogen van het peroxidatieniveau.

In het algemeen kunnen we uit [Hoofdstuk 3](#) concluderen dat oxidatie van de lipiden resulteert in expansie van het membraanoppervlak, wat een merkbare verandering in de membraanpermeabiliteit veroorzaakt.

In [Hoofdstuk 4](#) hebben we het effect van oxidatie op een van de belangrijkste celcomponenten, nl. eiwitten, bestudeerd.

Experimenten hebben aangetoond dat CAP-blootstelling efficiënt amyloïde fibrillen degradeert in waterige oplossingen. Omdat amyloïde beta ( $A\beta$ ) peptide-aggregaten neurodegeneratieve ziekten in de hersenen teweegbrengen, zoals de ziekte van Alzheimer, bestudeerden we in [Hoofdstuk 4](#) (sectie [4.1](#)) het effect van oxidatie op de stabiliteit van het  $A\beta$ -pentameer, met behulp van MD en “umbrella sampling” (US) simulaties, voor experimentele condities. De resultaten toonden aan dat een lage en middelmatige graad van oxidatie een beperkte invloed heeft op de conformatie en stabiliteit, terwijl een hogere oxidatiegraad, wat aanleiding geeft tot verstoring van de zoutbrug, een aanzienlijke verstoring van de structuur oplevert. We hebben US simulaties uitgevoerd om de dissociatie vrije energieën van de eindstandige peptiden in de pentameerstructuur te berekenen. Deze berekeningen toonden ook aan dat de dissociatie vrije energie daalt bij het verhogen van de oxidatiegraad in de structuur. Dit is een “kenmerk” op moleculair niveau voor de mogelijke remming van  $A\beta$ -pentameer-aggregatie door CAP-oxidatie.

In [Hoofdstuk 4](#) (sectie [4.2](#)) hebben we MD en “docking” simulaties uitgevoerd om de rol van CAP-oxidatie op de enzymatische functie van cytoglobine (Cygb) te onderzoeken. Onze resultaten toonden aan dat de vorming van disulfidebindingen in Cygb de structuur beïnvloedt, waardoor de toegang tot de heemgroep wordt geopend via de “gate”-functie van His117, wat op zijn beurt leidt tot een hogere bindingsaffiniteit. Met andere woorden, de modificatie van  $Cygb_{S-S}$  moet leiden tot intense peroxidatie, evenals een hogere scavenger-activiteit van  $Cygb_{S-S}$ . Onze resultaten zijn in lijn met experimentele waarnemingen van J. De Backer. Bovendien bieden ze moleculair inzicht in de rol van Cygb in de cellulaire respons tegen oxidatieve stress.

Verder hebben we in [Hoofdstuk 4](#) (sectie [4.3](#)) de structurele conformatie en bindingsaffiniteit van humane epidermale groeifactor (hEGF) voor zijn receptor onder oxidatieve stress onderzocht. hEGF is een van de belangrijke signaleiwitten die een rol speelt bij wondgenezing, evenals bij de behandeling van kanker. Onze MD en “docking” simulaties tonen aan dat een lage graad van oxidatie een gering effect heeft op de bindingsaffiniteit van hEGF met zijn receptor. Dit heeft hoogstwaarschijnlijk geen grote invloed op de signaalroutes in een cel en daarmee op de celproliferatie, wat zou kunnen verklaren waarom CAP bij korte behandelingstijden gunstig is voor chronische wondgenezing. Een hogere graad van oxidatie van hEGF veroorzaakt minder interactie met zijn receptor, wat hoogstwaarschijnlijk een verstoring van de signaalroutes in een cel veroorzaakt, uiteindelijk leidend tot een verstoring van de celproliferatie. Dit zou het effect van CAP bij langere

behandelingsduur kunnen verklaren, in het remmen van de proliferatie van kankercellen en zelfs de dood van kankercellen.

Tenslotte onderzochten we in [Hoofdstuk 4](#) (sectie [4.4](#)) de interactie tussen immuuncel- en kanker-eiwitten onder oxidatieve stress. Meer specifiek hebben we de impact van plasma-oxidatie op de interactie tussen CD47 en SIRP $\alpha$ -eiwit bestudeerd, omdat CD47 een "do not eat me" signaal tot expressie brengt door binding aan SIRP $\alpha$ -eiwit, waardoor de activiteit van immuuncellen tegen kankercellen gerduceerd wordt. Onze US MD simulaties tonen aan dat oxidatie van CD47 de vrije energie van binding tussen eiwitten vermindert, wat het "do not eat me" signaal voor immuuncellen zou kunnen verstoren. Blokkering van het "do not eat me" signaal kan uiteindelijk leiden tot het verzwelgen van de kanker cel door de immuuncellen. Deze eiwit-eiwit interactiestudies kunnen helpen om een beter inzicht te krijgen in plasma voor kankerimmunotherapie.

In conclusie, onze MD simulaties hebben getracht inzicht te bieden op moleculair niveau in de onderliggende mechanismen van bepaalde toepassingen in de plasmageneeskunde, en vooral in kankeronderzoek. Experimenten hebben inderdaad aangetoond dat de behandeling van kankercellen met CAP leidt tot de dood van deze kankercellen. Om dit basisonderzoek te vertalen naar klinische toepassingen, is echter nog veel meer wetenschappelijk onderzoek nodig, om onze kennis over CAP-celinteracties uit te breiden. Naast klinische studies, nodig om de klinische toepasbaarheid van CAP te evalueren, zou het onderzoek in de plasmageneeskunde erbij gebaat zijn om meer gedetailleerd inzicht te verwerven in de onderliggende mechanismen, door fundamenteel onderzoek. Onlangs hebben studies aangetoond dat plasma de immunorespons van een patiënt kan stimuleren via inductie van immunogene kankerceldood (ICD). Dit is een nieuw paradigma van plasmabehandeling voor kanker: 'plasma-oncoimmunotherapie'. Ondanks veelbelovende resultaten staat het experimentele onderzoek naar plasma-geïnduceerde ICD nog in de kinderschoenen, en is de precieze werking van plasma nog niet volledig opgehelderd. Daarom vereisen de onderliggende mechanismen meer fundamenteel onderzoek. Ik zou daarom graag computersimulaties op atomaire schaal uitvoeren om de rol van plasma in immuun-oncologie nauwkeurig te bepalen, door het effect van oxidatie op het interactiemechanisme van signaal-eiwitten te onderzoeken, die normaal de cytotoxiciteit van de immuuncellen kunnen remmen. Deze onderzoeken zullen helpen om de mechanismen op moleculair niveau van de rol van plasma-gegenereerde RONS in kankerimmunotherapie te verduidelijken.



# **Academic curriculum vitae**



## List of publications included in this thesis

1. Razzokov, J., Yusupov, M. and Bogaerts, A. Oxidation destabilizes toxic amyloid beta peptide aggregation. *Scientific Reports*. in press (2019)
2. De Backer J, Razzokov J, Hammerschmid D, Mensch C, Hafideddine Z, Kumar N, van Raemdonck G, Yusupov M, Van Doorslaer S, Johannessen C, Sobott F. The effect of reactive oxygen and nitrogen species on the structure of cytoglobin: A potential tumor suppressor. *Redox Biology*. 19, 1-10. (2018)
3. Razzokov, J., Yusupov, M., Cordeiro, R.M. and Bogaerts, A. Atomic scale understanding of the permeation of plasma species across native and oxidized membranes. *Journal of Physics D: Applied Physics*. 51(36), p.365203. (2018)
4. Razzokov, J., Yusupov, M. and Bogaerts, A., Possible Mechanism of Glucose Uptake Enhanced by Cold Atmospheric Plasma: Atomic Scale Simulations. *Plasma*, 1(1), p.119-125. (2018) (special issue on Plasma Medicine)
5. Yusupov, M., Lackmann, J.W., Razzokov, J., Kumar, S., Stapelmann, K. and Bogaerts, A., Impact of plasma oxidation on structural features of human epidermal growth factor. *Plasma Processes and Polymers*, 15(8), p.e1800022. (2018)
6. Razzokov J, Yusupov M, Vanuytsel S, Neyts EC, Bogaerts A. Phosphatidylserine flip-flop induced by oxidation of the plasma membrane: a better insight by atomic scale modeling. *Plasma Processes and Polymers*. 1;14(10). (2017)



## List of publications not included in this thesis

1. Ghasemitarei, M., Yusupov, M., Razzokov, J., Shokri, B., Bogaerts, A. Transport of cystine across  $x\text{C}^-$  antiporter. *Archives of Biochemistry and Biophysics*. 664, 117-126, (2019)
2. Vanmeert M, Razokov J, Mirza MU, Weeks S, Schepers G, Froeyen M, Herdewijn P, Pinheiro V.B, Bogaerts A, Lescrinier E.. Docking unbound nucleic acids into ring-shaped proteins to engineer the first XNA ligase. *Nucleic Acid Research*. submitted (2019)
3. Razzokov J, Naderi S, Van Der Schoot P. Nanoscale insight into silk-like protein self-assembly: effect of design and number of repeat units. *Physical Biology*. 15(6). (2018)
4. Kumar N, Shaw P, Razzokov J, Yusupov M, Attri P, Uhm HS, Choi EH, Bogaerts A. Enhancement of cellular glucose uptake by reactive species: a promising approach for diabetes therapy. *RSC advances*. 8(18). (2018)
5. Razzokov J, Naderi S, Van Der Schoot P. Prediction of the structure of a silk-like protein in oligomeric states using explicit and implicit solvent models. *Soft matter*. 10(29). (2014)
6. Razzokov J, Ismailova O, Mamatkulov S, Trunilina O, Kokhkharov A. Heteromolecular structures in aqueous solutions of dimethylformamide and tetrahydrofuran, according to molecular dynamics data. *Russian Journal of Physical Chemistry A*. 88(9). (2014)



## Conference contributions

1. Razzokov J, Yusupov M, Bogaerts A. Will oxidation stimulate or destabilize amyloid fibril formation? Answers from atomic scale simulations. 6th International Workshop on Plasma for Cancer Treatment. April 1-3, 2019. Antwerp, Belgium. (*poster presentation*)
2. Razzokov J, Yusupov M, Bogaerts A. Permeation of RONS and glucose across the native and oxidized membranes: answers from molecular dynamics simulations. 3rd Strasbourg Workshop on Membrane Biophysics. December 3-4, 2018. Strasbourg, France. (*poster presentation*)
3. Razzokov J, Yusupov M, Bogaerts A. Effect of oxidation on the stability of amyloid protofibril. 5th International Conference "Dynamics of Systems on the Nanoscale". October 8 -12, 2018. Potsdam, Germany. (*oral presentation*)
4. Razzokov J, Lin A, Bogaerts A. Impact of plasma oxidation to the interaction between CD47 and SIRP $\alpha$  protein: atomic scale study. 7th Young Professionals Workshop on Plasma Medicine. September 23-26, 2018. Rostock, Germany. (*oral presentation*)
5. Razzokov J and Bogaerts A. Transport of reactive oxygen and nitrogen species across native and oxidized phospholipid membrane. 7th International Conference on Plasma Medicine. June 17-22, 2018. Philadelphia, USA. (*oral presentation*)
6. Razzokov J, Kumar N, Bogaerts A. Glucose intake in native plasma membrane vs oxidized plasma membrane: an atomic scale study. 6th Young Professionals Workshop on Plasma Medicine. October 23-26, 2017. Rostock, Germany. (*oral presentation*)
7. Razzokov J, Bogaerts A. Effect of plasma oxidation on properties of globular proteins: an atomic scale study. iPlasmaNano-VIII, July 2-6, 2017. Antwerp, Belgium. (*poster presentation*)
8. Razzokov J, Bogaerts A. Modeling phosphatidylserine flip-flop in the plasma membrane of cells: a better insight in apoptosis. 6th International Conference on Plasma Medicine (ICPM-6). September 4-9, 2016. Bratislava, Slovakia. (*poster presentation*)